



UNIVERSITY OF WEST ATTICA  
DEPARTMENT OF MECHANICAL  
ENGINEERING

AERODYNAMIC STUDY AND DESIGN OF AN FSAE-  
TYPE VEHICLE'S FRONT WING

PERIFANAS ALEXANDROS

REGISTRATION NUMBER: 461272017031

SUPERVISOR: I. SARRIS

ATHENS, OCTOBER 2023



ΠΑΝΕΠΙΣΤΗΜΙΟ ΔΥΤΙΚΗΣ  
ΑΤΤΙΚΗΣ  
ΤΜΗΜΑ ΜΗΧΑΝΟΛΟΓΩΝ  
ΜΗΧΑΝΙΚΩΝ

ΑΕΡΟΔΥΝΑΜΙΚΗ ΜΕΛΕΤΗ ΚΑΙ ΣΧΕΔΙΑΣΜΟΣ  
ΕΜΠΡΟΣΘΙΑΣ ΑΕΡΟΤΟΜΗΣ ΟΧΗΜΑΤΟΣ ΤΥΠΟΥ FSAE

ΠΕΡΙΦΑΝΑΣ ΑΛΕΞΑΝΔΡΟΣ

ΑΡΙΘΜΟΣ ΜΗΤΡΩΟΥ: 461272017031

ΕΠΙΒΛΕΠΩΝ ΚΑΘΗΓΗΤΗΣ: Ι. ΣΑΡΡΗΣ

ΑΘΗΝΑ, ΟΚΤΩΒΡΙΟΣ 2023

Η ΤΡΙΜΕΛΗΣ ΕΞΕΤΑΣΤΙΚΗ ΕΠΙΤΡΟΠΗ

ΙΩΑΝΝΗΣ ΣΑΡΡΗΣ	
ΓΕΩΡΓΙΟΣ ΣΟΦΙΑΔΗΣ	
ΕΥΑΓΓΕΛΟΣ ΚΑΡΒΕΛΑΣ	

## ΔΗΛΩΣΗ ΣΥΓΓΡΑΦΕΑ ΔΙΠΛΩΜΑΤΙΚΗΣ ΕΡΓΑΣΙΑΣ

Ο κάτωθι υπογεγραμμένος ΠΕΡΙΦΑΝΑΣ ΑΛΕΞΑΝΔΡΟΣ του ΔΗΜΗΤΡΙΟΥ ΑΝΑΣΤΑΣΙΟΥ, με αριθμό μητρώου 461272017031 φοιτητής του Πανεπιστημίου Δυτικής Αττικής της Σχολής Μηχανικών του Τμήματος Μηχανολόγων Μηχανικών, δηλώνω υπεύθυνα ότι:

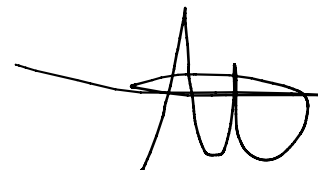
«Είμαι συγγραφέας αυτής της διπλωματικής εργασίας και ότι κάθε βοήθεια την οποία είχα για την προετοιμασία της είναι πλήρως αναγνωρισμένη και αναφέρεται στην εργασία. Επίσης, οι όποιες πηγές από τις οποίες έκανα χρήση δεδομένων, ιδεών ή λέξεων, είτε ακριβώς είτε παραφρασμένες, αναφέρονται στο σύνολό τους, με πλήρη αναφορά στους συγγραφείς, τον εκδοτικό οίκο ή το περιοδικό, συμπεριλαμβανομένων και των πηγών που ενδεχομένως χρησιμοποιήθηκαν από το διαδίκτυο. Επίσης, βεβαιώνω ότι αυτή η εργασία έχει συγγραφεί από μένα αποκλειστικά και αποτελεί προϊόν πνευματικής ιδιοκτησίας τόσο δικής μου, όσο και του Ιδρύματος.

Παράβαση της ανωτέρω ακαδημαϊκής μου ευθύνης αποτελεί ουσιώδη λόγο για την ανάκληση του πτυχίου μου».

Ημερομηνία

19/09/2023

Ο Δηλών



ΠΕΡΙΦΑΝΑΣ ΑΛΕΞΑΝΔΡΟΣ



Copyright © ΠΕΡΙΦΑΝΑΣ ΑΛΕΞΑΝΔΡΟΣ 2023

Με επιφύλαξη παντός δικαιώματος. All rights reserved. Απαγορεύεται η αντιγραφή, αποθήκευση και διανομή της παρούσας εργασίας, εξ ολοκλήρου ή τμήματος αυτής, για εμπορικό σκοπό. Επιτρέπεται η ανατύπωση, αποθήκευση και διανομή για σκοπό μη κερδοσκοπικό, εκπαιδευτικής ή ερευνητικής φύσεως, υπό την προϋπόθεση να αναφέρεται η πηγή προέλευσης και να διατηρείται το παρόν μήνυμα. Ερωτήματα που αφορούν στη χρήση της εργασίας για κερδοσκοπικό σκοπό πρέπει να απευθύνονται προς τον συγγραφέα. Οι απόψεις και τα συμπεράσματα που περιέχονται σε αυτό το έγγραφο εκφράζουν τον συγγραφέα και δεν επιτρέπεται να ερμηνευθεί ότι αντιπροσωπεύουν τις επίσημες θέσεις του Πανεπιστημίου Δυτικής Αττικής.

## ACKNOWLEDGEMENTS

First and foremost, I would like to thank my supervisors, Mr. G. Sofiadis and Dr. I. Sarris, who helped me throughout the whole process of writing my thesis as their advice and guidance was vital for the completion of my research, as well as Mr. E. Karvelas for being a part of the committee.

I would also like to thank my family for the invaluable support and faith they have had in me throughout my studies to obtain my degree. The tolerance my parents and my sister have had for me all these years and the selfless help they have given me cannot be repaid, and for that they deserve the greatest gratitude.

Last but not least, I would like to thank my friends who helped me in the preparation of my thesis presentation, as well as for the encouragement they gave me, even though they were mocking me every day by calling me geek and nerd.

## ABSTRACT

The field of motorsport requires extensive study for the design of a prototype racing car, as the parameters that affect the final result are numerous and complex. In this thesis, a detailed aerodynamic and static study is carried out in order to optimize the front wing of the Poseidon Racing Team's (UniWA) racing vehicle, aiming for the most efficient design solution. All the main aerodynamic variables governing the field of fluid mechanics, the objectives and main characteristics related to motorsport (more specifically the Formula Student institution), as well as the necessary information concerning the methodology, which mainly includes design solutions, computational fluid dynamics (CFD) and finite element analysis (FEA), are described in the first chapter of the thesis. The methodology applied was based on the objectives set from the beginning of the study, which in brief are to achieve the maximum negative lift that the front airfoil can produce, and to keep drag forces at low values. As part of the design, the dimensions and geometries were based on the regulations set by the Formula Student competition and literature references regarding the most dominant standard airfoil geometries used in motorsport. In addition, the available computational and time resources of the team were taken into account, as the facilities and time for the study and design of the airfoil are limited. The parameters and settings of the CFD analyses in which the computational model, the mesh properties, and the area in which the geometries (fluid domain) will be placed were determined by specific processes described in the methodology chapter. The CFD model that has been used is RANS. The optimal solution, according to the available resources, was found through 5 sets of analyses, which determined the standard airfoil that was used, the height at which the front airfoil was placed, the angles of attack of the two wings that were used, as well as the horizontal and vertical distance between the two. Once the CFD analyses were completed, the final design, which includes the wing mounts and external wing supports, which also help in optimizing the flow as described in Chapter 3, was statically analyzed by means of Finite Element Analysis, in order to prove that the final geometry complies with the regulations concerning the airfoil structure. Using the space available from the regulations, the length, width, and height of the airfoil are 545, 1305 and 180 mm respectively. The standard airfoil used is the Selig 1223, at an angle of attack of 3 degrees for the primary flap which was placed 50 mm above the ground, and 35 degrees for the secondary (flap), as the horizontal distance between them is 10 mm, and the vertical distance is 30 mm respectively. For the static analysis, a vertical equally distributed force of 5000 N, was applied on the geometry in order to test its maximum displacement. The material of the assembly was decided to be carbon fiber reinforced with epoxy (due to its high strength and its low weight). The maximum displacement of the geometry resulted to be 2.87 mm, which is within the acceptable range of 10 mm that is set by the competition. For design and safety reasons, the maximum acceptable displacement of the geometry was reduced to 6.5 mm (1.5 safety factor was applied).

Keywords: Aerodynamics, Computational fluid dynamics (CFD), Finite element analysis (FEA), Formula Student, Motorsport

## ΠΕΡΙΛΗΨΗ

Ο τομέας του μηχανοκίνητου αθλητισμού απαιτεί εκτεταμένη μελέτη για το σχεδιασμό ενός πρωτότυπου αγωνιστικού αυτοκινήτου, καθώς οι παράμετροι που επηρεάζουν το τελικό αποτέλεσμα είναι πολυάριθμες και πολύπλοκες. Στην παρούσα διπλωματική εργασία πραγματοποιείται λεπτομερής αεροδυναμική και στατική μελέτη με σκοπό τη βελτιστοποίηση της εμπρός πτέρυγας του αγωνιστικού οχήματος της Poseidon Racing Team (UniWA), με στόχο την αποδοτικότερη σχεδιαστική λύση. Στο πρώτο κεφάλαιο της διπλωματικής περιγράφονται όλες οι βασικές αεροδυναμικές μεταβλητές που διέπουν τον τομέα της ρευστομηχανικής, οι στόχοι και τα κύρια χαρακτηριστικά που σχετίζονται με τον μηχανοκίνητο αθλητισμό (πιο συγκεκριμένα με τον θεσμό Formula Student), καθώς και οι απαραίτητες πληροφορίες σχετικά με τη μεθοδολογία, η οποία περιλαμβάνει κυρίως σχεδιαστικές λύσεις, υπολογιστική ρευστοδυναμική (CFD) και ανάλυση πεπερασμένων στοιχείων (FEA). Η μεθοδολογία που εφαρμόστηκε βασίστηκε στους στόχους που τέθηκαν από την αρχή της μελέτης, οι οποίοι συνοπτικά είναι η επίτευξη της μέγιστης αρνητικής άντωσης που μπορεί να παράγει η εμπρόσθια αεροτομή και η διατήρηση των δυνάμεων οπισθέλκουσας σε χαμηλές τιμές. Στο πλαίσιο του σχεδιασμού, οι διαστάσεις και οι γεωμετρίες βασίστηκαν στους κανονισμούς που θέτει ο διαγωνισμός Formula Student και σε βιβλιογραφικές αναφορές σχετικά με τις επικρατέστερες τυπικές γεωμετρίες αεροτομών που χρησιμοποιούνται στον μηχανοκίνητο αθλητισμό. Επιπλέον, λήφθηκαν υπόψη οι διαθέσιμοι υπολογιστικοί και χρονικοί πόροι της ομάδας, καθώς οι εγκαταστάσεις και ο χρόνος για τη μελέτη και το σχεδιασμό της αεροτομής είναι περιορισμένοι. Οι παράμετροι και οι ρυθμίσεις των CFD αναλύσεων στις οποίες θα τοποθετηθεί το υπολογιστικό μοντέλο, οι ιδιότητες του πλέγματος και η περιοχή στην οποία θα τοποθετηθούν οι γεωμετρίες (πεδίο ρευστού) καθορίστηκαν με συγκεκριμένες διαδικασίες που περιγράφονται στο κεφάλαιο της μεθοδολογίας. Το μοντέλο CFD που χρησιμοποιήθηκε είναι το RANS. Η βέλτιστη λύση, σύμφωνα με τους διαθέσιμους πόρους, βρέθηκε μέσα από 5 σειρές αναλύσεων, οι οποίες καθόρισαν την πρότυπη αεροτομή που χρησιμοποιήθηκε, το ύψος στο οποίο τοποθετήθηκε η μπροστινή αεροτομή, τις γωνίες προσβολής των δύο πτερύγων που χρησιμοποιήθηκαν, καθώς και την οριζόντια και κάθετη απόσταση μεταξύ τους. Αφού ολοκληρώθηκαν οι αναλύσεις CFD, το τελικό σχέδιο, το οποίο περιλαμβάνει τις βάσεις των πτερύγων και τα εξωτερικά στηρίγματα των πτερύγων, τα οποία βοηθούν επίσης στη βελτιστοποίηση της ροής, όπως περιγράφεται στο κεφάλαιο 3, αναλύθηκε στατικά μέσω της ανάλυσης πεπερασμένων στοιχείων, προκειμένου να αποδειχθεί ότι η τελική γεωμετρία συμμορφώνεται με τους κανονισμούς που αφορούν τη δομή και την αντοχή της αεροτομής. Χρησιμοποιώντας τον διαθέσιμο χώρο από τους κανονισμούς, το μήκος, το πλάτος και το ύψος της αεροτομής είναι 545, 1305 και 180 mm αντίστοιχα. Η πρότυπη αεροτομή που χρησιμοποιήθηκε είναι η Selig 1223, με γωνία προσβολής 3 μοίρες για το πρωτεύον πτερύγιο που τοποθετήθηκε 50 mm πάνω από το έδαφος και 35 μοίρες για το δευτερεύον (πτερύγιο), καθώς η οριζόντια απόσταση μεταξύ τους είναι 10 mm και η κάθετη απόσταση 30 mm αντίστοιχα. Για τη στατική ανάλυση, εφαρμόστηκε στη γεωμετρία μια κατακόρυφη ισοκατανεμημένη δύναμη 5000 N, προκειμένου να δοκιμαστεί η μέγιστη παραμόρφωση της. Το υλικό της διάταξης αποφασίστηκε να είναι ανθρακόνημα ενισχυμένο με εποξικό υλικό (λόγω της υψηλής αντοχής του και του χαμηλού βάρους του). Η μέγιστη μετατόπιση της γεωμετρίας προέκυψε 2,87 mm, η οποία βρίσκεται εντός του αποδεκτού εύρους των 10 mm που ορίζει ο διαγωνισμός. Για λόγους σχεδιασμού και ασφάλειας, η μέγιστη αποδεκτή μετατόπιση της γεωμετρίας μειώθηκε στα 6,5 mm (εφαρμόστηκε συντελεστής ασφαλείας 1,5).





## AERODYNAMIC STUDY AND DESIGN OF AN FSAE-TYPE VEHICLE'S FRONT WING



Λέξεις κλειδιά: Αεροδυναμική, Υπολογιστική ρευστομηχανική (CFD), Ανάλυση πεπερασμένων στοιχείων (FEA), Μηχανοκίνητος αθλητισμός

## NOMENCLATURE

P	Pressure
$\rho$	Density
$\nu$	Kinematic Viscosity
$\mu$	Dynamic Viscosity
CFD	Computation Fluid Dynamics
FEA	Finite Element Analysis
Re	Reynolds Number
L	Lift Force
D	Drag Force
$C_L$	Lift Coefficient
$C_D$	Drag Coefficient
Ma	Mach Number
$V_\infty$	Freestream Velocity
AOA	Angle of Attack
$\delta$	Boundary Layer Thickness
A	Reference Area
$C_p$	Pressure Coefficient
FSG	Formula Student Germany
N-S	Navier-Stokes
RANS	Reynolds-Averaged Navier-Stokes
DNS	Direct Numerical Simulation
LES	Large Eddy Simulation
URANS	Unsteady RANS
k- $\epsilon$	k-epsilon
k- $\omega$	k-omega
BOI	Body of influence
$C_L/C_D$	Lift/Drag ratio

## TABLE OF CONTENTS

<b>1. Introduction.....</b>	<b>20</b>
1.1. Historical Retrospect.....	20
1.2. Motorsport Aerodynamics .....	21
1.2.1. Introduction .....	21
1.2.2. Basic Aerodynamic Terms.....	22
1.2.2.1 Air Properties.....	22
1.2.2.2 Dimensionless Numbers.....	23
1.2.2.3 Boundary Layer.....	25
1.2.2.4 Flow Visualization (Streamlines).....	26
1.2.2.5 Aerodynamic Forces .....	27
1.2.2.6 Aerodynamic Coefficients.....	30
1.2.2.7 Bernoulli equation .....	33
1.3. Formula Student .....	34
1.3.1. Brief overview.....	34
1.3.2. Formula Student Regulations .....	35
1.3.3. Formula Student Car Aerodynamic Parts .....	35
1.4. Airfoil Theory .....	40
1.4.1. Definition of an airfoil.....	40
1.4.2. Anatomy of airfoils.....	42
1.5. Computational Fluid Dynamics (CFD).....	43
1.5.1. Introduction to Computational Fluid Dynamics .....	43
1.5.2. Advantages and disadvantages of CFD.....	44
1.5.3. Meshing properties .....	44
1.5.4. Governing equations of fluid dynamics.....	46
1.5.5. Navier Stokes Equations .....	47
1.5.6. CFD Solving Models .....	49
1.6. Current Literature .....	50
1.7. Scope of the Thesis.....	51
<b>2. Methodology .....</b>	<b>52</b>
2.1. Basic Methodology Steps .....	52



2.2.	Design Approach.....	53
2.2.1.	Design constraints.....	53
2.2.2.	Basic design steps .....	56
2.3.	Computational Fluid Dynamics Simulations (CFD) .....	59
2.3.1.	Pre-processing .....	59
2.3.1.1	Enclosure creation .....	59
2.3.1.2	Mesh generation.....	62
2.3.1.3	Mesh independence study .....	65
2.3.2.	Solving.....	68
2.3.2.1	Boundary conditions.....	68
2.3.2.2	Model selection .....	69
2.3.2.3	Type of flow .....	70
2.3.2.4	Reference values and simulation run settings.....	72
2.3.3.	Post-processing.....	75
2.4.	Finite Element Analysis (FEA) .....	76
<b>3.</b>	<b>Simulation runs and results.....</b>	<b>79</b>
3.1.	Main Element (Airfoil Profile Selection) .....	79
3.2.	Ground Clearance .....	87
3.3.	Secondary Element (flap) .....	93
3.4.	Vertical Distance Between Elements .....	96
3.5.	Horizontal Distance Between Elements .....	100
3.6.	Final Assembly .....	104
3.7.	FEA simulation results .....	109
<b>4.</b>	<b>Conclusions and Future Study .....</b>	<b>112</b>
4.1.	CFD simulations conclusions.....	112
4.2.	Design and manufacturing conclusions.....	113
4.3.	Future study.....	114
	<b>References .....</b>	<b>117</b>
	<b>Appendix A .....</b>	<b>121</b>
	A.1 Velocity and pressure contours of Selig 1223, Selig 3021, Selig 1210 and Eppler 423 at -3°, 0° and 9° AOA .....	121



A.2 Pressure contours of Selig 1223 at 3° AOA for h1=10 mm and h1=90 mm .....	129
A.3 Velocity and pressure contours of Selig 1223 (flap) at 15°, 20° and 45° AOA .....	130
A.4 Velocity and pressure contours of vertical distance h2=15 mm and h2= 20 mm .....	132
A.5 Velocity and pressure contours of horizontal distance h3=-30 mm, h3= -20 mm, h3=-10 mm, h3=10 mm, h3=20 mm and h3=30 mm .....	134
<b>Appendix B .....</b>	<b>137</b>
B.1 Selig 1223 coordinates .....	137
B.2 Selig 1210 coordinates .....	139
B.3 Selig 3021 coordinates .....	141
B.4 Eppler 423 coordinates .....	143

## LIST OF FIGURES

<b>Figure 1.1</b> First engine powered flight (Wright Brothers, 1903) .....	20
<b>Figure 1.2</b> Wind tunnel testing of Wright brothers' airplane (NASA, 1999) .....	20
<b>Figure 1.3</b> CFD simulation of a wind turbine (Simscale, 2017) .....	20
<b>Figure 1.4</b> Formula 1 car Simca Gordini 15 (Great Britain, 1952) .....	21
<b>Figure 1.5</b> Michael Schumacher's 2003 Ferrari F2003-GA (Fiorano, 2022) .....	22
<b>Figure 1.6</b> Transition process from a laminar to a turbulent boundary layer over a flat plate.....	23
<b>Figure 1.7</b> Flow around a cylinder.....	24
<b>Figure 1.8</b> Boundary layer on flat plate .....	26
<b>Figure 1.9</b> Attached and separated flow around circular cylinder (James Ramsay,2019) .....	27
<b>Figure 1.10</b> Attached and separated flow on a commercial car .....	27
<b>Figure 1.11</b> Components of drag force on a solid body.....	28
<b>Figure 1.12</b> Aerodynamic Forces acting on an airfoil.....	29
<b>Figure 1.13</b> Aerodynamic Force R as a combination of the lift force and drag force components (Nakayama, 2018) .....	29
<b>Figure 1.14</b> Measure drag coefficients for various shapes (Sape A. Miedema, 2011).....	31
<b>Figure 1.15</b> Typical lift and drag coefficients for various ground vehicles (Joseph Katz, 2016) .....	31
<b>Figure 1.16</b> Two-dimensional flow around a cylinder (Williams,2021) .....	32
<b>Figure 1.17</b> Pressure distribution around and airfoil .....	32
<b>Figure 1.18</b> Air flow around a vehicle where the Bernoulli equation can be used at points A, B and $\infty$ ...	33
<b>Figure 1.19</b> Formula Student East competition contestants (FS East, 2021) .....	34
<b>Figure 1.20</b> Main aerodynamic devices of a Formula Student race car (SPbPU,2022).....	36
<b>Figure 1.21</b> Formula Student car side pod.....	36
<b>Figure 1.22</b> Venturi effect diagram .....	37
<b>Figure 1.23</b> Underbody of a 2022 F1 car (Gary Anderson, 2022) .....	37
<b>Figure 1.24</b> (a) one-element without endplates; (b) one-element with endplates; (c) three-element without endplates; (d) three-element with endplates (Xabier Castro and Zeeshan A. Rana, 2020)..	38
<b>Figure 1.25</b> Basic configuration of a FSAE car rear wing.....	39
<b>Figure 1.26</b> Nose cone of a Formula Student Car (Poseidon Racing Team, 2023) .....	39
<b>Figure 1.27</b> Typical airfoils (Reymer, 2018). .....	40
<b>Figure 1.28</b> Symmetrical and Asymmetrical (Cambered) wing profiles.....	41
<b>Figure 1.29</b> Selig 1223 wing profile (high lift airfoil) .....	41
<b>Figure 1.30</b> NACA 0009 wing profile (low lift airfoil) .....	42
<b>Figure 1.31</b> Cross-section of an airfoil (Kevadiya, 2013).....	43
<b>Figure 1.32</b> Flow visualization of a Formula Student Car using CFD software (Simscale, 2018) .....	43
<b>Figure 1.33</b> Triangular and quadrilateral shaped cells for surface meshing .....	45
<b>Figure 1.34</b> Tetrahedral, hexahedral and pyramid shaped cells for volume meshing .....	45
<b>Figure 1.35</b> Layering (inflation) around a wing profile.....	45
<b>Figure 1.36</b> The anatomy of a meshing element (Philip Luke K, 2021).....	46
<b>Figure 1.37</b> Conservation of mass within a control volume (Hautala, 2020).....	46
<b>Figure 1.38</b> Characteristics of turbulence models in CFD .....	48
<b>Figure 1.39</b> Simulation accuracy of RANS, LES, and DNS modelling methods.....	49
<b>Figure 1.40</b> K-omega SST model (combination of k- $\epsilon$ and k- $\omega$ models) (Simscale, 2023) .....	50
<b>Figure 2.1</b> Diagram presenting the basic methodology steps of the study .....	52
<b>Figure 2.2</b> FSG regulation regarding the design around the wheels (FSG, 2023) .....	54
<b>Figure 2.3</b> FSG design limitations on dimensions of aerodynamic devices (FSG, 2023).....	54
<b>Figure 2.4</b> Restrictions in dimensions of the front wing assembly (side view).....	55



<b>Figure 2.5</b> Restrictions in dimensions of the front wing assembly (front view) .....	55
<b>Figure 2.6</b> Bounding box of the available for the front wing assembly (3D view) .....	56
<b>Figure 2.7</b> Selig 1210 (S1210) wing profile.....	57
<b>Figure 2.8</b> Selig 1223 (S1223) wing profile.....	57
<b>Figure 2.9</b> Eppler 423 (E423) wing profile.....	57
<b>Figure 2.10</b> Selig 3021 (S3021) wing profile .....	57
<b>Figure 2.11</b> 3D design of the S1210 wing profile .....	58
<b>Figure 2.12</b> Example of two-element front wing assembly design.....	59
<b>Figure 2.13</b> Dimensions of the enclosure (Simscale, 2023) .....	60
<b>Figure 2.14</b> Enclosure and body of influence around the airfoil.....	61
<b>Figure 2.15</b> Mesh sizing for coarse mesh quality (250,000 elements) .....	64
<b>Figure 2.16</b> Mesh sizing for moderate mesh quality (500,000 elements) .....	64
<b>Figure 2.17</b> Mesh sizing for fine mesh quality (1,000,000 elements).....	65
<b>Figure 2.18</b> Mesh sizing for very fine mesh quality (2,000,000 elements) .....	65
<b>Figure 2.19</b> Lift coefficient results for S3021 airfoil at different mesh qualities.....	66
<b>Figure 2.20</b> Drag coefficient results for S3021 airfoil at different mesh qualities .....	67
<b>Figure 2.21</b> Simulation time per iteration for all mesh qualities .....	67
<b>Figure 2.22</b> Boundary conditions on enclosure walls .....	68
<b>Figure 2.23</b> Total simulation time for k-epsilon, k-omega, and k-omega SST models.....	70
<b>Figure 2.24</b> Simulation time per iteration for steady and transient flow .....	72
<b>Figure 2.25</b> Reference values set on solver of the simulations.....	72
<b>Figure 2.26</b> Frontal area of a commercial vehicle (Wu and Liu, 2011) .....	73
<b>Figure 2.27</b> Projected area of Selig 1223 airfoil .....	73
<b>Figure 2.28</b> Convergence of residuals of the S1223 (0° AOA) simulation run .....	74
<b>Figure 2.29</b> Static pressure and velocity magnitude of a NACA 0012 airfoil geometry (Ganesh Ram et al., 2014) .....	75
<b>Figure 2.30</b> Streamline around an airfoil geometry (Ahmed et al., 2011).....	76
<b>Figure 2.31</b> Forces and fixed geometries on the front wing assembly .....	77
<b>Figure 2.32</b> Solid mesh a front wing configuration using Solidworks Simulation .....	78
<b>Figure 3.1</b> Selig 1210 in 3° AOA placed in the simulation's enclosure .....	79
<b>Figure 3.2</b> Lift coefficient in all AOA from the first set of simulations .....	81
<b>Figure 3.3</b> Drag coefficient in all AOA from the first set of simulations.....	82
<b>Figure 3.4</b> Lift/Drag ratio in all AOA from the first set of simulations .....	82
<b>Figure 3.5</b> Velocity contour of S1210 at 3° AOA .....	83
<b>Figure 3.6</b> Velocity contour of S1223 at 3° AOA .....	83
<b>Figure 3.7</b> Velocity contour of E423 at 3° AOA .....	83
<b>Figure 3.8</b> Velocity contour of S3021 at 3° AOA .....	83
<b>Figure 3.9</b> Velocity contour of S1210 at 6° AOA .....	84
<b>Figure 3.10</b> Velocity contour of S1223 at 6° AOA .....	84
<b>Figure 3.11</b> Velocity contour of E423 at 6° AOA .....	84
<b>Figure 3.12</b> Velocity contour of S3021 at 6° AOA .....	84
<b>Figure 3.13</b> Pressure contour of S1210 at 3° AOA .....	85
<b>Figure 3.14</b> Pressure contour of S1223 at 3° AOA .....	85
<b>Figure 3.15</b> Pressure contour of E423 at 3° AOA .....	85
<b>Figure 3.16</b> Pressure contour of S3021 at 3° AOA .....	85
<b>Figure 3.17</b> Pressure contour of S1210 at 6° AOA .....	85
<b>Figure 3.18</b> Pressure contour of S1223 at 6° AOA .....	85
<b>Figure 3.19</b> Pressure contour of E423 at 6° AOA .....	86



<b>Figure 3.20</b> Pressure contour of S3021 at 3° AOA .....	86
<b>Figure 3.21</b> Road clearance ( $h_1$ ) of the main element .....	87
<b>Figure 3.22</b> Velocity contour of S1223 ( $h_1=10$ mm).....	88
<b>Figure 3.23</b> Velocity contour of S1223 ( $h_1=90$ mm).....	88
<b>Figure 3.24</b> Lift and drag coefficients results for all heights ( $h_1$ ) from the road.....	88
<b>Figure 3.25</b> Lift/drag ratio results for all heights ( $h_1$ ) from the road.....	89
<b>Figure 3.26</b> Velocity contour for $h_1=30$ mm.....	89
<b>Figure 3.27</b> Velocity contour for $h_1=50$ mm.....	90
<b>Figure 3.28</b> Velocity contour for $h_1=70$ mm.....	90
<b>Figure 3.29</b> Pressure contour for $h_1=30$ mm.....	91
<b>Figure 3.30</b> Pressure contour for $h_1=50$ mm.....	91
<b>Figure 3.31</b> Pressure contour for $h_1=70$ mm.....	91
<b>Figure 3.32</b> Velocity streamline of S1223 300 mm from the road.....	91
<b>Figure 3.33</b> Velocity streamline of S1223 50 mm from the road.....	91
<b>Figure 3.34</b> Two element configuration placed in the simulation's fluid domain .....	93
<b>Figure 3.35</b> Lift and drag coefficients results for all AOA of the flap .....	94
<b>Figure 3.36</b> Lift/drag ratio results for all AOA of the flap.....	94
<b>Figure 3.37</b> Velocity contour for S1223 flap (25° AOA).....	95
<b>Figure 3.38</b> Velocity contour for S1223 flap (30° AOA).....	95
<b>Figure 3.39</b> Velocity contour for S1223 flap (35° AOA).....	95
<b>Figure 3.40</b> Velocity contour for S1223 flap (40° AOA).....	95
<b>Figure 3.41</b> Pressure contour for S1223 flap (25° AOA).....	95
<b>Figure 3.42</b> Pressure contour for S1223 flap (30° AOA).....	95
<b>Figure 3.43</b> Pressure contour for S1223 flap (40° AOA).....	96
<b>Figure 3.44</b> Pressure contour for S1223 flap (45° AOA).....	96
<b>Figure 3.45</b> Vertical distance ( $h_1$ ) between the two elements of the front wing assembly .....	96
<b>Figure 3.46</b> Lift and drag coefficients for all vertical distances ( $h_2$ ) between the two elements.....	97
<b>Figure 3.47</b> Velocity contour of the front wing ( $h_2=25$ mm).....	98
<b>Figure 3.48</b> Velocity contour of the front wing ( $h_2=30$ mm).....	98
<b>Figure 3.49</b> Velocity contour of the front wing ( $h_2=35$ mm).....	98
<b>Figure 3.50</b> Pressure contour of the front wing ( $h_2=25$ mm).....	99
<b>Figure 3.51</b> Pressure contour of the front wing ( $h_2=30$ mm).....	99
<b>Figure 3.52</b> Pressure contour of the front wing ( $h_2=35$ mm).....	99
<b>Figure 3.53</b> Horizontal distance ( $h_3$ ) between the two elements of the front wing assembly .....	100
<b>Figure 3.54</b> Lift and drag coefficients for all horizontal distances ( $h_3$ )between the two elements .....	101
<b>Figure 3.55</b> Lift/drag ratio for all horizontal distances ( $h_3$ )between the two elements .....	102
<b>Figure 3.56</b> Velocity contour of the front wing ( $h_3=10$ mm).....	102
<b>Figure 3.57</b> Velocity contour of the front wing ( $h_3=20$ mm).....	103
<b>Figure 3.58</b> Pressure contour of the front wing ( $h_3=10$ mm).....	103
<b>Figure 3.59</b> Pressure contour of the front wing ( $h_3=20$ mm).....	104
<b>Figure 3.60</b> Final assembly for CFD with 440 mm gap in the middle of the secondary element .....	105
<b>Figure 3.61</b> Turbulence visualization of the two-element no-endplate configuration with velocity magnitude contour .....	105
<b>Figure 3.62</b> Turbulence visualization of the final assembly with velocity magnitude contour.....	106
<b>Figure 3.63</b> Turbulence visualization of the final assembly with velocity magnitude contour.....	106
<b>Figure 3.64</b> 3D velocity magnitude streamlines of two-element configuration without endplates .....	107
<b>Figure 3.65</b> Velocity magnitude streamlines of the two-element configuration without endplates .....	107
<b>Figure 3.66</b> Velocity magnitude streamlines of the final assembly with endplates .....	108





<b>Figure 3.67</b> Pressure contour of the final assembly .....	108
<b>Figure 3.68</b> Pressure contour of the final assembly .....	109
<b>Figure 3.69</b> Reference area of the front wing assembly .....	110
<b>Figure 3.70</b> Displacement of the geometry after the force application .....	110
<b>Figure 3.71</b> Front wing assembly with nerves to prevent deformation on its edges .....	111
<b>Figure 4.1</b> 3D velocity magnitude streamlines of the final assembly .....	112
<b>Figure 4.2</b> Maximum dimensions of the front wing assembly in each axis .....	113
<b>Figure 4.3</b> Final design for the racing vehicle's front wing assembly of Poseidon Racing Team (UniWA) .....	114
<b>Figure 4.4</b> Front wing assembly example for future reference.....	116



## LIST OF TABLES

<b>Table 1.1</b> Air properties at 20° C and at sea level .....	23
<b>Table 1.2</b> Typical values of the pressure coefficient (Cp) .....	33
<b>Table 2.1</b> Maximum dimensions for the front wing assembly.....	56
<b>Table 2.2</b> Dimensions of the fluid domain (enclosure and body of influence).....	61
<b>Table 2.3</b> Number of elements and sizing properties for different mesh qualities .....	62
<b>Table 2.4</b> Lift and Drag coefficients results for coarse, moderate, fine, and very fine mesh qualities .....	66
<b>Table 2.5</b> Lift and Drag coefficients results for k-epsilon, k-omega standard, and k-omega SST solving models.....	69
<b>Table 2.6</b> Results of the steady and transient flow types in Selig 3021 at 3 degrees angle of attack .....	71
<b>Table 2.7</b> Results of the steady and transient flow types in Selig 3021 at 6 degrees angle of attack .....	71
<b>Table 3.1</b> Results of the first set of simulations for the Selig 3021 airfoil.....	80
<b>Table 3.2</b> Results of the first set of simulations for the Selig 1223 airfoil.....	80
<b>Table 3.3</b> Results of the first set of simulations for the Selig 1210 airfoil.....	80
<b>Table 3.4</b> Results of the first set of simulations for the Eppler 423 airfoil.....	81
<b>Table 3.5</b> Selig 1223 road clearance simulations results .....	87
<b>Table 3.6</b> Results of simulation for Selig 1223 as secondary element .....	93
<b>Table 3.7</b> Lift and drag coefficients results for all vertical distances ( $h_2$ ) between the two elements.....	97
<b>Table 3.8</b> Lift and drag coefficients results for all horizontal distances ( $h_3$ ) between the two elements	101



## LIST OF EQUATIONS

Equation 1.1.....	20
Equation 1.2.....	20
Equation 1.3.....	20
Equation 1.4.....	20
Equation 1.5.....	20
Equation 1.6.....	20
Equation 1.7.....	20
Equation 1.8.....	20
Equation 1.9.....	20
Equation 1.10.....	20
Equation 1.11.....	20
Equation 1.12.....	20
Equation 1.13.....	20
Equation 1.14.....	20
Equation 1.15.....	20
Equation 2.1.....	20
Equation 2.2.....	20
Equation 2.3.....	20
Equation 2.4.....	20
Equation 2.5.....	20

## 1. Introduction

### 1.1. Historical Retrospect

The term Aerodynamics is used to describe the field of study that surrounds the interaction between solid bodies and the motion of air. To understand the way these solid bodies are affected by the flow of the air around them, principles of fluid dynamics and thermodynamics are involved. The field of aerodynamics is implicated with various applications, including transportation, structures, and internal flows. The main goal of this field of study is to optimize efficiency, performance, and safety (Anderson, 2017).

The field of aerodynamics has a long history, starting from the ancient Greeks through observations of the flight of birds. However, Aerodynamics in the form that we are more familiar with nowadays started in the late 19th and early 20th centuries. The Wright brothers' development of the first powered flight (Figure 1.1) (National Air and Space Museum), and the subsequent innovations in aircraft design and technology, were the first recorded breakthroughs that set the foundations for a whole new field of study.

Throughout the spectacular development of aerodynamics, the work of Ludwig Prandtl (a German physicist and engineer known as the father of modern aerodynamics) on boundary layers and turbulence led to the development of revolutionary methods and principles that helped to better understand how air flows behave around objects (Eckert, 2017).

In the following years, methods were introduced in the field that helped researchers to study the behavior of airflows. Initially, wind tunnels (Figure 1.2) allowed engineers to conduct real-world simulation experiments in a controlled environment (Baals, Donald D, 1981). In the mid-20th century, an entirely new field, known as Computational Fluid Dynamics (CFD) (Figure 1.3), developed (Wendt et al., 2008). Through the use of computer simulations, researchers were able to analyze and model airflows and fluid flows in general. All the above led to major breakthroughs regarding design and optimization in the field of aerodynamics.

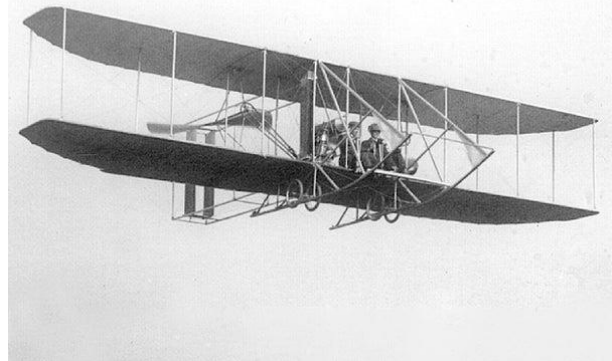


**Figure 1.1** First engine powered flight (Wright Brothers, 1903)



**Figure 1.2** Wind tunnel testing of Wright brothers' airplane (NASA, 1999)

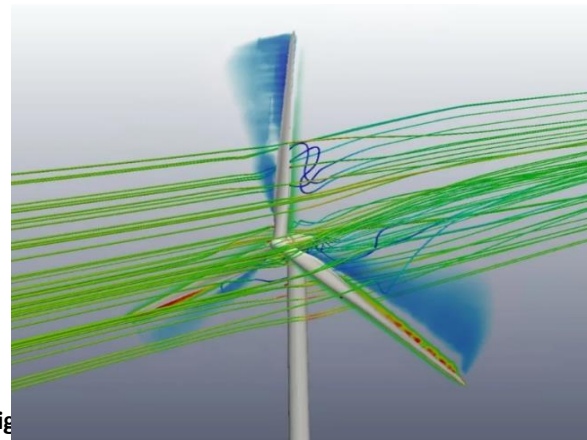


**Figure 1.3** Computational Fluid Dynamics (CFD) simulation of a propeller and wing (Wendt et al., 2008)

With all the above being said, aerodynamic studies vary from case to case. To be more specific, in order to start a simulation or experiment, all parameters and assumptions must be known, as well as the desired outcome of the study. For example, a study of the flow around a road vehicle must be approached in a completely different way than an aerodynamic study of an aircraft. This happens due to the fact that the main objectives, environmental properties, and other parameters are different from one another.

## 1.2. Motorsport Aerodynamics

### 1.2.1. Introduction

Since the following thesis is dedicated to the aerodynamic study of the front wing of a racing car, it is of major importance to mention the development of the field of aerodynamics in motorsport. Initially, as will be discussed below, engineers began to design road vehicles aiming at reducing the car's resistance to air (Rossis et al., 1993). This design achieved low drag forces and thus optimized the vehicle's fuel efficiency, performance, and handling. In the commercial automotive industry this type of design was quite common, because by using small resources and a low budget it was possible to achieve the desired result.

On the other hand, since the first years of motorsport, there have been a lot of factors that played a major role in a racing vehicle's performance. Unfortunately, the aerodynamic factor was the one with the less contribution while engine power and other parts in the design of the car had larger impact on every car's performance. The fact that all these factors required a significant budget, less financially supported teams in every kind of motorsport couldn't keep up with teams that acquired a larger budget. Once low-field teams couldn't improve much in these sectors, new economic ways to enhance a car's performance had to be introduced to the motorsport community.

Aerodynamics made their first appearance in the automotive industry (both commercial and racing). Teams were constantly discovering new ways to take advantage of the forces that were applied on the car by its contact with the air. Firstly, the shape of the vehicle was designed in ways that its resistance (drag) to the air was significantly smaller (Figure 1.4). In later years, more innovative ideas came up such as wings, which were made in the exact opposite way compared to the wings on airplanes, in order to apply forces that instead of lifting the car, they were pushing it down known as negative lift or downforce (Figure 1.5). To understand how these forces affected the car, the scientific community started analysing the way all solids interacted with air flows that passed around them. Forces and coefficients started to be measured and categorized to study a vehicle's behaviour and performance (Witheridge, 2020).



**Figure 1.4** Formula 1 car Simca Gordini 15 (Great Britain, 1952)



Figure 1.5 Michael Schumacher's 2003 Ferrari F2003-GA (Fiorano, 2022)

## 1.2.2. Basic Aerodynamic Terms

The air flow around a vehicle and a solid body in general can be studied and described in some basic terms, the knowledge of which is necessary to understand in order to make conclusions on how any body is affected by this air flow and how. There are forces, coefficients and air properties that can be measured to determine the aerodynamic behavior of a solid body.

### 1.2.2.1 Air Properties

Firstly, every fluid has its own properties, such as density and viscosity. These properties are severely connected with the commonly known terms of Pressure and Temperature; therefore, it is implied that the properties of air and the effects they have on the interaction between the air flow and the vehicle is extremely dependent to the altitude and the environment of the study.

- i. **Air density ( $\rho$ )** is a certain mass per unit volume of Earth's atmosphere. However, it is commonly assumed to be constant from circuit to circuit as it doesn't affect the air flow as much as its viscosity.
- ii. **Viscosity ( $\mu$ )** on the other hand, has a larger impact on the way the air flow behaves. The term viscosity refers to the amount of force required to cause relative movement of one layer of the fluid over the other. In our case, air luckily is one of the least viscous fluids, which means less force is required to pass movement from one layer to another. For instance, water's, or even, motor oil's viscosity is larger making it more difficult for solids to move inside them. That is why a solid body can reach higher speeds in air easier than if it was underwater. Viscosity majorly affects the racing car's movement through air since it causes the creation of the "Boundary Layer" around it which will be discussed below in this thesis.

The table below represents air properties at 20° C and at sea level:

Atmospheric Pressure, P	101325 N/m <sup>2</sup>
Density, ρ	1.204 kg/m <sup>3</sup>
Viscosity, μ	1.8 * 10 <sup>-5</sup> Pa * sec

**Table 1.1** Air properties at 20° C and at sea level

### 1.2.2.2 Dimensionless Numbers

Two of the most important dimensionless numbers that surround Fluid Dynamics and especially Aerodynamics, are the Reynolds number and the Mach number.

- **Reynolds number** is a nondimensional figure that represents the ratio between inertial and viscous forces created in the air and determines the type of a specific flow and can help us demonstrate how this flow affects the solid that impacts. For lower Reynolds numbers the air flow is laminar and from a certain amount of the Reynolds number and above the air flow becomes turbulent (Figure 1.6). As we will see, this figure depends on the fluid's properties, the surface of the body that impacts and the velocity of the fluid.

$$Re_L = \frac{\rho * V_{\infty} * L}{\mu} = \frac{V_{\infty} * L}{\nu} \quad (\text{eq. 1.1})$$

Where:

- ρ: Fluid density (kg/m<sup>3</sup>)
- V<sub>∞</sub>: Free stream velocity (m/s)
- L: Distance from the leading edge of the plate (m)
- μ: Fluid dynamic viscosity (kg/m\*s)
- ν: Fluid kinematic viscosity (ν = μ/ρ) (m<sup>2</sup>/s)

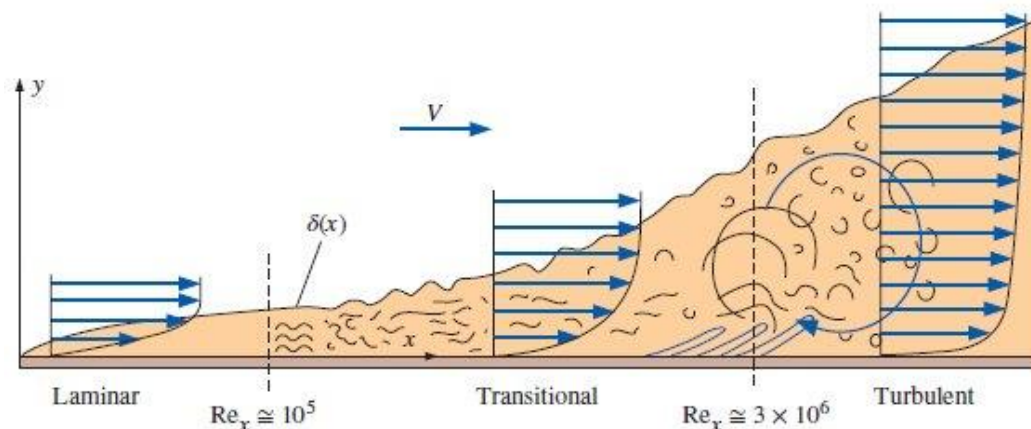


**Figure 1.6** Transition process from a laminar to a turbulent boundary layer over a flat plate

Reynolds number when used in the field of race car aerodynamics is able to quantify the product speed times size. This means, for example, that when a  $\frac{1}{4}$  scale model car is tested at actual air flow speeds, the Reynolds number is the same with the full sized one's.

With all the above being said, a lot of automotive industries and motorsport teams don't have the facilities to test full sized cars. As a result, teams and industries are "forced" to test scaled model cars in wind tunnels. At this point, Reynolds number comes in handy as all experiments can be compared to each other leading to conclusions regarding the development of the car. Unfortunately, the drawback is that when a scaled model car is tested at lower speeds, the Reynolds number might fall below a certain amount leading to inaccurate results that don't match the result of an experiment that took place using a real sized car.

Around a solid body, depending on the Reynolds number, the behavior of the flow is different at lower values compared to higher values. When the Reynolds number is small, the air flow around the body has very little separation and wake, while at higher values of Reynolds, the wake of the flow behind the body is significantly larger and the separation of the air flow occurs earlier at the surface of the solid body (Figure 1.7).

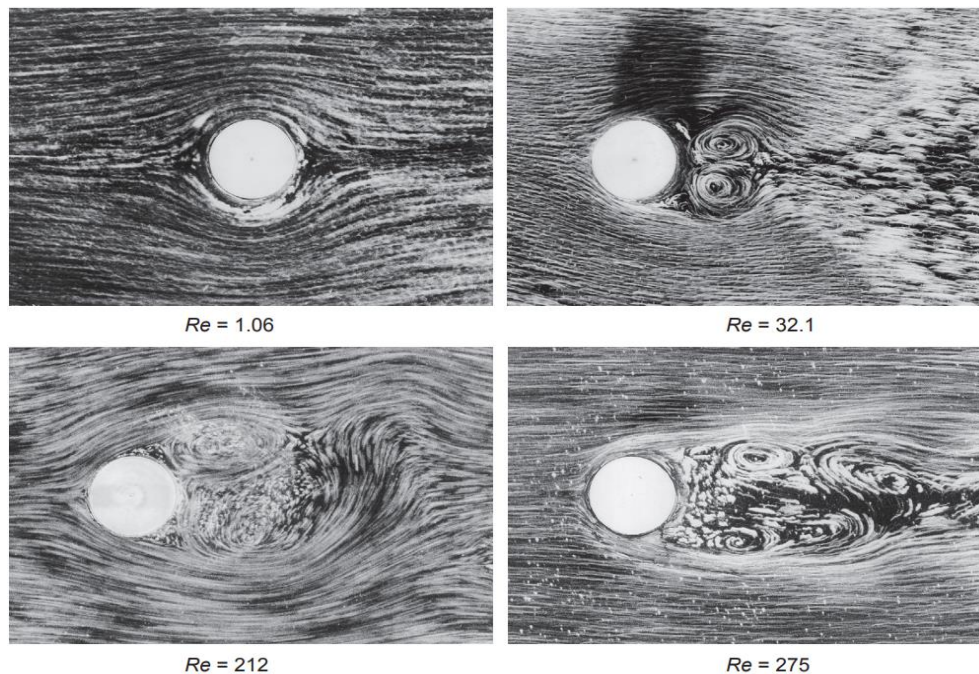


**Figure 1.7** Flow around a cylinder

- **Mach Number:** The compressibility of the air depends on another nondimensional number called the Mach number and its value is related with the speed of the moving object. Its calculation occurs from Equation 1.2:





$$Ma = \frac{\text{Objective speed of the air flow}}{\text{Speed of sound}} \quad (\text{eq. 1.2})$$

The speed of sound is related to environmental conditions and differs from one altitude to another (different temperature and pressure values). Also, the speed of sound is considered to be around 330 m/s (1188 kph).

The Mach number allows us to define flight regimes in which compressibility effects vary:

- Subsonic ( $M < 1$ ): In this occasion compressibility can be ignored on some terms. In our calculations though, we consider the flow incompressible for Mach number below 0.3.
- Transonic ( $M = 1$ ): The speed of the object approaches the speed of sound. Compressibility effects are most important in transonic flows and lead to the early belief in a sound barrier.
- Supersonic ( $M > 1$ ): Compressibility effects are important for supersonic aircraft, and shock waves are generated by the surface of the object.

### 1.2.2.3 Boundary Layer

By the term **boundary layer**, we describe an area close to the surface of solid bodies where a specific phenomenon takes place. In the boundary layer, the velocity on the surface of the stationary plate becomes zero. As we move towards the upper limit of the boundary layer, which is called boundary layer thickness, the velocity of the air flow increases. When we reach the boundary layer thickness the velocity of the flow near the body reaches the outer velocity  $V_\infty$  which is equal to the velocity of the free stream. The interaction of a solid body with the air flow depends on the existence and the form of the boundary layer (Figure 1.8). This happens because when the solid body is merging the air flow with a certain velocity, a boundary layer is created, and its thickness depends on this velocity and increases as the air flow reaches the back of it. When the thickness of this boundary layer grows larger abruptly causing more viscous friction drag, causing the phenomenon we discussed, flow separation (Burr et al.).

Boundary layer thickness (Blasius):

$$\delta = 5 \frac{x}{\sqrt{Re_x}} \quad (\text{eq. 1.3})$$

Where:

- $x$ : distance on the flat plate
- $Re$ : Nondimensional Reynolds number

To sum up, the following conclusion are extracted:

Due to the viscosity we have the no slip condition at the plate

$$u = 0 \text{ at } y = 0$$

At infinity (outside the boundary layer), away from the plate, we have that

$$u \rightarrow U \text{ as } y \rightarrow \infty$$

Where:

- $u$ : velocity at a specific height (m/s)
- $U$ : freestream velocity (m/s)
- $y$ : height from the flat plate (m)

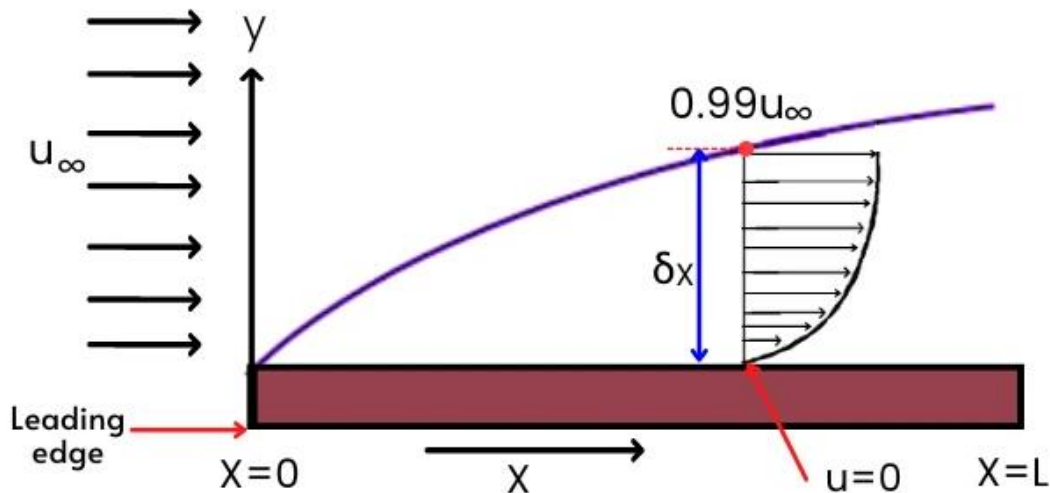


Figure 1.8 Boundary layer on flat plate

#### 1.2.2.4 Flow Visualization (Streamlines)

Another major aspect in aerodynamics is the term **streamlines**, which are the optical description of the flow motion around solid bodies. Streamlines can be visible using methods like smoke injection in the air flow during wind tunnel testing or with a feature called particle trace in Computation Fluid Dynamics programs. Using this method, we are able to point out when an air flow is attached or separated according to the smoke tracing that is produced around the solid body.

An **attached flow** is the flow that is constantly following the curves of the racing car which is an ideal situation that is impossible to achieve completely. Making the air flow the most attached to the car possible, we accomplish lower drag. On the other hand, a **separated flow** is the one that is not able to follow the solid surface (Figure 1.9, 1.10). The point where the flow detaches from the surface of the body is called separation point.

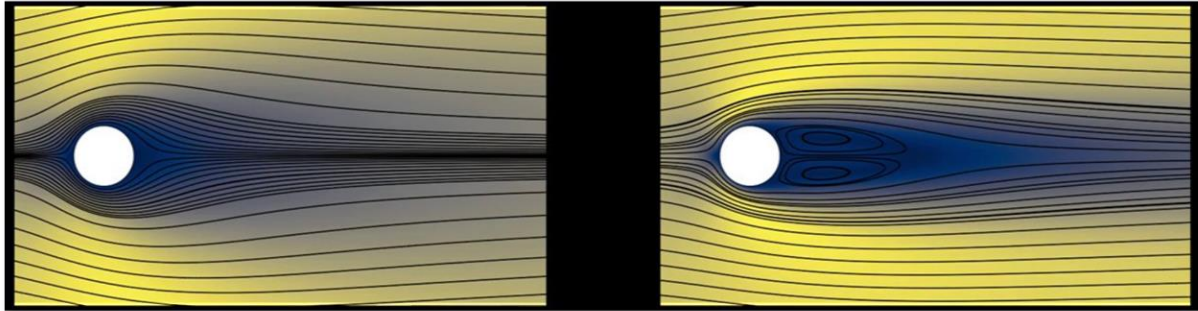


Figure 1.9 Attached and separated flow around circular cylinder (James Ramsay,2019)

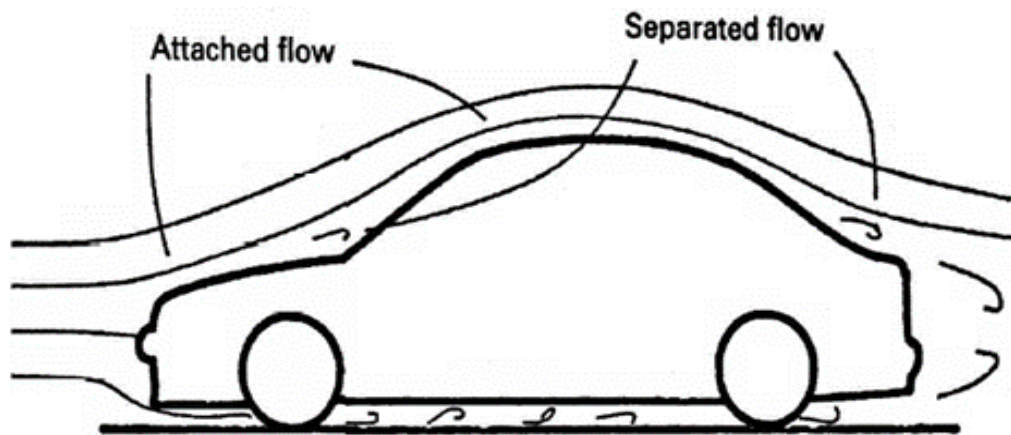


Figure 1.10 Attached and separated flow on a commercial car

### 1.2.2.5 Aerodynamic Forces

When a solid body, or in our case an airfoil, is merged with a particular airflow, there are four main forces acting on it. These are lift, drag, weight, and thrust. In this section of the chapter, drag and lift will be explained and analyzed, as they are the main forces encountered in the field of aerodynamics (Nakayama, 2018).

- Drag Forces:** The forces that act on a solid body in the direction opposite to its movement direction are called drag forces and are caused by several factors (Figure 1.12). Drag over an airfoil might be caused by either shear forces that are caused by friction between the air and the surface or even by friction between the streamline layers of the air. Another way that drag force can be generated is due to flow separation that might occur in several regions over the body, or most importantly, behind the airfoil creating a region of very low pressure called wake. The drag  $D$ , on a solid body is divided in two types of forces, the friction drag  $D_f$ , and the pressure drag  $D_p$ . The two equations that helps us calculate these two components of the drag force, are the following:

$$D_f = \int_A \tau \, dA \sin\theta \quad (\text{eq. 1.4})$$

and

$$D_p = \int_A p \, dA \sin\theta \quad (\text{eq. 1.5})$$

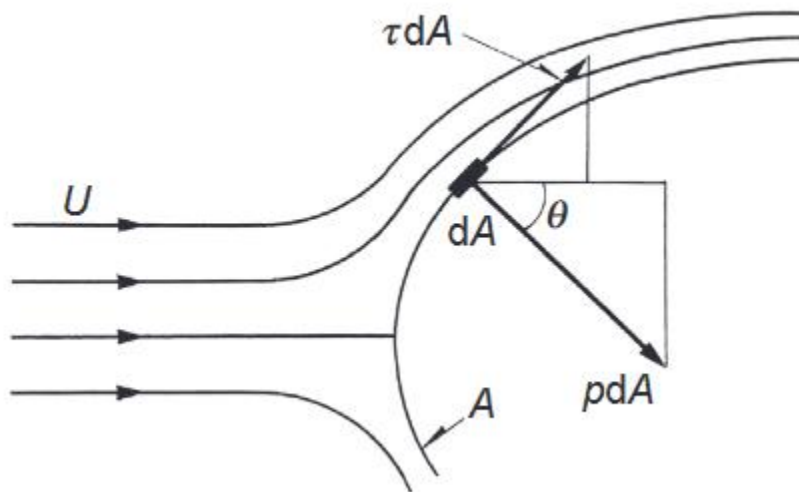


**Figure 1.11** Components of drag force on a solid body

- **Lift Forces:** Just as drag forces, there are also lift forces that act on the vehicle vertical to its moving direction (Figure 1.12). In motorsport, these forces are referred to as **downforce** or **negative lift** and are responsible for the better drivability, traction, and performance of the car. As a result, the car behaves better on turns and accelerates better because it stays attached to the track.

The amount of lift that is generated depends on the difference of pressure above and below the solid body. If the amount of pressure under the solid body is larger compared to the amount above it, the lift force will have a positive value, meaning that the body will ascend. If the opposite happens, then the lift will have a negative value, something that is known to us as downforce.

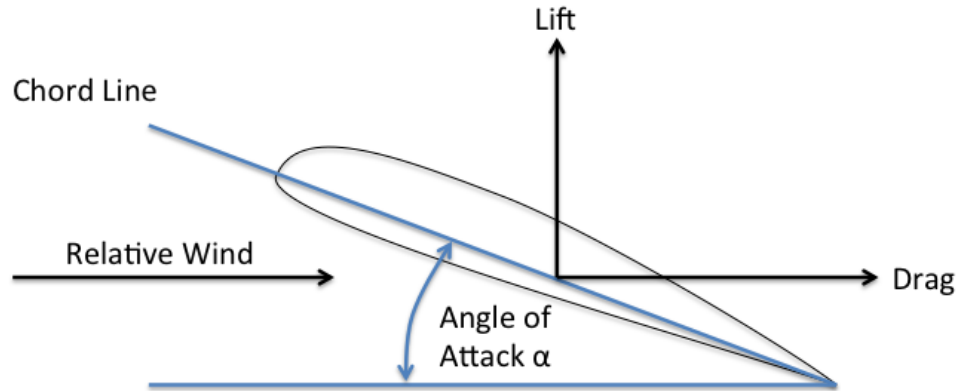


Figure 1.12 Aerodynamic Forces acting on an airfoil

The two forces mentioned before combined, result in a final force acting on every body (airfoil, in our occasion) which is commonly referred to as  $R$  and is shown in the following (Figure 1.13):

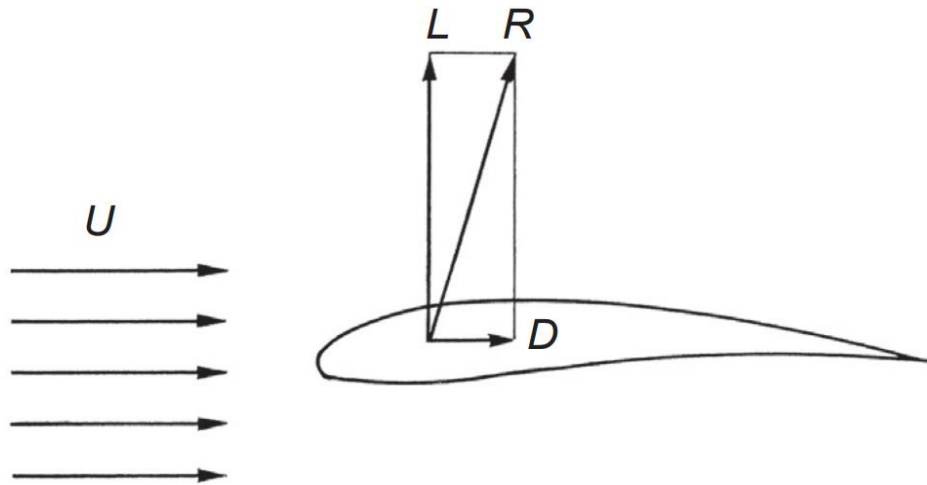


Figure 1.13 Aerodynamic Force  $R$  as a combination of the lift force and drag force components (Nakayama, 2018)

In order to calculate these forces, there are two governing equations which allow us to experimentally estimate the amount of Lift and Drag acts on a solid body:

$$L = \frac{1}{2} \rho C_L A U^2 \quad (\text{eq. 1.6})$$

and



$$D = \frac{1}{2} \rho C_D A U^2 \quad (\text{eq. 1.7})$$

Where:

- L: Lift Force (N)
- $\rho$ : Fluid (Air) Density ( $\text{kg/m}^3$ )
- $C_L$ : Lift Coefficient
- A: Reference Area ( $\text{m}^2$ )
- U: Freestream Velocity (m/s)
- D: Drag Force (N)
- $C_D$ : Drag Coefficient

### 1.2.2.6 Aerodynamic Coefficients

Having discussed the main forces acting on a solid body when it interacts with airflows, it is important to list and explain the coefficients governing these forces. These coefficients help us to categorize and understand how each body interacts with an air flow (Williams, 2021).

- **Lift Coefficient ( $C_L$ ):** One way to determine how much downforce a race car produces is the lift coefficient. Lift coefficient is a number that engineers use to model all the complex dependencies of shape and certain flow conditions on lift. The lift coefficient also helps us determine the amount of lift generated, and in motorsports, its values are usually negative in order to be considered a downforce factor. In industrial cars, downforce is not as critical because the main goal in this type of car is to have the lowest fuel consumption in order to be as economical as possible by reducing drag. The lift coefficient includes all complex dependencies and is usually calculated experimentally. If the amount of Lift is known, eq. 1.6 transforms into the following:

$$C_L = \frac{L}{\frac{1}{2} \rho A U^2} \quad (\text{eq. 1.8})$$

- **Drag Coefficient ( $C_D$ ):** The amount of drag that a body generates is determined by its geometry and the conditions of the air flow. To help us easily understand how different shapes and types of airfoil act aerodynamically we use the drag coefficient  $C_D$ . The drag coefficient is a number that engineers use to model all of the complex dependencies of shape (Figure 1.14) and flow conditions on drag. The following equation is a transformation of eq. 1.7 which helps us calculate the drag coefficient all the other parameters are known:

$$C_D = \frac{D}{\frac{1}{2} \rho A U^2} \quad (\text{eq. 1.9})$$

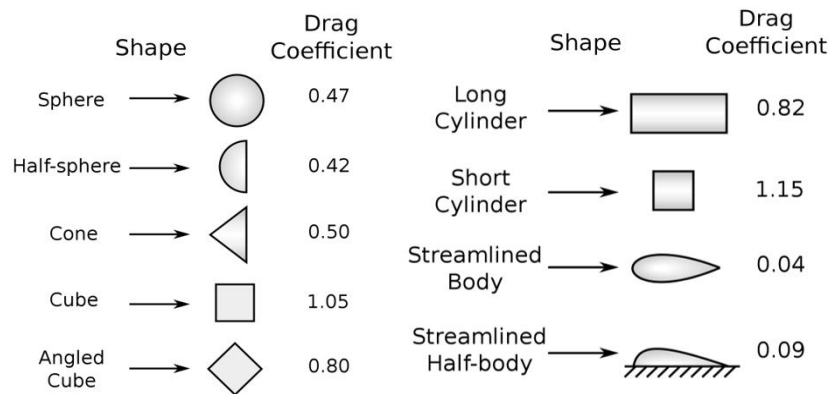


Figure 1.14 Measure drag coefficients for various shapes (Sape A. Miedema, 2011)

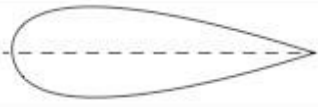
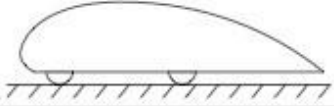
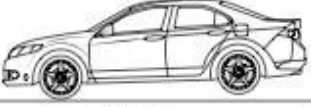
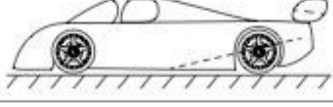
			$C_L$	$C_D$
1	Low drag body of revolution		0	0.04
2	Low drag vehicle near the ground		0.18	0.15
3	Generic automobile		0.28	0.35
4	Prototype race car		-3.00	0.75

Figure 1.15 Typical lift and drag coefficients for various ground vehicles (Joseph Katz, 2016)

- **Pressure Coefficient ( $C_P$ ):** The pressure coefficient is another non-dimensional parameter commonly used by scientists and engineers to describe the pressure field around an object. It is useful to express pressure as a non-dimensional variable, such as lift and drag. The coefficient of pressure is given as follows:

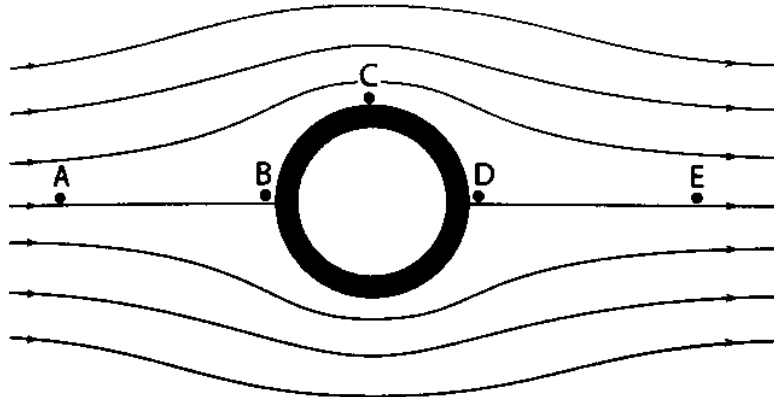
$$C_P = \frac{P - P_\infty}{\frac{1}{2} \rho_\infty V_\infty^2} \quad (\text{eq. 1.10})$$

Where:

- $P$ : Pressure ( $N/m^2$ )
- $P_\infty$ : Freestream Pressure ( $N/m^2$ )

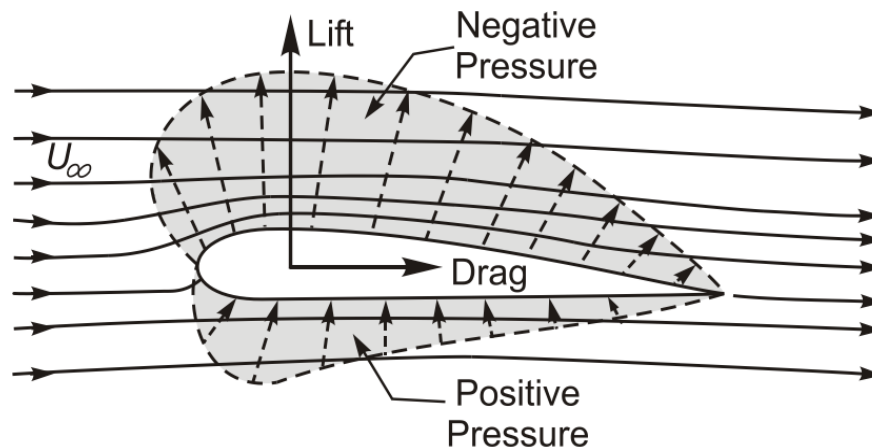
- $V$ : Freestream Velocity (m/s)
- $\rho_{\infty}$ : Freestream density ( $\text{kg/m}^3$ )

Figure 1.16 will help us understand how the pressure around a cylinder is distributed.



**Figure 1.16** Two-dimensional flow around a cylinder (Williams,2021)

First of all, it is clear that at points A and E, the flow is called freestream flow due to the fact that it is undisturbed by the solid body. Point B and is called stagnation point which means, pressure is maximized, and velocity is zero. Lastly, point C, is the point where pressure is reducing due to the acceleration of the fluid, which means we have higher velocity and lower pressure.



**Figure 1.17** Pressure distribution around and airfoil

When examining an airfoil (Figure 1.17), in the foremost point which as mentioned before is called stagnation point, the airflow has zero velocity and maximum pressure. The difference between an airfoil and a cylinder is that the pressure above and below is different in the airfoil (depending on its shape and angle of attack).



Location	Velocity	Cp
Stagnation Point	0	1.0
Solid body	$V < V_{\infty}$	0.0 – 1.0
Solid body	$V > V_{\infty}$	Negative (0.0 - 3.0)

**Table 1.2** Typical values of the pressure coefficient (Cp)

### 1.2.2.7 Bernoulli equation

The Bernoulli equation is based on the idea that when the velocity of a fluid increases, the pressure decreases, and vice versa. We need to clarify that the equation can be used to calculate the air flow's velocity and pressure only under specific circumstances. In order to use the Bernoulli equation in any of the following forms that we will see, the fluid that we will study must be non-viscous, incompressible, the flow must be laminar and lastly, it must be assumed that the total energy of the particle along a streamline of the flow, remains constant. The forms of the total energy are the following:

- Pressure energy:  $P \cdot V$
- Kinetic energy from velocity and mass of the fluid:  $\frac{1}{2} \cdot m \cdot U^2$
- Potential energy from the mass and elevation of the fluid:  $m \cdot h$

Where:

- P: Pressure of the fluid (N/m<sup>2</sup>)
- U: Velocity of the fluid (m/s)
- V: Volume of the fluid (m<sup>3</sup>)
- m: Mass of the fluid (kg)
- h: Elevation of the fluid (m)

The general equation of Bernoulli is:

$$\frac{1}{2} \cdot m \cdot v^2 + P \cdot V + m \cdot h = \text{constant} \quad (\text{eq. 1.11})$$

Most of the instruments of measuring velocity and pressure of an airflow are based on the Bernoulli equation. But the most important factor that we have to take into account is that the specific equation is applied only in the conditions we mentioned before, so several calculations must be made to have results that we can take advantage of in real conditions.

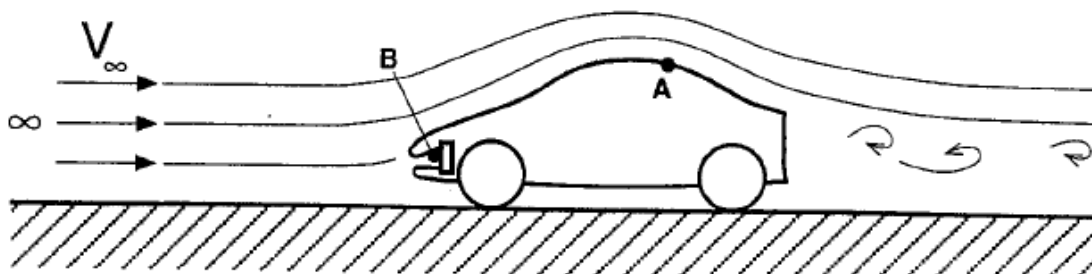


**Figure 1.18** Air flow around a vehicle where the Bernoulli equation can be used at points A, B and  $\infty$ .

The figure above (Figure 1.18) will help us understand the following equation:

$$\frac{P_A}{\rho} + \frac{V_A^2}{2} = \frac{P_\infty}{\rho} + \frac{V_\infty^2}{2} \quad (\text{eq. 1.12})$$

A transformed equation like this assumes that the contribution of the energy from the mass elevation is very small and does not affect the results of our calculations. So, in a system that we know the free stream velocity and its pressure, by measuring the pressure in any point on the surface of the vehicle, we can calculate the velocity at this exact same point.

### 1.3. Formula Student

#### 1.3.1. Brief overview

The development of aerodynamics in motorsport plays a major role in the design of FSAE cars as well. Every team tries to develop the most efficient car in every sector, such as powertrain, vehicle dynamics and aerodynamics, while staying within the regulations that limit the maximum performance and efficiency of the car. That is the reason why every team tries to maximize performance while using all the resources in the best possible way (IMechE, 2023).

Formula Student teams have been interested in the design of wings and other aerodynamic devices in order to create downforce, which improves grip and cornering performance. This has led to the development of increasingly complex designs, including front and rear wings, diffusers, undertrays and sidepods. Computational Fluid Dynamics software that will be discussed in chapter 1.5 is a crucial tool for FS teams that offers the ability to model and optimize the aerodynamic performance of the car without building a physical prototype. This led to a reduction in additional costs and time in the design process.



**Figure 1.19** Formula Student East competition contestants (FS East, 2021)



### 1.3.2. Formula Student Regulations

Every competition in motorsport has rules that teams must follow for a variety of reasons. The first and most important is safety, which is common to both racing and commercial automotive industry. In addition, in motorsport, specific rules are set in order to make each championship competitive, from Indy car to Formula 1. However, each type of motorsport has its own rules, such as Formula Student, has rules that are mainly based on safety and the results in each event are determined by the performance and efficiency of design based on the resources available to each team.

The main restrictions apply on the size of the car, the materials that must be used, the minimum stresses that all aerodynamic devices can withstand and others. Another rule of major importance is that only current university students are allowed to participate due to the fact that the competition is focused on the upcoming engineers and not professionals. The regulations of the Formula Student competitions vary from one competition to another (e.g., Formula Student Germany and Formula Student East). In addition, rules change every year in order to make improvements to the already existing ones (FSG, 2023).

To sum up, when designing both the front wing and the whole car, it is crucial to follow the rules and regulations set in order to pass the technical inspection held by every competition before the start of the dynamic events. As we will see in chapter 2, all dimensions and properties of the front wing will be determined so that they comply with the regulations.

### 1.3.3. Formula Student Car Aerodynamic Parts

Over the years, racing teams have continually pushed the boundaries of aerodynamics, creating innovative devices, advanced measuring instruments and sophisticated techniques to optimise performance. The ultimate focus remains on achieving maximum performance, although the interpretation of this goal varies depending on the unique requirements of each track.

For commercial cars, the primary goal is to reduce drag to enhance fuel efficiency, presenting a simple objective. However, in the world of motorsports, the primary goal for each team is to create downforce. This emphasis on downforce stems from the importance of cornering on most tracks, where it makes a significant difference to the outcome of a race. However, there are exceptions where minimising downforce takes precedence, particularly on tracks characterised by long straights. As mentioned earlier, more downforce translates into improved traction, allowing the car to perform with better handling and overall performance. This improvement allows the car to effectively convert wheel movement into seamless linear movement on the track. The four most important parts on an F1 and an FSAE car are the front and rear wings, the underbody (inlet and diffuser) and the sidepods (Figure 1.20) (Boccuzzi, 2022).

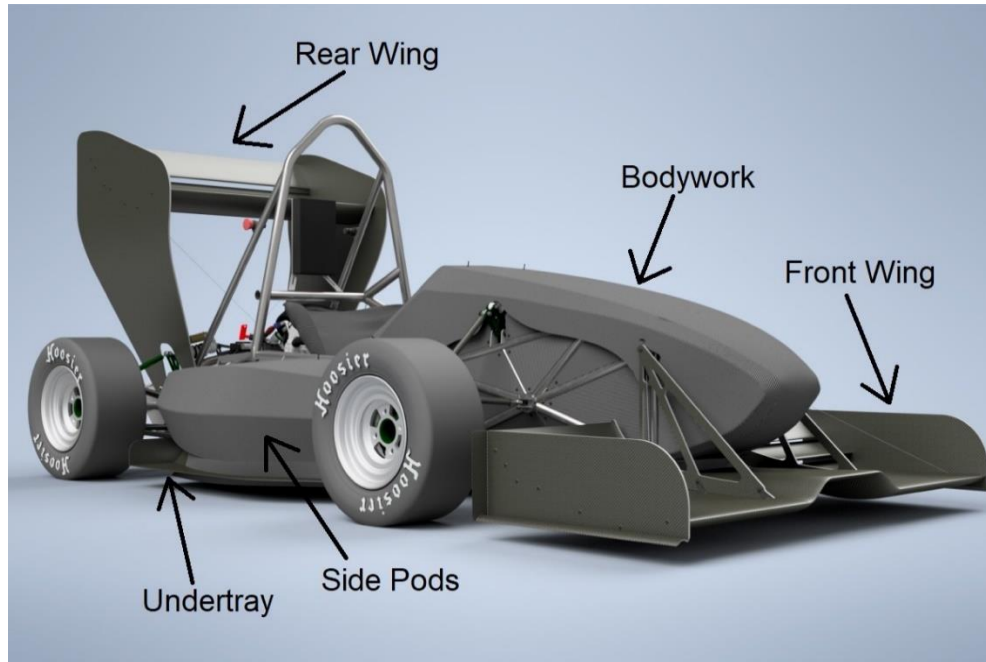


**Figure 1.20** Main aerodynamic devices of a Formula Student race car (SPbPU,2022)

- Side Pods:** Side pods are placed on the sides of the cockpit and their main goal is to provide the air-cooling system with enough air, in order to prevent engine's overheating. Although its main goal is this, sidepods can be designed in a way that can generate a flow that stays attached to the vehicle or even produce downforce (Macknight, 1998). Sidepods have been around for years in motorsport, and we have seen them in all kinds of different shapes and sizes (Figure 1.21).

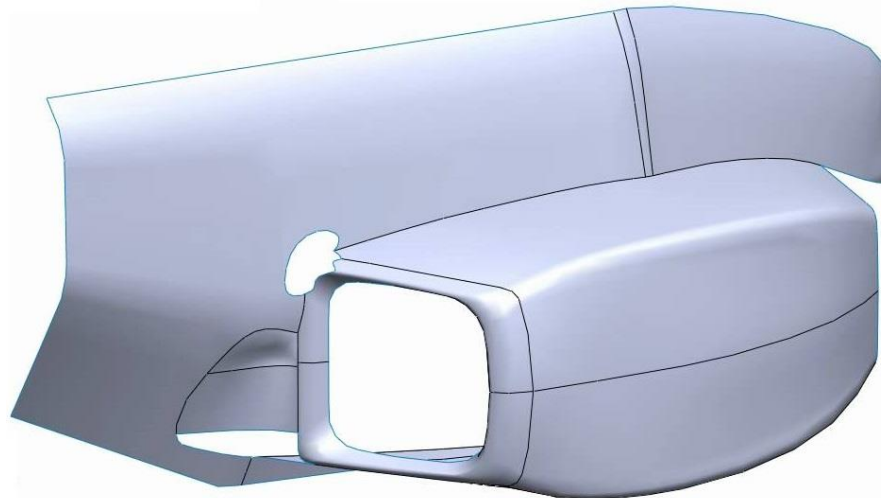


**Figure 1.21** Formula Student car side pod

- Underbody:** Based on the theory of the Venturi tube (Figure 1.22), the underbody of the car consists of the infuser, the narrowed section of the underbody (throat), and the diffuser (Seward, 2014). This aerodynamic system is one of the most important parts of an F1 or FSAE car producing almost half of the downforce a car can generate. Just as the Venturi tube works

## AERODYNAMIC STUDY AND DESIGN OF AN FSAE-TYPE VEHICLE'S FRONT WING

(White and Xue, 2021), air flow enters the underbody of the car via the infuser which has several features to guide the flow in way that that it doesn't get turbulent, and once it reaches the narrowed section, the pressure is minimized. Lastly, the airflow is guided to the diffuser where it leaves the underbody of the car with less pressure than the freestream flow (Figure 1.23). Now with all the above that we have discussed, the pressure over the vehicle pushes the car towards the ground and once this is done, the car gets "sucked" on the floor leading to the commonly known, **ground effect** (Shehadi, 2021). By accomplishing this, the car sticks to the road and as a result, it has better traction, better drivability and in general, better performance. Another function of the diffuser is to be in an angle that leads the air flow in a way that can get attached to the air flow above the car and behind the rear wing without separating, something that would cause induced drag.

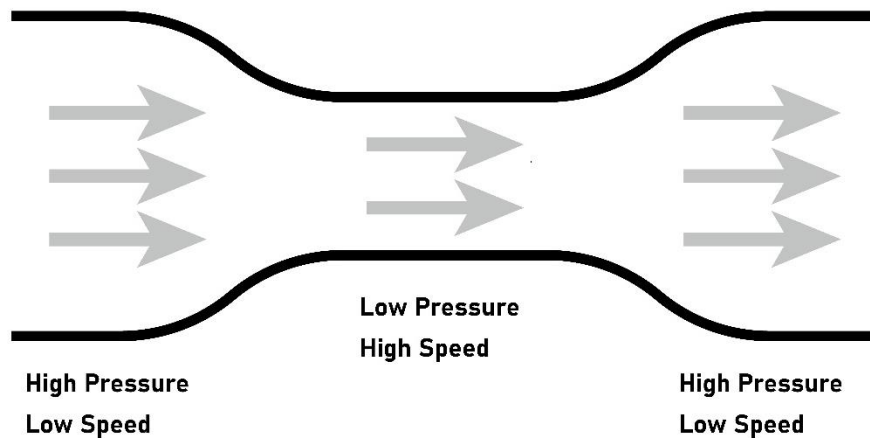


Figure 1.22 Venturi effect diagram

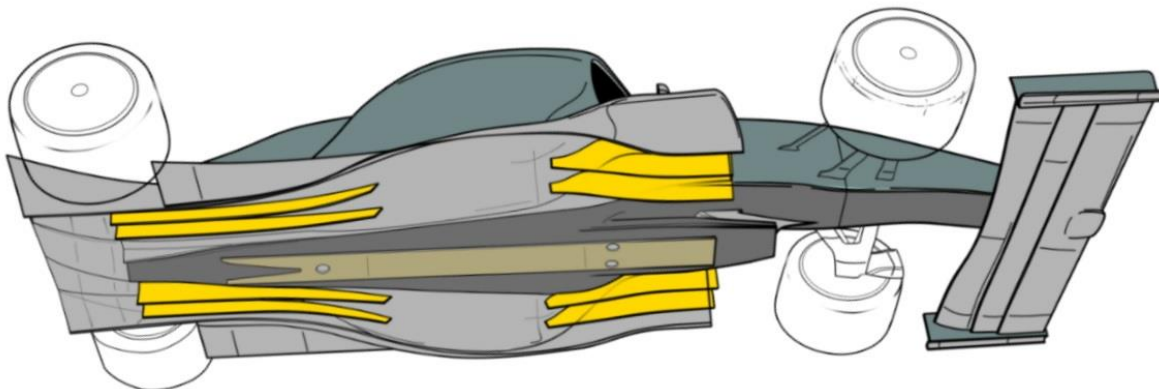
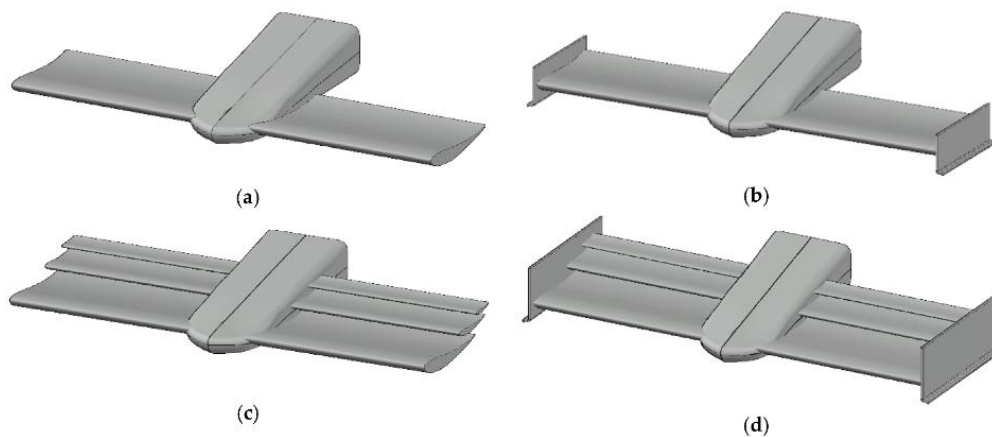


Figure 1.23 Underbody of a 2022 F1 car (Gary Anderson, 2022)

- **Front Wing:** The front wing of an FSAE car serves various key objectives, with the primary goals of generating downforce and allowing an even distribution of airflow both under and over the vehicle. In addition, an important purpose of the front airfoil is to divert the incoming airflow towards the side pods for cooling and redirecting it away from the wheels which create significant drag forces. There are a lot of types of front wings (Figure 1.24) which are categorized

by the number of elements that apart the front wing assembly such as single-element and multi-element wings (Castro and Rana, 2020). To guide airflow over the cars in a favourable way at speed, an aerodynamic element called vortices is used. These are high-energy spirals of air that effectively allow fast moving airflow to remain attached to a given surface, such as the bodywork of the car. Also, front wings have endplates on the sides that help in the creation of vortices that keep that “dirty” air of the wheels, away from the attached to the car flow. In addition, endplates prevent the flow to spoil around the elements, something that would have a major effect on the forces that are being generated.

To sum up, the front wing behaves like any object we mentioned before that has asymmetric pressure distributed around it. Wings in FSAE and F1 are similar to those used on aircraft but turned upside down. This is because instead of lift, the desired force is the opposite one called downforce, as we already know.



**Figure 1.24** (a) one-element without endplates; (b) one-element with endplates; (c) three-element without endplates; (d) three-element with endplates (Xabier Castro and Zeeshan A. Rana, 2020)

- Rear Wing:** Its principles are similar to the ones of the front wing, as it works in the same way taking advantage of the pressure distribution around it. It can also be adjusted and modified according to the requirements of every racetrack. The rear wing is mounted on the back of the car and its usually the tallest part on the FSAE car. About a third of the car's total downforce can come from the rear wing assembly (McBeath, 2006). The rear wings are the ones that are varied the most from track to track. As the rear wings of the car create the most drag the teams adjust the rear aerodynamic load to suit a particular track configuration. For example, a track with several large straights, a rear wing with less angle of attack is preferred, while on racetracks consisted of many turns, a steeper rear wing is preferred (for more downforce). As air flows over the wing, it is disturbed by the shape, causing a drag force. Although this force is usually less than the lift or downforce, it can seriously limit top speed and causes the engine to use more fuel to get the car through the air. The rear wing such as the front wing, consists of the main element, secondary elements (flaps), endplates, mountings and sometimes gurney flaps (Figure 1.25).

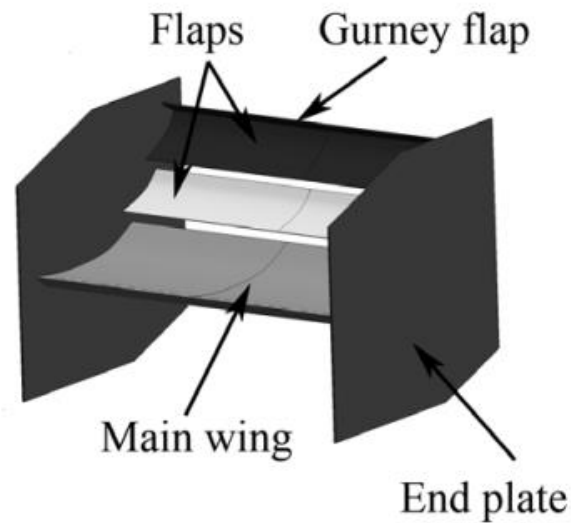


Figure 1.25 Basic configuration of a FSAE car rear wing

- Nose Cone:** While not typically classified as an aerodynamic component, particularly in Formula 1 where it is integrated into the car's bodywork, the nose cone holds significant aerodynamic importance within the context of an FSAE car (Figure 1.26). Its primary objective revolves around facilitating streamlined airflow circulation around it, with a particular emphasis on directing a majority of the airflow beneath the car. This strategic airflow management aims to optimize the utilization of the ground effect (as previously discussed), ultimately leading to enhanced downforce generation (Savliya, 2019).

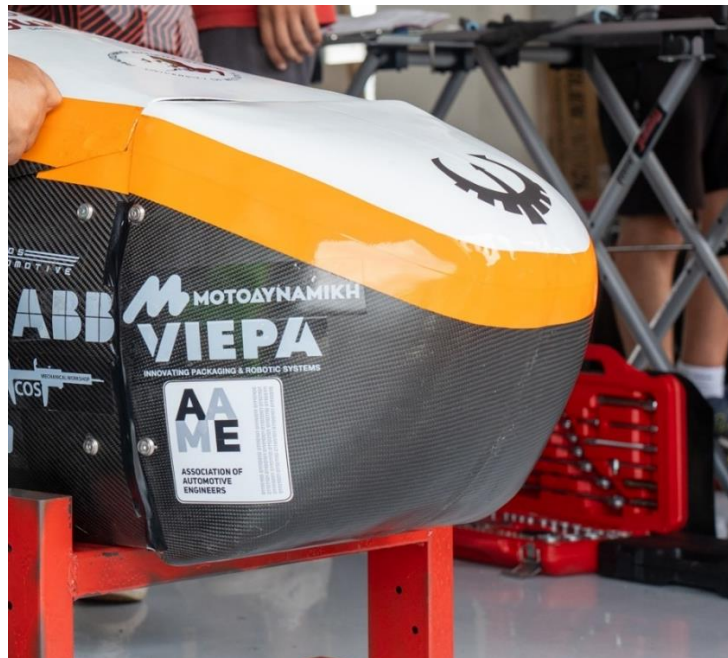


Figure 1.26 Nose cone of a Formula Student Car (Poseidon Racing Team, 2023)

## 1.4. Airfoil Theory

### 1.4.1. Definition of an airfoil

An airfoil, also known as a wing profile, is a shape designed to provide lift and control for an object as it moves through a fluid, such as air or water. Airfoils are most commonly used in aviation for the wings of aircraft, in automotive industry but they are also used in a variety of other applications, including wind turbines, and jet-engines. The shape of the airfoil creates a difference in air pressure above and below the wing, which results in lift. The amount of lift generated by an airfoil depends on its shape, size, angle of attack, and the speed of the fluid moving over it. The most aerodynamic shape in nature is known to be the teardrop. When a teardrop is compared to a symmetrical airfoil, the differences are insignificant. Symmetrical airfoils have the same shape on both the upper and lower surfaces and produce equal lift at zero angle of attack. The design and the characteristics of each airfoil depends on the purpose of it (Figure 1.27). For example, in motorsport, where maximum negative lift is required, airfoils are designed in an asymmetrical shape in order to maximize the difference in pressure distribution above and below the profile (Pope, 2009).

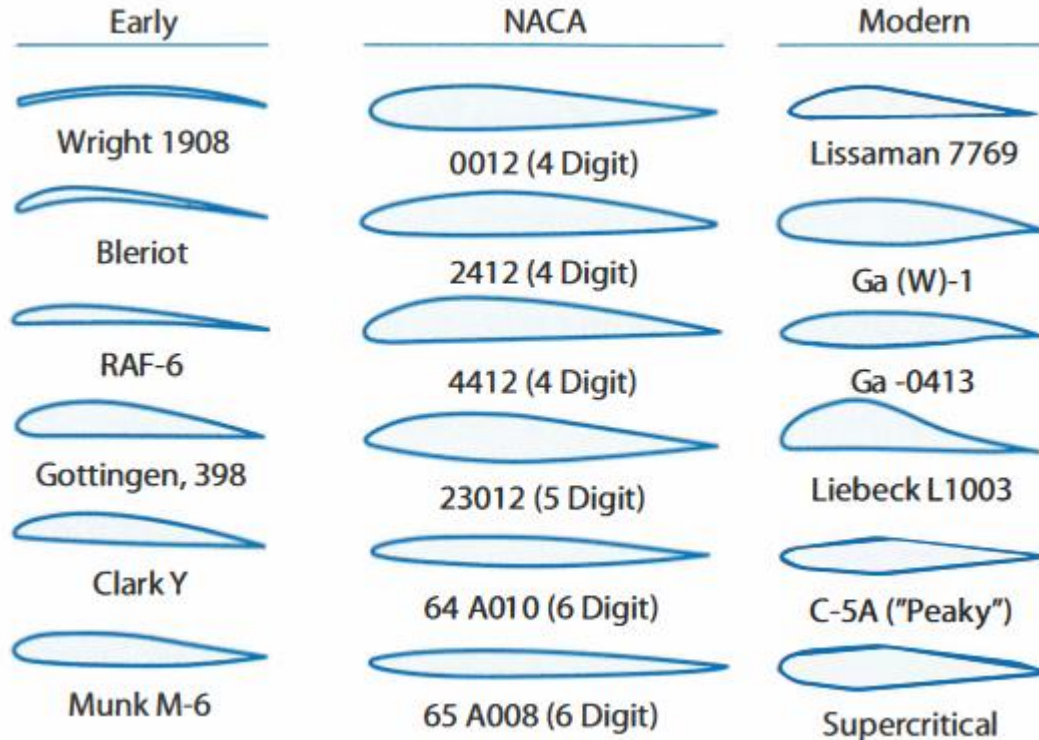


Figure 1.27 Typical airfoils (Reymer, 2018).

Airfoils can be categorized in numerous ways, and the categorization can vary based on the specific context and criteria of interest. Some additional ways airfoils can be categorized are the following (Leishman, 2023):

- **Symmetrical or asymmetrical (cambered) airfoils:** It can be easily understood that the difference between the two categories is that the first one consists of fully symmetrical airfoil shapes on the direction of the airflow (at zero angle of attack) as seen in Figure 1.28,





while the other by airfoils that have different shape above and below the airfoil (Figure 1.28).

- **High lift and low lift airfoils:** High lift airfoils are designed to produce significant lift at lower angles of attack and are commonly used in lower speeds which is the main element of Formula Student Competition, Selig 1223 for example, shown in Figure 1.29. On the other hand, low lift airfoils like NACA 0009 shown in Figure 1.30, are optimized for efficient cruising at higher speeds and produce less lift compared to high lift airfoils. The main differences between the two, is that the high lift ones consist of larger camber than the low lift, and they are usually thicker. When the profile produces more lift, it is inevitable that additional drag will be produced as well. The important factor that helps engineers select which profile is more suitable, depends on the application.
- **High speed and low speed airfoils:** High speed airfoils are commonly used at higher speeds and their main feature is that they produce significantly small drag, while producing the desired amount of lift. Low speed airfoils aim to maximize lift and are usually thicker than the high-speed ones, and this is the reason why they generate a noticeable amount of drag.

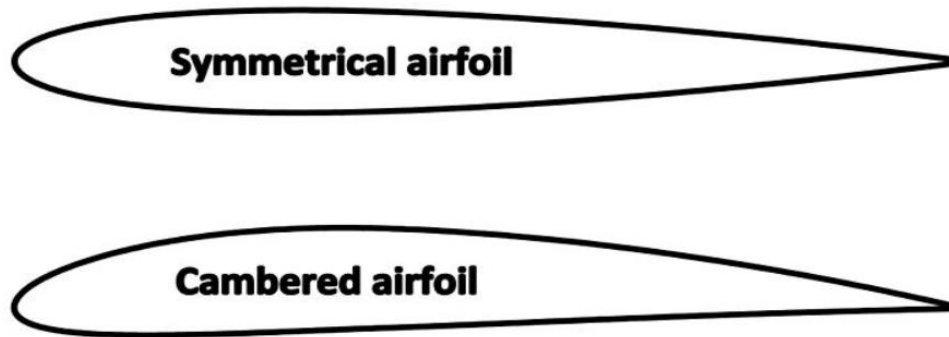


Figure 1.28 Symmetrical and Asymmetrical (Cambered) wing profiles

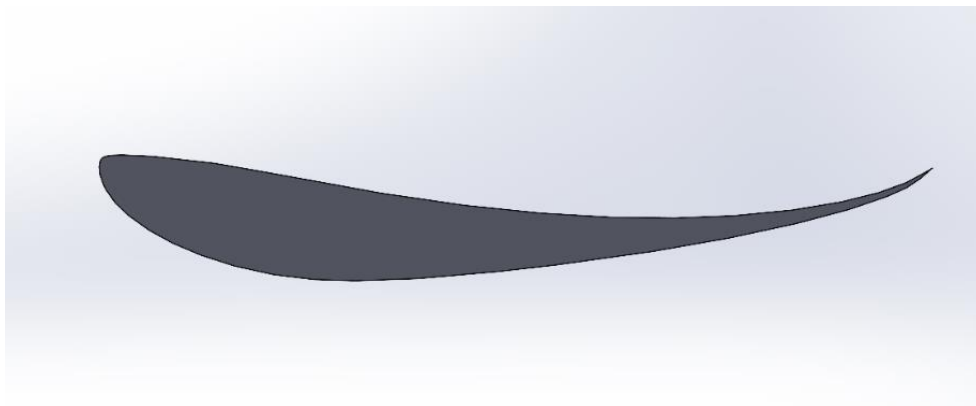
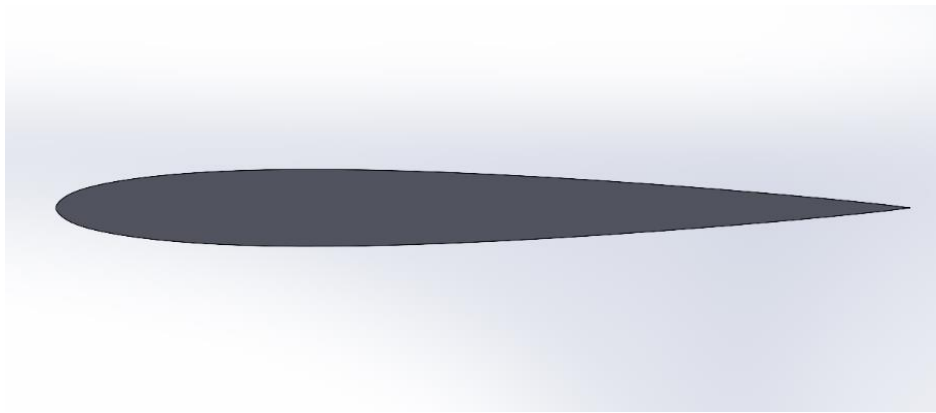


Figure 1.29 Selig 1223 wing profile (high lift airfoil)



**Figure 1.30** NACA 0009 wing profile (low lift airfoil)

### 1.4.2. Anatomy of airfoils

When discussing airfoils, in addition to their general categorization, there exist crucial characteristics that define the properties they will exhibit and determine their most suitable applications. These main characteristics are the following (Figure 1.31) (Raymer, 2018):

- **Leading edge:** The foremost point of the airfoil is referred to as the leading edge. This is where the airflow initially makes contact with the surface, typically forming a stagnation point characterized by maximum pressure.
- **Trailing edge:** The trailing edge is the rearmost point of the airfoil, and this is where the airflow separates from the surface.
- **Chord line:** The chord line is the straight line that connects the leading and the trailing edge of the airfoil.
- **Camber:** Camber is the mean curvature of the airfoil from its chord line. A cambered airfoil has a curved upper surface and a flatter lower surface or the opposite when negative lift is desired.
- **Thickness:** Thickness is known as the distance between the upper and lower surfaces of the airfoil, perpendicular to the chord line. One method of labeling an airfoil is by specifying its maximum thickness and its location along the chord line, measured from the leading edge.
- **Angle of attack:** Although it is not basically a characteristic of the airfoil but still defines its properties, the angle of attack (AOA) is the angle that occurs between the chord line of the airfoil and the direction of the flow.

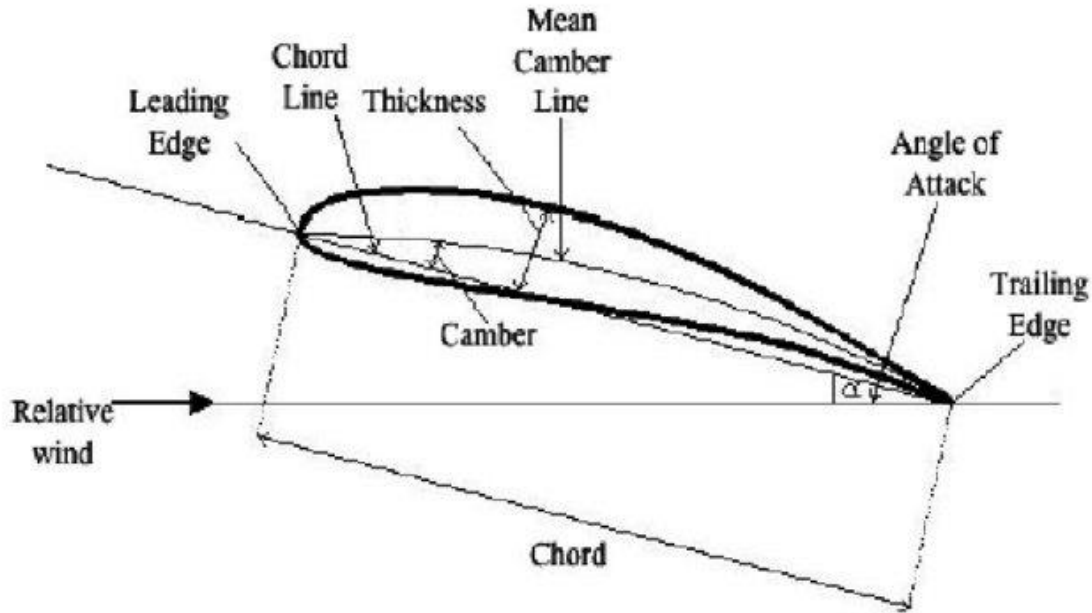


Figure 1.31 Cross-section of an airfoil (Kevadiya, 2013)

## 1.5. Computational Fluid Dynamics (CFD)

### 1.5.1. Introduction to Computational Fluid Dynamics

Computational Fluid Dynamics (CFD) is a powerful tool for the analysis and simulation of fluid flows, allowing Formula Student teams to improve vehicle aerodynamics and optimise performance without real testing (Figure 1.32). Using numerical methods and computer simulations, CFD can visualize and predict airflow patterns around solid bodies using governing equations from fluid dynamics (such as Navier-Stokes). This helps to improve various aspects such as downforce, drag reduction and cooling efficiency (Khalil, 2012).

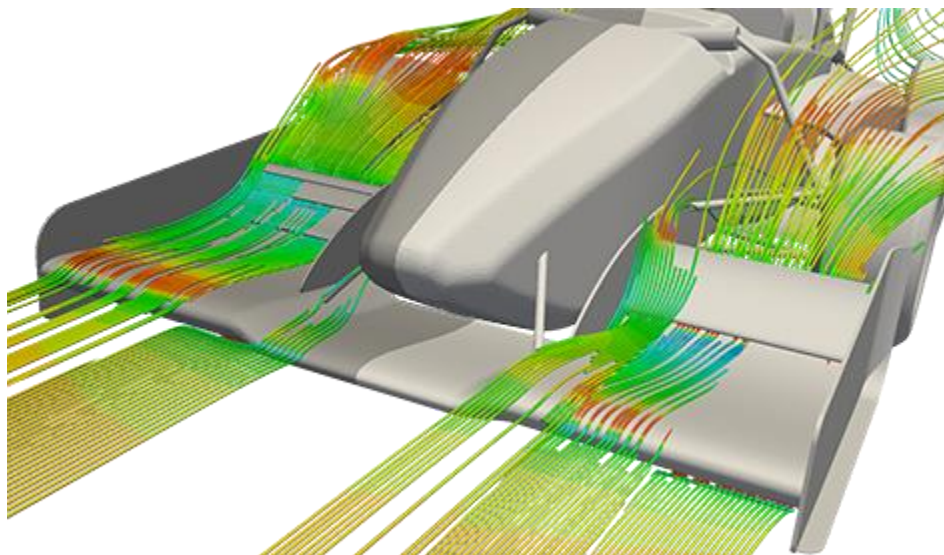


Figure 1.32 Flow visualization of a Formula Student Car using CFD software (Simscale, 2018)



### 1.5.2. Advantages and disadvantages of CFD

When proceeding with CFD simulations, there are some advantages and disadvantages that must be taken into consideration in order to reach the conclusion if it is suitable or not for the specific case (Linfield and Mudry, 2008). In Formula Student teams, one of the most important factors is to utilize limited resources, to achieve the best possible results.

The most significant benefit of CFD is that it is cost-efficient as it allows teams run simulations instead of conducting high-cost experiments which require time and a high budget. Also, the time needed to set up a CFD simulation is usually significantly smaller than setting up an experiment, which allows teams to run multiple simulations for design optimisation. When the general idea of the design is decided, physical testing and experimentation takes place to verify the results.

However, it is important to acknowledge some limitations related to CFD simulations. While such simulations aim to reproduce real conditions, they are based on solutions of equations that involve the principles of fluid dynamics. As a consequence, the results provided by CFD simulations may not always achieve the desired level of accuracy or represent the actual results that would occur in reality.

To sum up, CFD is a useful tool that is appropriate for student teams and small businesses that don't have access to wind tunnels and experimental facilities. Student teams usually make mistakes while they design parts, which makes it impossible to build the actual part and test it in real time. On the other hand, it is vital that on CFD simulations, some deliverables and parameters might lead to unreliable results.

### 1.5.3. Meshing properties

The mesh is a link between the continuous physical field and the discrete numerical field, allowing CFD solvers to solve the governing equations in a manageable mesh structure. The geometry, density, and quality of the mesh significantly affect the accuracy of the simulated fluid behaviour. Meshes can take various forms from structured grids, where the elements are arranged in a distinct pattern, to unstructured grids, which offer flexibility to adapt to irregular shapes. Each type has its advantages and disadvantages, and the choice depends on the complexity of the geometry and the desired accuracy.

In order to understand the methodology that is going to be used in this thesis, it is crucial to clarify some basic terminology regarding mesh generation. Meshing is divided into the following features (Oxyzoglou, 2017):

- **Surface meshing:** Surface meshing is the first step in the meshing procedure, and it consists of the cells that surround the geometry that is being simulated. The most common cells used in surface meshing is triangular cells due to their simplicity, but when a more complicate geometry is being studied, different types of cells like quadrilaterals, higher polygons or even mixed cells are used for more accuracy (Figure 1.33).
- **Volume meshing:** Volume meshing is the process of dividing the fluid domain into cells where the all the equations will be solved. Tetrahedral, hexahedral, pyramid or a combination of mixed cells is usually selected in volume meshing, and their selection depends on each case (Figure 1.34).
- **Layering:** Between surface and volume meshing, it is important to set up a layered grid to demonstrate the boundary layer that exists around the solid body that is being studied (Figure 1.35). Its resolution and the thickness of the layers depends on several factors, such as the type of the flow (speed, viscosity of the fluid etc.) and the quality and shape of the surface.

## Surface Meshing (2D)

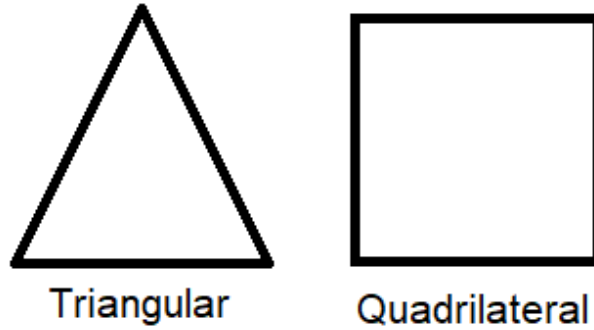


Figure 1.33 Triangular and quadrilateral shaped cells for surface meshing

## Volume Meshing (3D)

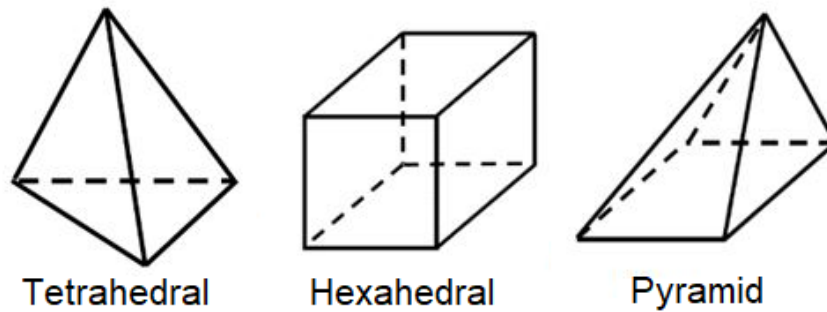


Figure 1.34 Tetrahedral, hexahedral and pyramid shaped cells for volume meshing

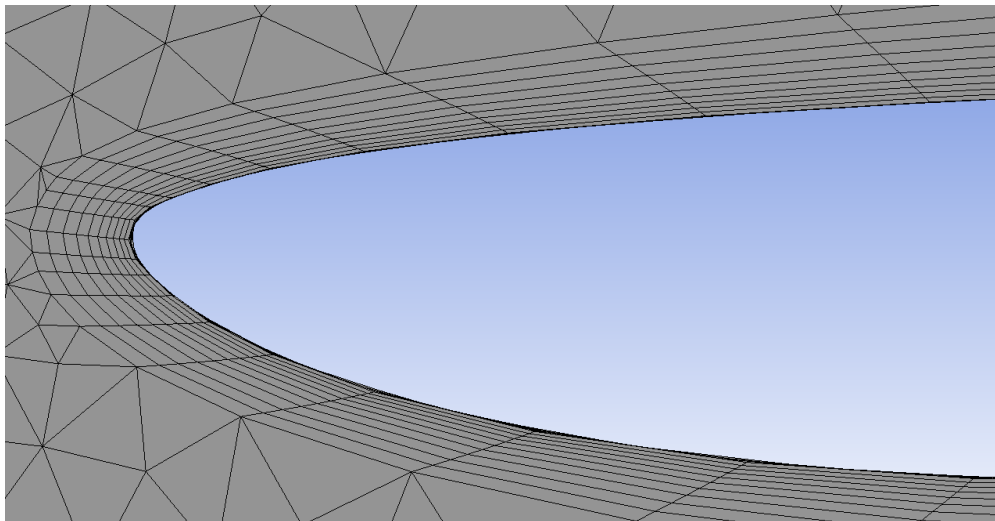
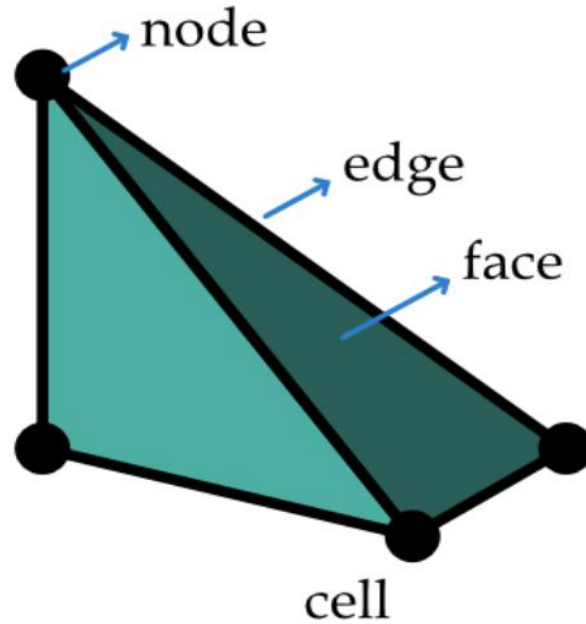


Figure 1.35 Layering (inflation) around a wing profile.

Now that all the governing cell shapes are mentioned, their basic features are shown in Figure 1.36.



**Figure 1.36** The anatomy of a meshing element (Philip Luke K, 2021)

It is easy to understand that 2D cells such as triangular and quadrilateral have one surface, three or four nodes (vertices) and no edges. Volume mesh cells (3D cells) have at least 4 surfaces, 4 nodes and 6 edges if they are tetrahedral, or even 6 surfaces, 8 nodes and 12 edges if they are hexahedral.

#### 1.5.4. Governing equations of fluid dynamics

Computational Fluid Dynamics is a whole field of study based on fundamental physical principles which is progressing all the time. The three mathematical statements that are mainly applied are (Versteeg and Malalasekera, 2007):

1. Conservation of Mass: In fluid dynamics, it is common that mass is conserved within a control volume when the density of the fluid is thought to be constant.

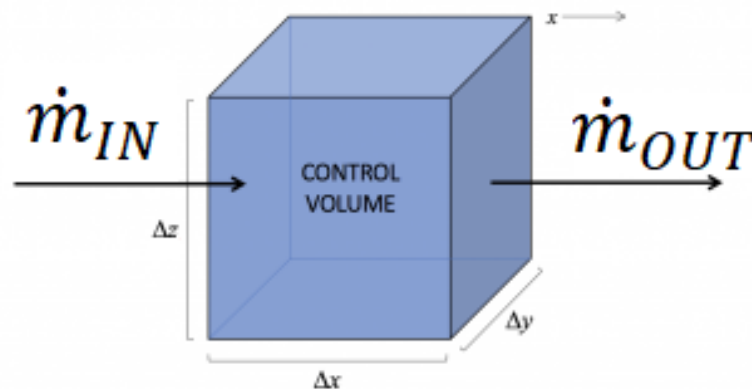


**Figure 1.37** Conservation of mass within a control volume (Hautala, 2020)



2. Conservation of Momentum (Newton's second law): A fluid particle's rate of momentum change is equal to the sum of the forces that act on the particle.

$$\Sigma F = m * a \quad (\text{eq. 1.13})$$

- Where:
  - $\Sigma F$ : the sum of the forces that act on the particle (N)
  - $m$ : mass of the particle (kg)
  - $a$ : acceleration of the particle ( $m/s^2$ )

3. Conservation of energy (First law of thermodynamics): The first law of thermodynamics known as Conservation of energy, states that the sum of heat and work given to a system increases the total energy of that system:

$$\Delta E = Q + W \quad (\text{eq. 1.14})$$

- Where:
  - $\Delta E$ : the difference in the energy of the fluid (enthalpy for open systems and internal energy for closed systems) (J)
  - $Q$ : the amount of heat transferred to the fluid (J)
  - $W$ : the amount of work done by the fluid (J)

### 1.5.5. Navier Stokes Equations

Based on the statements and equations above, the Navier-Stokes equation, which has multiple forms, is used to calculate the change of fluid flow properties, like velocity, pressure, and density. The general form of the N-S equation in one direction is the following (White, 1999):

$$\rho \left( \frac{\partial u}{\partial t} + u \frac{\partial u}{\partial x} + v \frac{\partial u}{\partial y} + w \frac{\partial u}{\partial z} \right) = \rho g_x - \frac{\partial p}{\partial x} + \mu \left( \frac{\partial^2 u}{\partial x^2} + \frac{\partial^2 u}{\partial y^2} + \frac{\partial^2 u}{\partial z^2} \right) \quad (\text{eq. 1.15})$$

- Where:
  - $\rho$ : the density of the fluid ( $kg/m^3$ )
  - $u$ : the velocity of the fluid (x-axis) ( $m/s$ )
  - $v$ : the velocity of the fluid (y-axis) ( $m/s$ )
  - $w$ : the velocity of the fluid (z-axis) ( $m/s$ )
  - $g_x$ : gravitational acceleration (x-axis) ( $m/s^2$ )
  - $p$ : pressure ( $N/m^2$ )
  - $\mu$ : dynamic viscosity of the fluid ( $kg/m*s$ )

In motorsport and especially in Formula Student where the velocity of the vehicles is significantly smaller than the speed of sound, Mach number which was mentioned in chapter 1.2.2.2, is smaller than 0.3, which means the flow is incompressible.

Another derivative is that when Reynolds number approaches infinity, all viscous effects are thought to be significantly small, and so they are thrown away from the N-S equation.

Once the main background theory is briefly mentioned, the next subchapter is dedicated to the solving models that are based on the Navier-Stokes equations and are constantly used in CFD.



The Navier-Stokes equations have various forms and methods to be solved. The most common methods of solving the N-S equations are the following (Cebeci, 2005):

- **Reynolds-Averaged Navier-Stokes (RANS):** The Reynolds-Averaged Navier-Stokes equations are usually applied to solve turbulent flows by setting specific boundary conditions and initial values that contain time-varying quantities. RANS is applied in most cases (especially for industrial use), due to the fact that it is more efficient than other methods such as DNS and LES but is more inaccurate (Figure 1.39). All governing models such as k-omega, k-epsilon and k-omega SST which will be discussed in chapter 1.5.6 are RANS based.
- **Direct Numerical Simulation (DNS):** Direct numerical simulation is the most complex method, because it deals with turbulent flows by directly solving a wide range of small and large scales in both space and time, without relying on any simplifications. This approach is used for simple shapes and mainly in research, as it is quite demanding. As shown in Figure 1.38, it is the most computationally intense method, but provides the most degrees of freedom. However, in Formula Student and motorsport in general, where the shapes are more complex, this method is not practical.
- **Large Eddy Simulation (LES):** In this approach, the largest scales of turbulence are the ones that are directly resolved, while the smallest scales (smaller eddies) are filtered out. Although LES is also quite complex and has high computational cost, by neglecting smaller scales of turbulence it is simpler than DNS method but a bit more inaccurate.
- **Hybrid RANS-LES:** As it is easily understood, hybrid RANS-LES modelling is a combination of RANS and LES which models turbulence with RANS near walls to avoid large computational power, and with LES away from them in order to reach a more accurate result in less computational time.
- **Unsteady RANS:** A variant of RANS is URANS which is not commonly used because its application is more complicated, but it is usually applicable to cases where the flow is featured by moving parts or periodic flows features.

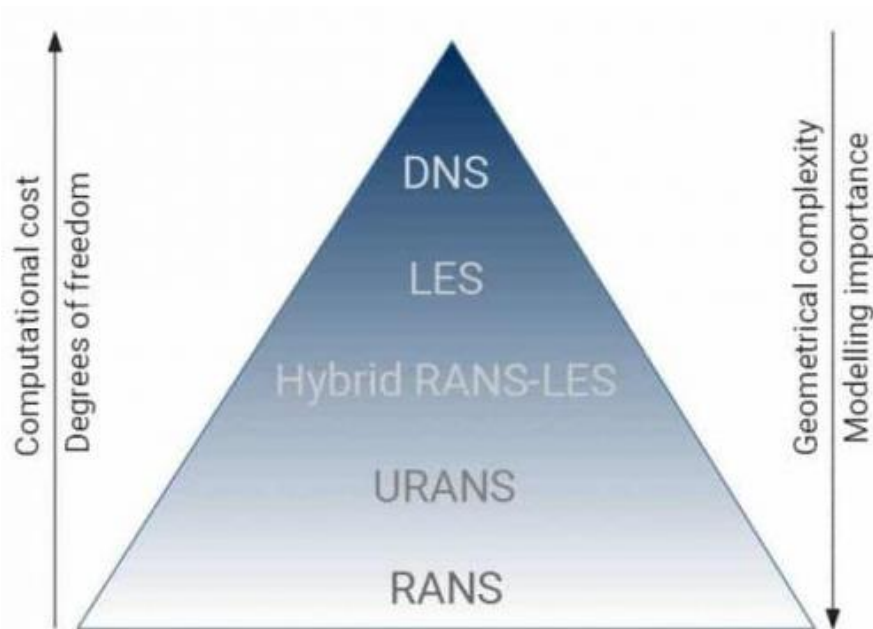


Figure 1.38 Characteristics of turbulence models in CFD



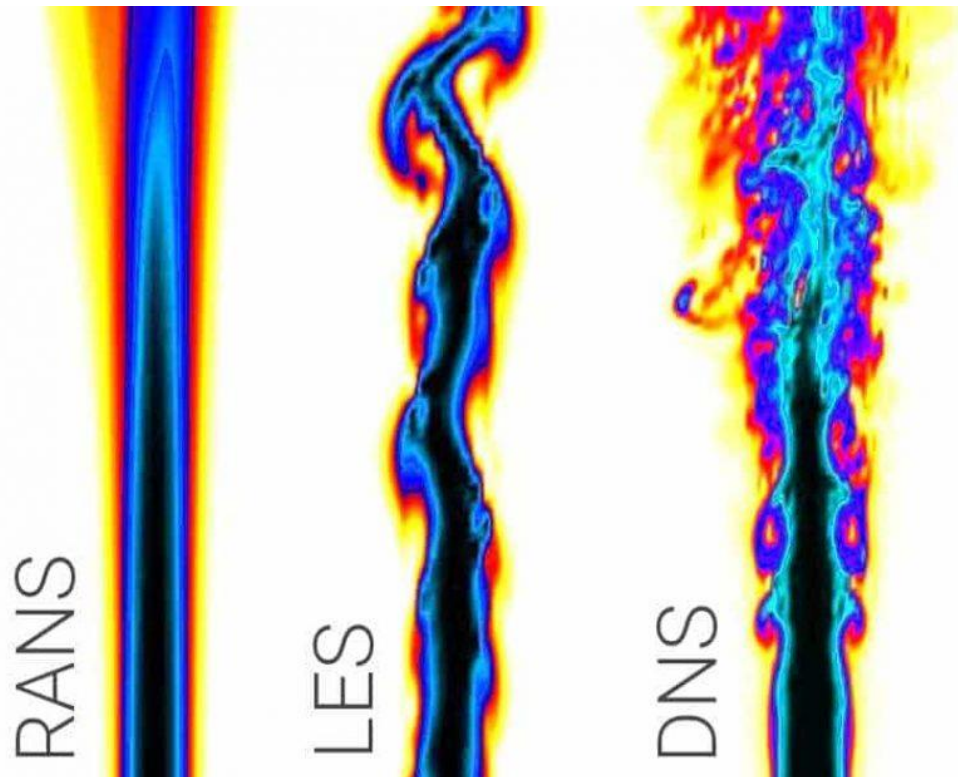


Figure 1.39 Simulation accuracy of RANS, LES, and DNS modelling methods

### 1.5.6. CFD Solving Models

In the context of this thesis, RANS modelling is the approach that is going to be used and furtherly discussed. As mentioned in chapter 1.5.5, in order to solve the N-S equations, various models have been studied and developed that simplify their solution by setting boundary conditions and assumptions about the flow, that will not alter the result significantly. These models are used in complex geometries efficiently, giving acceptable results in a small amount of time. The three main models that are being used in CFD are the following (Blazek, 2001):

- **k-epsilon (k- $\epsilon$ ):** The k- $\epsilon$  model is the most common model that is used for turbulent flow conditions to simulate their mean flow characteristics. This model is widely used in the automotive industry due to its efficiency. It is appropriate for freestream flows, but it lacks accuracy when applied in near wall flows compared to k-omega.
- **k-omega (k- $\omega$ ):** As mentioned above, k-omega is more applicable in near wall flows due to its accuracy when simulating boundary layers. The main disadvantage of this model is that it is not capable of simulating freestream flows accurately. This is the reason that CFD engineers developed the k-omega SST model which will be described below.
- **k-omega SST (k- $\omega$  SST):** K-omega model is a combination of the k- $\epsilon$  and k- $\omega$  models, with the main goal to achieve accuracy on both freestream and near wall flows. This model is a bit more complex than the others two are individually and usually result in higher computational cost and its application depends on the desired outcome.

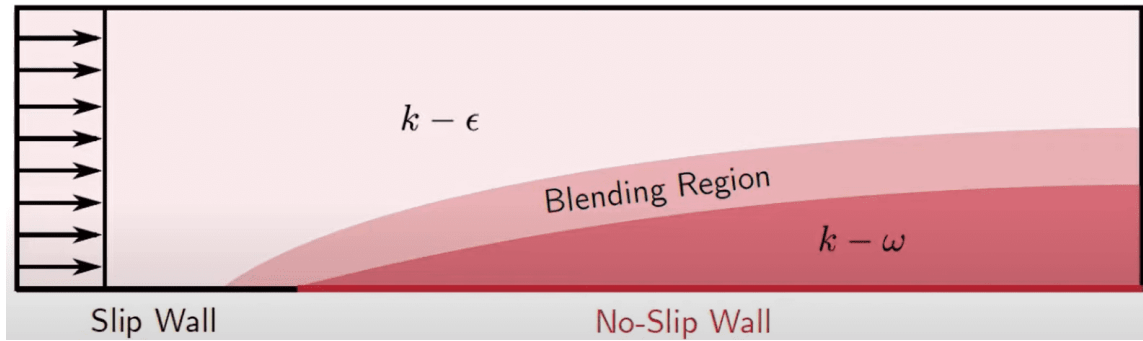


Figure 1.40 K-omega SST model (combination of k- $\epsilon$  and k- $\omega$  models) (Simscale, 2023)

The selection of the model that is used depends on the application, the desired outcome of the simulation, the properties that will be examined and other factors. In this thesis, a set of simulations will be conducted in chapter 2.3 to determine the most suitable model for our application.

## 1.6. Current Literature

Starting from the end of the 20th century, “Fundamentals of Aerodynamics” (Anderson, 2017) is the 6th edition of the book that was firstly released in 1984 surrounding and explaining all the fundamental aspects that surround the field of aerodynamics leading to major research breakthroughs. It is important to clarify that there are various books published before the above but are not so well known.

Hucho et al. (1987), Barnard (2001) and Rossis et al. (1993) released the first books that were dedicated entirely on the field of aerodynamics on a road vehicle and the main goals of the application. All of the above, as much as other books and published articles, led to the further development of the field, which was also applied in motorsport and race vehicles in general. The most common books that set the ground for this specific field of study were, Race Car Aerodynamics (Katz, 2003), Competition Car Downforce (McBeath, 2006) and Race Car Design (Seward, 2014). All three books describe the effect of airflows over racing vehicles and the ways that by specific designs, engineers can take advantage of the physics that take place.

From another perspective, the scientific community started advancing in the subfield of Computational Fluid Dynamics in the middle of the 20th century. (Blazek, 2001), (Versteeg and Malalasekera, 2007) and (Wendt et al., 2008), have published the most well-known books around the field of CFD, which are focused on explaining the ways in which variant aerodynamic behaviours can be calculated through the use of governing equations like the Navier-Stokes equation. Furthermore, fundamentals of CFD are described, including calculation models (k-epsilon, k-omega, k-omega SST etc.) that are based on various equations, meshing and other aspects.

The theory behind airfoils is also another subfield of aerodynamics, since every slight difference in the design of a wing profile, can have major effects on its aerodynamic behaviour. The publications that surround this field were mainly published in the 20th century with the first one being “Theory of Wing Sections: Including a Summary of Airfoil Data”, (Abbott and Doenhoff, 1959) and in the early 90s, “Low-speed aerodynamics: from wing theory to panel methods” (Katz and Plotkin, 1991).

In the field of motorsport (Formula Student, Formula One etc.) there are numerous reports, theses, and research articles published. Fundamentals of aerodynamics on race cars, methods of simulation and design approaches are listed and described. Most publications focus on the development and design of a full vehicle and not only on a specific aerodynamic device since every part of the car affects all the others. Some well-known publications are the following: (Wordley and Saunders, 2006), (Phersson et al.,



2009), (Dahlberg, 2014), (Prasanth et al., 2016), (Shreyas Vaidya et al., 2017), (Apostolidis et al., 2019) and (Oxyzoglou, 2017). All of the above focus on the design approach of a full aerodynamic package for a FSAE racing car, and optimization of the design to meet the requirements of the competition as well as the desired results in performance and efficiency. On the other hand, (Grabis and Agarwal, 2019), (Dhaneswar et al., 2021) and (Kalinowski and Szczepanik, 2021) focus on the design and optimization of the front wing using the method of computational fluid dynamics and mathematical models that was discussed in chapters above.

### **1.7. Scope of the Thesis**

The main purpose of this thesis is to design and optimize through several sets of simulations the front wing assembly of the Formula Student Vehicle for Poseidon Racing Team in obedience to the regulations that are set by the competition. A number of CFD simulations will be conducted in various wing profiles, configurations, and other parameters, using verified simulations, so that the resulted design of the front wing assembly, is optimized and efficient regarding the available resources of the team. Once the final geometry is determined and optimized by the CFD simulations, its resistance to the minimum forces that are set by the regulations of the competition will be tested through FEA simulations.

It is important that the goal of this thesis and research is determined prior to the start of the design and simulations. Poseidon Racing Team will compete in the Formula Student for the first time with an aerodynamic package, which means its study and design should be simple. The main goal for the front wing is to produce as much negative lift as possible without any complex geometries. The amount of drag produced is of secondary importance, but for the better performance of the car, should be remain at low values.

## 2. Methodology

### 2.1. Basic Methodology Steps

The aerodynamic and static study and design of the front wing assembly for the Poseidon Team's Formula Student 2023-2024 race car is divided into several methodological steps. The first step of the methodology is the definition of all objectives before the process starts, ensuring compliance with competition regulations; this step is called design approach. Once the general design constraints have been defined and imprinted into CAD documents in Solidworks, the next stage of the study consists of CFD simulations through ANSYS and META, which has three main steps: pre-processing, solving and post-processing. A virtual wind tunnel will be created to test the airfoil designs, simulating real conditions within a controlled environment. All designs will be tested extensively and then optimized through these simulations. Once this process is complete, the resulting design will be tested using FEA simulations to determine its ability to withstand the minimum forces required by the competition regulations. The process described above can be easily understood by observing Figure 2.1.

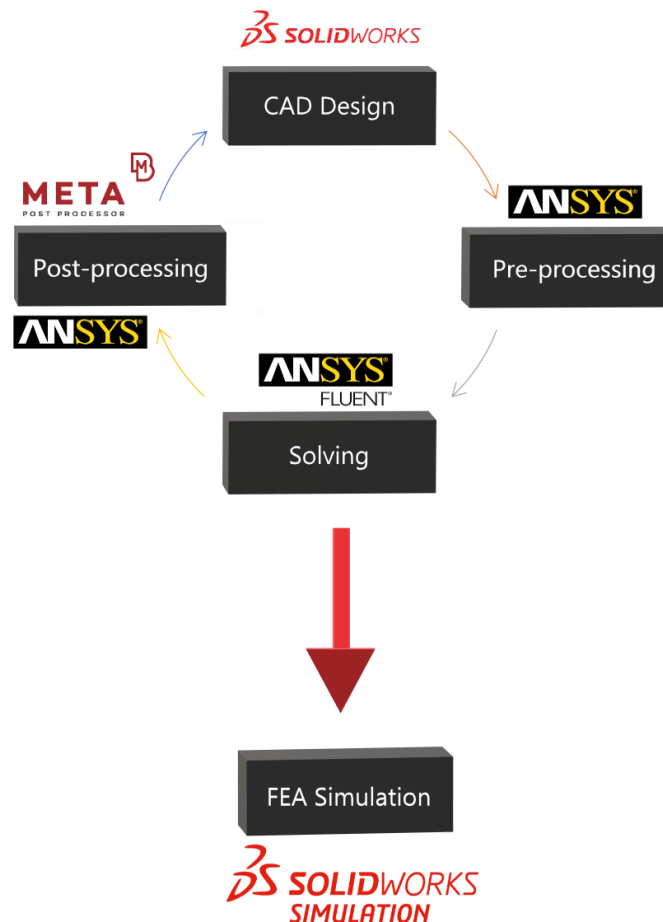


**Figure 2.1** Diagram presenting the basic methodology steps of the study



To sum up, the 3 basic steps of the methodology are the following:

1. Design approach, in which all the airfoil profiles and configurations will be designed,
2. CFD simulations, where several sets of simulations will be conducted to result in the most efficient design, and
3. FEA simulation, where the final design will be submitted to specific forces set by the regulations.

## 2.2. Design Approach

### 2.2.1. Design constraints

In the initial stages of the design of the front wing assembly, the competition regulations put constraints that limit the options and spaces available. As a result, the design cannot be optimal, but it can be made as efficient as possible. These limitations are set by the competition mainly for safety reasons and competitiveness among the teams.

The most significant regulations regarding the front wing assembly design, as seen in Figures 2.2 and 2.3 are the following (FSG, 2023):

- Height restrictions:
  - All aerodynamic devices forward of a vertical plane through the rearmost portion of the front face of the driver head restraint support, excluding any padding, set to its most rearward position, must be lower than 500 mm from the ground.
  - All aerodynamic devices in front of the front axle and extending further outboard than the most inboard point of the front tire/wheel must be lower than 250 mm from the ground.
- Length restrictions:
  - All aerodynamic devices must not extend further forward than 700 mm from the fronts of the front tires.
  - No part of the vehicle may enter a keep-out-zone defined by two lines extending vertically from positions 75 mm in front of and 75 mm behind the outer diameter of the front and rear tires in the side view of the vehicle, with steering straight ahead.
- Width restrictions:
  - There are no width restrictions for the front wing.
- Position restrictions:
  - The ground clearance of every part of the vehicle must be higher than 30mm.

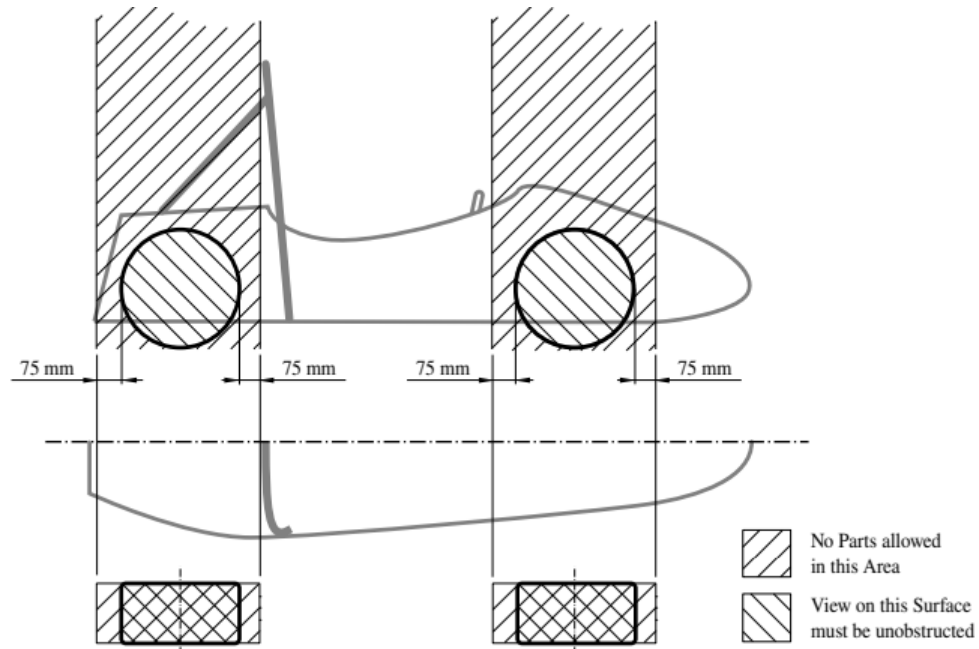


**Figure 2.2** FSG regulation regarding the design around the wheels (FSG, 2023)

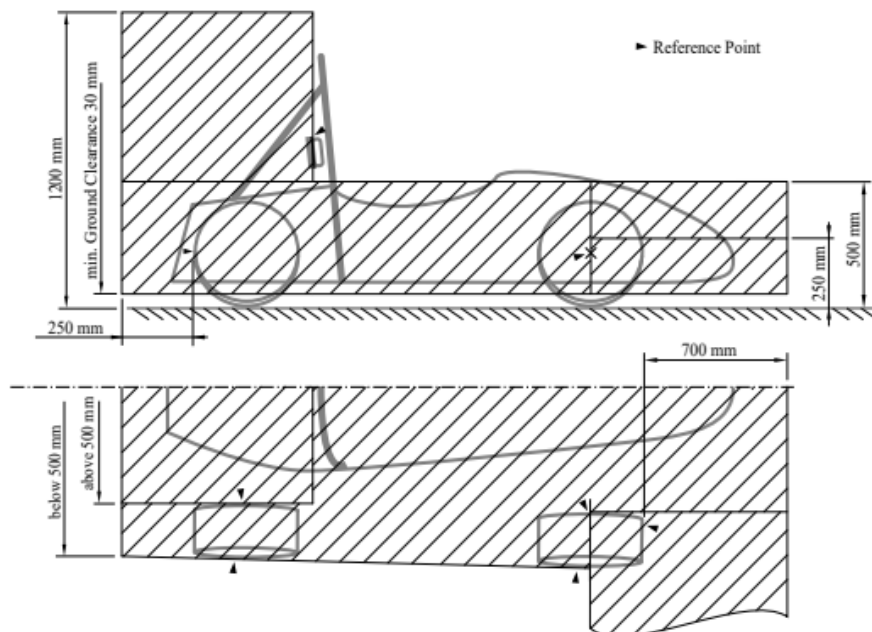


**Figure 2.3** FSG design limitations on dimensions of aerodynamic devices (FSG, 2023).

Following the regulations above, using Dassault Systemes's CAD program Solidworks, initial bounding boxes were designed to define the available space for the front wing assembly (Figures 2.4 and 2.5)

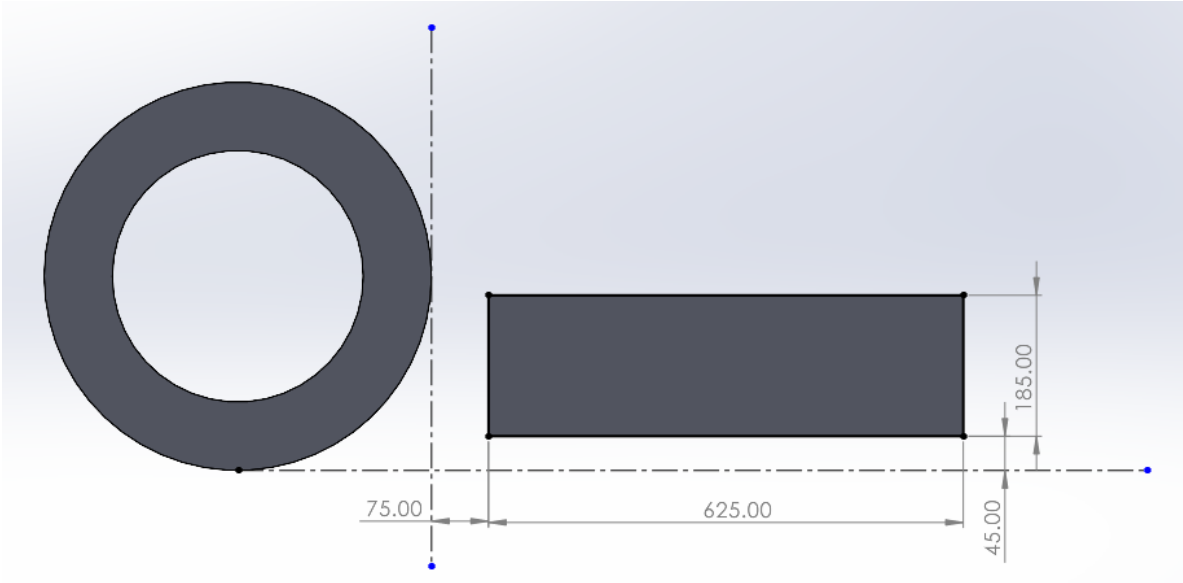


Figure 2.4 Restrictions in dimensions of the front wing assembly (side view)

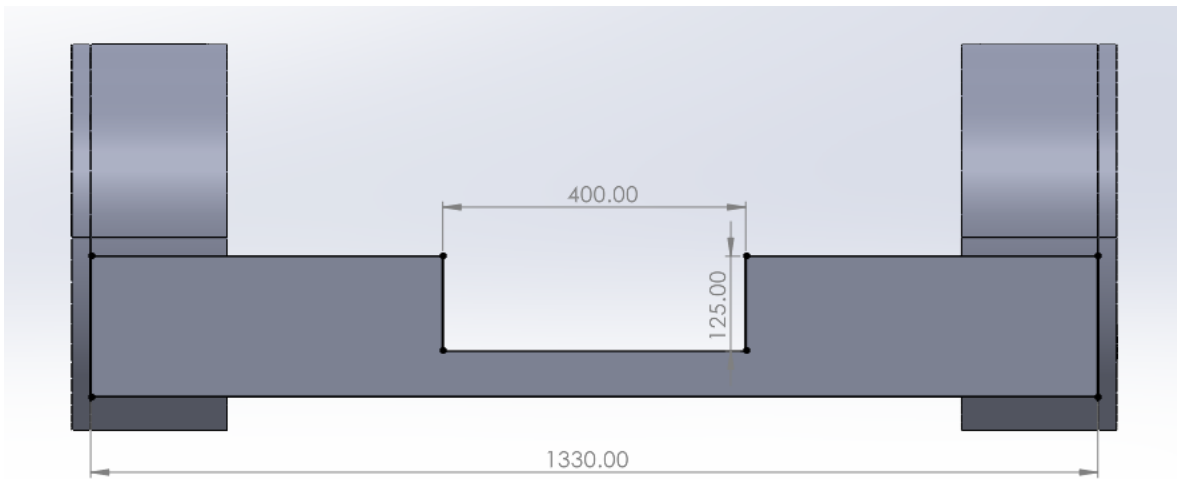
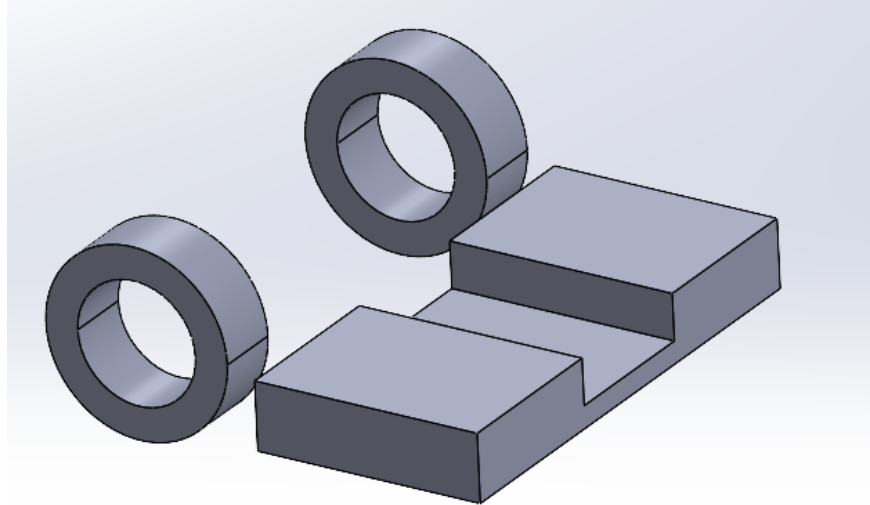


Figure 2.5 Restrictions in dimensions of the front wing assembly (front view)



**Figure 2.6** Bounding box of the available for the front wing assembly (3D view)

In Figures 2.4 and 2.5, the maximum dimensions for the front wing are established with a tolerance of a few millimetres. This allowance ensures that the final construction will remain within limitations, in case of potential design or construction errors that may arise. Considering all the above, the maximum dimensions for the front wing assembly are:

<b>Length:</b>	625 mm
<b>Width:</b>	1330 mm
<b>Height:</b>	185 mm
<b>Gap in the middle (for the nose cone):</b>	400x125 mm
<b>Ground clearance:</b>	45 mm

**Table 2.1** Maximum dimensions for the front wing assembly

Complying with the design constraints that are set and considering the most common design solutions used in Formula Student, the decision was taken to deliver an airfoil design consisting of two standard airfoil profiles, with the primary one having a chord length of about 360 mm at an angle from -3 to 9 degrees (AoA) and the secondary one with a chord length of about 144 mm (40% of main element's chord length) (McBeath, 2006) and an angle from 15 to 45 degrees (the angles will be determined from the simulations).

### 2.2.2. Basic design steps

This chapter is dedicated to the design of the four different airfoil profiles that are going to be examined through CFD simulations. All four airfoils that will be used are characterized as high lift airfoils which are used repeatedly in motorsport, and are the following:

- Selig 1210 (Figure 2.7)
- Selig 1223 (Figure 2.8)
- Eppler 423 (Figure 2.9)



- Selig 3021 (Figure 2.10)

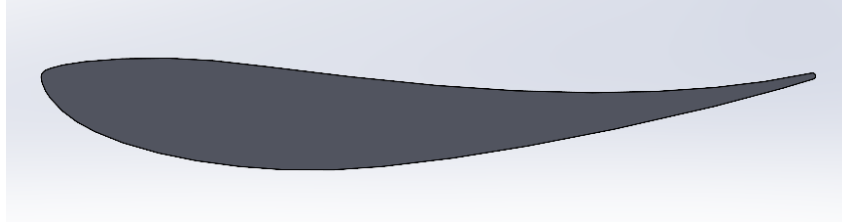


**Figure 2.7** Selig 1210 (S1210) wing profile

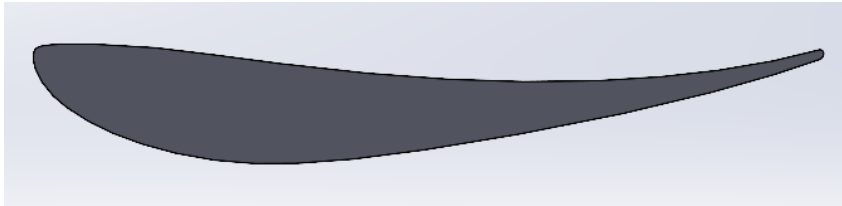


**Figure 2.8** Selig 1223 (S1223) wing profile

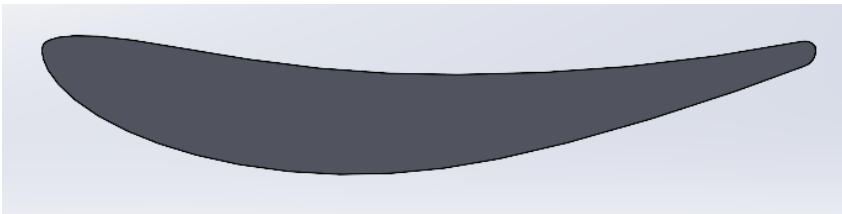


**Figure 2.9** Eppler 423 (E423) wing profile

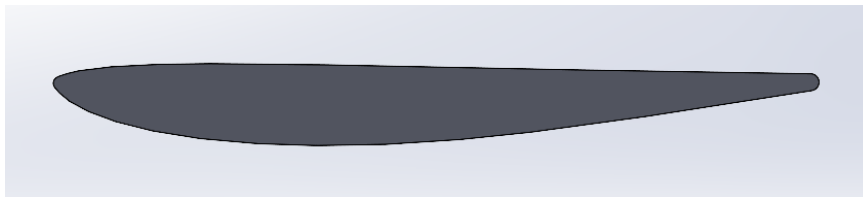


**Figure 2.10** Selig 3021 (S3021) wing profile

The airfoils presented above will be designed and tested in CFD in various angles of attack which are  $-3^\circ$ ,  $0^\circ$ ,  $3^\circ$ ,  $6^\circ$ , and  $9^\circ$ , with a chord length at 360 mm as mentioned in chapter 2.2.1 and will have a span of 1300 mm to achieve higher values of negative lift due to its larger surface. In Figure 2.11, an example of the first step of the design is visible where the Selig 1210 is presented.

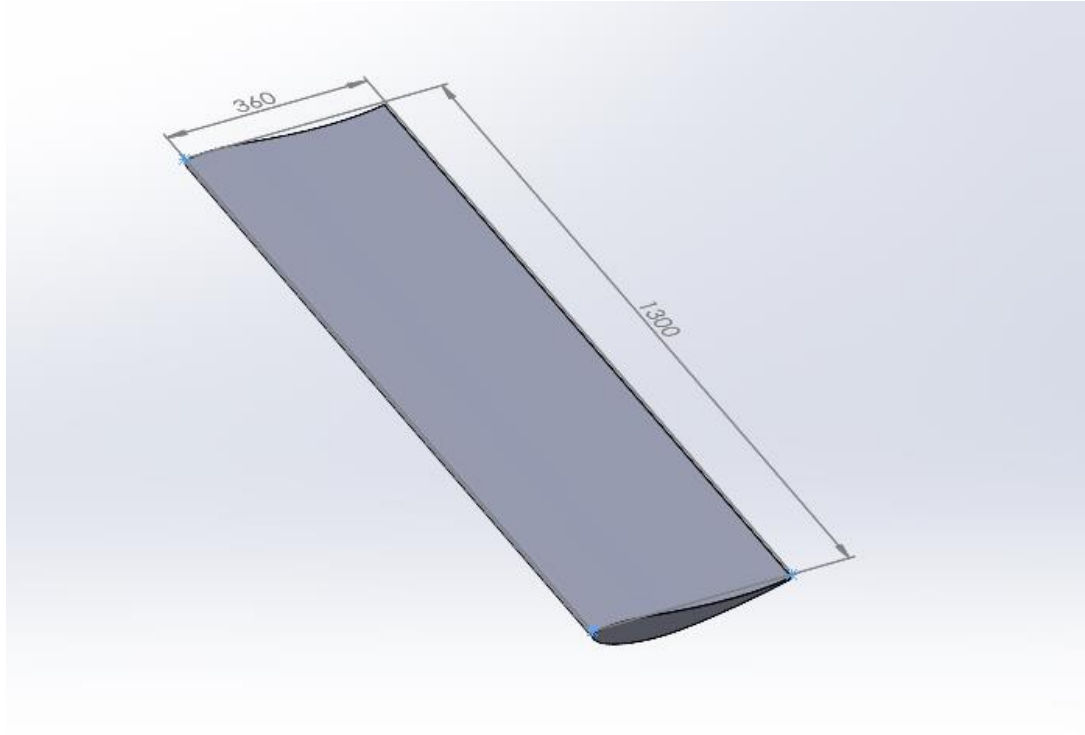


**Figure 2.11** 3D design of the S1210 wing profile

Once the main profile that will be used is determined from the CFD simulation results, the next step is to design a two-element front wing assembly in Solidworks, with a specific spacing between them (both horizontal and vertical) which will be further adjusted after the completion of the simulations in chapters 3.4 and 3.5. The airfoil that is going to be used as a secondary element will be the same as the first which will present the best results and will have a span of 1300 mm and a chord length of 144 mm (40% of the main element's chord length) as mentioned in chapter 2.2.1. The secondary element will be designed as well in various degrees, from 15 to 45 degrees because its purpose is to produce the most amount of downforce due to its aggressive angle of attack. All the above are parameters that will be decided once the CFD simulations are completed. An example of the design of the two-element front wing assembly is shown in Figure 2.12.

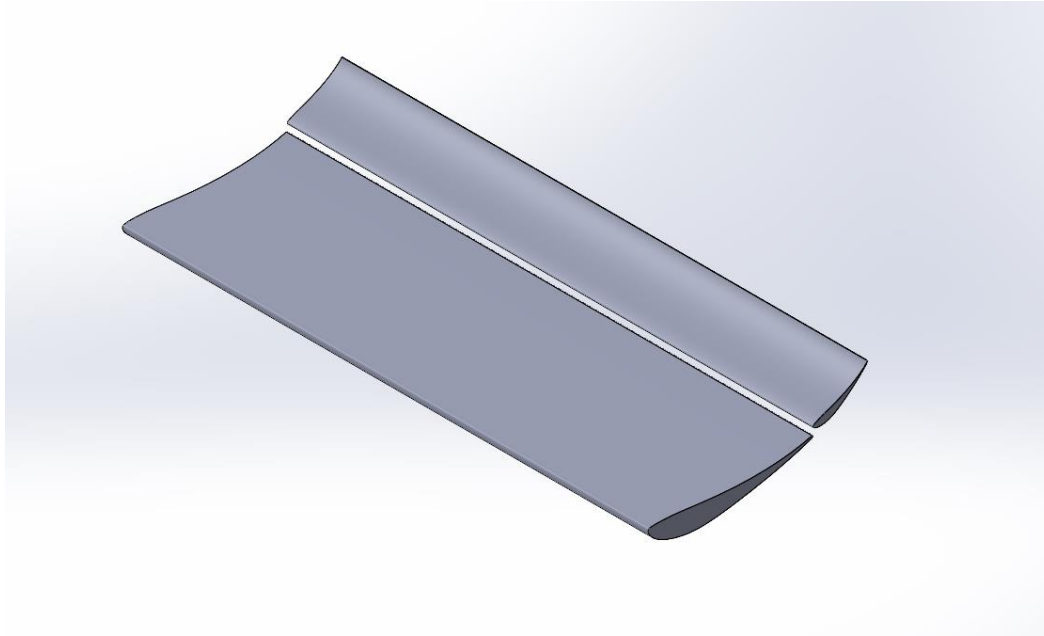


**Figure 2.12** Example of two-element front wing assembly design

After the conclusion of the CFD simulations, the final basic geometry will be extracted and will be slightly redesigned to fit in the bounding boxes that were set from the previous subchapter. In addition, endplates will be added to optimize the airflow, prevent the airflow from spoiling at the sides of the elements and generate a vortices that will 'seal' the air flow under the car (Park and Lee, 2008).

The last step of the design process is the selection of the material which is mainly carbon fiber due to its high stiffness and low weigh. Furthermore, the thickness of every element will be selected in order to withstand the required minimum forces that are set by the competition rules, which will be tested in chapter 2.4 through Finite element analysis in Solidworks Simulation.

## **2.3. Computational Fluid Dynamics Simulations (CFD)**

### **2.3.1. Pre-processing**

The initial step of the CFD simulations is called pre-processing in which the fluid domain (enclosure) is created where all the designs will be tested. In this process, a lot of factors that will be mentioned below must be taken into consideration when forming the enclosure of the airflow (virtual wind tunnel). Additionally, in this stage of the simulation set up, is the generation of the mesh that will surround the wings that will be designed, where all the calculations will be taking place.

#### **2.3.1.1 Enclosure creation**

After the geometries are tested for design, errors such as multiple or bad surfaces, the fluid domain will be formed in Ansys Workbench where the designs will be placed and tested in simulated conditions that will be set in the solving stage of the simulations set up. The fluid domain, known as enclosure, as well, surrounds the solid body of interest, but its size and features are dependent on the case and situation that is being studied. The fluid domain is consisted of two main feature which are created for various reasons including accuracy. The first feature is called enclosure and it's the one that we discussed



already, in which the air flow is inserted from its front face known as inlet, and it exits from the back of it which is called outlet. The other feature that is within the enclosure is called Body of influence, and it is a smaller domain near the solid body, in which more accuracy is desired. Their meshing properties will be mentioned and described in chapter 2.3.1.2 extensively, where the importance of their existence is going to be comprehended.

- Enclosure sizing: The size of the enclosure depends on the study, but there are some features that do not alter from one case to another. In our study, the dimensions of the enclosure will be the same in all simulations for both single and two-element configurations and will be according to documentation from the CFD program called Simscale (Simscale, 2023) are the following (Figure 2.13):
  - Length: 20 times the chord length of the airfoil ( $4c$  forward and  $16c$  rearward). The length of the domain is necessarily large, in order to give space to the air flow to fully develop (forward length), and to capture the wake that is generated behind the airfoil (rearward length).
  - Width: 6 times the chord length. (In our simulations the width cushion is set to zero in order to avoid the effects of the flow in the side of the airfoil because endplates will be placed at the end of the wing assembly)
  - Height: 5 times the chord length. (symmetric for the first simulations that will decide the profile of the airfoil, and asymmetric for the rest, in order to place the airfoil close to the bottom surface that will represent the road under it).

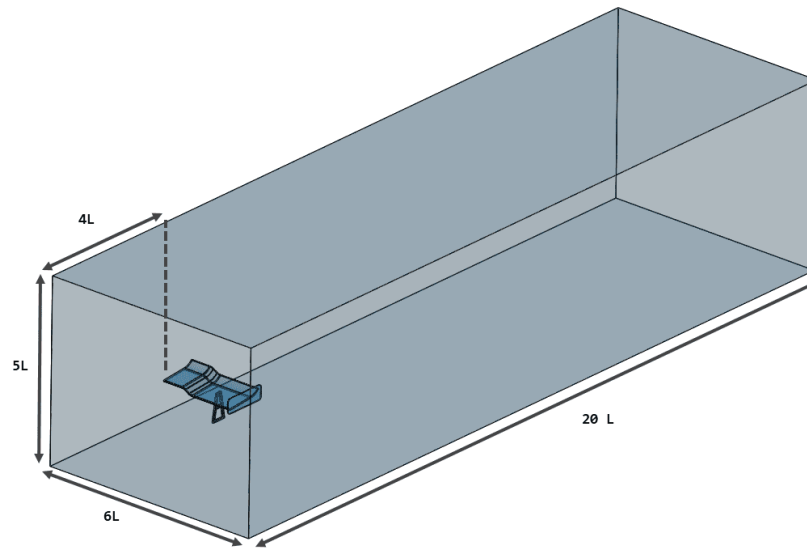


**Figure 2.13** Dimensions of the enclosure (Simscale, 2023)

- Body of influence (BOI) sizing: The size of the BOI is not set by an equation or a methodology, but it must be large enough to capture the physics around and behind the airfoil as it leaves a wake. In this subdomain that closely surrounds the studied body, a finer mesh will be formed in the following chapter, where more accuracy is desired. The two features that form the fluid domain are shown in Figure 2.14.

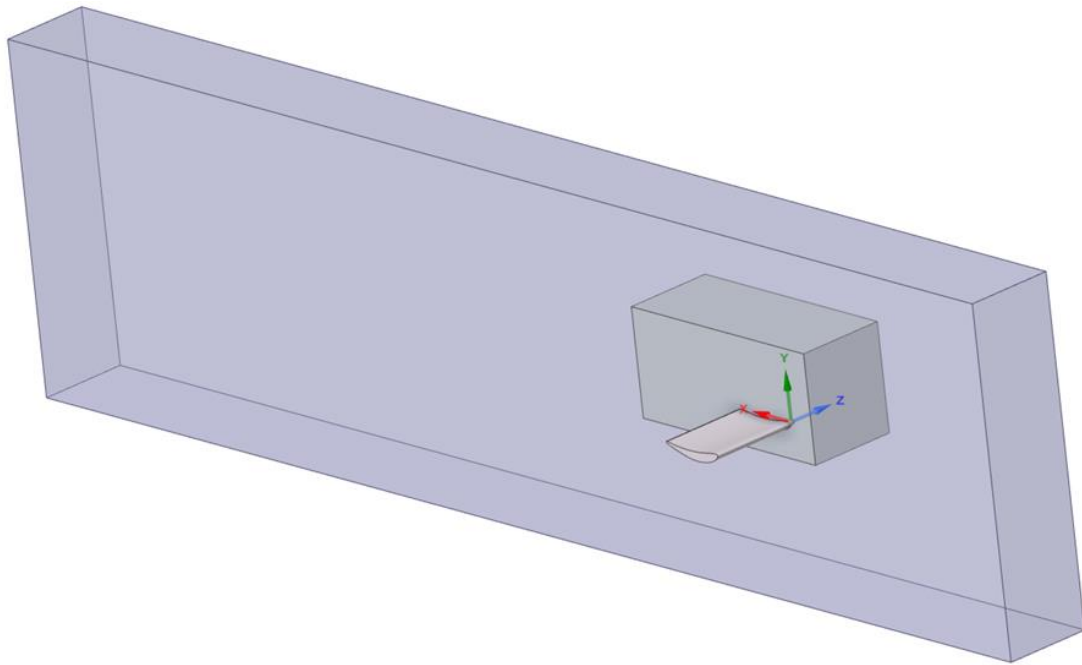


**Figure 2.14** Enclosure and body of influence around the airfoil

It can be easily observed that only half of the airfoil is inside the fluid domain; the reason is because the wall that cuts the airfoil in half will be set as a symmetry wall. This process is done in symmetric geometries reducing the mesh size, and by extension, the number of elements dramatically (about - 50%). The symmetry wall demonstrates the existence of the other half of the solid body that is being studied, and the assumption that it will react to the flow exactly like the first half does.

In summary, the enclosure and the BOI will have the following dimensions:

	Enclosure	Body of influence (BOI)
<b>Height (mm)</b>	1800	700 (150 mm below the airfoil and 550 mm above)
<b>Width (mm)</b>	650	650
<b>Length (mm)</b>	7200 (1440 mm forward and 5760 mm rearward)	2000 (150 mm forward, and 1850 mm rearward)

**Table 2.2** Dimensions of the fluid domain (enclosure and body of influence)



### 2.3.1.2 Mesh generation

When the full geometry is designed (airfoil and fluid domain), the next step is to form the mesh in the flow region. Meshing in the fluid domain is divided in the three following regions (Lu et al., 2021):

1. **Enclosure meshing:** The mesh in this region that is mainly away from the airfoil is coarser compared to the mesh sizing close to it. This happens because we are more interested in the physics that take place closely around the solid body, and the accuracy away from it is of secondary importance. By doing this, we achieve lower numbers of elements without significantly altering the outcome.
2. **Body of influence meshing:** The body of influence has finer mesh than the rest flow region, and its purpose is to provide more accurate results close to the solid body that we are interested in. Its existence is vital to the validity of the calculations, as a coarse around the solid body will lead to untrustworthy and incorrect results.
3. **Inflation:** The inflation feature is a region in meshing in which the cells are forming layers close to the object that we study, so that the boundary layer that forms due to the no-slip condition is represented correctly, and the equations are solved properly.

There is no equation or methodology that is widely used for the formation of the mesh but depending on the complexity of the geometry and the desired accuracy, the elements that is consisted of may vary from 100,000 to 5 million, or even more. It can be easily comprehended that the computational power that is required is significantly higher, when the elements are dramatically increased. The quality of the mesh in the simulations of this thesis will be determined through a set of simulations that will be conducted in a simple airfoil geometry (Grabis and Agarwal, 2019). The four different mesh qualities are coarse (Figure 2.15) which will consist of around 250,000 elements, moderate (Figure 2.16) with 500,000 elements, fine (Figure 2.17) that will have 1,000,000 elements, and very fine (Figure 2.18) that will contain around 2,000,000 elements. The properties for each mesh quality are shown in Table 2.3.

Mesh Sizing				
Mesh Quality	Coarse	Moderate	Fine	Very Fine
Number of elements	250,000	500,000	1,000,000	2,000,000
Enclosure sizing (growth rate)	200 mm (1.5)	180 mm (1.5)	150 mm (1.5)	120 mm (1.4)
Body of influence sizing (growth rate)	40 mm (1.4)	22 mm (1.4)	16 mm (1.4)	13 mm (1.4)
Inflation properties (growth rate)	0.1026 mm (1.2)	0.1026 mm (1.15)	0.1026 mm (1.15)	0.1026 mm (1.1)

**Table 2.3** Number of elements and sizing properties for different mesh qualities

The properties of the sizing for the enclosure and the body of influence were set by default, according to the mean element sizing that was set for each quality (200 mm, 180 mm etc.). The main parameter that alters the BOI element size is the thickness of the inflation which is vital to the accuracy of the calculations. Inflation was set according to the feature that sets the first layer thickness, which is calculated through the  $y^+$  value and is usually set between 1 and 5 ( $1 < y^+ < 5$ ). The layers and the growth rate depends on the situation and in this case, the number of layers will be set to 15 and the growth rate is shown in Table 2.3.



In this section of the chapter, the calculation of the first layer thickness will be calculated through a series of calculations. The parameters that need to be known is, the Reynolds number which will then help in the calculation of the skin friction coefficient, shear stress and lastly, the friction velocity. Once all the above are known, the thickness of the first layer thickness will be then calculated. All the equations are taken by Frank M White's book called Fluid Mechanics, that set the first layer thickness on a flat plate (White, 1999).

- First, the Reynolds number must be known in order to proceed with the calculations:

$$Re_x = \frac{\rho * U_\infty * L}{\mu} \quad (\text{eq. 2.1})$$

Where:

- $\rho$ : fluid density ( $\text{kg/m}^3$ )
- $U_\infty$ : freestream velocity (m/s)
- L: reference length (m)
- $\mu$ : dynamic viscosity ( $\text{kg/m*s}$ )

In our case, the freestream velocity ( $U_\infty$ ) is set as the average velocity of Formula Student cars, which is approximately 54 km/h or 15 m/s. The density of the fluid ( $\rho$ ) as mentioned in chapter 1.2.2.1., is around  $1.2 \text{ kg/m}^3$ , the dynamic viscosity  $\mu$  is  $1.825 * 10^{-5} \text{ kg/m*s}$ , and the reference length (L) is the chord length of the airfoil which is 360 mm or 0.36 m. By replacing the figures in Equation 2.1, the result for the Reynolds number is 355,000.

- The second value that needs to be calculated is the skin friction coefficient ( $C_f$ ):

$$C_f = \frac{0.026}{Re_x^{1/7}} \quad (\text{eq. 2.2})$$

Using the Reynolds number found from Equation 2.1, the skin friction coefficient is calculated to be 0.00419.

- The next step is the calculation of the wall shear stress through Equation 2.3:

$$\tau_{\text{wall}} = \frac{1}{2} C_f * \rho * U_\infty^2 \quad (\text{eq. 2.3})$$

All the values are known, so the wall shear stress can be easily calculated and is found to be 0.566 Pa.

- The last figure that must be calculated is the friction velocity, which can be calculated through Equation 2.4:

$$U_{\text{friction}} = \sqrt{\frac{\tau_{\text{wall}}}{\rho}} \quad (\text{eq. 2.4})$$

Wall shear stress and fluid density are both known, so the friction velocity is 0.688 m/s.

- Now that friction velocity is known for our case, the first layer thickness,  $\Delta s$ , is calculated by the Equation 2.5:

$$\Delta s = \frac{y^+ * \mu}{U_{\text{friction}} * \rho} \quad (\text{eq. 2.5})$$

In our case, the  $y^+$  value is set to 5, due to the limited availability in computational power. Through Equation 2.5, the thickness of the first layer that will be used in the inflation of the mesh is calculated, and is equal to 0.1026 mm.

It is important to point out that, in the case of the secondary element (flap), which has a chord length of 0.144 m, the first layer thickness is calculated accordingly, and is equal to 0.0938 mm. For technical reasons, the first layer thickness will be set for both cases at 0.1026 mm, because the difference in the calculations is insignificant.

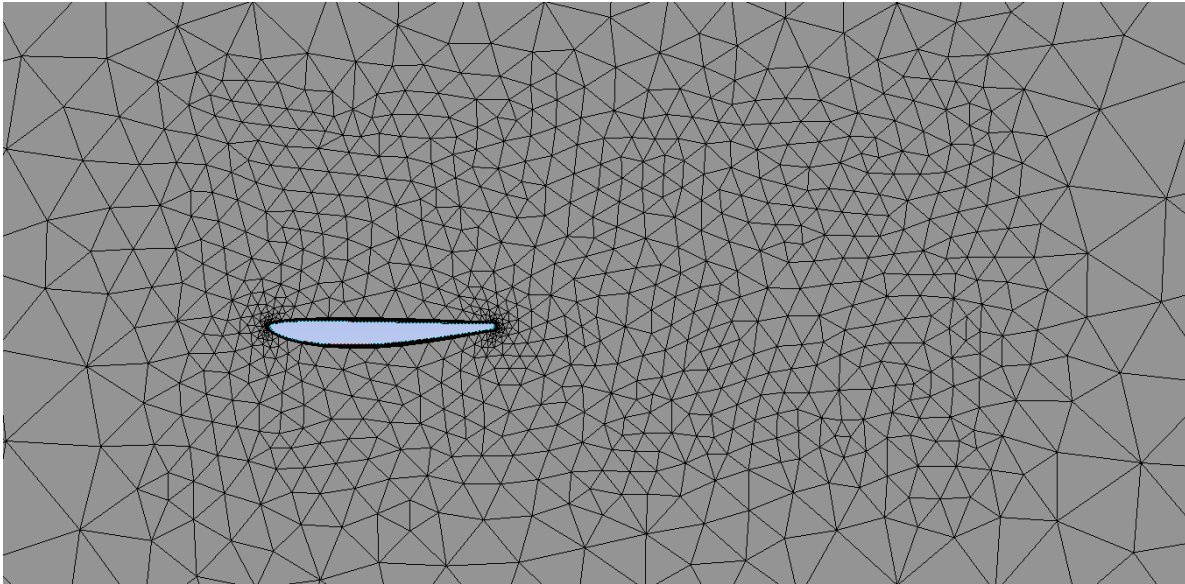


**Figure 2.15** Mesh sizing for coarse mesh quality (250,000 elements)

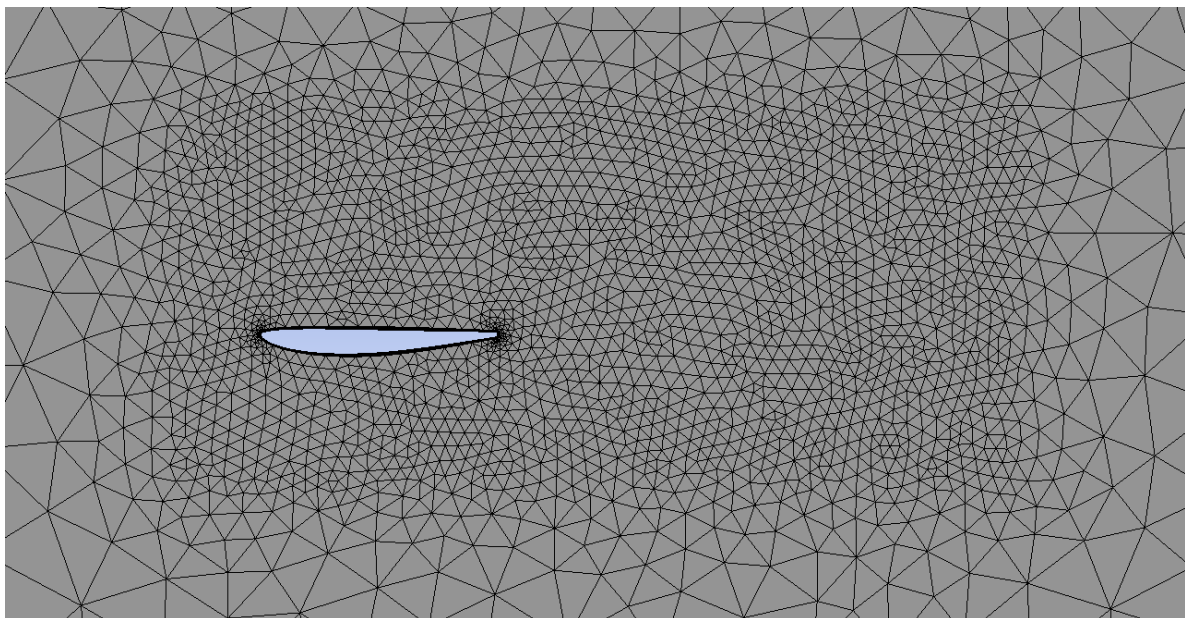


**Figure 2.16** Mesh sizing for moderate mesh quality (500,000 elements)



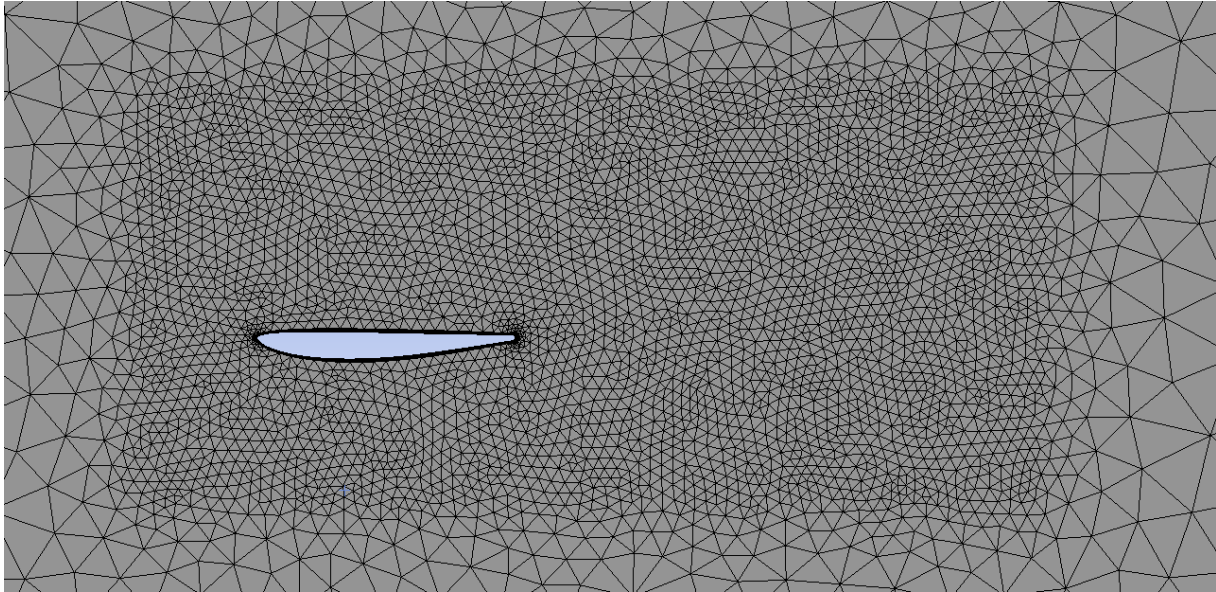


**Figure 2.17** Mesh sizing for fine mesh quality (1,000,000 elements)

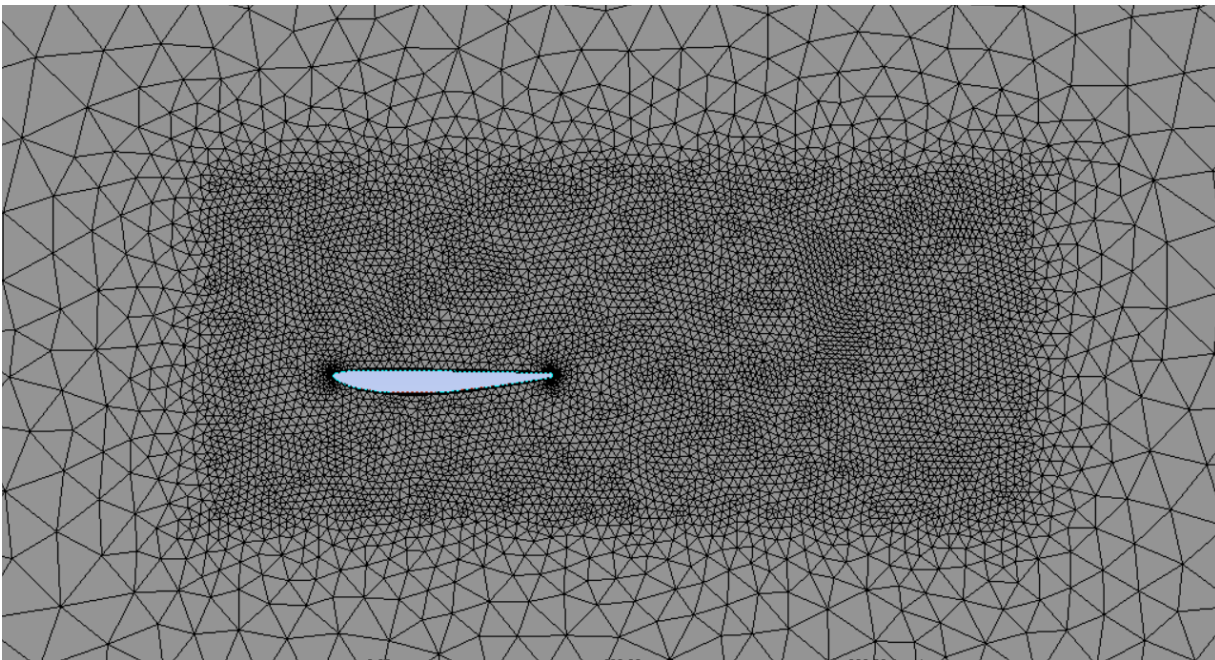


**Figure 2.18** Mesh sizing for very fine mesh quality (2,000,000 elements)

### 2.3.1.3 Mesh independence study

The mesh quality that is going to be used for all the simulations will be determined through a set of simulations as mentioned before. All the parameters between the simulations including the solving settings, the fluid domain, and the geometry will be the same in all four simulations. The purpose of this process is to decide the number of elements that is enough to calculate and represent the air flow accurately, without additional computational cost and time.

The parameters of the simulations are the following:

- Geometry: Selig 3021 airfoil (zero angle of attack and dimensions from chapter 2.2.2)
- Velocity: 15 m/s
- Enclosure: Dimensions mentioned in chapter 2.3.1.1
- Model: k-epsilon (the model that is going to be used will be decided in chapter 2.3.2.2)

The four different mesh qualities present the following results:

S3021 (0 angle of attack)				
Quality	Coarse	Moderate	Fine	Very Fine
Number of Cells	250,000	500,000	1,000,000	2,000,000
$C_L$	-0.266	-0.282	-0.284	-0.286
$C_D$	0.028	0.025	0.0245	0.024
Time (sec/iteration)	1.56	3.42	7.68	30.06

**Table 2.4** Lift and Drag coefficients results for coarse, moderate, fine, and very fine mesh qualities

In order to decide which quality is more suitable for this case, considering the available resources and time of the team and the accuracy desired, the results will be compared with reference values for the Selig 3021 airfoil that were posted from Michael S. Selig (Selig et al., 1989). The values that are compared are the lift and drag coefficients, which from reference are equal to,  $C_L = -0.285$  and  $C_D = 0.0235$ .

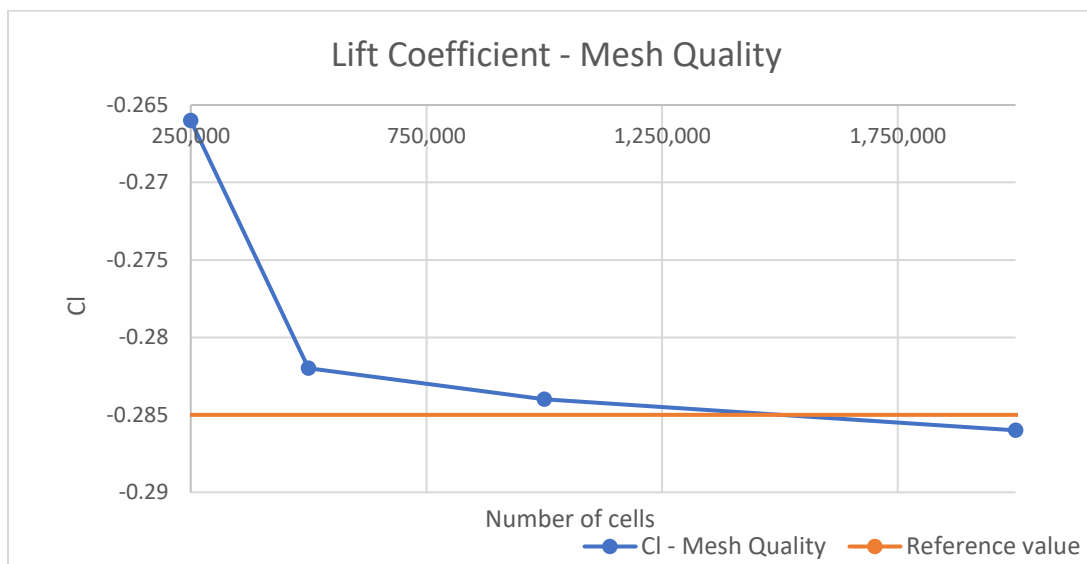


**Figure 2.19** Lift coefficient results for S3021 airfoil at different mesh qualities

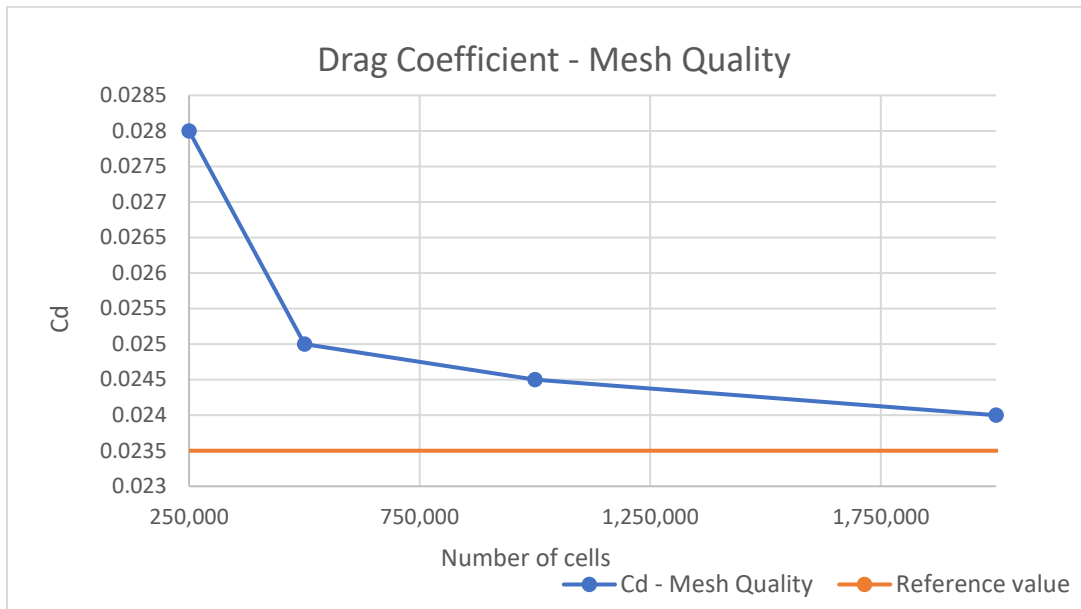


**Figure 2.20** Drag coefficient results for S3021 airfoil at different mesh qualities

By comparison, the values that are extracted from the set of simulations, moderate, fine, and very fine qualities, show slight differences. As mentioned, multiple times, the drag coefficient is of secondary importance while remaining on low levels. Keeping that in mind, Figure 2.19 represents the results from the simulations compared to the reference value of lift coefficient, the only mesh quality that presents significant inaccuracy and is not suitable for this application is the coarse one. All three that have 500,000 or more elements show acceptable results. Regarding the drag coefficient, it can be observed that all simulations have a small difference compared to the reference value, but again, the coarse one has the larger gap and is considered to be unreliable. In order to determine which of the three mesh qualities are going to be used, we will compare the times needed for each simulation run, which is shown in Figure 2.21.

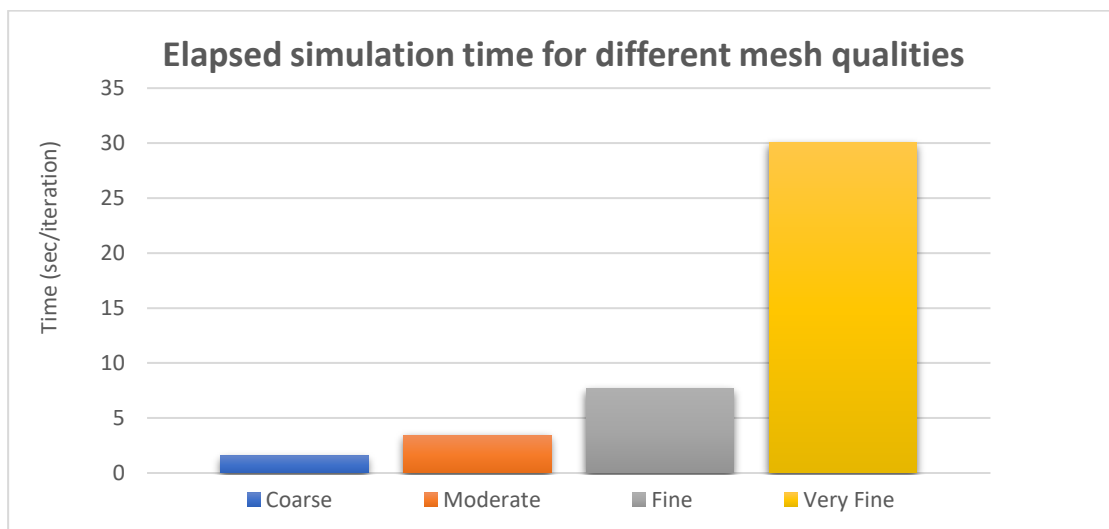


**Figure 2.21** Simulation time per iteration for all mesh qualities



Observing Figure 2.21, it is noticeable that the simulation time of the very fine mesh shows a significant increase (10 times more than the moderate mesh, and almost 5 times more than the fine mesh). The required time for an iteration of the very fine mesh is approximately 30 seconds per iteration, while for the simulation of the moderate and fine qualities, the elapsed times are 3.42 and 7.68 seconds per iteration accordingly. The first decision is to narrow the selection between the moderate and the fine quality, since with much more computational power, in just a simple geometry, the difference in accuracy is insignificant. In addition to that, the time required for the fine mesh simulation is twice the time needed for the moderate mesh one, while the results of the two simulations present very little changes as seen in Figures 2.19 and 2.20. The final decision to proceed with the moderate mesh quality is taken by considering all the above and the available time and resources of the team.

### 2.3.2. Solving

Once the pre-processing is completed, the next step of the simulation, is to set all the solving settings that will be used in all simulations, so that the results of each one are comparable. Solving, which is done through Ansys Fluent, is equally important with meshing, as they are the two most important and complex factors that can determine whether a simulation is reliable and legitimate or not. This process is divided into several subchapters, in which the settings that will be set are going to be thoroughly explained and tested for validity.

#### 2.3.2.1 Boundary conditions

Firstly, the fluid domain is consisted of walls that are known to form the enclosure. In each wall, including the geometry, which is considered to be one, a boundary condition must be set, which will decide the behaviour of the airflow (Figure 2.22).

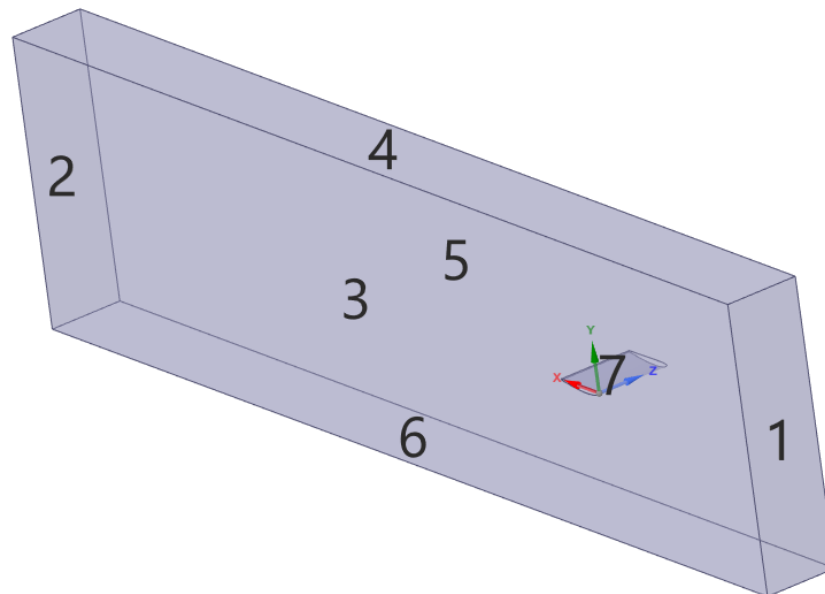


**Figure 2.22** Boundary conditions on enclosure walls



In figure 2.22, where all walls are shown, the boundary conditions set in each wall are the following:

1. Inlet: This wall is set as inlet of the airflow, where the velocity of the air has a mean value of 15 m/s on x-axis.
2. Outlet: This wall is set as outlet of the airflow, and the pressure on this wall is set to 0 Pascal and is defined as a free-draining surface which means the air will be able to leave the enclosure through this surface.
3. Symmetry wall: This wall is set to symmetry, as mentioned in chapter 2.3.1.1., so that it simulates the airflow like there is no wall there, but an extension of the whole enclosure and the airfoil geometry.
4. Top wall: This wall is also set to symmetry, in order to avoid possible disturbance to the airflow from this wall. This surface can also be set as a slip stationary wall for the same reason, and the outcome will be similar to the one with the symmetry boundary condition.
5. Side wall: This wall is similar to the top wall and the settings are exactly the same.
6. Road: In the first set of simulations (chapter 3.1), this wall is also set to symmetry, where the airfoil is on the middle of the enclosure. In the rest simulations, this wall is set to moving no-slip wall at a velocity of 15 m/s, that will represent the road that is moving relatively to the airfoil.
7. Airfoil: The airfoil is set as a no-slip stationary wall which means the velocity of the fluid is zero on the surface, where the boundary layer is formed.

The settings that were set above, are consulted from Ansys introductory notes on boundary conditions (Ansys, 2006) and previously ran simulations in Poseidon Team.

### 2.3.2.2 Model selection

The next step is the selection of the solving RANS model that will be used for the simulations. In order to do so, another set of simulations will be conducted, where the exact same geometry as in chapter 2.3.1.3 will be tested. The three solving models for this set of simulations are k-epsilon, k-omega standard, and k-omega SST, that were mentioned in chapter 1.5.6.

The results from the set of simulations are shown in Table 2.5:

S3021 a0				
Solving Model	k-epsilon	k-omega	k-omega SST	Reference
$C_L$	-0.282	-0.302	-0.287	-0.285
$C_D$	0.025	0.017	0.024	0.0235
Sim. Time (sec)	275.15	281.65	301.24	-

**Table 2.5** Lift and Drag coefficients results for k-epsilon, k-omega standard, and k-omega SST solving models

Comparing the results from Table 2.5, it is easily noticed that the k-epsilon is superior against the other two solving models, both in terms of accuracy of the results and required time for the simulation run. The k-omega model that is suitable for near wall flows, presented the most inaccurate results, which is something worth studying in future projects like this one. The k-omega SST can calculate the flow both



near and away from the wall, but in our case its results are not as accurate as the k-epsilon model, which is governing in CFD simulations in motorsport and especially Formula Student. Total simulation times do not show significant changes as seen in Figure 2.23, but it must be noted that when the geometry of the simulations is more complex, like these in the following chapters, this difference in simulation time may be further increased. Considering the above, the most suitable solving model for this specific case is the k-epsilon due to the fact that it presents the best and most accurate results in less simulation time, compared to the other two.

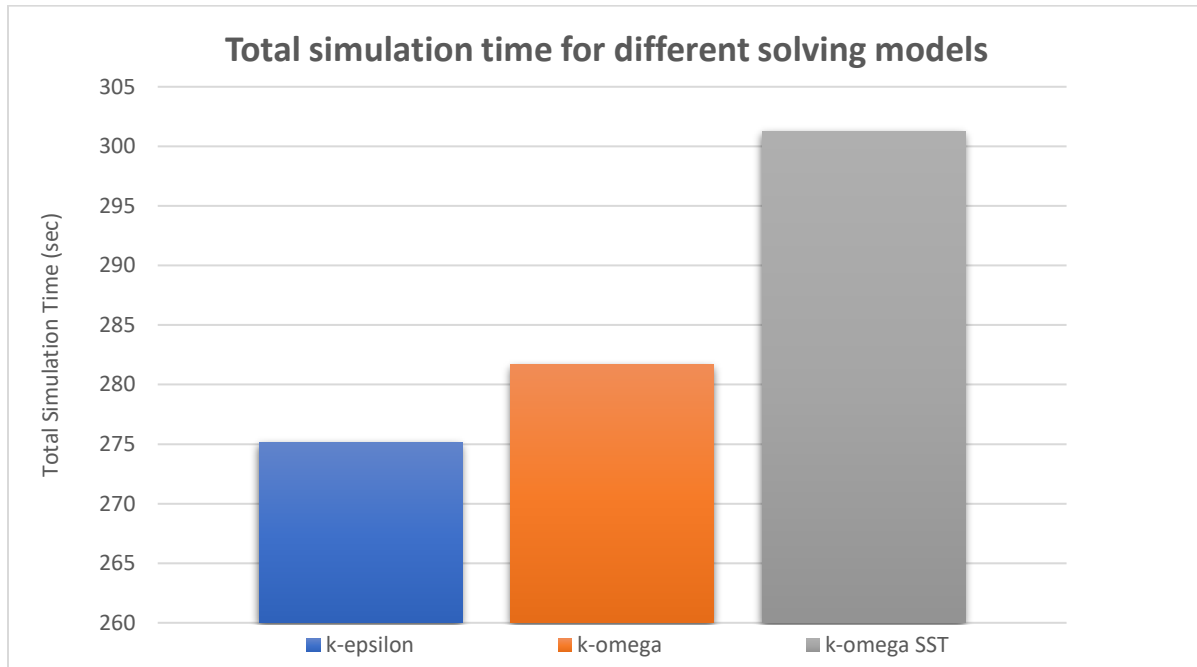


**Figure 2.23** Total simulation time for k-epsilon, k-omega, and k-omega SST models

### 2.3.2.3 Type of flow

It is commonly known that steady flows are almost impossible to exist in real world, as the behaviour and its properties change over time. For simplicity, there are cases that a fluid flow can be considered to be steady even if it is transient, but this must be proven for reliability and validity reasons. In this thesis, a set of simulations will be conducted for the selection of the type of flow, between steady state and transient flow.

The settings that are going to be used for this set of simulations are the one mentioned and decided from the previous subchapters. To sum them up, the boundary conditions are the same, the solving model is k-epsilon, the mesh quality is moderate, and the geometry is the S3021 in 3 degrees and 6 degrees angle of attack. This set of simulation will be consisted of 4 simulations for better validation of the type that will be selected.



S3021 (3° angle of attack)		
Type of flow	Steady	Transient
$C_L$	-0.903	-0.902
$C_D$	0.038	0.038
Sim. Time (sec)	2.6	12.65

**Table 2.6** Results of the steady and transient flow types in Selig 3021 at 3 degrees angle of attack

S3021 (6° angle of attack)		
Type of flow	Steady	Transient
$C_L$	-0.601	-0.601
$C_D$	0.03	0.03
Sim. Time (sec/iteration)	2.5	12.12

**Table 2.7** Results of the steady and transient flow types in Selig 3021 at 6 degrees angle of attack

With a simple observation on Tables 2.6 and 2.7, the results for the steady and the transient flow simulations are almost identical, which leads to the conclusion that either the first one or the second one, can be used for the simulations that are going to be conducted in the context of this thesis. In order to decide which, one is more efficient, the required time for each iteration is noted in the last row of Tables 2.6 and 2.7 and presented in Figure 2.24.

The conclusion of this process is that conducting the simulations with either steady or transient flow setting, the results are approximately the same. The major drawback of the transient flow simulation, which is visible in Figure 2.24, is the required time for its run, that is almost 6 times larger than the steady flow simulation, both in 3- and 6-degrees angle of attack. According to the above, the final decision is to proceed with the assumption that the flow is considered to be steady instead of transient, aiming to reduce simulation time and computational cost.

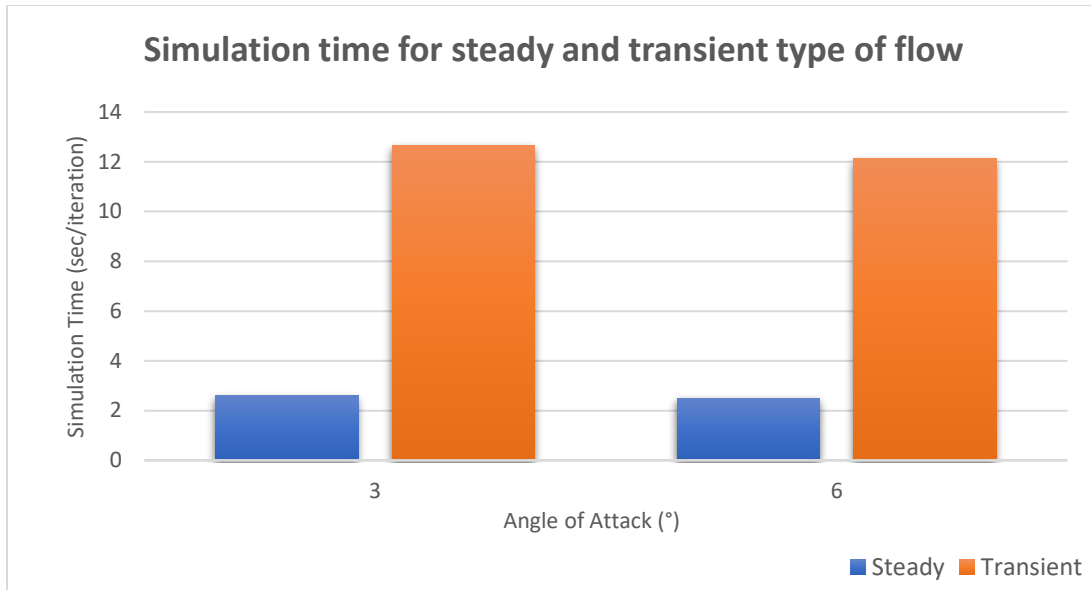


**Figure 2.24** Simulation time per iteration for steady and transient flow

#### 2.3.2.4 Reference values and simulation run settings

The last solving settings that have to be set prior to run of the simulation in Ansys fluent are the reference values, in which the results that will be presented are based on. The main reference values that are set, contain figures, like the properties and the size of the geometry, the air properties, and the velocity of the flow. To be more specific, the reference values that are set are the following and are shown in Figure 2.25.

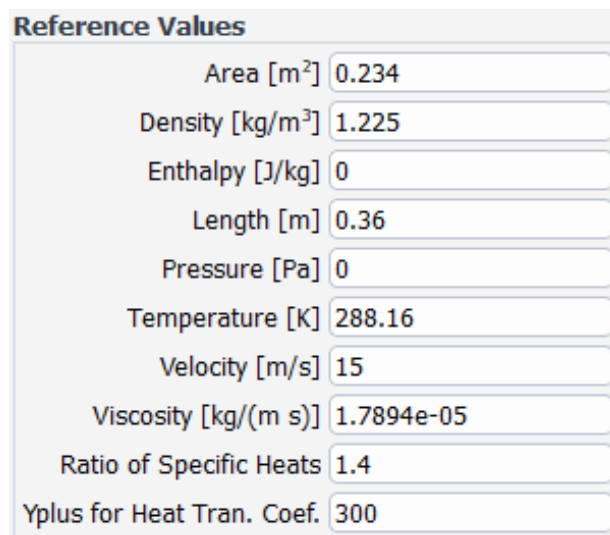


**Figure 2.25** Reference values set on solver of the simulations

- The most important reference value that needs to be set prior to solving, is the area which is the projected area that all the calculations use in their equations as reference. The frontal or projected area of the geometry is the projection of the geometry on the vertical plane to the flow direction (Sathyabama, 2022). On most occasions this area is used for the calculations, but



when geometries on angles of attack near zero, the reference area is the projection of the geometry on the plane that is parallel to the airflow. For better understanding, in Figure 2.26, the reference area of a vehicle is presented, while in Figure 2.27, the reference area of Selig 1223 airfoil is also shown.

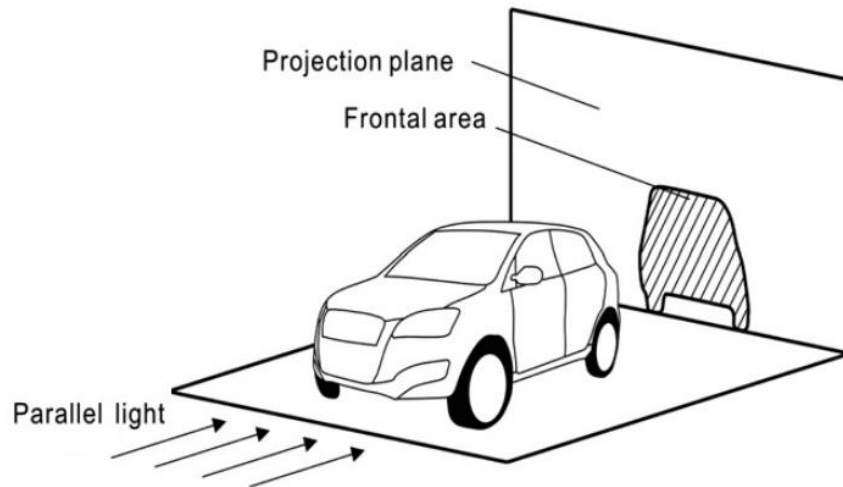


**Figure 2.26** Frontal area of a commercial vehicle (Wu and Liu, 2011)

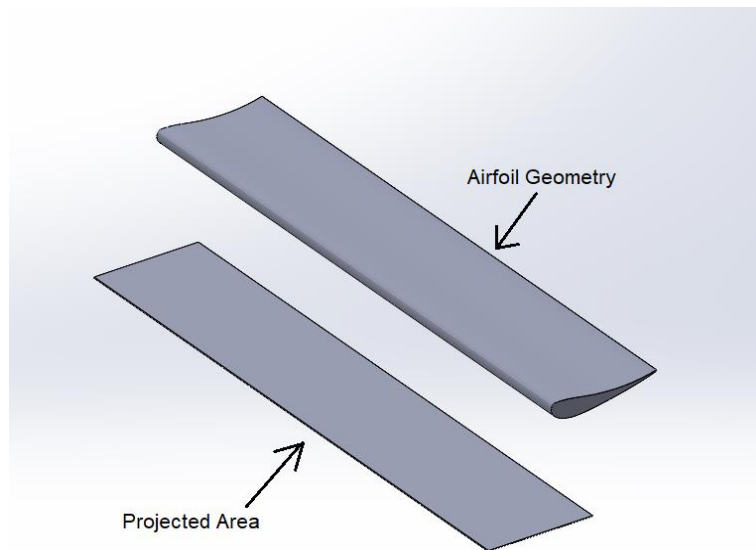


**Figure 2.27** Projected area of Selig 1223 airfoil

The explanation behind the projected area of the airfoil is because the airflow mostly interacts with the geometry on top and below the wing, while its frontal area is significantly smaller, and the physical phenomena are of secondary importance. By taking the above into account, the projected area of the S1223 is  $0.468 \text{ m}^2$ , once the chord length is 360 mm, and the span is 1300 mm. It needs caution when



setting the reference values, because it is agreed in chapter 2.3.1.1, that only half of the geometry is going to be studied, using the symmetry feature that is commonly used in CFD for reduction in computational cost. The reference area that is set only for the S1223 airfoil at zero angle of attack is  $0.234\text{m}^2$ . Another factor that must be considered when measuring the projects area is the angle of attack of the airfoil, which affects the projection of the chord length.

- Properties of the environment are set by default as they are commonly known when on around  $15^\circ\text{C}$ , and at sea level. The density of air is set to  $1.225\text{ kg/m}^3$ , the temperature is set to  $288.15\text{ K}$ , the dynamic viscosity of the air is approximately  $1.8\text{e-}05\text{ kg/m s}$ , the ratio of specific heats is  $1.4$ , the Yplus for heat transfer coefficient is also by default at  $300$ , while the enthalpy and pressure is set to zero as they do not affect the calculations of the simulation significantly.
- The value for the length is set as the chord length at zero angle of attack, alternatively it is set as the projection of the chord length on the x-axis.
- The velocity is set to  $15\text{ m/s}$  which is mentioned multiple times in previous subchapters.

The last step before the run of the simulation, is to set the number of iterations that will be conducted, and the values that will be calculated and plotted after the completion of the run. The number of iterations is set to  $600$ , as it was visible from the first simulations that the residuals of the k-epsilon model as well as the continuity, converged after around  $100$  iterations (Figure 2.28). The convergence of the residuals depends on reduction of the class size which is set by the user, and its reduction is related to the desired accuracy of the simulation (reduction by 3 class sizes is selected in this case) (Kuron, 2015). Considering this fact, a number of  $600$  iterations is determined, as more complex geometries require more iterations for the stabilization of the convergence of the residuals. The output values that we are interested in are the lift and drag forces and coefficients, which must be set in the right axis, in order to present valid results.

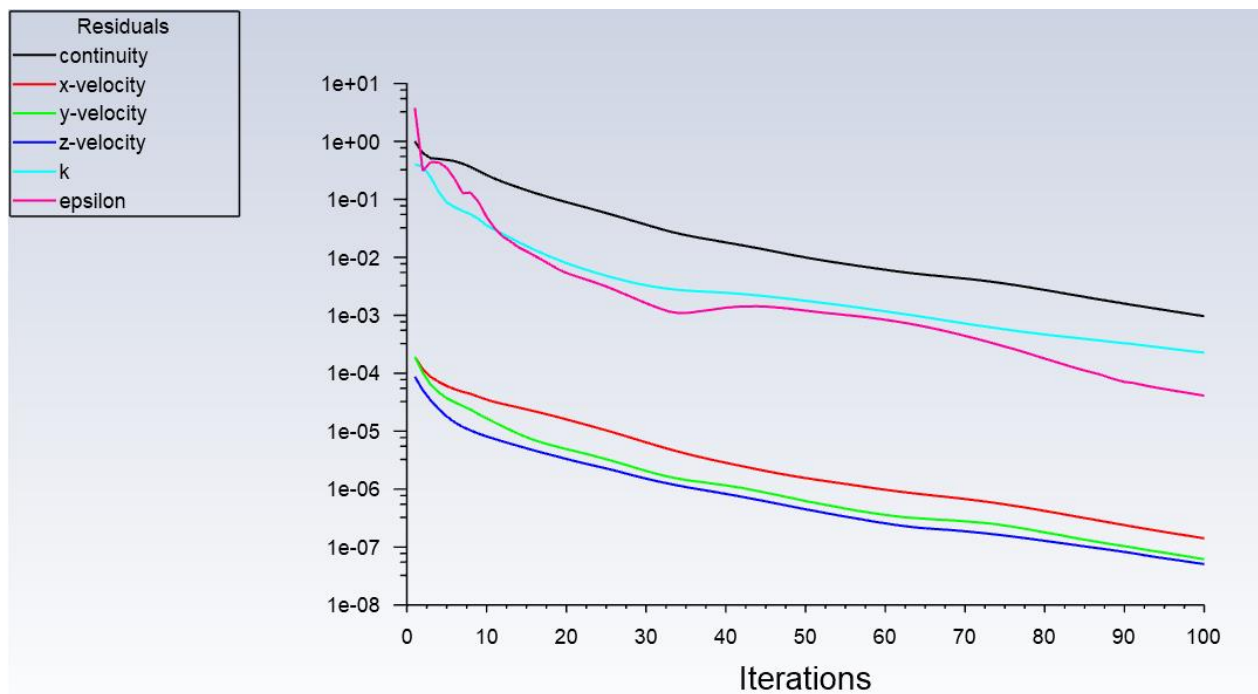


**Figure 2.28** Convergence of residuals of the S1223 ( $0^\circ$  AOA) simulation run

### 2.3.3. Post-processing

The last aspect of the CFD simulations is post-processing, which all results are being examined through contours, streamlines, graphs, and other visualization forms. Post-processing in this thesis will be done through Ansys Post for the contours and results of the simulation, and Ansa Meta, in which the turbulence and the streamline around each geometry is going to be visualized. The contours that will help in the selection of the most suitable geometry for each set of simulations, are the velocity and pressure contours projected on the symmetry wall, while the streamlines that will be presented only on the selected geometries in each set, will better represent the airflow around the airfoils, for better understanding of the phenomena that take place around them, such as separation. Examples of contours and streamlines are shown in Figures 2.29 and 2.30.

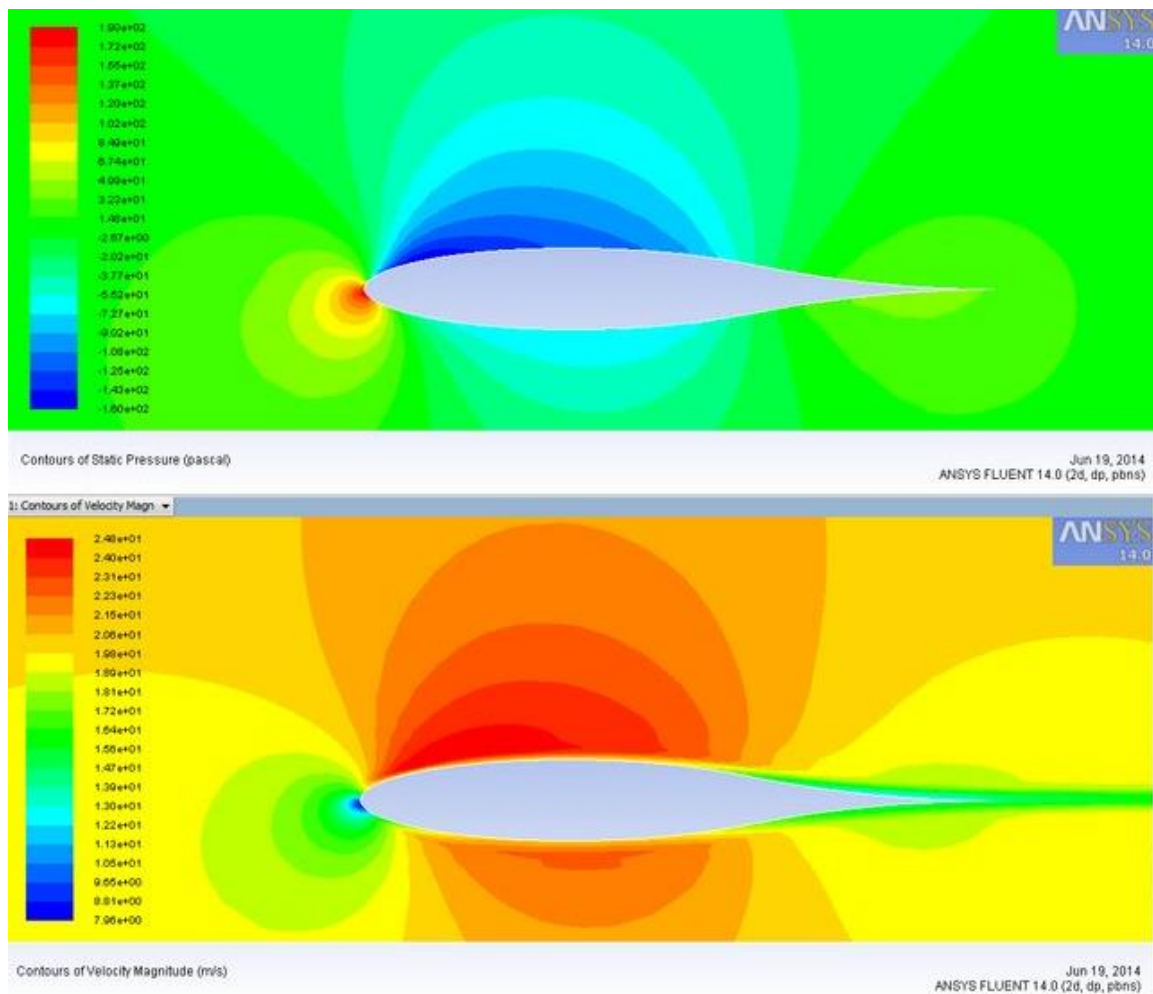


**Figure 2.29** Static pressure and velocity magnitude of a NACA 0012 airfoil geometry (Ganesh Ram et al., 2014)

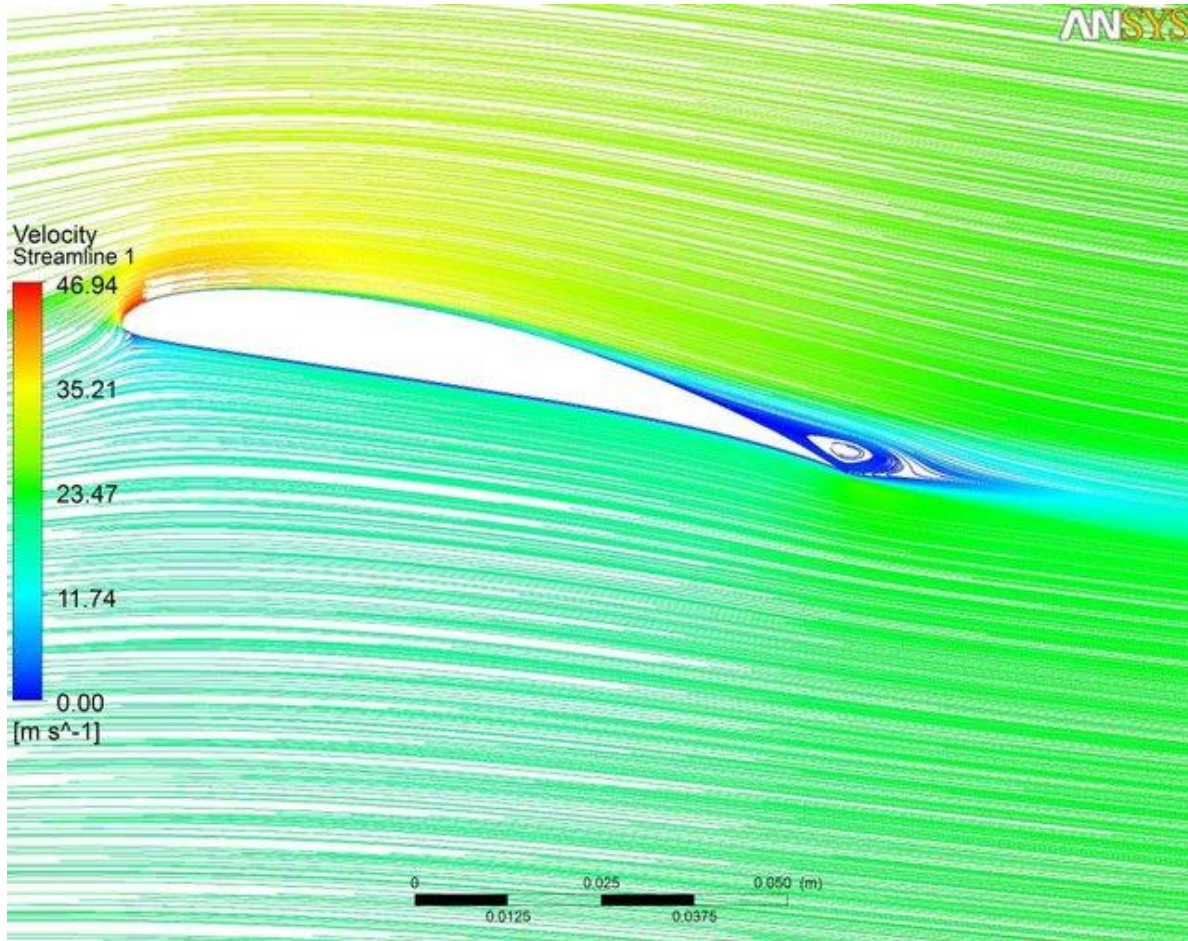


Figure 2.30 Streamline around an airfoil geometry (Ahmed et al., 2011)

## 2.4. Finite Element Analysis (FEA)

In the last chapter of the methodology, a static simulation will be conducted in Solidworks CAE add-in called Solidworks Simulation. The scope of this simulation, is to prove that the final geometry that will be used, is able to withstand the necessary forces that are set by the regulations of the Formula Student regulations. The material and thickness of each element will be decided by the result of this simulation. The regulation that needs to be followed strictly is the following:

- Any aerodynamic device must be able to withstand a force of 200 N distributed over a minimum surface of 225 cm<sup>2</sup> and not deflect more than 10 mm in the load carrying direction.

The two parameters that can be adjusted without losing efficiency (reducing the span of the wing), are the material that will be used, and the thickness of the construction. Carbon fiber is the most commonly used material in Formula Student and motorsport in general, due to its high stiffness, and low weight. In other applications such as aviation, more secure materials are used for safety such as aluminum.

The assumption for this simulation is that the mechanical properties are these of an averaged carbon fiber, reinforced with epoxy (Matweb, 2023). The thickness used for the main element is around 5 mm, while the flap's thickness is approximately 2 mm. The properties of the custom material made in Solidworks are the following:

- Elastic modulus:  $1.28 \times 10^{11} \text{ N/m}^2$
- Poisson's ratio: 0.27
- Shear modulus:  $1.24 \times 10^8 \text{ N/m}^2$
- Mass density:  $1780 \text{ kg/m}^3$
- Tensile strength:  $22.63 \times 10^8 \text{ N/m}^2$
- Thermal conductivity:  $0.2256 \text{ W/(m} \cdot \text{K)}$
- Specific heat:  $1386 \text{ J/(kg} \cdot \text{K)}$

After this step, the necessary forces are applied on the surfaces of the elements, while the mounting of the design will be set as a fixed geometry (Figure 2.31), as this simulation is to check the deflection of the wings and not the tolerance of their mounting. In the figure below, the green arrows represent the fixed surfaces and edges (mounting of the front wing assembly), while the purple arrows represent the position and the direction in which the force is applied. The value of the force that is going to be applied to the geometry will be resulted from the dimensions of the final design.

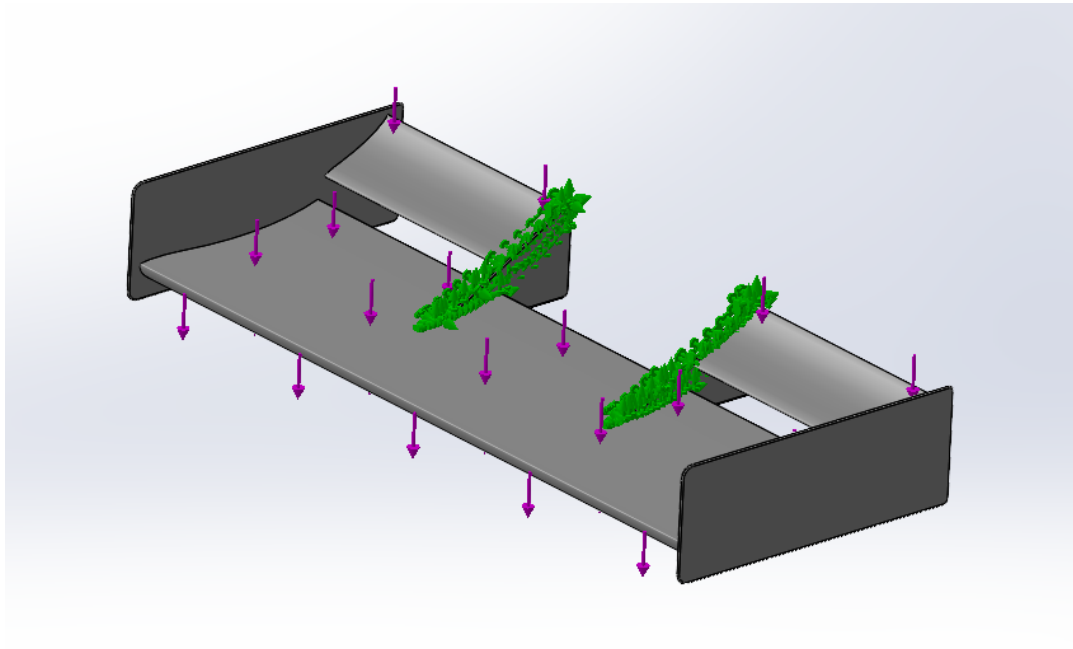


**Figure 2.31** Forces and fixed geometries on the front wing assembly

In static simulations, fluid domains, boundary layers and other features that are included in CFD simulations, do not exist, which makes mesh forming much simpler. Meshing in Solidworks Simulation, has some default options, which will be used in this study, including the shape of the mesh elements, which are triangular for surface meshing and tetrahedral for volume meshing. The mesh quality is set to the maximum possible, in Solidworks and the element sizing is set as the following:

- Maximum element size: 14.814 mm
- Minimum element size: 0.741 mm
- Element size growth ratio: 1.2

After the formation of the solid mesh, the total number of elements is 765040, while the total number of nodes is 1311180. The settings are set aiming for high mesh by neglecting the computational cost, since it is a single static simulation, and its solving is much simpler than CFD. To be more specific, for a two-element front wing assembly with the dimensions mentioned in chapter 2.2.2., the generation of the solid mesh required approximately 2 minutes, which is significantly less than the time required for the CFD mesh generation and simulation run.

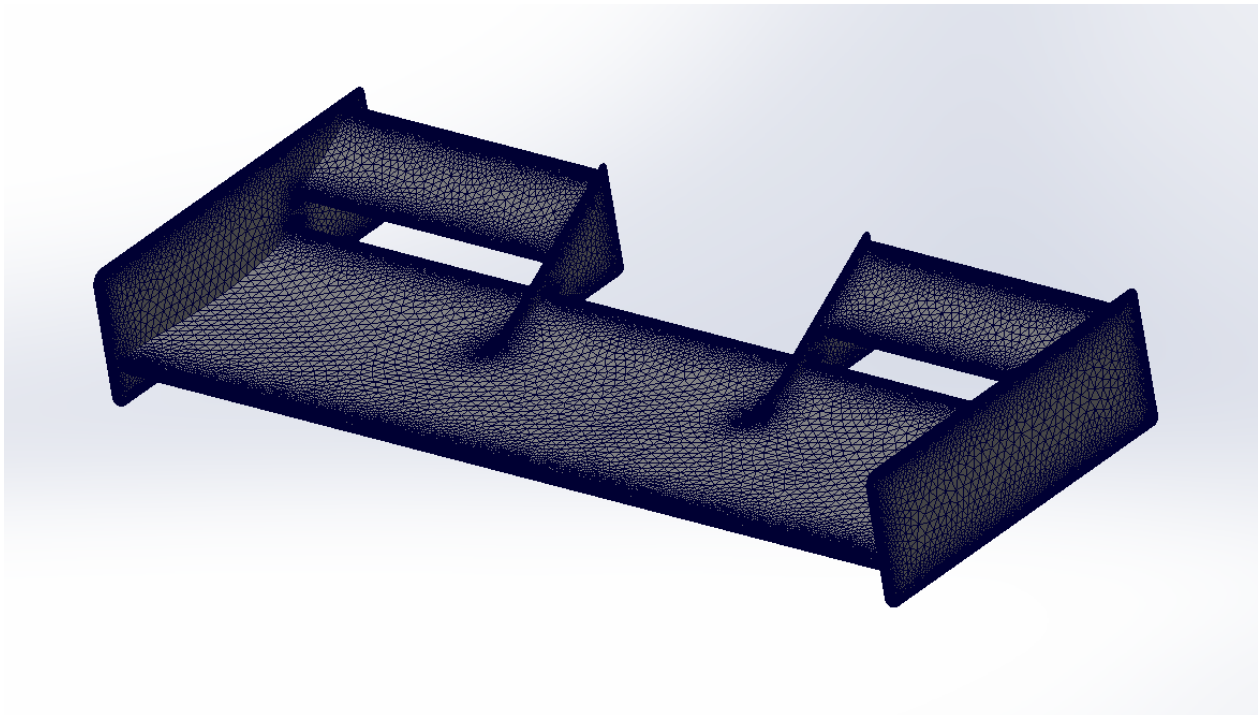


**Figure 2.32** Solid mesh a front wing configuration using Solidworks Simulation

Once the mesh generation is completed, the last step is to run the static simulation which as mentioned before requires significant less time than CFD simulations. The results that we are interested in this thesis is the deformation of the airfoil wings, that must be within 10 mm after the application of the force. It is important to consider construction and design inaccuracies that exist; thus, the safety factor is set to around 1.5. This means the maximum acceptable amount of deformation is around 6.5 mm. Once the design is decided through the CFD and FEA simulations, a final redesign and optimization for weight reduction will be conducted for efficiency.

### 3. Simulation runs and results

In the following chapter of the thesis, the configurations and designs that are studied in each set of simulation will be described in detail. In every set of simulations, the most suitable profile and configuration will be determined through various factors. The main goal that was set from the beginning, is to achieve the generation of the maximum possible negative lift; thus, the most important factor in deciding the most appropriate design, is the lift coefficient ( $C_L$ ). Although drag forces are usually insignificant compared to the lift forces and their contribution to the selection of the design is small, the Lift/Drag ratio is another vital derivative that must be considered. Lastly, the pressure and velocity contours are going to be studied and analyzed in order to assess the flow behavior around each geometry for potential wake generation or flow separations that might occur.

#### 3.1. Main Element (Airfoil Profile Selection)

In the first set of simulations the profile of airfoil that is going to be used as the main element of the front wing configuration will be selected. As mentioned in Chapter 2.2.2, four different high-lift airfoils (Selig 1223, Selig 1210, Selig 3021, Eppler 423) will be tested in 5 different angles of attack ( $-3^\circ$ ,  $0^\circ$ ,  $3^\circ$ ,  $6^\circ$ ,  $9^\circ$ ), and through the previously discussed factors, the most efficient one will be used to proceed to the rest sets of simulations. The airfoils in the first set of simulations will be placed in the middle of the enclosure as the ground effect that appears near the road, has insignificant differences through different wing profiles. In Figure 3.1, example of the first set design configuration is presented:

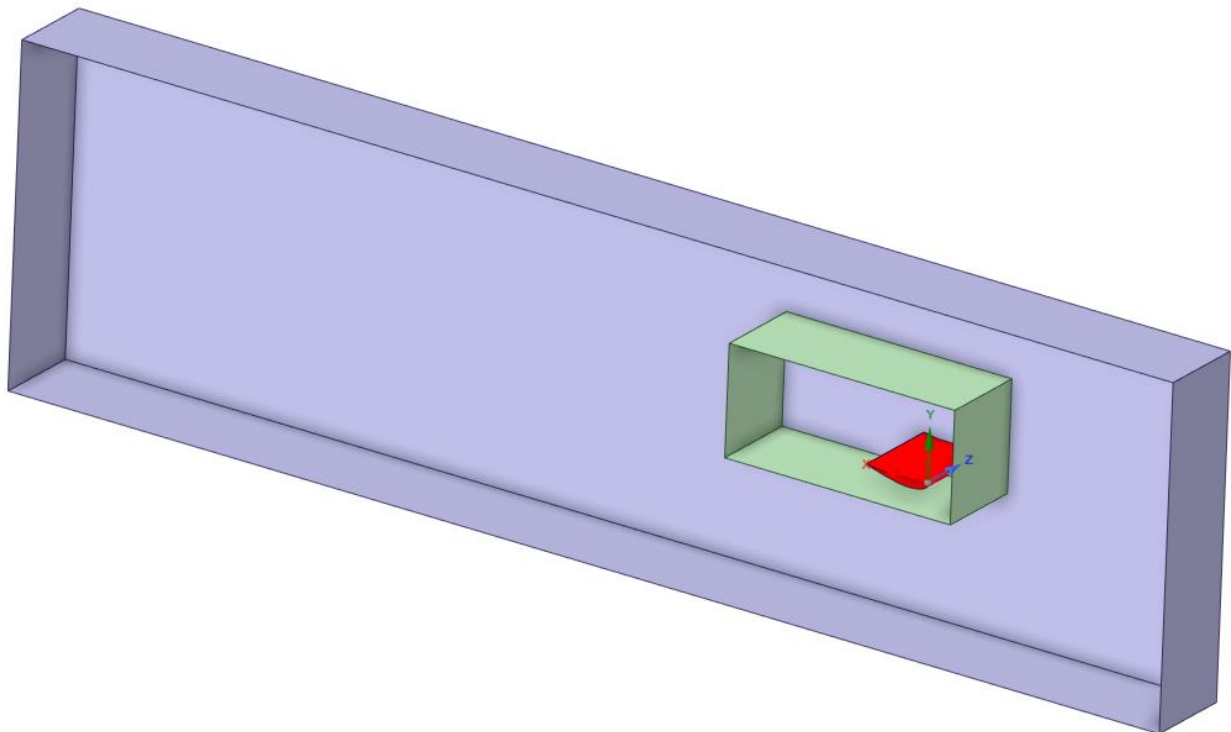


**Figure 3.1** Selig 1210 in  $3^\circ$  AOA placed in the simulation's enclosure

The results of the first set of simulations are the following, since all the settings for the simulations, both for pre-processing and solving, are mentioned in Chapter 2.2:

Selig 3021					
AOA (°)	-3	0	3	6	9
$C_L$	0.153	-0.282	-0.601	-0.903	-1.15
$C_D$	0.03	0.026	0.03	0.038	0.053
$C_L/C_D$	5.10	-10.85	-20.03	-23.76	-21.70

**Table 3.1** Results of the first set of simulations for the Selig 3021 airfoil

Selig 1223					
AOA (°)	-3	0	3	6	9
$C_L$	-0.466	-0.798	-1.1	-1.359	-1.577
$C_D$	0.037	0.036	0.042	0.054	0.072
$C_L/C_D$	-12.59	-22.17	-26.19	-25.17	-21.90

**Table 3.2** Results of the first set of simulations for the Selig 1223 airfoil

Selig 1210					
AOA (°)	-3	0	3	6	9
$C_L$	-0.31	-0.636	-0.941	-1.227	-1.436
$C_D$	0.032	0.032	0.037	0.047	0.064
$C_L/C_D$	-9.69	-19.88	-25.43	-26.11	-22.44

**Table 3.3** Results of the first set of simulations for the Selig 1210 airfoil



Eppler 423					
AOA (°)	-3	0	3	6	9
$C_L$	-0.51	-0.811	-1.081	-1.355	-1.535
$C_D$	0.042	0.041	0.047	0.057	0.073
$C_L/C_D$	-12.14	-19.78	-23.00	-23.77	-21.03

**Table 3.4** Results of the first set of simulations for the Eppler 423 airfoil

In Tables 3.1, 3.2, 3.3 and 3.4, the results for all 20 different designs (4 different airfoils and 5 different angles of attack) are presented, where it is visible that the only airfoil with significantly less values in lift coefficient is the Selig 3021. Once the first observation is made, all results will be assessed through graphs that will help in the better demonstration of the outcome. In Figures 3.2 and 3.3, the lift and drag coefficients for each airfoil and angle of attack are shown:

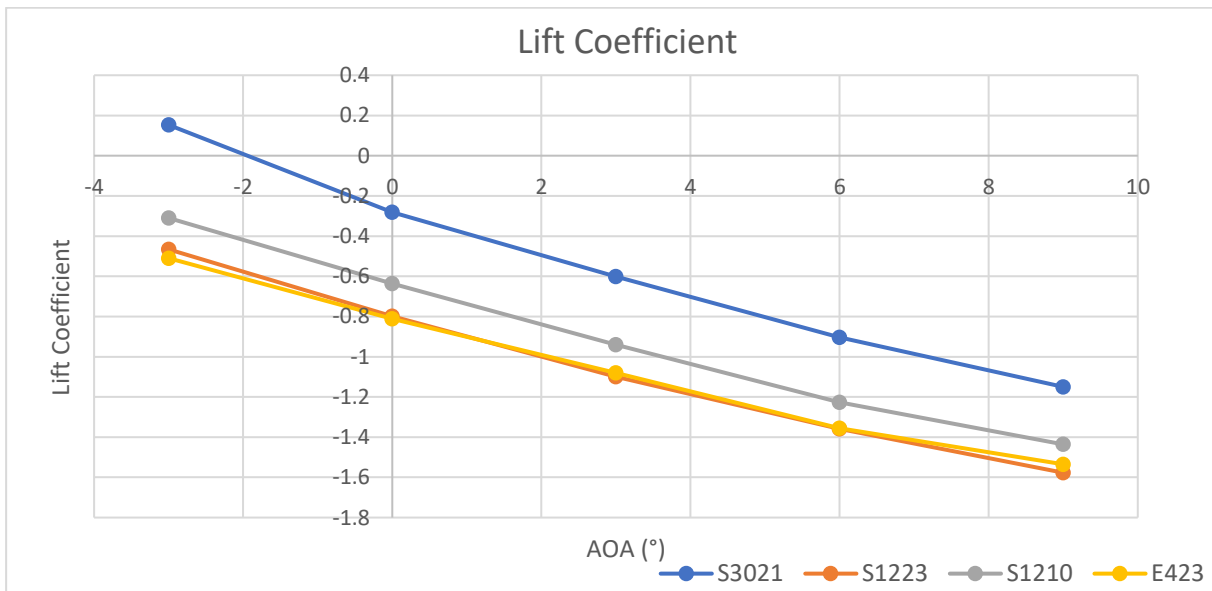


**Figure 3.2** Lift coefficient in all AOA from the first set of simulations

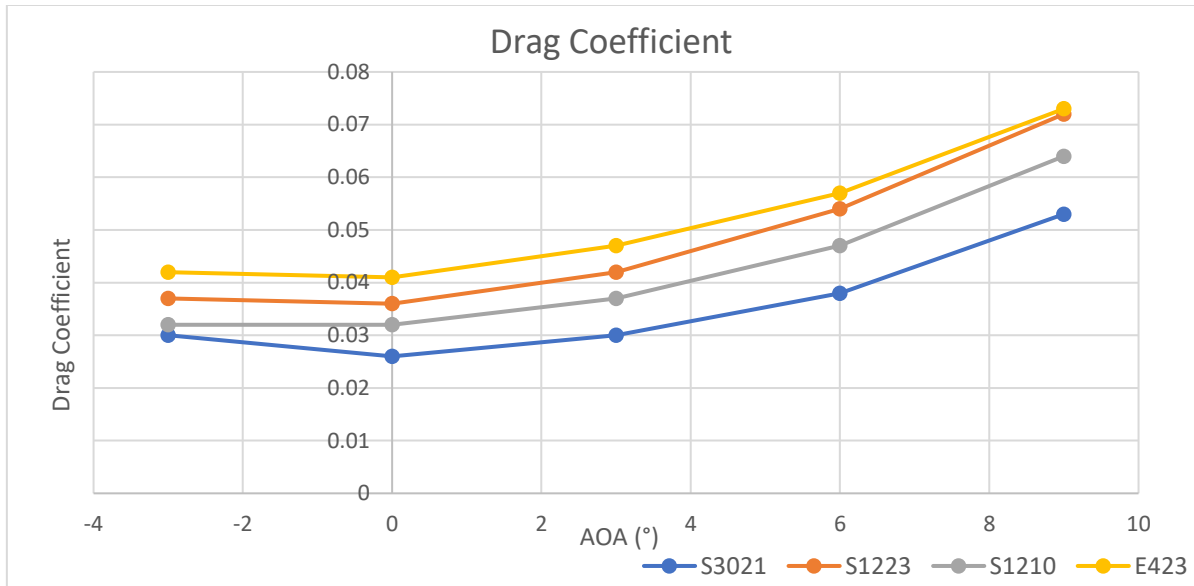


**Figure 3.3** Drag coefficient in all AOA from the first set of simulations

By observing the figures above, there are several conclusions that can be made; firstly, while the Selig 3021 airfoil has significantly less negative lift compared to the rest profiles, the amount of drag that it produces remains at very low levels. Despite the fact that S3021 has low drag, the main factor that is being considered in the selection of the profile is lift, leading to the rejection of this profile. Selig 1223 and Eppler 423 produce almost identical amounts of negative lift, with the second one generating slightly more drag than the first one. The Selig 1210 airfoil produces less downforce and drag since its lift and drag coefficients are smaller than those of S1223 and E423, in all angles of attack. Since the graphs are not enough to reach a final decision on the profile that is more suitable for the front wing, in Figure 3.4, the lift/drag ratio in all angles of attack is imprinted. Another remark that occurs is that although negative lift increases almost linear, drag increases rapidly as the airfoil's angle of attack get higher.

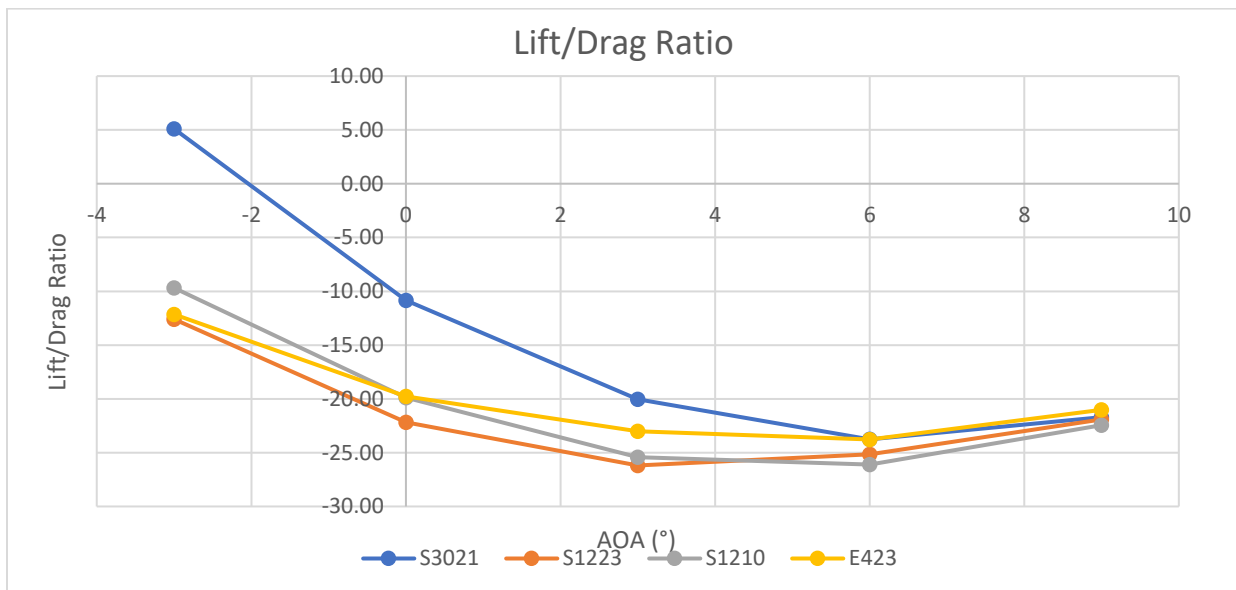


**Figure 3.4** Lift/Drag ratio in all AOA from the first set of simulations

From the figure above, it is clear that Selig 1223 and Selig 1210 are superior from the Eppler 423, since their lift/drag ratio is noticeably larger. Considering the importance of the factors that were set from before, S1223 and S1210 are the two possible airfoil profiles that will be used for the front wing assembly. Furthermore, it must be noted that the lift/drag ratio of S1223 peaks at 3 degrees angle of attack, while S1210's maximum lift/drag ratio is at 6 degrees angle of attack. There are two reasons why the first one is a better option than the later one; 1. when an airfoil is set at higher Angles of attack, it produces more drag, which might be caused from flow separation and possible wake generation behind it, and 2. there is no point in choosing the S1210 profile which must be set in higher angle than the S1223 to equal its performance, since the height of the main element will be increased which is not efficient for the design of the front wing.

To ensure that the selection of S1223 profiles is the most suitable for the front wing assembly, the velocity and pressure contours at the most efficient angles of attack (3 and 6 degrees) of the four wing profiles will be presented below, while the rest contour will be shown in Appendix A.

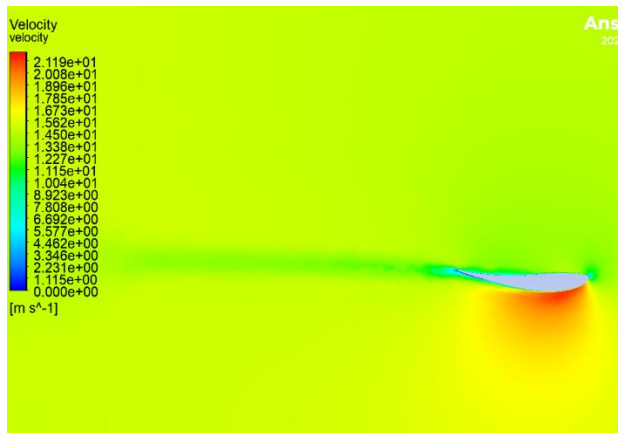


Figure 3.5 Velocity contour of S1210 at 3° AOA

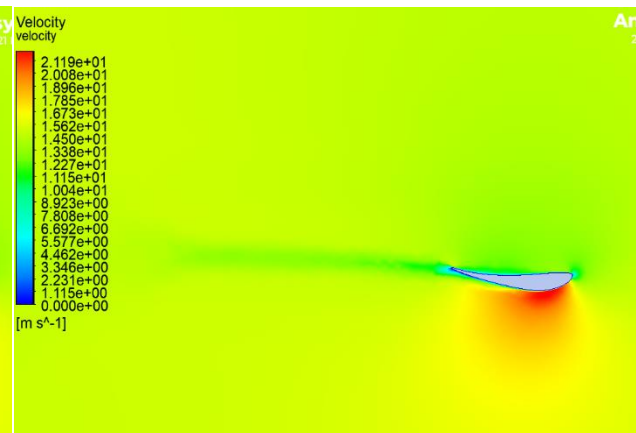


Figure 3.6 Velocity contour of S1223 at 3° AOA

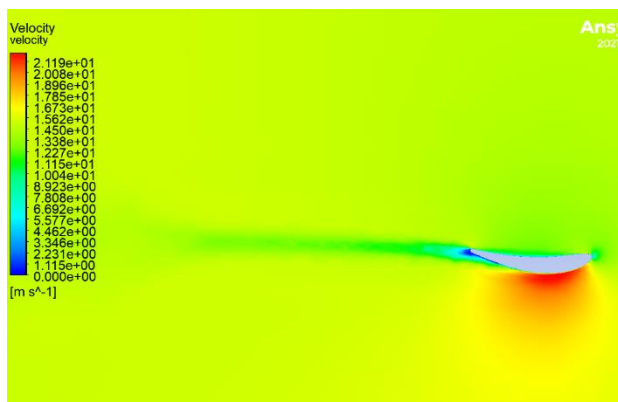


Figure 3.7 Velocity contour of E423 at 3° AOA

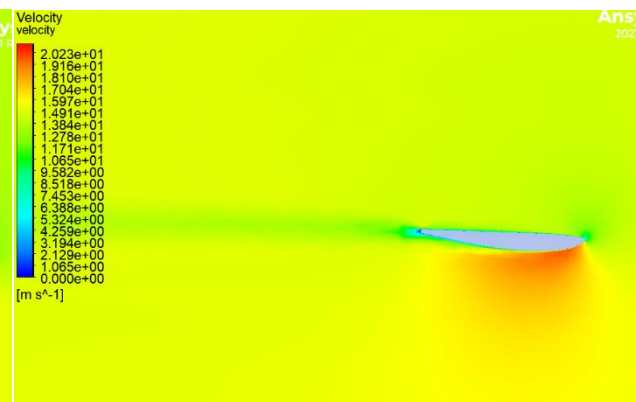


Figure 3.8 Velocity contour of S3021 at 3° AOA

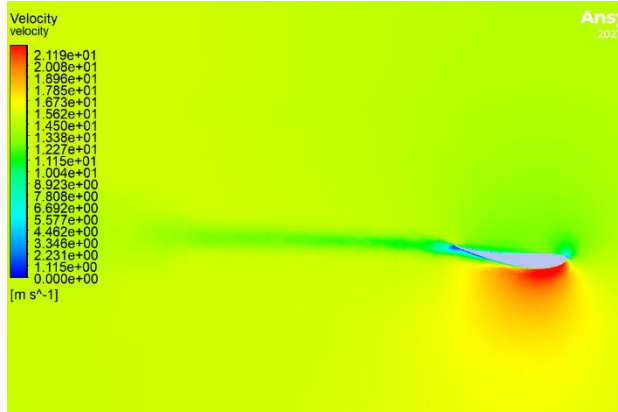


Figure 3.9 Velocity contour of S1210 at 6° AOA

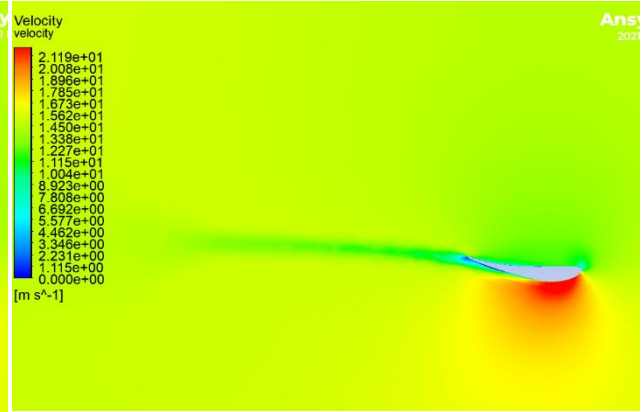


Figure 3.10 Velocity contour of S1223 at 6° AOA

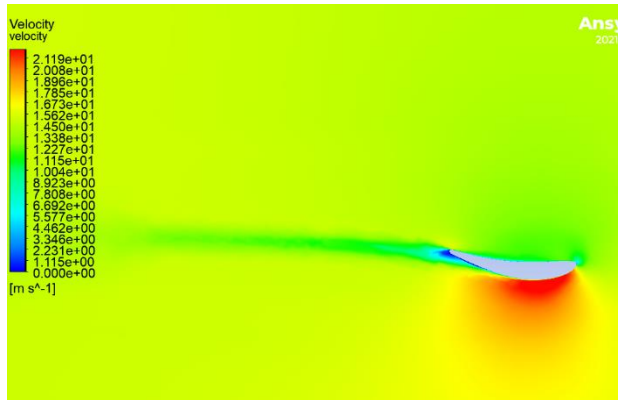


Figure 3.11 Velocity contour of E423 at 6° AOA

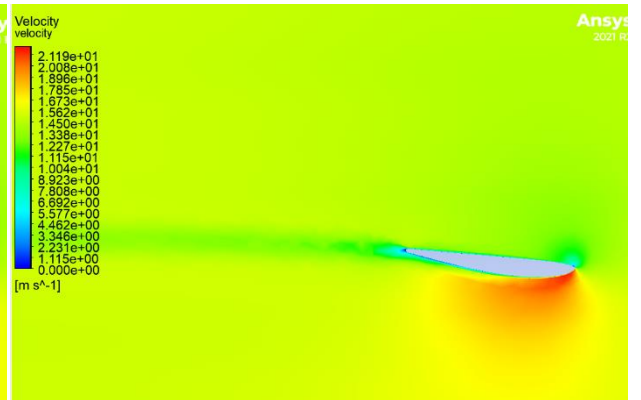


Figure 3.12 Velocity contour of S3021 at 6° AOA

The figures above validate the conclusions that were made previously, as it is visible that the Selig 3021 generates almost no wake behind it. Eppler 423 has significantly larger wake behind it and flow separation on its bottom side compared to the other three, which is the main reason why it was rejected from the results that were presented before. The two most important contours that must be observed and discussed is the velocity contour of the S1223 at 3° AOA (Figure 3.6), and velocity contour of S1210 at 6° AOA (Figure 3.9). Although the two designs produce almost the same amount of lift/drag ratio, the first one has  $C_L = -1.1$  while the second one has  $C_L = -0.941$ , which leads us to the conclusion that the first one is considered superior regarding the lift factor. Also, the wake behind the S1210 at 6° AOA is larger than that of S1223 at 3° AOA, which means more drag is produced. This observation is also seen in Tables 3.2 and 3.3, where the S1210 has  $C_D = 0.047$  and the S1223 has  $C_D = 0.042$ , and although the difference is small, the final decision can be easily made taking all comments into account, that Selig 1223 is more efficient than the Selig 1210 for this application.

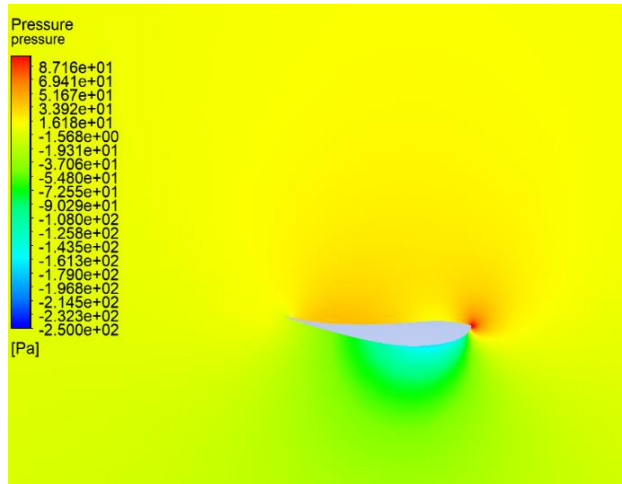


Figure 3.13 Pressure contour of S1210 at 3° AOA

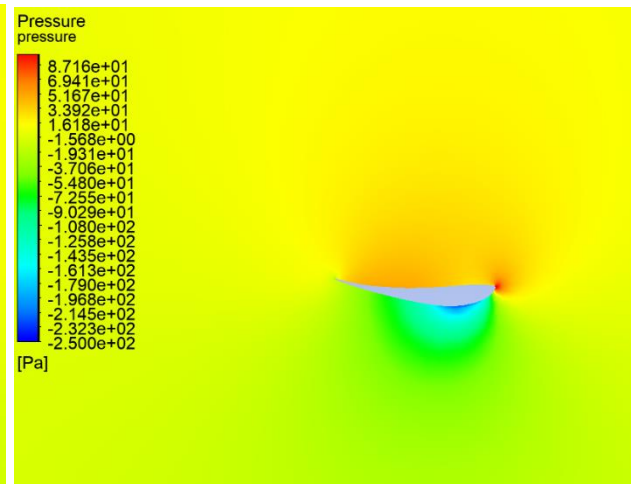


Figure 3.14 Pressure contour of S1223 at 3° AOA

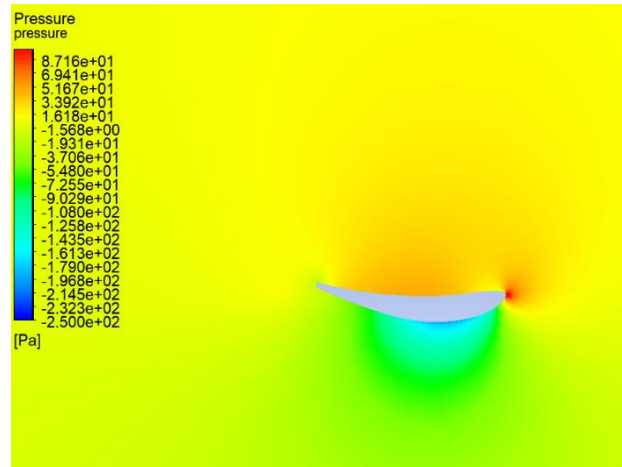


Figure 3.15 Pressure contour of E423 at 3° AOA

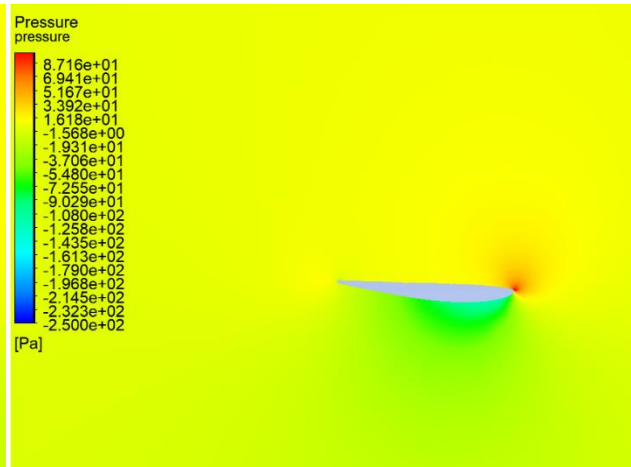


Figure 3.16 Pressure contour of S3021 at 3° AOA

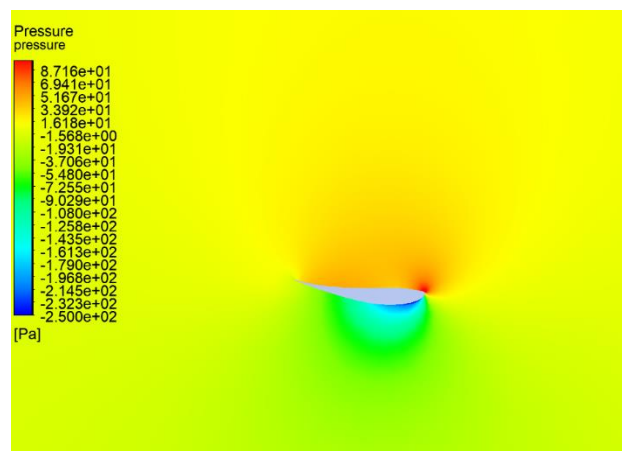


Figure 3.17 Pressure contour of S1210 at 6° AOA

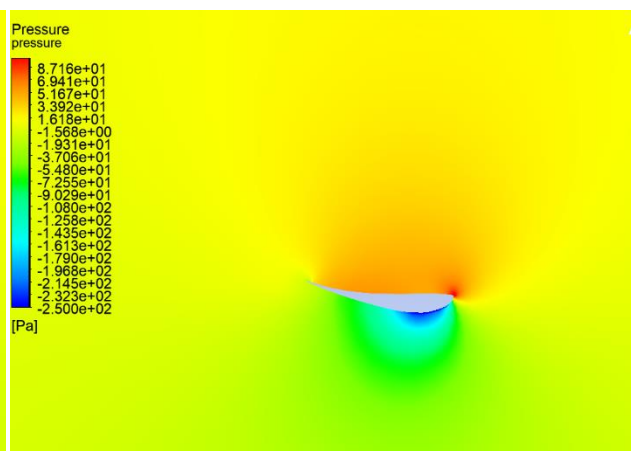
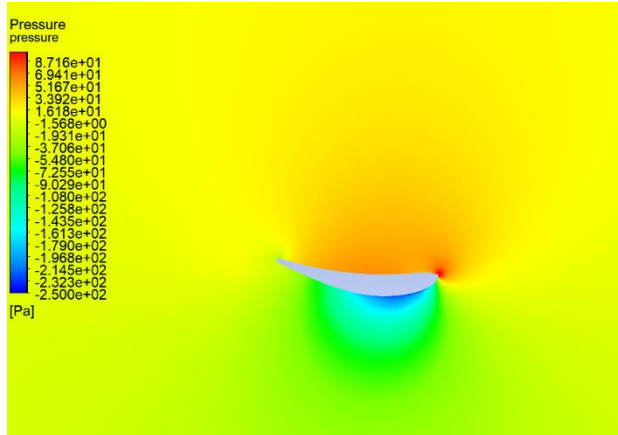
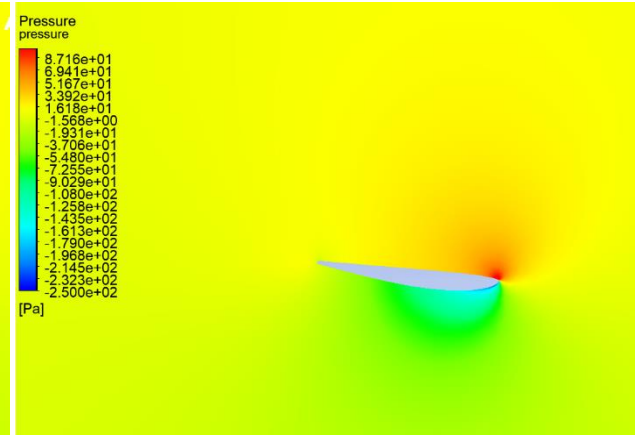


Figure 3.18 Pressure contour of S1223 at 6° AOA



**Figure 3.19** Pressure contour of E423 at 6° AOA



**Figure 3.20** Pressure contour of S3021 at 3° AOA

The pressure contours shown in Figures 3.13-3.20 visualize the amount of negative lift that is generated for each design. Again, the Selig 3021 shows significantly less pressure difference above and below it, which is translated to less downforce, while the other three profiles are comparable in terms of pressure distribution. At 3° angle of attack, E423 and S1223 present higher values of pressure on top of them, than the S1210, something that is repeated in 6° angle of attack. This leads to the general conclusion that S1210 can perform better in higher angles of attack which also means it might stall in higher angles, and it produces less drag than the other two.

The final decision for the geometry and design of the main element is made through all the analysis of the results above, and the conclusion is that Selig S1223 is more suitable for this case compared to the S1210, E423 and S3021. To sum up, the advantages of the S1223 compared to the other are:

- It produces higher values of negative lift
- Its performance is maximized in lower angles of attack where there is almost no flow separations and wake generations
- Its construction is slightly simpler than the one of S1210 as its trailing edge is thicker
- The airflow behind it is smoother as seen in the velocity contours

### 3.2. Ground Clearance

After the selection of the airfoil profile and its angle of attack that is going to be used as main element of the configuration, the next step is to place it near the road, where it is going to be placed practically. As discussed in chapter 1.3.3., due to ground effect, an airfoil that is placed close to the road, generates more downforce due to the increased pressure difference above and below it, as the flow of air below is accelerating because of the path narrowing.

In this set of simulations, the Selig 1223 airfoil at 3° AOA is going to be placed near the road which as mentioned will be set as a moving no-slip wall with a velocity of 15 m/s. The five different heights ( $h_1$ ) that the airfoil will be placed are 10, 30, 50, 70 and 90 mm from the road (Figure 3.21).

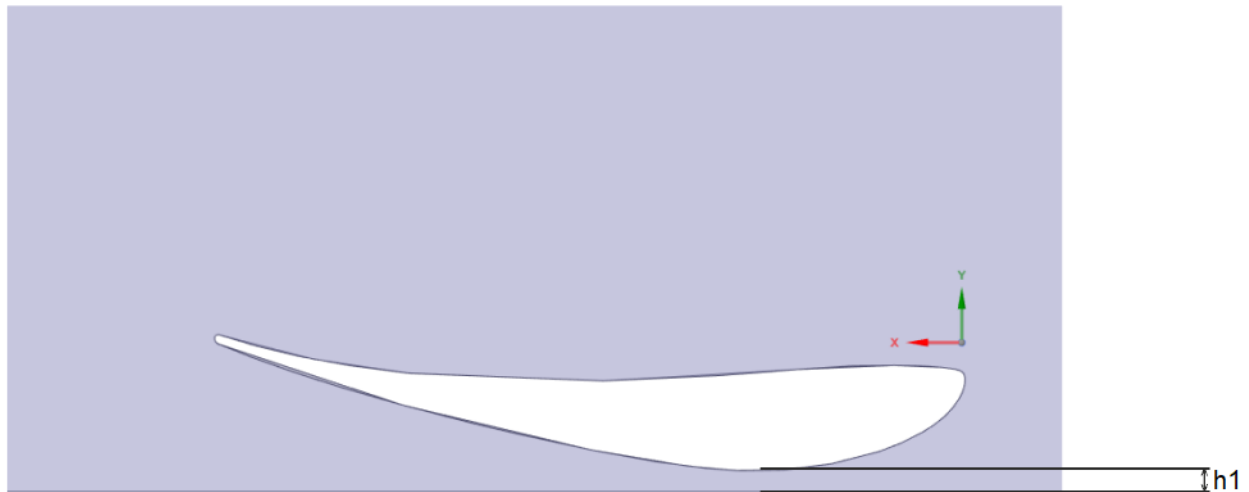


**Figure 3.21** Road clearance ( $h_1$ ) of the main element

It is expected that very close to the road the flow might be get strangled which leads to massive kinetic energy loss, while away from the road, the ground effect will get less efficient and a drop in the downforce generation will occur. To find the best possible distance between the airfoil and road, this set of simulations is conducted and the results are presented in Table 3.5 below.

Selig 1223 (3° angle of attack)					
$h_1$ (mm)	10	30	50	70	90
$C_L$	-1.046	-1.618	-1.718	-1.672	-1.592
$C_D$	0.164	0.136	0.109	0.092	0.079
$C_L/C_D$	-6.38	-11.9	-15.76	-18.17	-20.15

**Table 3.5** Selig 1223 road clearance simulations results

The first comment that can be extracted from the table above is that maximum drag is witnessed close to the road, and it decreases as the airfoil is placed away from it. This happens, as mentioned in the previous paragraph, due to the stagnation of the air flow as the cross-section below the airfoil is too small (Figure 3.22). This means the flow of air cannot manage to pass below the geometry without losing energy, something that leads to induced drag generation. Once the airfoil is high enough, the drag coefficient dramatically decreases (Figure 3.23), until it reaches the values of the previous simulation that the effect of the road is neglected and does not affect the behavior of the airflow around the wing. This element is not seen in Table 3.5, because this phenomenon occurs in larger heights than 90 mm).

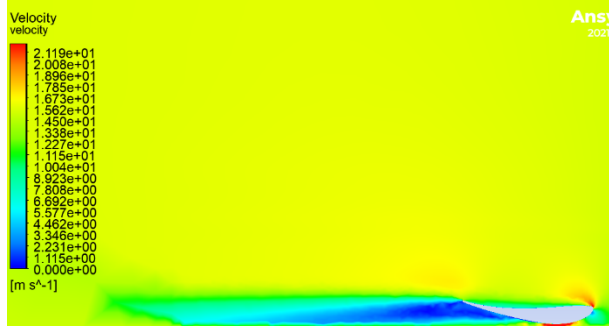


Figure 3.22 Velocity contour of S1223 ( $h_1=10$  mm)

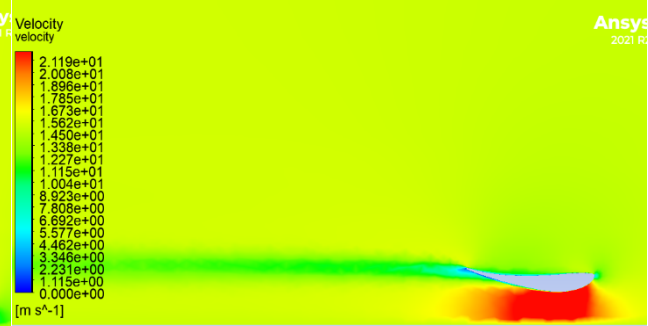


Figure 3.23 Velocity contour of S1223 ( $h_1=90$  mm)

The stagnation of the airfoil under the airfoil when it is placed 10 mm from the road leads to massive wake generation behind it, which results in large drag forces which are negatively affecting the performance of the wing, while when the airfoil is placed 90 mm from the surface of the road, this effect does not exist and there is almost no wake that generates drag behind it. This observation is not enough for reaching the decision of the appropriate road clearance, as reducing drag is not the primary goal of this study. As it is clarified from the beginning of this thesis, the main goal is to achieve maximum lift, without totally neglecting the amount of drag that is produced, so in Table 3.5, it is visible that  $h_1=50$  mm outperforms the other heights. In figures 3.24 and 3.25 the results of this set of simulation are presented.

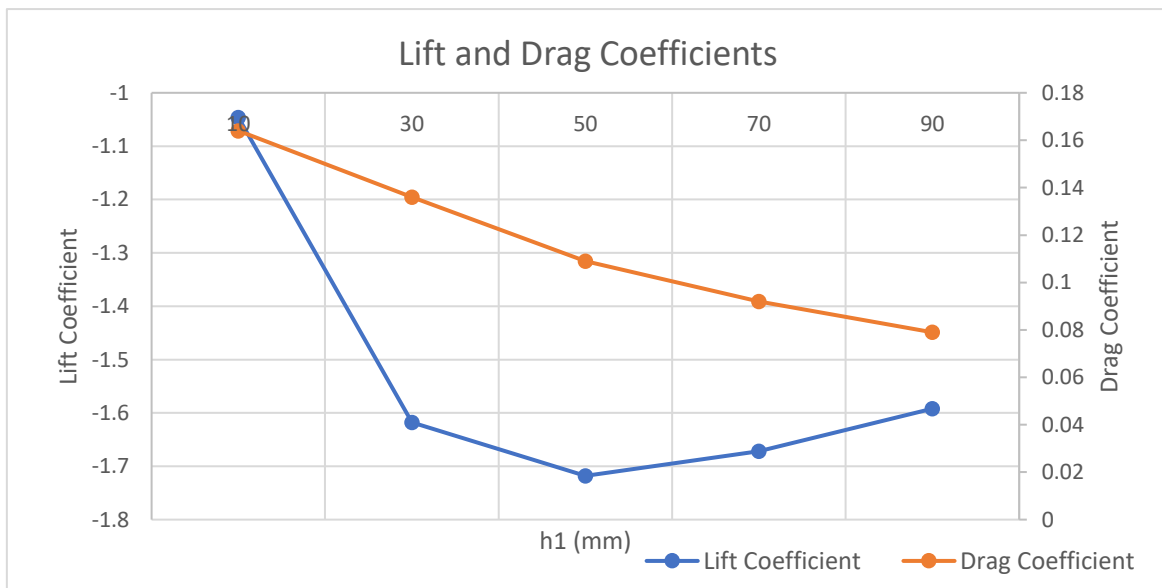
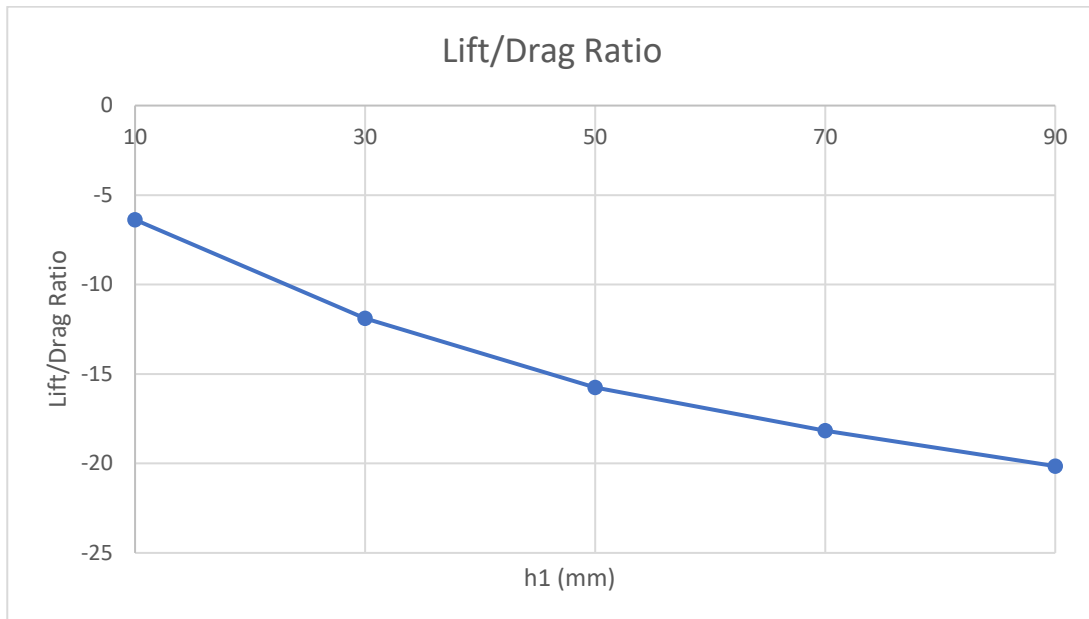


Figure 3.24 Lift and drag coefficients results for all heights ( $h_1$ ) from the road





**Figure 3.25** Lift/drag ratio results for all heights ( $h_1$ ) from the road

Figure 3.24 validates the conclusion that for  $h_1=50$  mm, the airfoil's negative lift is maximized, while for  $h_1=30$  mm and  $h_1=70$  mm, the value of the lift coefficient is reduced. In this set of simulations, lift/drag ratio is insignificant, while it will keep increasing until the height of the airfoil reaches the region where the road does not affect the behaviour of the air. All the above lead to the conclusion that the most efficient road clearance is 50 mm, which will be further validated from the figures below that present the velocity and pressure contours of the airfoil at heights 30, 50 and 70 mm from the road (pressure contours for 10- and 90-mm heights are shown in Appendix A).

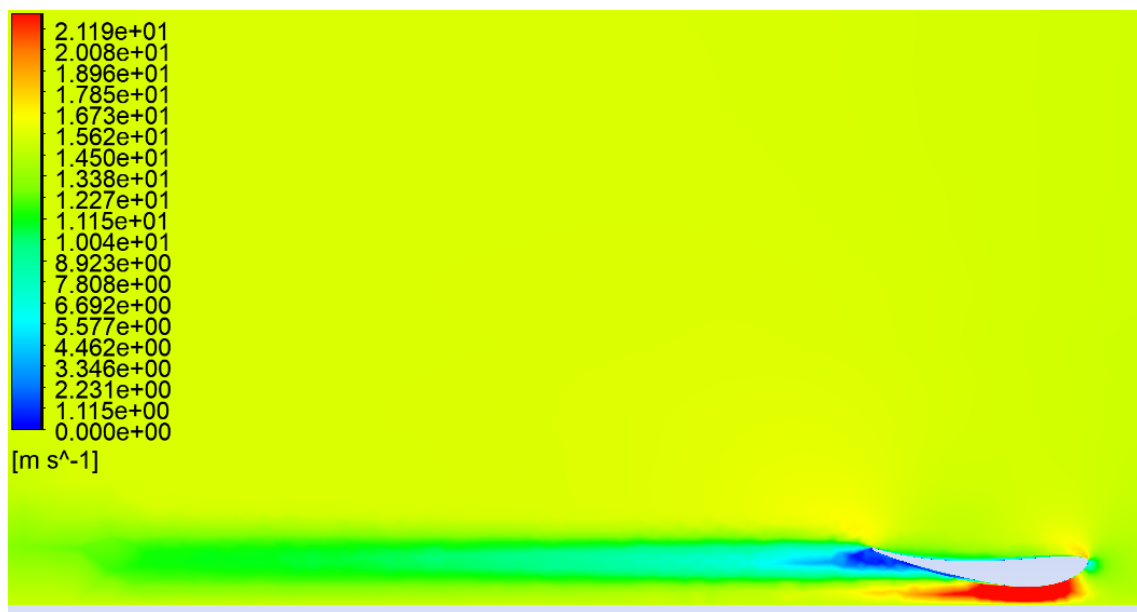


**Figure 3.26** Velocity contour for  $h_1=30$  mm

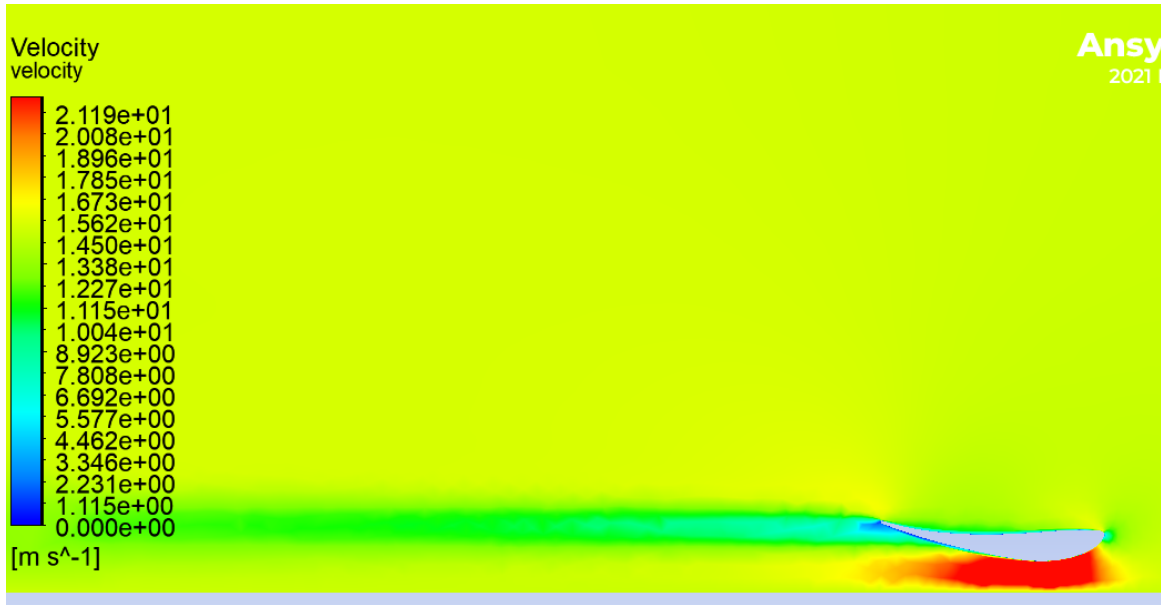


Figure 3.27 Velocity contour for  $h_1=50$  mm

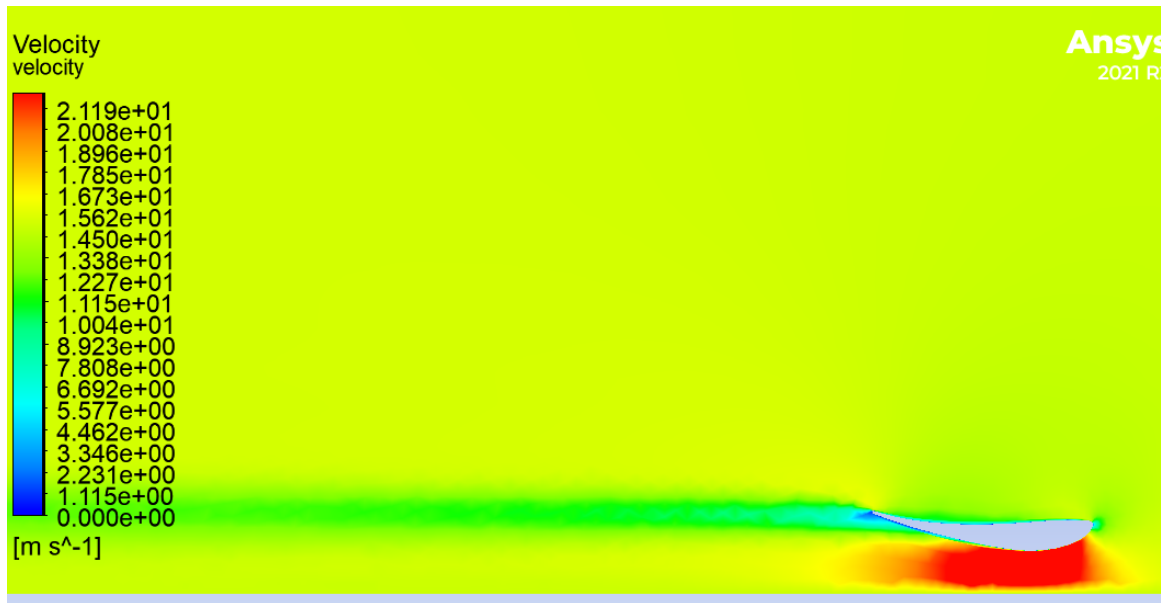


Figure 3.28 Velocity contour for  $h_1=70$  mm

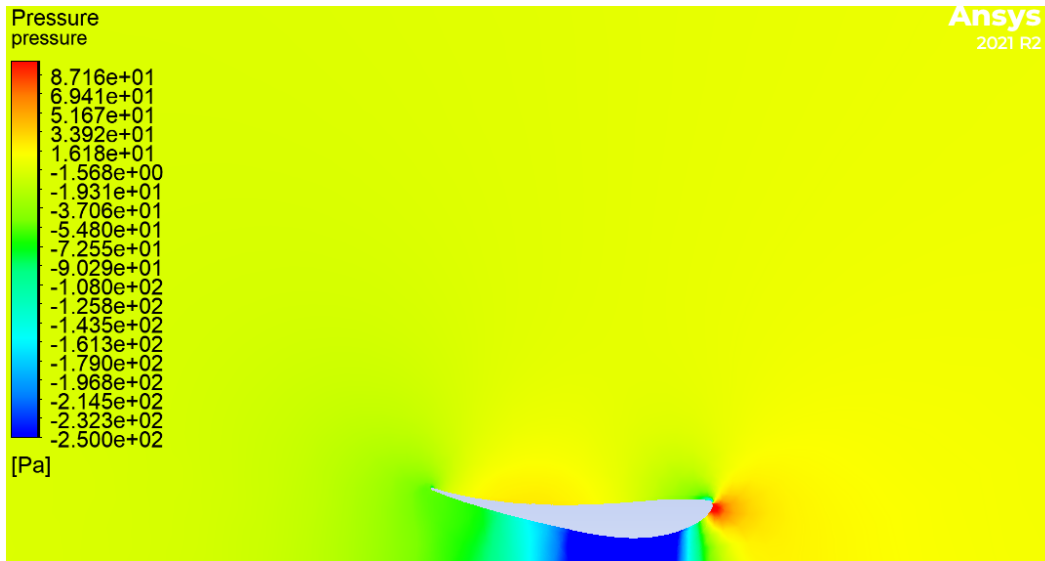


Figure 3.29 Pressure contour for  $h_1=30$  mm

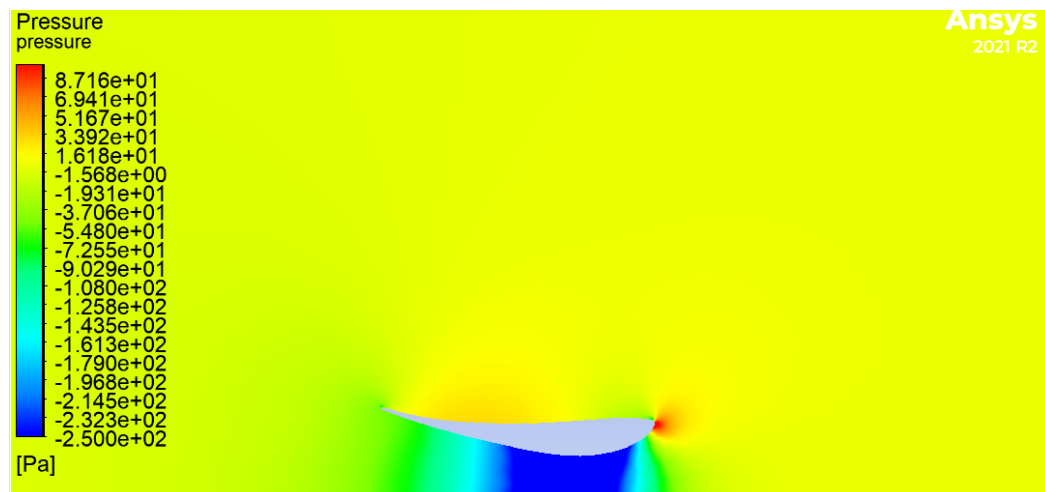


Figure 3.30 Pressure contour for  $h_1=50$  mm

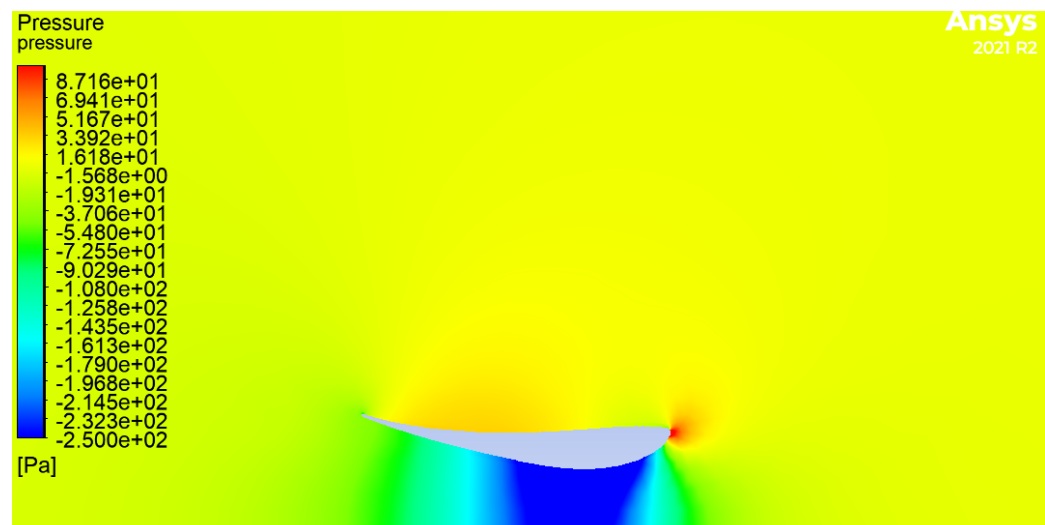
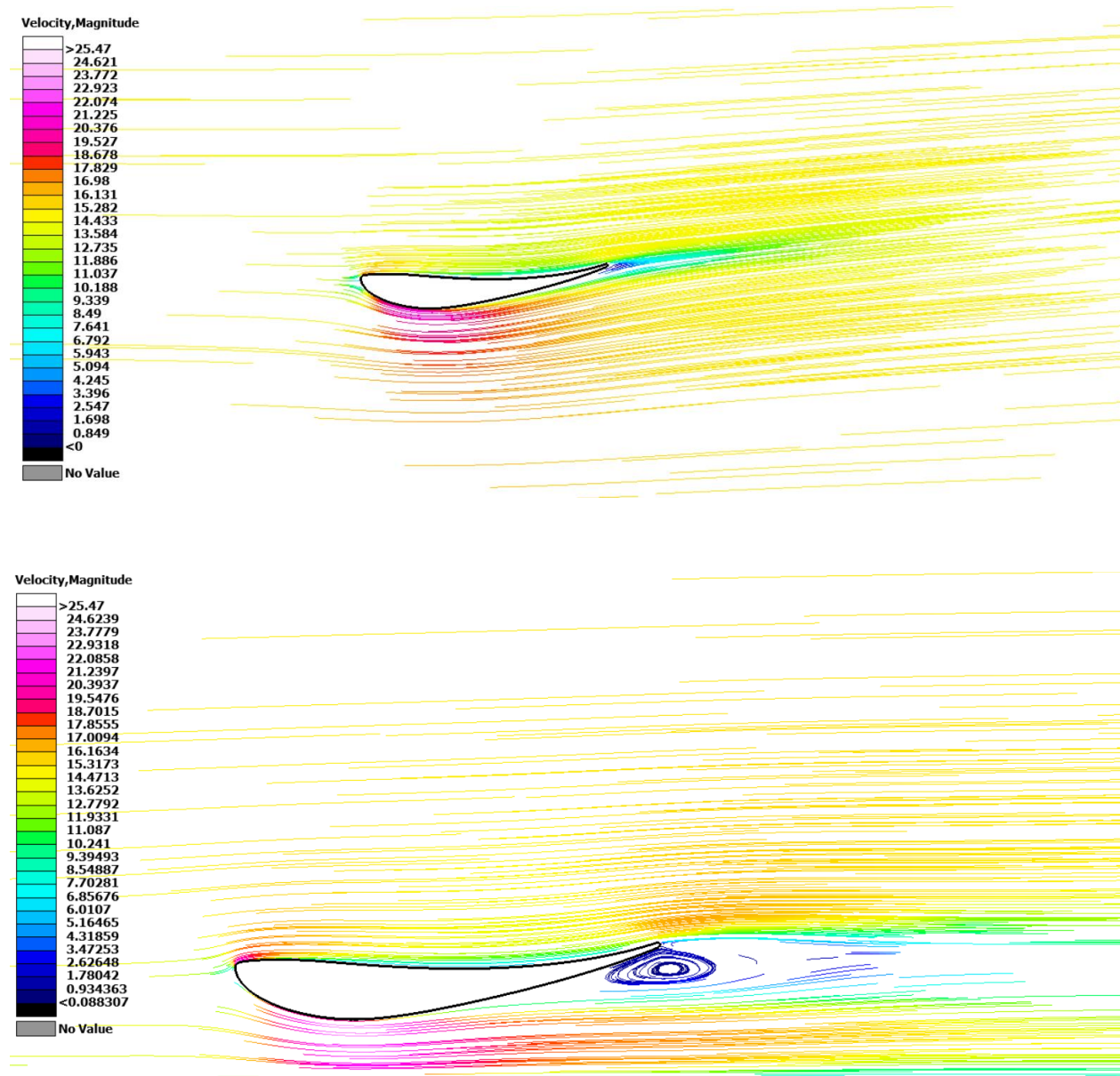


Figure 3.31 Pressure contour for  $h_1=70$  mm

From Figures 3.26, 3.27 and 3.28, it is visible that at 50 mm and 70 mm, the wake behind the airfoils is significantly smaller than that seen at 30 mm. This wake which is usually produced due to flow separation of the bottom rear of the airfoil, affects its aerodynamic performance, and especially its potential downforce generation. Taking this into consideration, road clearance of 50 and 70 mm is more likely to be chosen for the main element's placement. The visualization of the results in this set of simulation is not so helpful, as almost no difference between the two heights (50 and 70 mm) is visible, so the decision for the most efficient design is being made through analysis of the results that are presented in Table 3.5. As mentioned before,  $h_1=50$  mm presents the peak value of negative lift coefficients and so, this is the one that will be selected and used in the rest set of simulations. For comparison of the airflow around the S1223 close to the road and away from it, Figures 3.32 and 3.33 are observed, and it is clear that in the second case, the velocity under the airfoil is slightly increased which leads to greater pressure difference above and below the wing and thus, more downforce.



### 3.3. Secondary Element (flap)

The next step of the process is to add a secondary element to the front wing configuration, which will be responsible for the most amount of downforce that will be produced from the assembly. Since it was clear from the first set of simulations that Selig 1223 is superior compared to the other three, it will also be used as a secondary element in higher angle of attack that will be determined in this chapter after the completion of the specific set of simulations. The airfoil will be tested from 15 to 45 angle of attack, as higher values of downforce are desired, and at first, it is placed 10 mm above the main element and the horizontal distance between them is 0 mm as seen in Figure 3.34. The relative distance between the two elements will be decided in the last two sets of simulation which are conducted in Chapter 3.4 and 3.5, to maximize the efficiency of the front wing. It is important to clarify that its chord length as mentioned before is 40% of the main element's chord length which equals to 144 mm, and its span is 1300 mm as well.

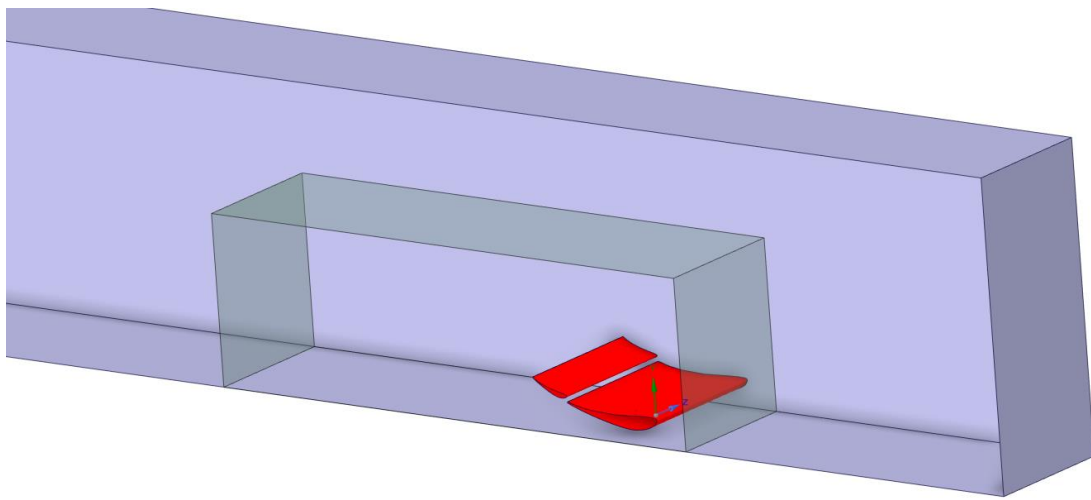


**Figure 3.34** Two element configuration placed in the simulation's fluid domain

In the fluid domain that is shown above, the body of influence is a little larger, because the height and length of the geometry that is being studied is increased. This has an impact on the number of elements that are formed, which is around 800,000, as the properties of the BOI and the quality of the mesh remain the same. Also, the reference values are set considering that the reference area and length is the sum of the two elements. As all the information about the third set of simulations is discussed, the results are presented in Table 3.6 below.

Selig 1223 (flap)							
AOA (°)	15	20	25	30	35	40	45
$C_L$	-3.067	-3.351	-3.603	-3.665	-3.8	-3.907	-3.845
$C_D$	0.218	0.259	0.313	0.357	0.448	0.474	0.54
$C_L/C_D$	-14.07	-12.94	-11.51	-10.26	-8.48	-8.24	-7.12

**Table 3.6** Results of simulation for Selig 1223 as secondary element

The table above, shows the performance of the S1223 wing as a secondary element, with the same wing at 3° AOA as main element. Conclusions regarding the fluctuations of the lift and drag coefficients are extracted, but it not clear which configuration is the most efficient one. It is reasonable that the drag coefficient increases for higher angles of attack, but the lift coefficient peaks at 40° AOA, which is a potential selection of design. Despite the fact that in this angle of attack the airfoil produces the most amount of negative lift, the lift/drag ratio must also be considered before reaching a final decision, which decreases as the angle of the wing increases. Once the decision cannot be made through the observation of the results of Table 3.6, Figures 3.35 and 3.36 show these results in graphic form.

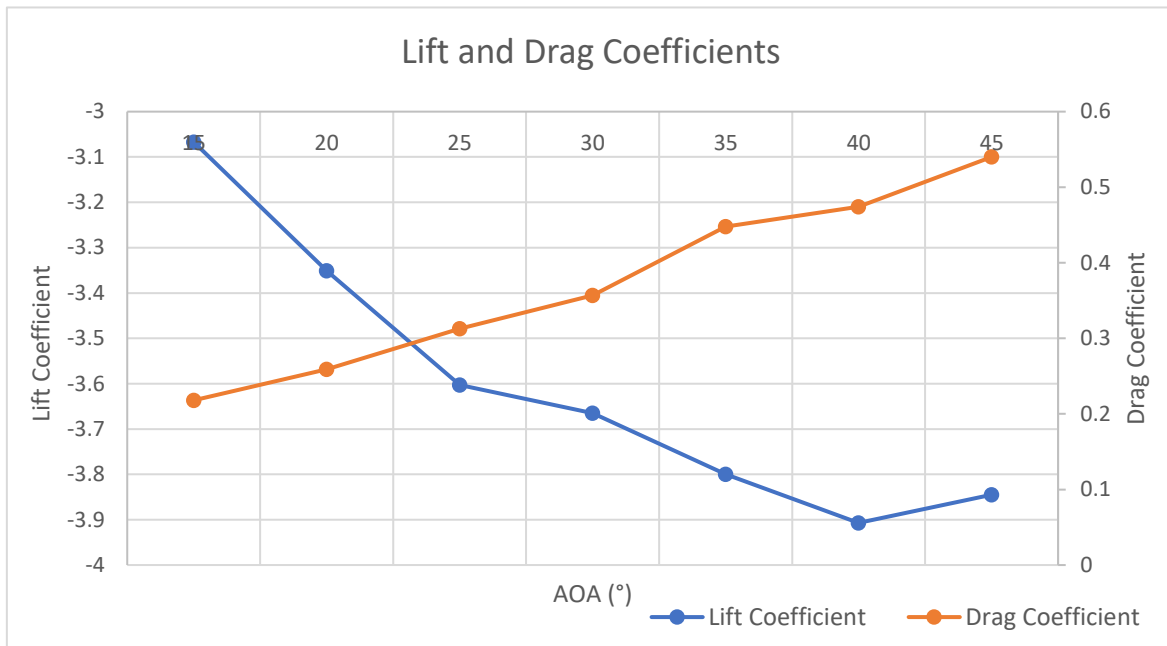


**Figure 3.35** Lift and drag coefficients results for all AOA of the flap

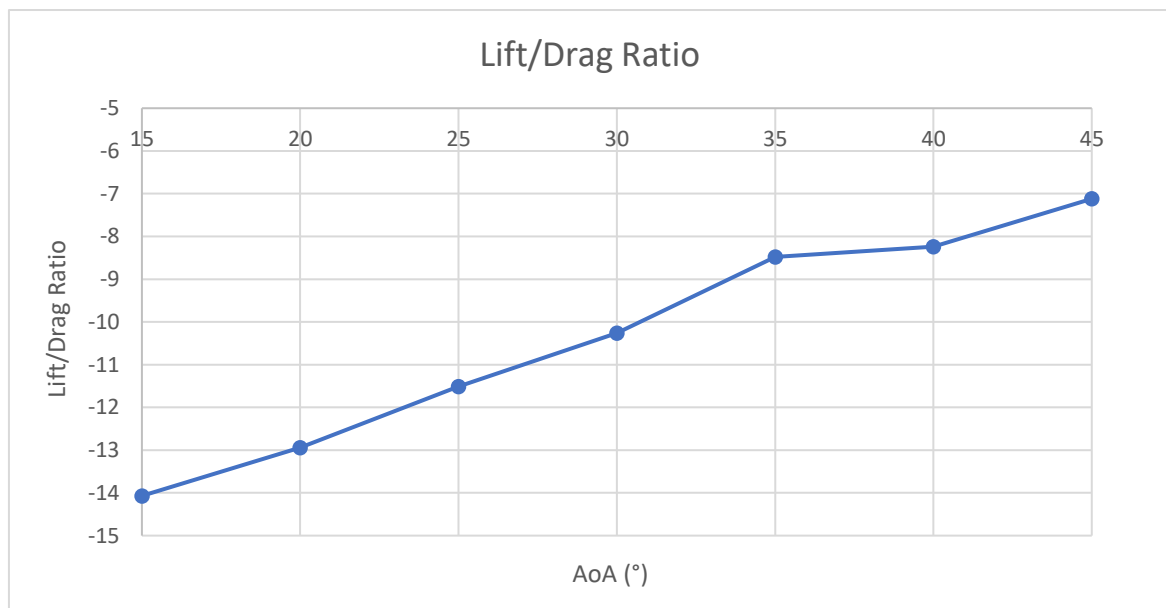


**Figure 3.36** Lift/drag ratio results for all AOA of the flap

In Figure 3.35, the comments made earlier are visible as the drag coefficient is constantly decreasing, while the lift coefficient increases until 40° AOA, and then in 45° decreases again. From the primary goals that are set, the design with the most potential is this with 40° angle of attack but observing Figure 3.36 and considering one of the most important factors which is efficiency, the lift/drag ratio must all be taken into account. For this reason, it is noted that after 30°, an abrupt increase in the lift/drag ratio is seen, which leads us to further review the situation before ending up with the final configuration of this simulation set. In addition, the lift coefficient shows a large increase after 25° compared to the first two samples, which means that there are four possible designs (from 25° to 40° AOA) that must be narrowed down to one (45° as the airfoil completely stalls and produces additional drag without generating further downforce). In order to select one design, a review of the velocity and pressure contours for the S1223 set from 25° to 40° angle of attack which are shown in the following figures is necessary (velocity and pressure contours for the rest angles are presented in Appendix A).

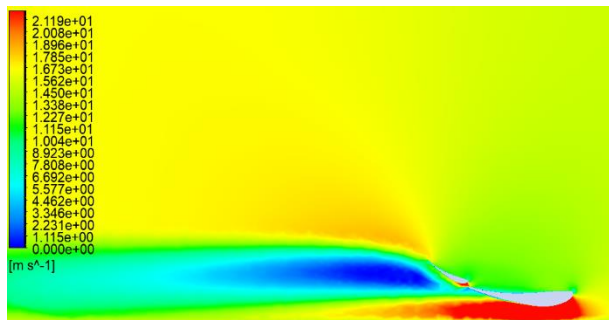


Figure 3.37 Velocity contour for S1223 flap (25° AOA)

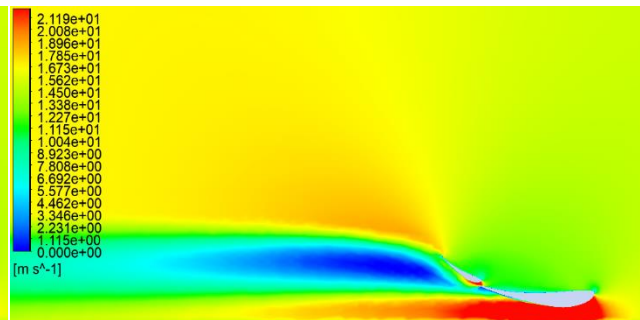


Figure 3.38 Velocity contour for S1223 flap (30° AOA)

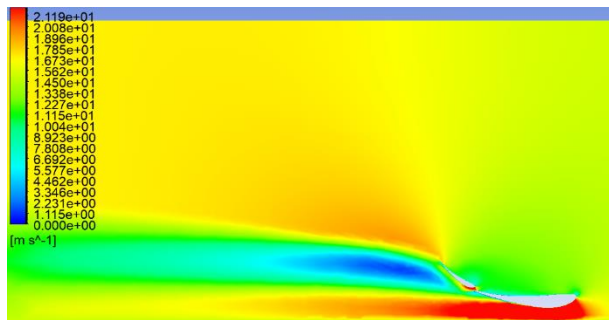


Figure 3.39 Velocity contour for S1223 flap (35° AOA)

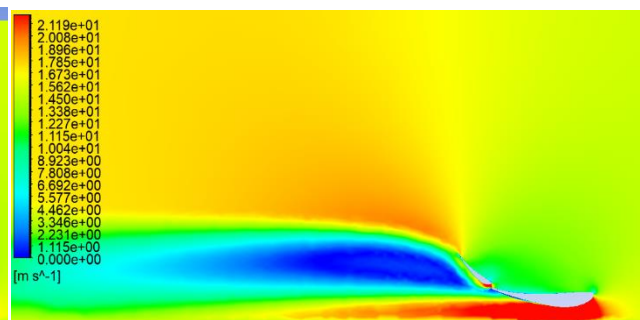


Figure 3.40 Velocity contour for S1223 flap (40° AOA)

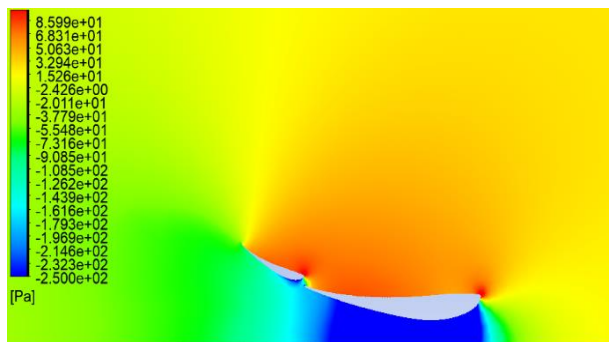


Figure 3.41 Pressure contour for S1223 flap (25° AOA)

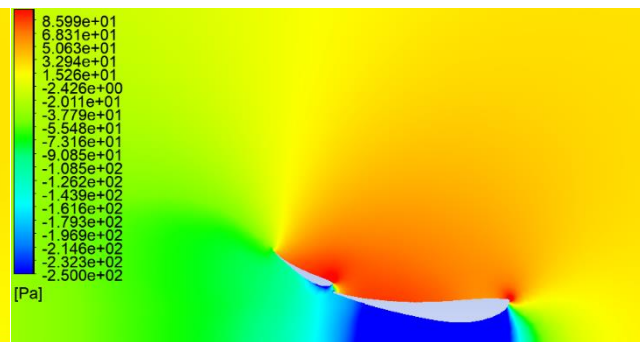


Figure 3.42 Pressure contour for S1223 flap (30° AOA)

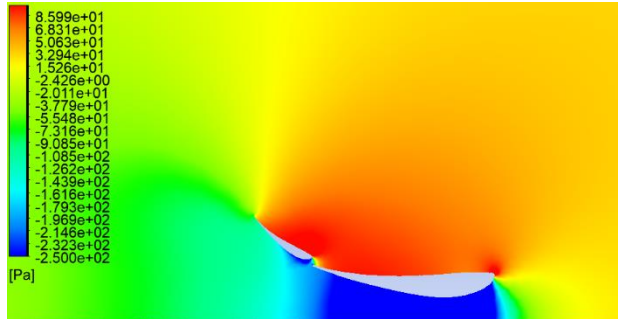


Figure 3.43 Pressure contour for S1223 flap (35° AOA)

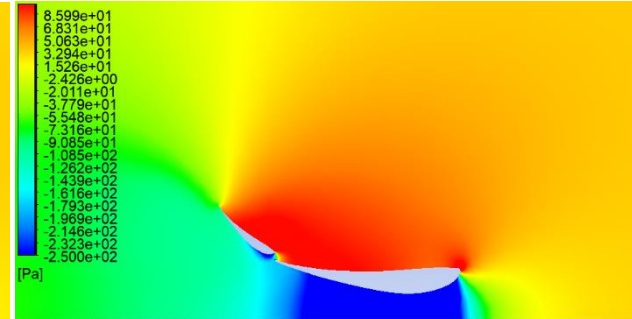


Figure 3.44 Pressure contour for S1223 flap (40° AOA)

Although the airflow of the airfoil at 35° shows less wake behind it as seen in the velocity contours, compared to the other designs, the drag that produces is significantly larger than that of the airfoil when is set at 25° and 30° angle of attack. The negative lift coefficient for the 30° design is -3.665, and for the 35°,  $C_L$  is equal to -3.800, which translates to 3.7% increase in downforce production, while the drag coefficient is increased by 26% (from 0.357 at 30° AOA to 0.448 at 35° AOA). According to these results and considering that the lift/drag ratio dramatically decreases after an angle of 30°, the designs that are above this angle are rejected. To sum up, the two angles that suit better this specific study are 25° and 30°, and by considering that the main goal of this project is high downforce and efficiency, the second one is the most appropriate.

### 3.4. Vertical Distance Between Elements

Another parameter that affects the performance of the front wing assembly performance except from the angles of attack of the elements and the distance from the road, is the relative distance between the two elements, as it is understandable that the first one can affect the airfoil that the later receives. To decide the gap between the two elements, two simulation sets are conducted that will determine the vertical and the horizontal distance between these two elements. In this step, the vertical distance will be adjusted in each simulation while the horizontal stays the same as this in the previous set, which is 0 mm. The vertical distance between the two elements which is called  $h_2$  (Figure 3.45), is adjusted from 10, to 35 mm, with a gap of 5 mm between these adjustments. This means the secondary element is placed 10, 15, 20, 25, 30 and 35 mm above the main element.

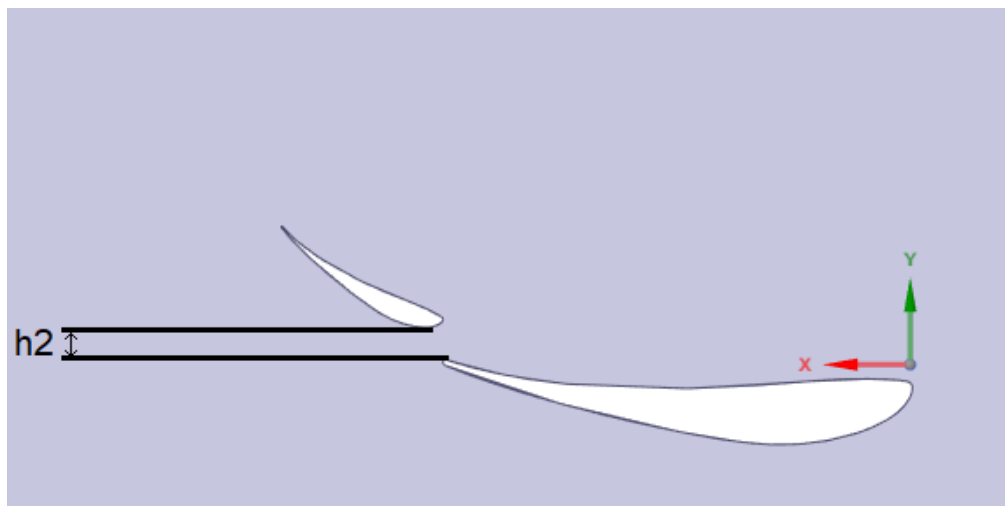


Figure 3.45 Vertical distance ( $h_1$ ) between the two elements of the front wing assembly



All the settings of the simulations are identical to the previous ones except for the reference values that change from one design to another which can be measured as described in Chapter 2.3.2.4. The results of the fourth set of simulations is presented in Table 3.7.

S1223 (vertical distance)						
$h_2$ (mm)	10	15	20	25	30	35
$C_L$	-3.665	-3.754	-3.767	-3.871	-3.93	-3.975
$C_D$	0.357	0.374	0.378	0.386	0.384	0.391
$C_L/C_D$	-10.26	-10.04	-9.97	-10.03	-10.23	-10.17

**Table 3.7** Lift and drag coefficients results for all vertical distances ( $h_2$ ) between the two elements

The phenomenon that was seen in the second set of simulation where the airflow is stagnated when the passage between two geometries is too narrow, is also visible in this simulation set as the negative lift, drag and efficiency of the airfoil in general, present better results once the two elements are placed with larger gap between them. It is difficult to judge which airfoil is superior from the others, so the results are presented in Figure 3.46.

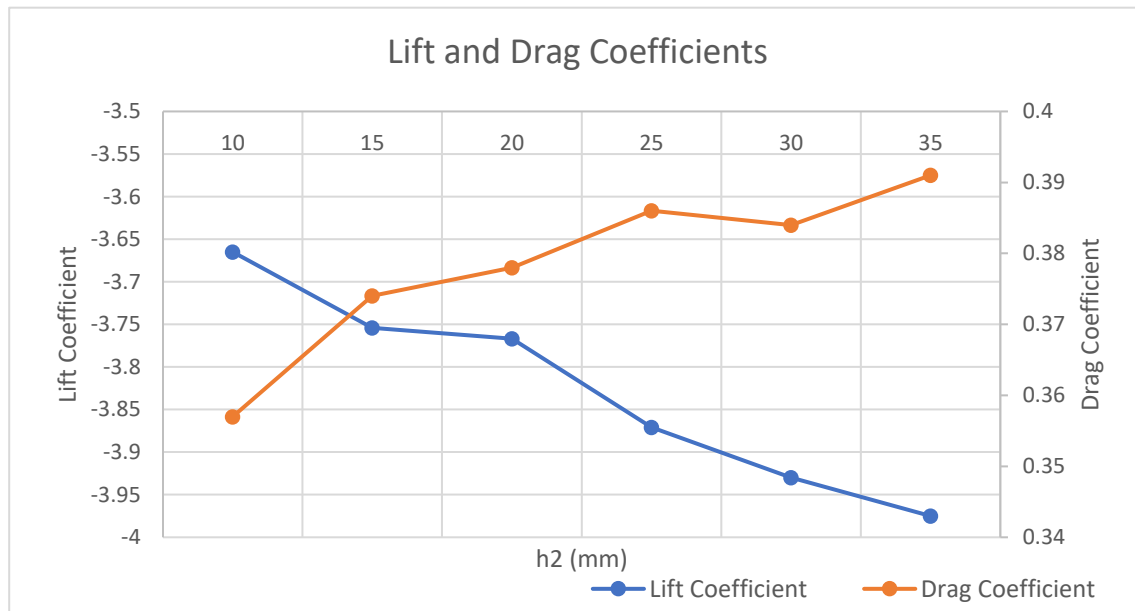


**Figure 3.46** Lift and drag coefficients for all vertical distances ( $h_2$ ) between the two elements

The first and most important comment on from the graph, is that the drag coefficient is constantly increasing as the gap between the two elements grows, but at a height of 30 mm, the drag coefficient presents a small decrease. This might happen because the main element at this distance help the airflow at the bottom of the second element follow the curvature of the geometry, which results in less flow separation below the flap. It can be noted that the airflow is not stable when the gap between the elements is too small, by observing the fluctuations in the lift/drag ratio value. As negative lift is the primary goal and the drag coefficient can be neglected when its values remain at low levels, the three most suitable designs for this case, is the last ones, where  $h_2$  is equal to 25, 30 and 35 mm as their value

of  $C_L$  is presenting a major increase. To narrow them down to the most efficient one, once again the velocity and pressure contours are shown below (velocity and pressure contours for the rest values of  $h_2$  are shown in Appendix A).

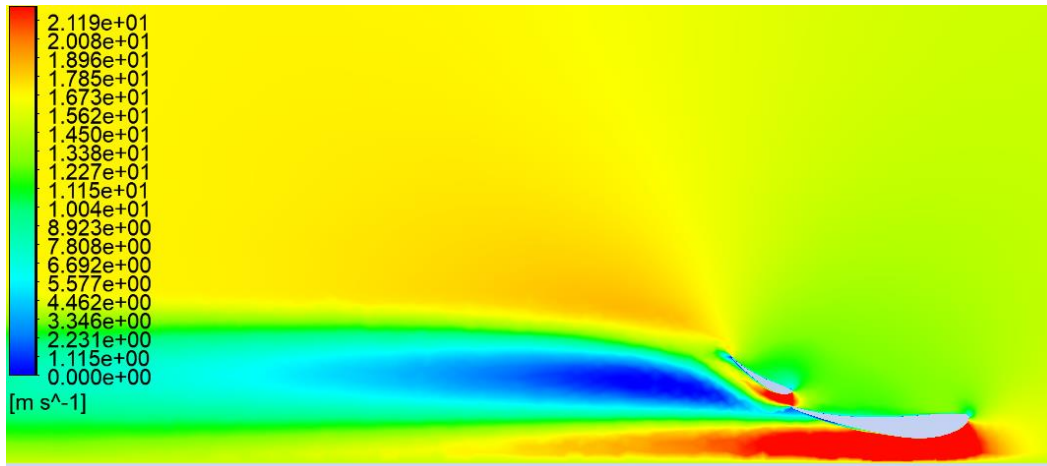


Figure 3.47 Velocity contour of the front wing ( $h_2=25$  mm)

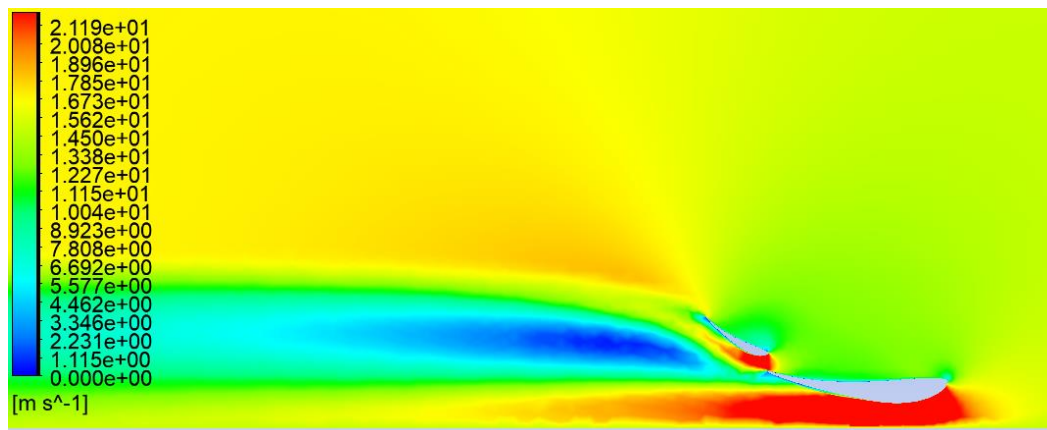


Figure 3.48 Velocity contour of the front wing ( $h_2=30$  mm)

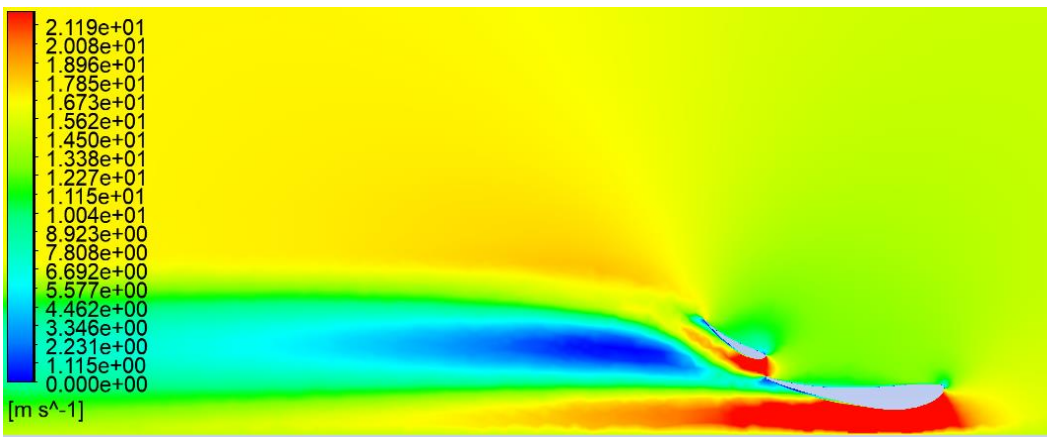


Figure 3.49 Velocity contour of the front wing ( $h_2=35$  mm)

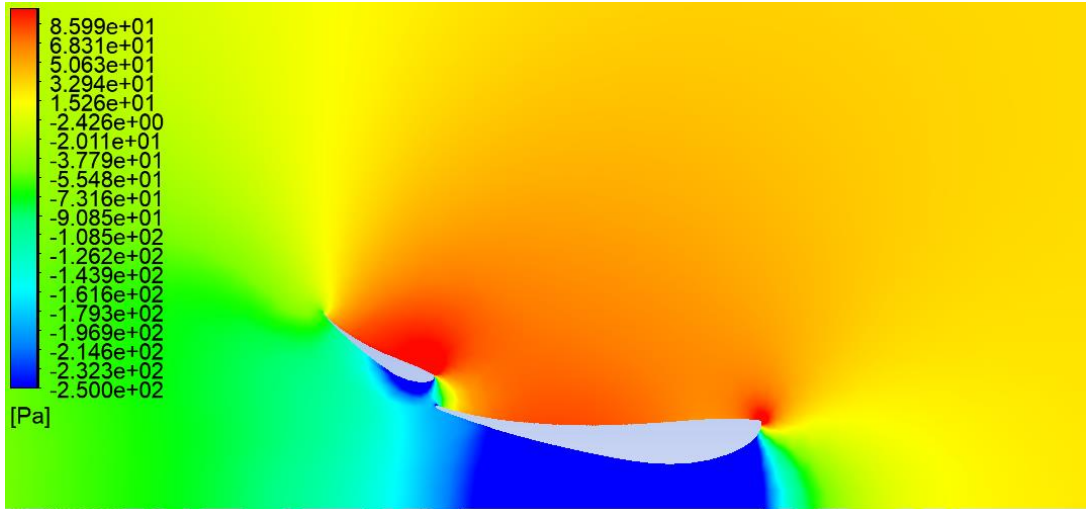


Figure 3.50 Pressure contour of the front wing ( $h_2=25$  mm)

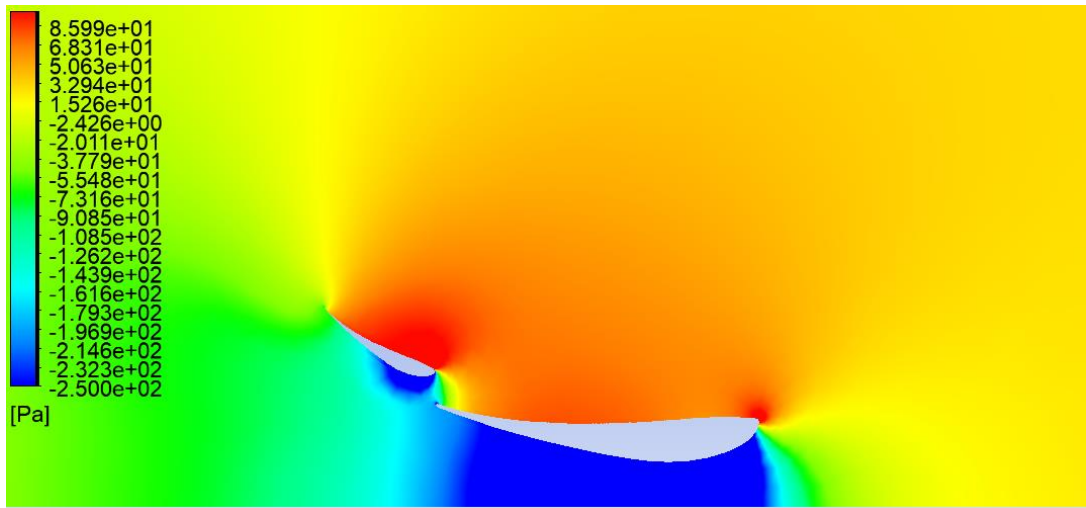


Figure 3.51 Pressure contour of the front wing ( $h_2=30$  mm)

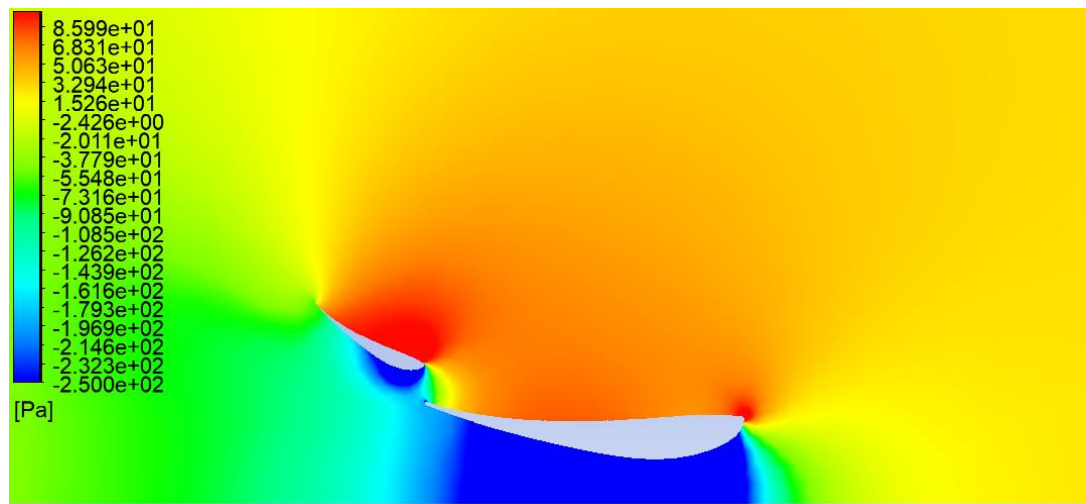
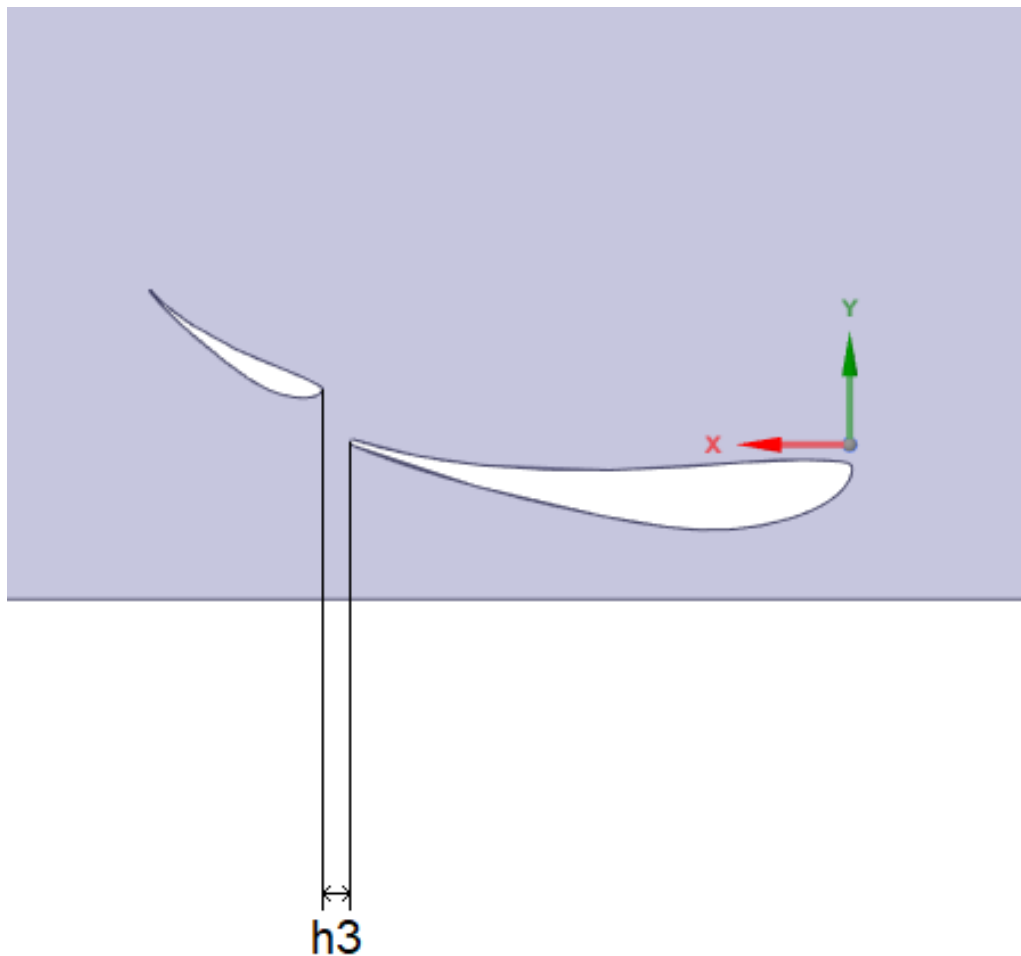


Figure 3.52 Pressure contour of the front wing ( $h_2=35$  mm)

The velocity contours presented in Figure 3.47, 3.48 and 3.49, validated the decrease in the drag that occurs for  $h_2=30$  mm, as it can be seen that the wake behind the geometry is slightly smaller compared to the other two designs. The airflow below the second element is smoother in the last two designs, while in the first one, the velocity of the air shows a slight decrease, which affects the aerodynamic efficiency of the wing. The pressure contours are almost identical and do not give further information that can help with the selection of the most efficient design. Summing up the above, the flap is most efficient when placed 30 and 35 mm above the main element, with the first placement being superior as the drag that is produced from it is slightly smaller, and so, the S1223 flap will be placed at  $h_2=30$  mm.

### 3.5. Horizontal Distance Between Elements

In this chapter the last set of simulations that will determine the horizontal distance of the flap from the main element will be conducted. The last parameter that affects and might improve the aerodynamic behaviour of the front wing assembly, is the horizontal relative distance between the two elements which is named  $h_3$ . The value of the parameter  $h_3$  will be set from -30 mm to 30 mm, with a gap of 10 mm between the adjustments, meaning the second element will be placed at -30, -20, -10, 0, 10, 20 and 30 mm relatively to the main element. Figure 3.53 demonstrates the horizontal distance  $h_3$  between the elements.



**Figure 3.53** Horizontal distance ( $h_3$ ) between the two elements of the front wing assembly

The results that were extracted from the set of simulations are shown in Table 3.8 below.

S1223							
$h_3$ (mm)	-30	-20	-10	0	10	20	30
$C_L$	-3.649	-3.683	-3.725	-3.93	-3.97	-3.62	-3.292
$C_D$	0.398	0.397	0.399	0.384	0.369	0.33	0.307
$C_L/C_D$	-9.168	-9.277	-9.336	-10.234	-10.759	-10.970	-10.723

**Table 3.8** Lift and drag coefficients results for all horizontal distances ( $h_3$ ) between the two elements

In this last simulation set, it is easy to decide which position of the flap in the horizontal axis is the most efficient one, as the value of the negative lift coefficient peaks at  $h_3=10$  mm, and the drag coefficient which although is not primary factor in the selection of the design, is lower once the horizontal distance between the two elements increases. Another observation that enhances the chance that 10 mm is the most suitable position for the flap, is that the lift/drag ratio is the second larger at this distance. To validate these decisions, Figures 3.54 and 3.55 that imprint the results into graphs are added.

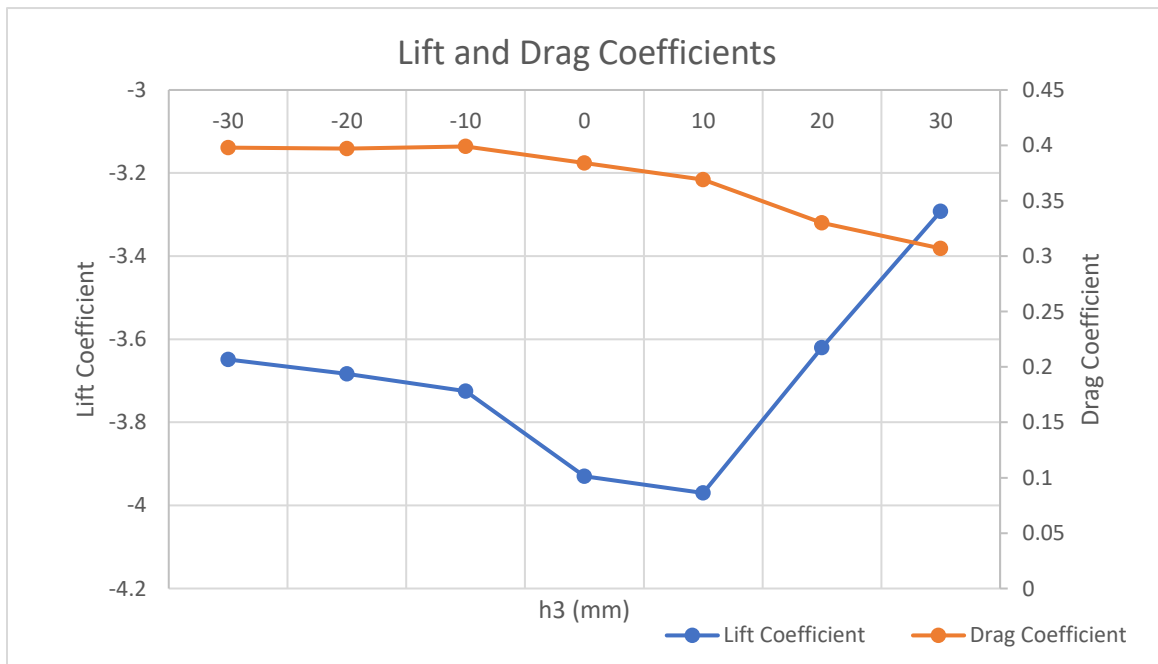


**Figure 3.54** Lift and drag coefficients for all horizontal distances ( $h_3$ ) between the two elements

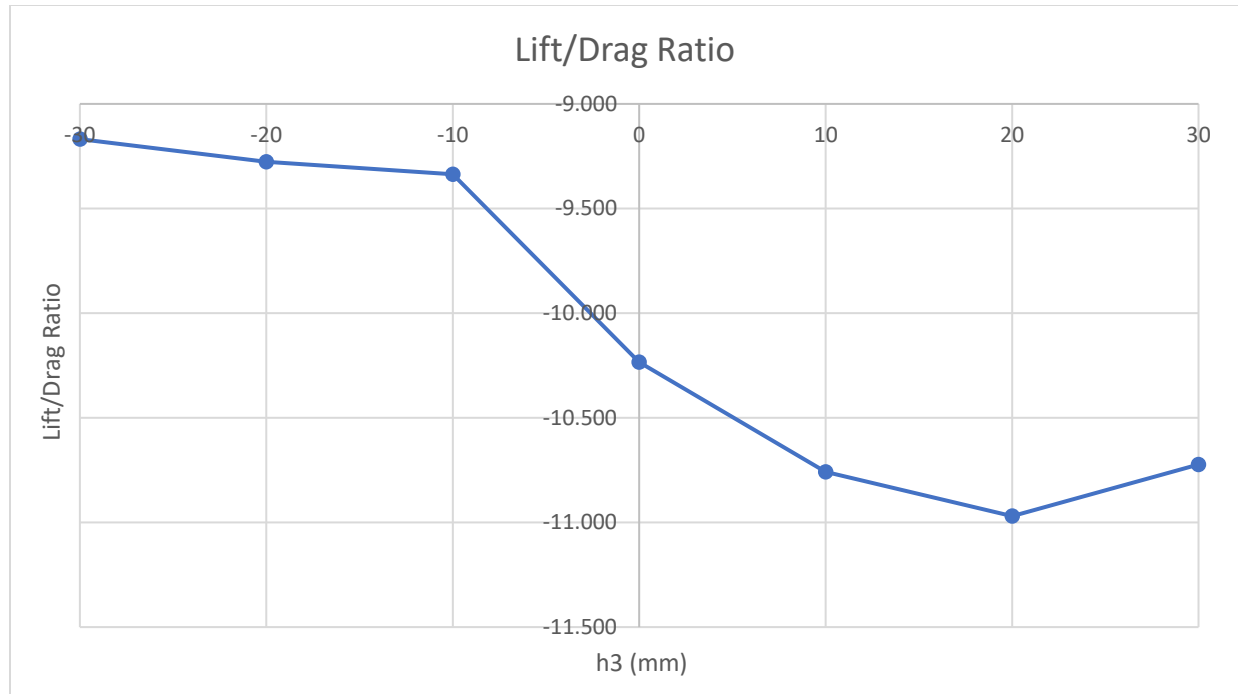


**Figure 3.55** Lift/drag ratio for all horizontal distances ( $h_3$ ) between the two elements

Observing the graphs above, the conclusions made before are validated as there is it can be seen that for  $h_3=10$  mm, the value of  $C_L$  peaks at -3.97, where the  $C_D$  and the lift/drag ratio is equal to 0.369 and -10.759. Once maximum lift is achieved at  $h_3=10$  mm, while the drag forces remain at low levels, this horizontal position is the most efficient and will be used for the front wing configuration. Although the lift/drag ratio peaks at 20 mm, the lift coefficient dramatically drops in this position, as the airflow that leaves the main element is not able to follow the curvature of the flap, resulting in flow separation, which leads to loss in the aerodynamic performance of the assembly. The two velocity and pressure contours for  $h_3= 10$  mm and  $h_3= 20$  mm are shown below, while the pressure and velocity contours for the rest distances are added in the Appendix A.

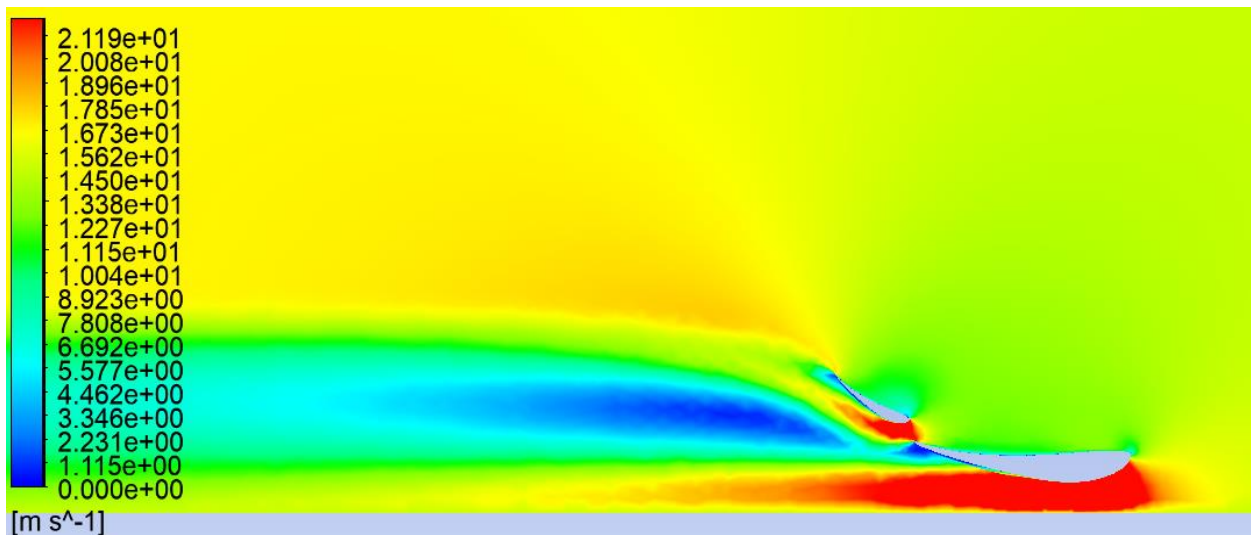


**Figure 3.56** Velocity contour of the front wing ( $h_3=10$  mm)

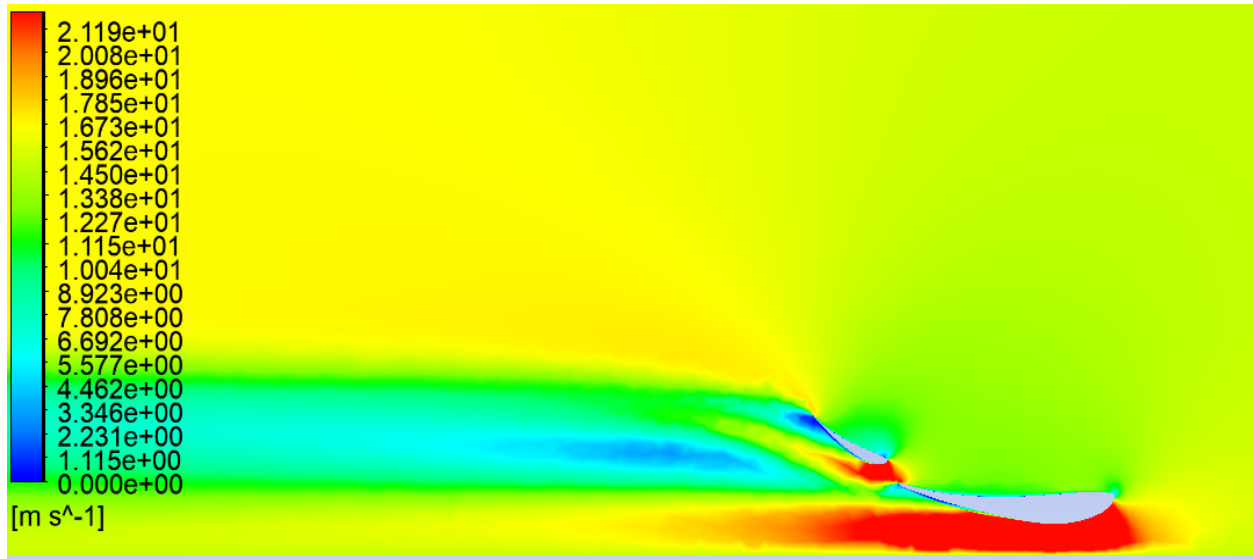


**Figure 3.57** Velocity contour of the front wing ( $h_3=20$  mm)

In Figures 3.56 and 3.57, the velocity contours for  $h_3=10$  mm and  $h_3=20$  mm, where the phenomenon that was described above is slightly visible. Although the flow separates from the surface at the leading edge of the first element in the first design, the separation of the flow that occurs at the leading edge of the flap in the second one, has bigger effect on the overall performance of the front wing. This happens due to the fact that, as discussed before, the primary goal of the addition of the second element is to produce higher percentage of downforce compared to the main element, so when the flow separates at the bottom it, its contribution in downforce production is significantly less, resulting in overall decrease of the downforce that is generated from the assembly. Lastly, in Figure 3.57, the separation of the flow occurs very early on the bottom surface of the flap, and the airflow is not as smooth as this seen in the bottom of the secondary element in Figure 3.56.

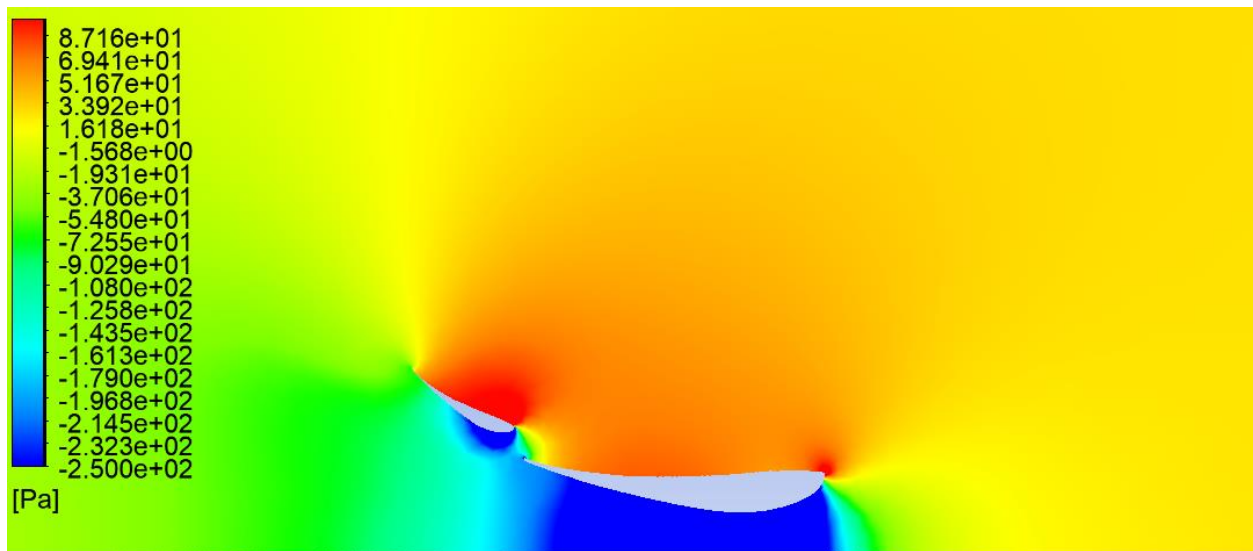


**Figure 3.58** Pressure contour of the front wing ( $h_3=10$  mm)

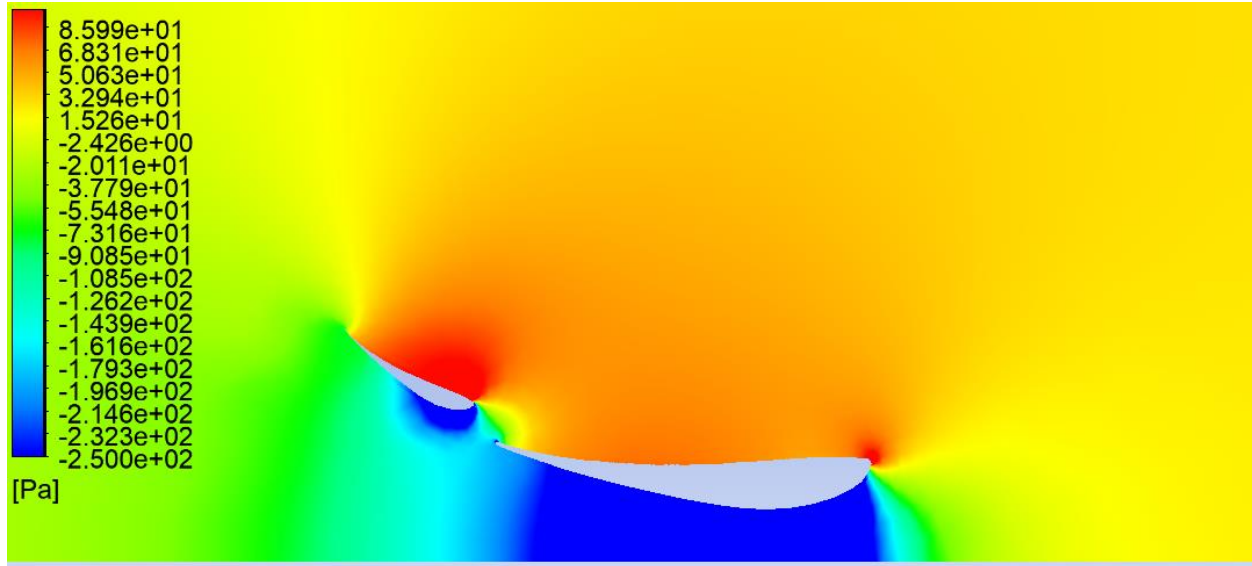


Figure 3.59 Pressure contour of the front wing ( $h_3=20$  mm)

### 3.6. Final Assembly

Once all simulation sets are completed, a final design regarding the CFD analysis is being made, where the airfoil is adjusted to the bounding box that was set in Chapter 2.2.1, where there is a 400 mm gap in the middle, that affects the design of the secondary element. In order to adjust to these restrictions, the secondary element is cut and removed from the middle of the geometry, as the nose cone will be placed there, and plates to hold it are added. Also, endplates that were mentioned in Chapter 1.3.3, are added to the assembly to prevent the airflow from spoiling from the sides of the elements, which results in large flow disturbances and efficiency reduction. The geometry that is designed and simulated in CFD is presented in Figure 3.60. Another advantage of endplates is that they are able to produce large vortices on their edges, which can seal the airflow below the car from spoiling or being disrupted by “dirty” airflow that might be a result from the wheels. The difference of the vortices that are being produced when there are no endplates, compared to the design with endplates, is presented in Figures 3.61 and 3.62, while the streamlines of the two designs are shown in Figures 3.65, 3.66 and the pressure contours of the final assembly is presented Figures 3.67, 3.68.

From the last CFD simulation that was conducted in this thesis the results of interest are the negative lift coefficient which equals to -3.714, and the drag coefficient which is equal to 0.513. The values that occurred from this simulation are realistic, as it can be easily understandable that the geometry is more complex, and the airflow is not as smooth as it was in the previous sets of simulations. Also, the secondary element’s span is reduced, which also slightly affects its  $C_L$  and  $C_D$  values. The final value of the lift/drag ratio is -7.24, which is acceptable considering the factors that were mentioned in the beginning of the simulation process. Once the final coefficients are measured, the total amount of downforce and drag that the assembly produces can be easily calculated through Equations 1.6 and 1.7. Considering air density ( $\rho$ ) constant and equal to  $1.2 \text{ kg/m}^3$ , velocity ( $U$ ) equal to 15 m/s, and reference area ( $A$ ) equal to  $0.579 \text{ m}^2$ , then Lift ( $L$ ) is -290.3 N, and Drag ( $D$ ) equals to 40.1 N.



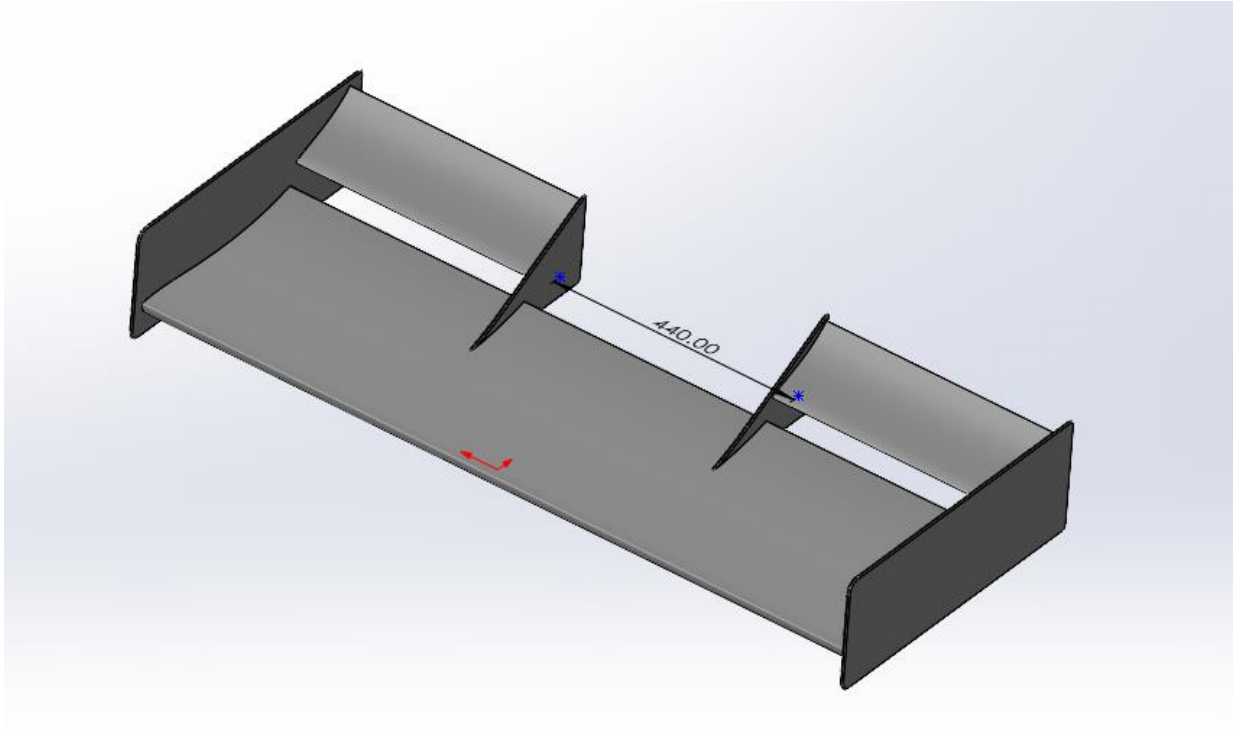


Figure 3.60 Final assembly for CFD with 440 mm gap in the middle of the secondary element

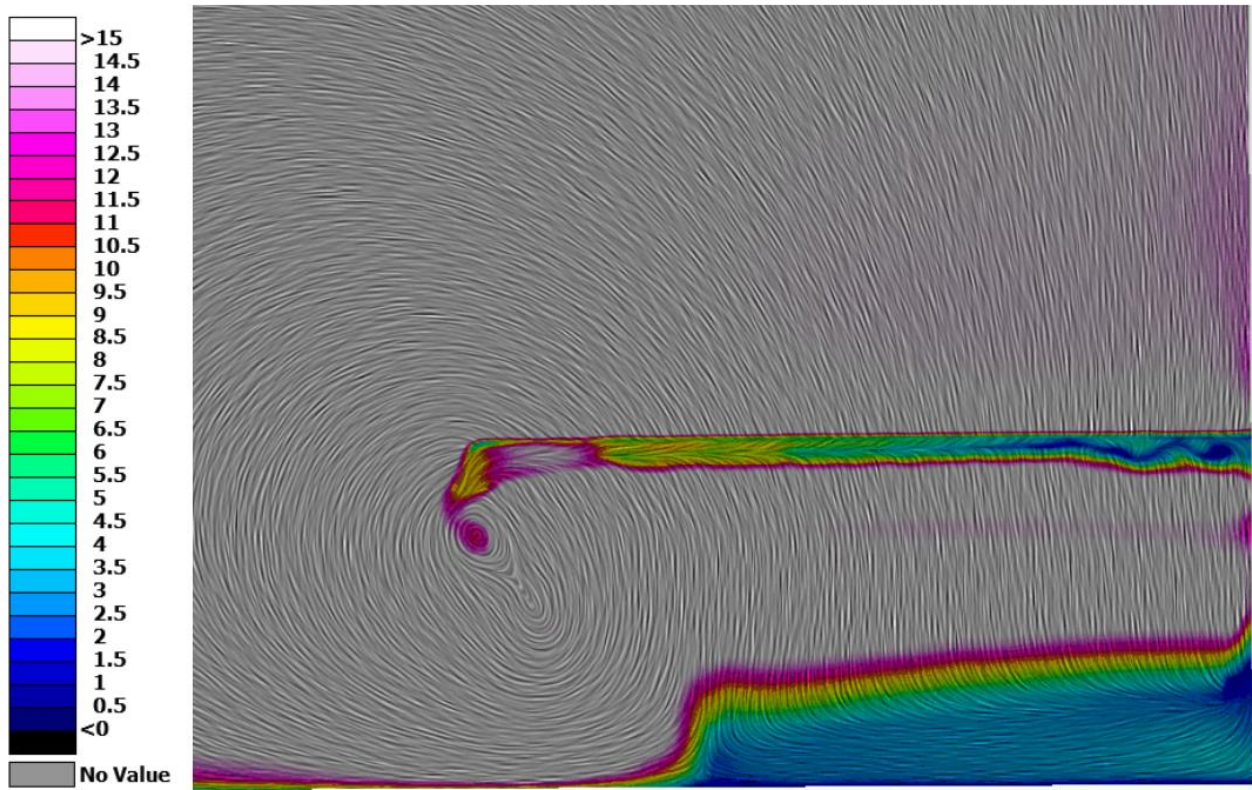
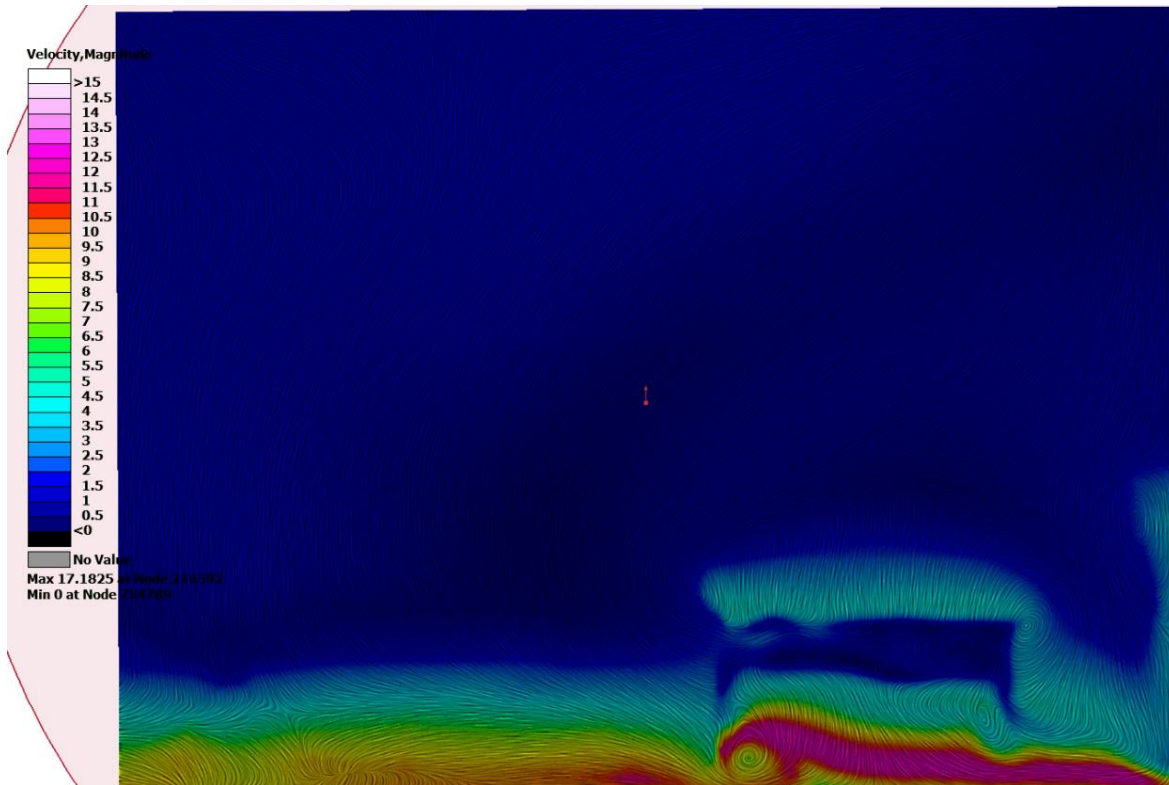
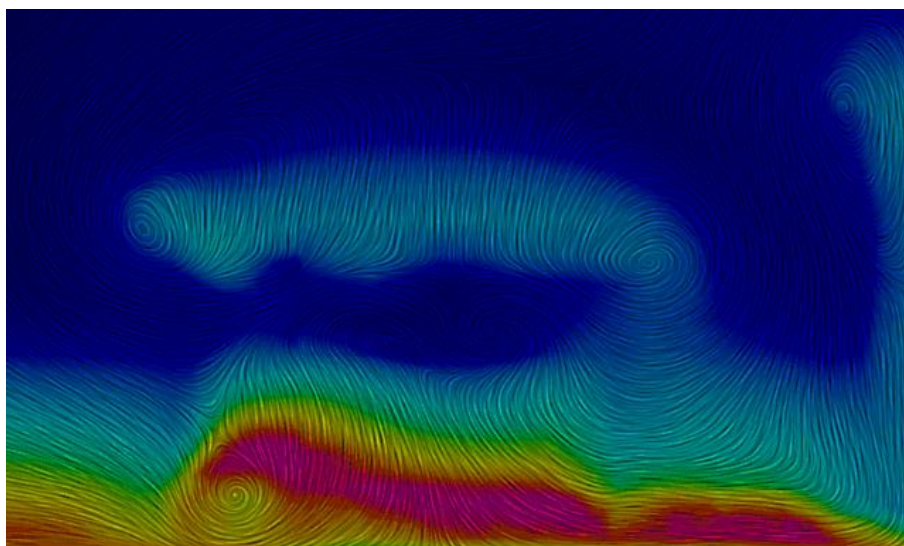


Figure 3.61 Turbulence visualization of the two-element no-endplate configuration with velocity magnitude contour



**Figure 3.62** Turbulence visualization of the final assembly with velocity magnitude contour

It can be observed that in the final assembly, there is a strong vortex generated at the bottom rear corner of the endplate, as the plane of the contour is right behind the airfoil geometry, while on the no-endplate geometry no significant vortices are witnessed. So, by adding endplates to the geometry, more energized vortices that seal the airflow below the car are generated, and the airflow from the high-pressure side of the airfoil is prevented from spoiling from the edge of the wing which is seen in Figure 3.62. Less powerful vortices can also be seen at the inner plate that holds the secondary plate, as well as at the top rear corner of the endplate. In order to better visualize the vortex that is generated at the top of the endplate, another plane 10 mm behind this one is set, and the result is shown in Figure 3.61.



**Figure 3.63** Turbulence visualization of the final assembly with velocity magnitude contour

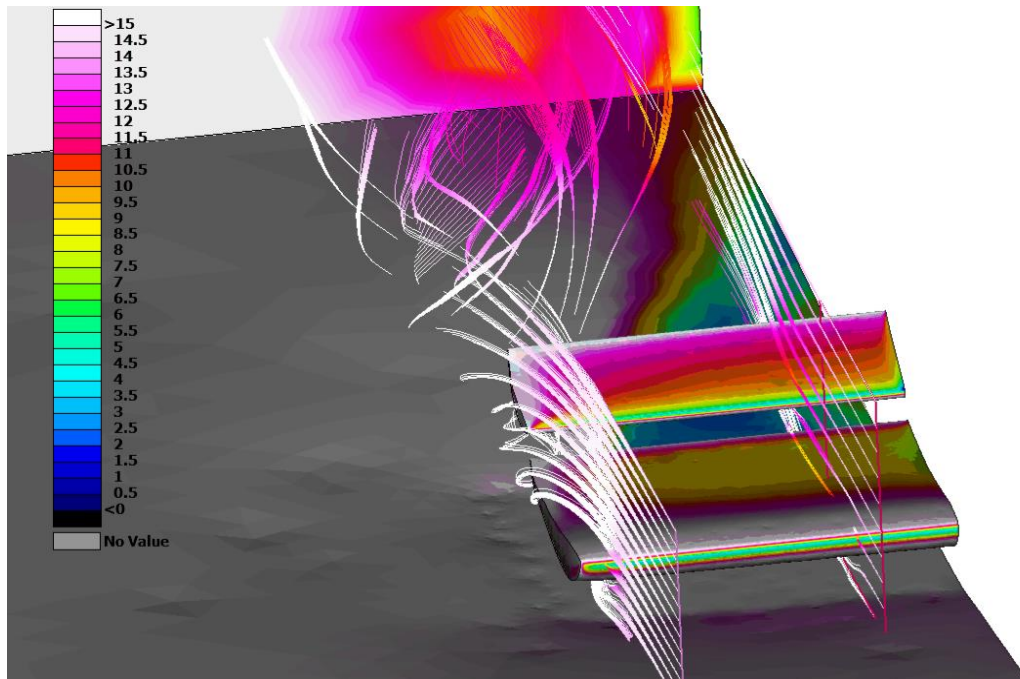


Figure 3.64 3D velocity magnitude streamlines of two-element configuration without endplates

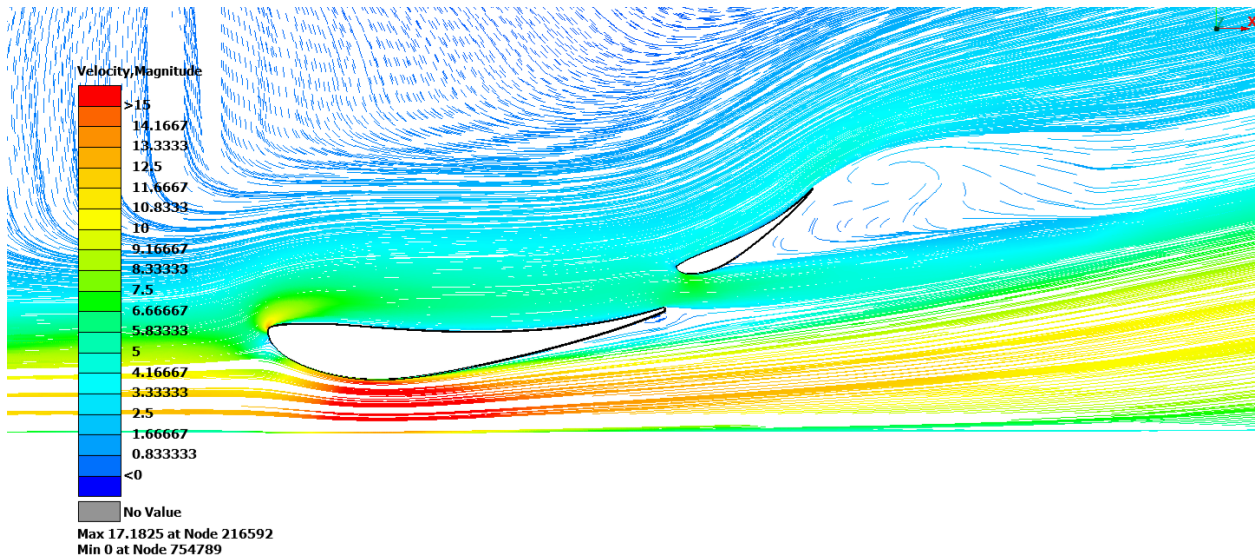
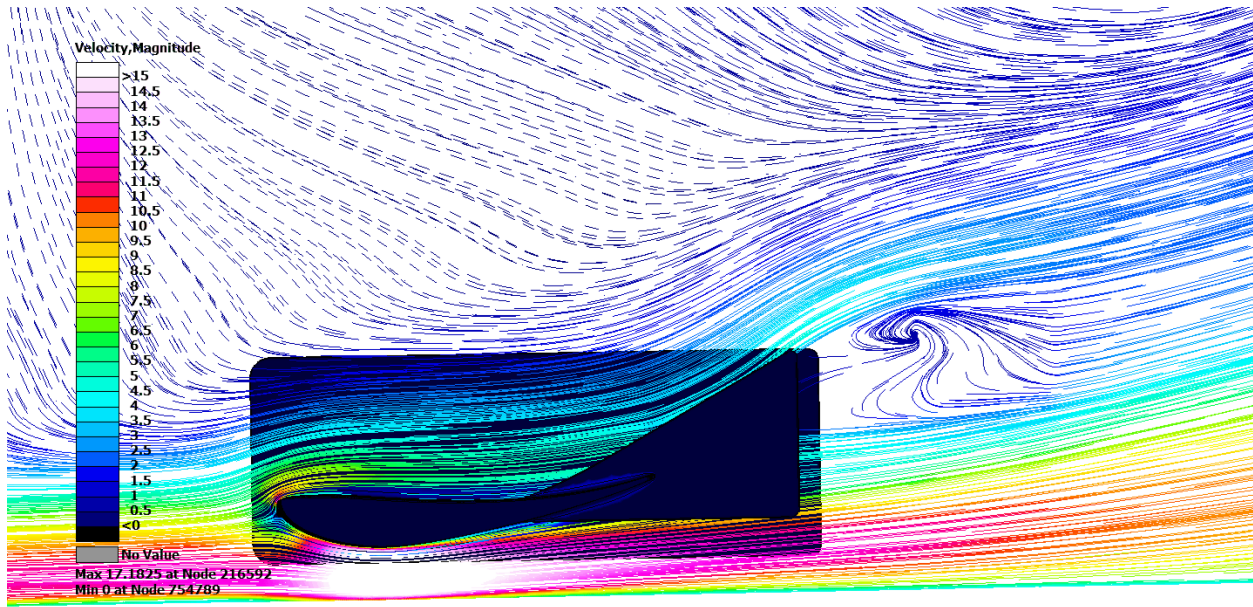
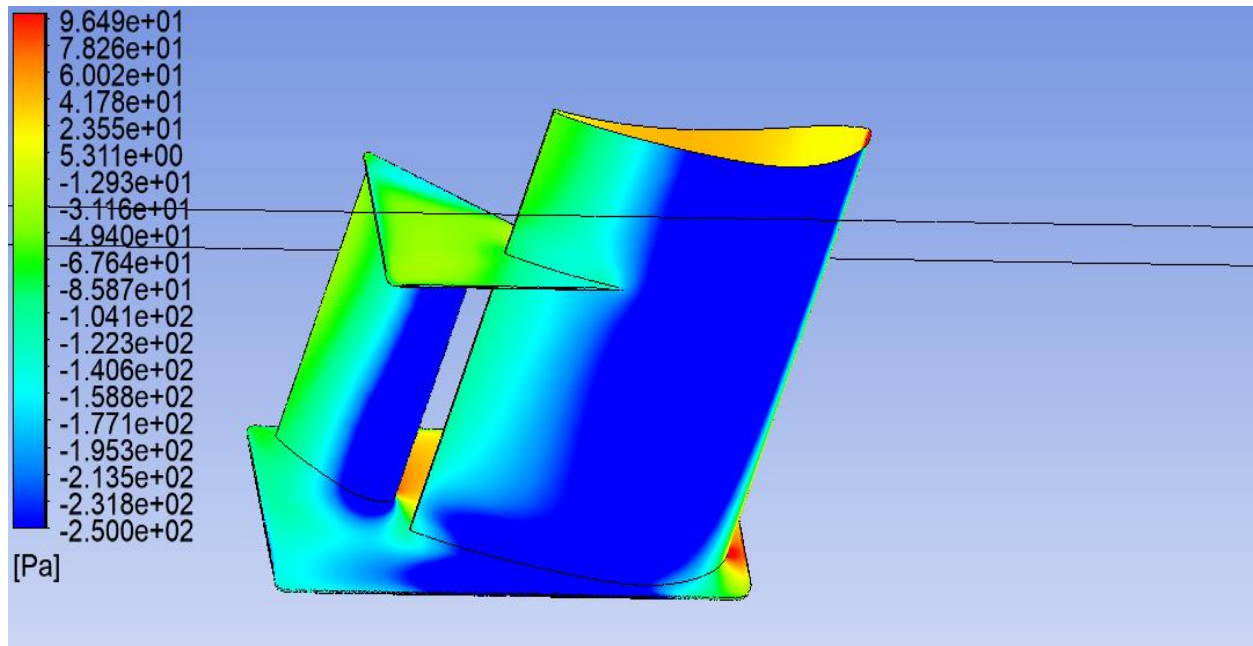


Figure 3.65 Velocity magnitude streamlines of the two-element configuration without endplates



**Figure 3.66** Velocity magnitude streamlines of the final assembly with endplates

The streamlines of the design without endplates and inner plates and the one without, do not alter significantly, as seen in Figure 3.65 and 3.66 above. The velocity and the path of the streamlines is almost identical, despite the difference in the coloring, as the legend remains in the same range. A flow separation is witnessed behind the assembly, which is mainly responsible for the increased value of the drag force, but as seen from the results, it is not negatively affecting the amount of downforce that is produced.



**Figure 3.67** Pressure contour of the final assembly

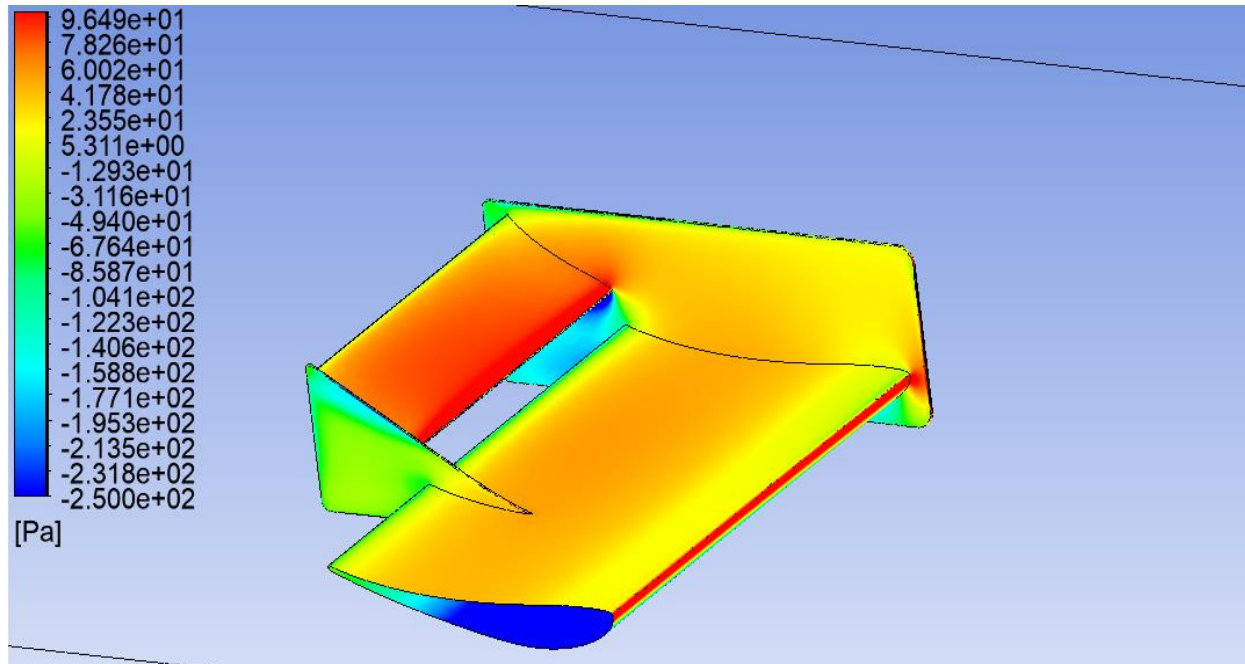


**Figure 3.68** Pressure contour of the final assembly

Lastly, it is visible from the pressure contours above, that the secondary element has significantly more pressure difference above and below it, compared to the main element. The maximum pressure is visible near the leading edge of the secondary element, where the accelerated airflow from the bottom of the main element reaches results in a low-pressure area. Although the secondary element presents more pressure differential above and below it, the main element produces more downforce as its surface is significantly larger than the surface of the flap.

### 3.7. FEA simulation results

The final results that must be presented relate to the static analysis that must be conducted, to ensure that the front wing assembly is able to withstand the forces that are set from the FSG regulations. The force that will be applied from the top of the assembly, equally distributed to  $225 \text{ cm}^2$  and its value is 200 N. In the following simulation, once the surfaces on the design of the wings are not divided into parts, it is difficult to apply the force in a small area of the airfoil, so an equally distributed force will be applied on all the assembly. To calculate the value of this force, the reference area of the assembly must be measured as seen from the direction of the force (top view) which is seen in Figure 3.69.

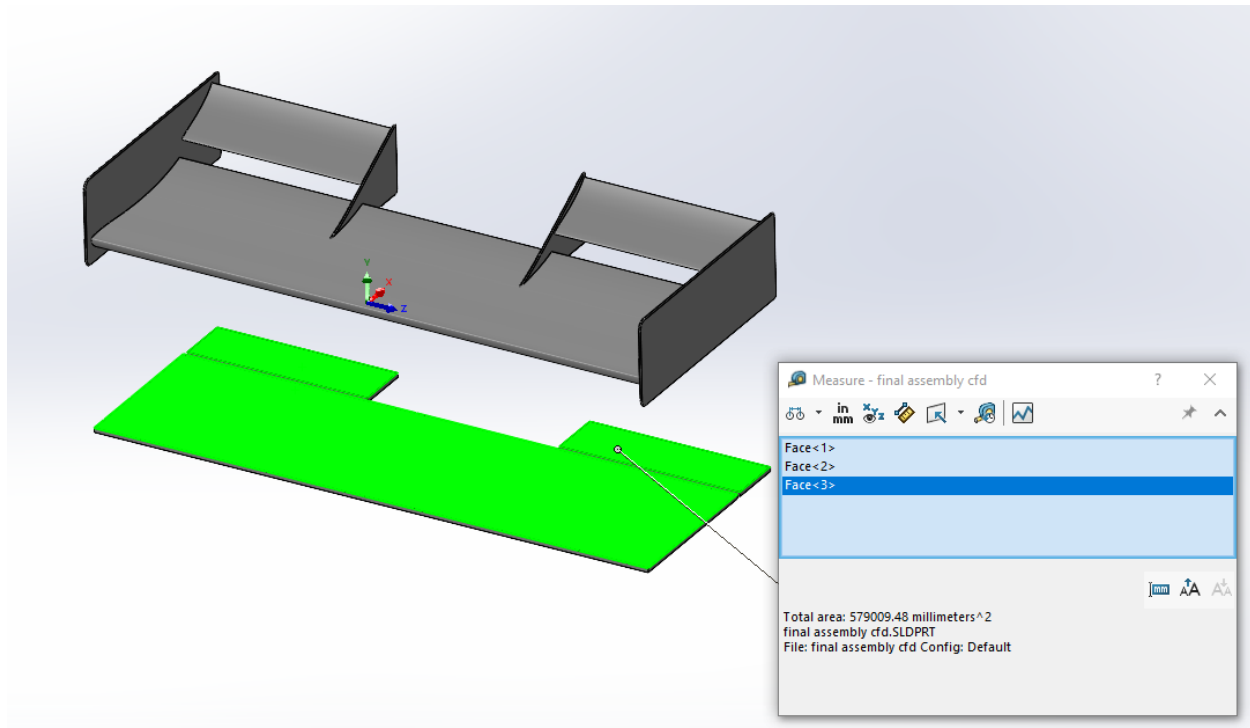


**Figure 3.69** Reference area of the front wing assembly

As seen in the figure above, the reference area of the front wing assembly is  $579,009.48 \text{ mm}^2$ , or  $5,790.1 \text{ cm}^2$ . Through simple calculations, it is found that the overall force that the whole assembly must withstand is equal to  $5,146.75 \text{ N}$  (once  $225 \text{ cm}^2$  of surface must withstand  $200 \text{ N}$ , then  $5,790.1 \text{ cm}^2$  must be able to withstand  $5,146.75 \text{ N}$  equally distributed). In order for the geometry to pass the inspection that is conducted prior to the competition, it must not deform more than  $10 \text{ mm}$  which is then reduced to  $6.5 \text{ mm}$  after the safety factor that was set in Chapter 2.4 which is equal to  $1.5$ . After the run of the simulation the result is presented Figure 3.70.

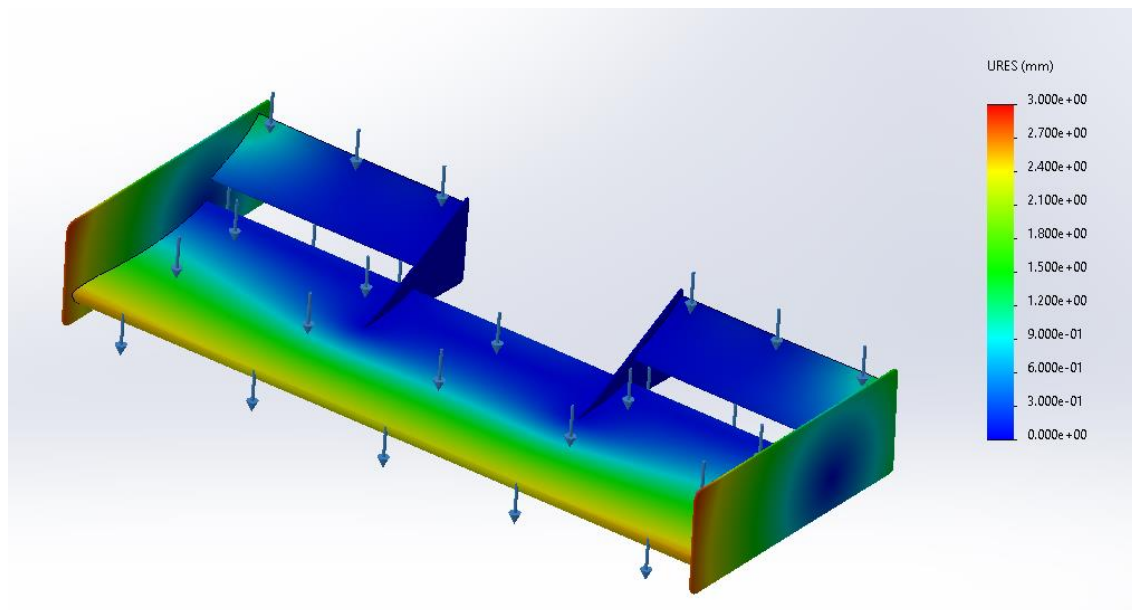


**Figure 3.70** Displacement of the geometry after the force application



In the figure above, it is visible that no part of the geometry exceeds a displacement of 3 mm, which is significantly less than the maximum acceptable value of 6.5 mm that is set. This means the geometry is within the range that is needed to pass the inspection of the competition. This means no changes in the material, thickness, or geometry in general must be made. To be more specific, maximum displacement is witnessed in the front of the main element and on the edges of its span, which equals to 2.87 mm. It is important, once again, to point out that this simulation is not conducted to check if the mountings of the assembly can withstand the overall force value which is 5,146.75 N. The simulation runtime was 1 minute and 34 seconds, which is significantly less than the time required for the CFD simulations, so this is the reason all the mesh settings were adjusted in order to achieve as much accurate results as possible in this FEA simulation.

It is understandable that maximum deformation is seen in the edges of the main elements profile and the front of the endplates, as the span of it is significantly larger than that of the secondary elements. Also, the mountings are put in the middle, which means the forces apply more torque in the edges due to the distance they have from the pivot point (the mountings in our case). Some teams that face problems with that kind of deformation add nerves that are attached to the endplate, to avoid this situation, as seen in Figure 3.71.

To sum up, the design of the front wing assembly in the context of this thesis does not require further support apart from the main mountings that are on the middle of the assembly and are attached to the nosecone or the bodywork.

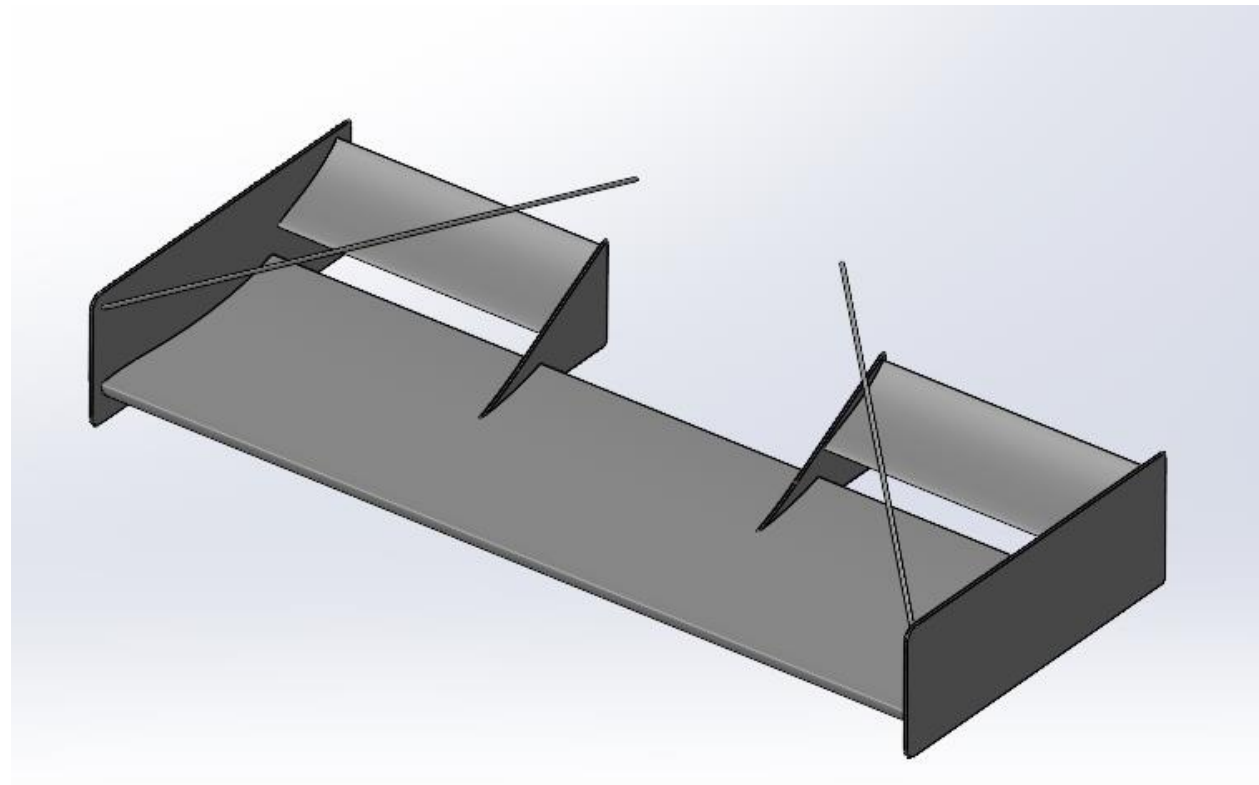


**Figure 3.71** Front wing assembly with nerves to prevent deformation on its edges

## 4. Conclusions and Future Study

### 4.1. CFD simulations conclusions

In Chapter 2.3, three sets of simulations were conducted to determine the mesh quality, the solving model and type of flow, that will be adapted to all the following simulations are done to extract the most efficient design for the front wing of the vehicle. Four different mesh qualities (coarse with 250,000 elements, moderate with 500,000 elements, fine with 1,000,000 elements, and very fine 2,000,000 elements) are tested in the same geometry (Selig 3021 at zero angle of attack), and the moderate one was judged to be the most appropriate considering the team's available computational power and time. Once the mesh was formed, a simulation set that will determine the solving model was done, and the outcome was that the k-epsilon solving model was superior compared to the other two governing models, k-omega standard, and k-omega SST. The last simulations showed that the flow can be assumed to be steady instead of transient, as both presented the same results, with the first one being significantly more time efficient than the second one.

As soon as the settings for the simulations were set, five different sets of CFD simulations were conducted to declare the most efficient design. The first set decided which of the airfoil profiles named S1223, S3021, S1210 and E423, present the best results considering the factors that were set to determine the most suitable geometry for this case. Once the Selig 1223 outperformed the others, it is the one that was chosen as the main element of the assembly at an angle of attack of  $3^\circ$  ( $C_L = -1.1$  and  $C_D = 0.042$ ). Secondary, this airfoil was placed in five different heights from the road, in order to decide in which position the ground effect that occurs is more powerful and affects positively the wing's performance. The outcome of this simulation set is that the appropriate height for the wing to be positioned is 50 mm above the road ( $C_L = -1.718$  and  $C_D = 0.109$ ). In the third simulation set, the Selig 1223 airfoil was used as a secondary element (flap) with a chord length equal to 40% of the main element's one, which is 144 mm. After the completion of this study, the flap was set to  $30^\circ$  angle of attack, where the wing showed its maximum potential ( $C_L = -3.665$  and  $C_D = 0.357$ ), while keeping drag at low levels. Another important parameter that was determined in the fourth and fifth set of simulations, is the vertical and horizontal distance between the two elements, and the most efficient ones are at 30 mm ( $C_L = -3.93$  and  $C_D = 0.384$ ) and 10 mm accordingly ( $C_L = -3.97$  and  $C_D = 0.369$ ). At last, the final design that was adjusted to the constraints that were set in the design process, was also simulated and the final lift coefficient  $C_L$  equals to -3.714 and the drag coefficient  $C_D$  is 0.513. After the necessary calculations, the final conclusion for the figures of interest is that Lift (L) and Drag (D) is equal to -290.3 N and 40.1 N accordingly. In figure 4.1 the streamlines around the front wing assembly in 3D view is presented to visualize the airflow around it, where the generation of vortices due to pressure difference is visible.

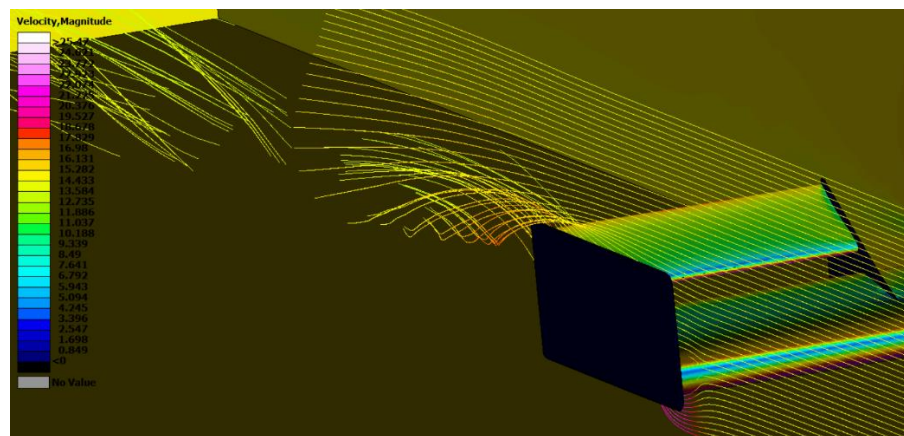


Figure 4.1 3D velocity magnitude streamlines of the final assembly



## 4.2. Design and manufacturing conclusions

This part of the conclusions relates to the process and outcomes of the design approach, as well as the FEA simulation that was conducted at the end of the study. First of all, the limitations of the competition's regulations were translated into bounding boxes and dimensions, in which the front wing assembly must stay within. The final span of the main element is 1305 mm, while the secondary element was split in two parts with a span of 430 mm, with a gap of 440 mm between them, in order for the nose cone to fit in. The chord length of the main element is 360 mm, while the secondary elements' chord is 144 mm. The final dimensions of the assembly are the following and presented in Figure 4.2:

1. Height:  $180 \pm 0.5$  mm
2. Width:  $1305 \pm 0.5$  mm
3. Length:  $545 \pm 0.5$  mm

The conclusions that can be made from the dimensions above is that height is almost at the limit of 185 mm that was set from the bounding boxes, while the other two dimensions are within range. The width is approximately 20 mm shorter than the limit, and the length is about 80 mm less than its limitation. Once the height is on the edge of the acceptable range, the manufacturing process by the team must be conducted with caution. Another observation is that there is no space for the secondary element to be placed higher than it is now, and its angle of attack cannot be increased either, which leads to the conclusion that the decisions that were made through the CFD simulation were on point. Furthermore, this configuration was decided to be a two-element configuration from the start of the study, which means, the elements' dimensions were determined to be larger than they would be in a three-element configuration. Lastly, the length of the assembly could be increased, meaning that the main and secondary elements would have larger chord length. This could result in higher production of downforce, as the surface of the airfoil increases.

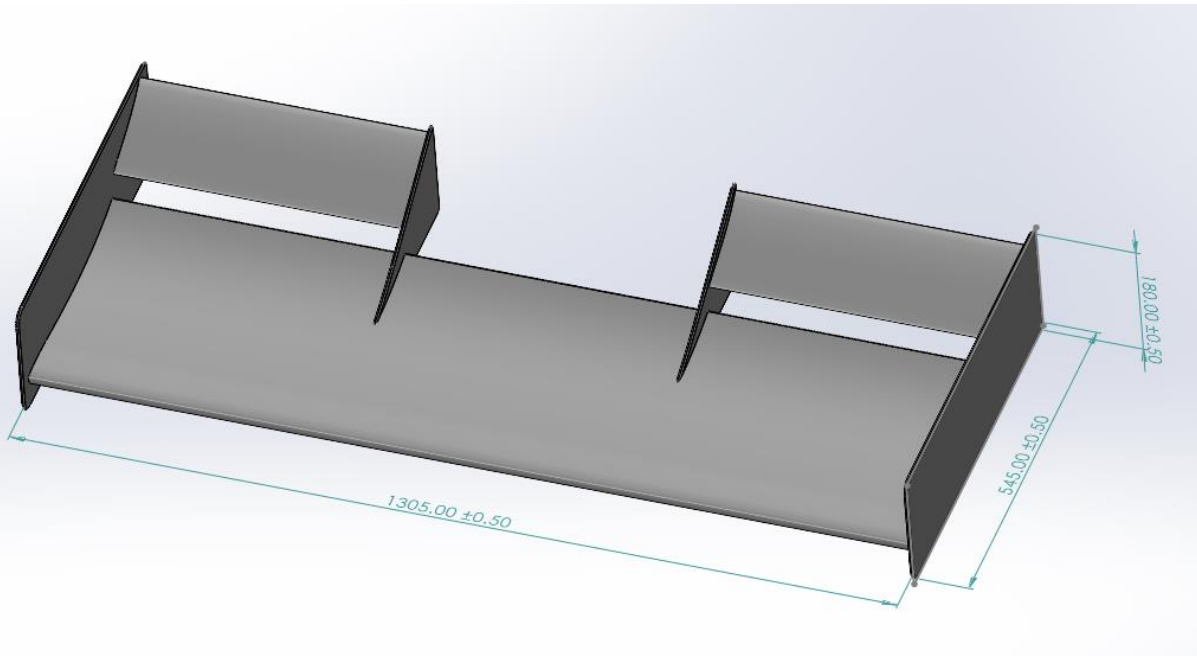


**Figure 4.2** Maximum dimensions of the front wing assembly in each axis

Although the design above, is withing regulations and optimized through CFD simulations, a redesign on the endplates is conducted for weight reduction, as the change that was made in its geometry does not affect the airflow's behaviour around the airfoils. The change in the geometry is one the front top corner where there is no interaction between the endplates and the elements, and its purpose is to reduce its weight, smoothen the flow above it, and enhance its appearance. Once it was decided from Chapter 3.7, the elements as well as the endplates are going to be manufactured by carbon fiber which is reinforced with epoxy, as the maximum deformation resulted from the FEA simulations was 2.87 mm which did not exceed the acceptable limitation of 6.5 mm, the overall design that results from the study of this thesis is presented in Figure 4.3. Finally, footplates (vortex tunnels) where added in the bottom of the airfoil as they are known to enhance the power of the vortices that are formed as explained earlier (Duran, 2022).

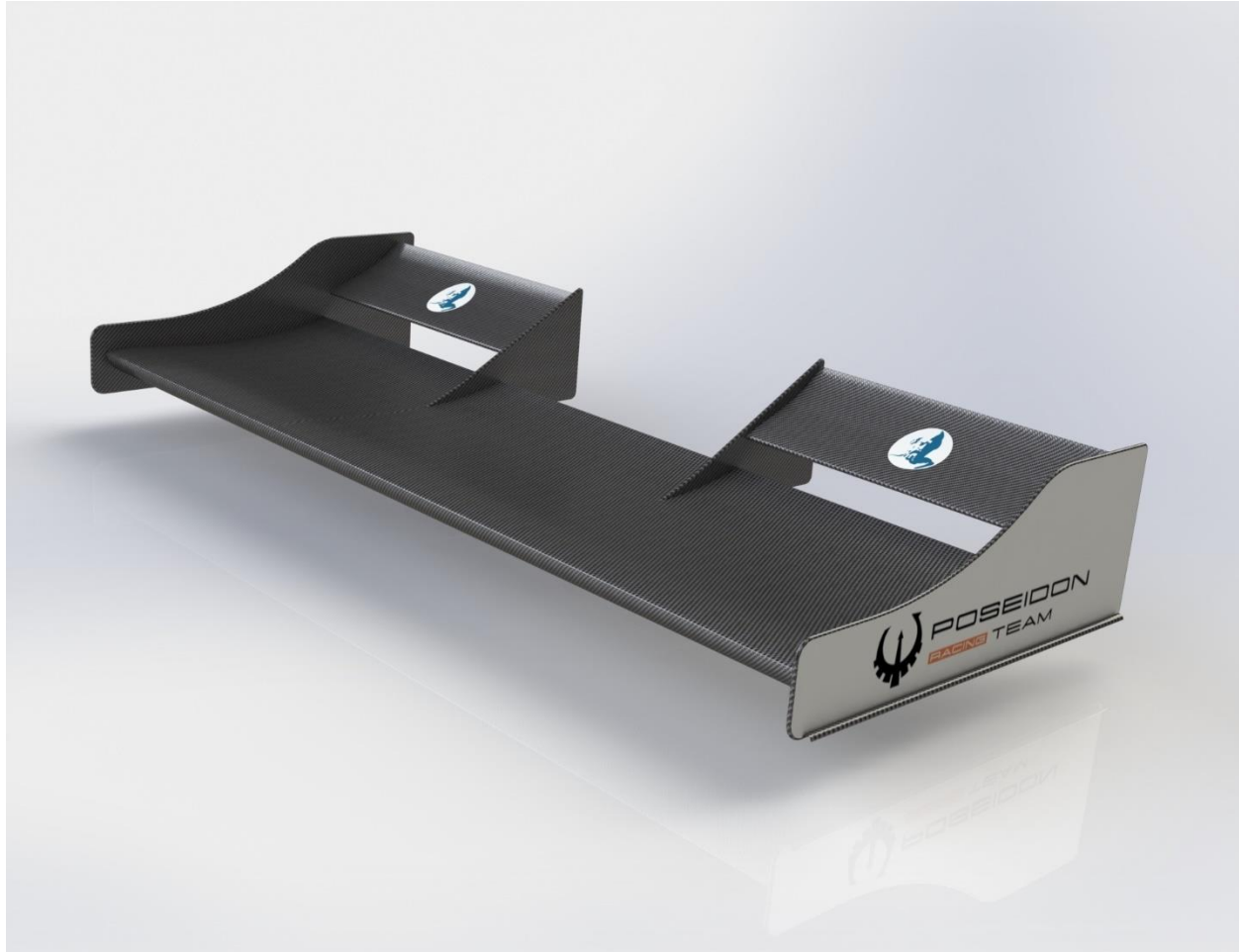


**Figure 4.3** Final design for the racing vehicle's front wing assembly of Poseidon Racing Team (UniWA)

### 4.3. Future study

The last chapter of this thesis is related to the future study that will be conducted in several parameters of this case, which may vary depending on the application. Once the diploma thesis is the first project that is being studied extensively from a student, there are a lot of variables that can be altered to improve the results of each application, which are still unknown when the researcher is in the first years



of his career. For this reason there is a list of things that will be further studied in detail, for the improvement of the work that is been done.

In this thesis, one main adjustment that could be made with the appropriate research, is the solving model that was used. It is known, as mentioned before, that k-omega standard is suitable when studying near wall flows, k-epsilon is appropriate for freestream flows, while k-omega SST is a combination of the two above. The fact that the k-omega standard and k-omega SST presented worse results than the k-epsilon solving model, needs further investigation as the flow around a complex geometry (like a front wing of a Formula Student racing vehicle), should need more accuracy near the walls as the boundary layers massively affect its behaviour. It is important to point out that k-omega standard and SST solving models require a finer mesh compared to the k-epsilon (Abd Halim et al., 2018), which plays a vital role in the outcome of this research. Once k-omega model is chosen, the quality of the mesh must be increased significantly in order to achieve reliable results, which is something that could not be done with the availability of the computational time and resources.

Another derivative that should be further studied is the number of elements of the configuration, which can be increased to three or maybe four elements. Once this is the first aerodynamic package of the team, the design and study had to remain simple and efficient, as every decision must be justified. The front wing has very strict height restrictions which makes three- and four-element front wings difficult to be designed and pass the inspection of the competitions. For this kind of research, more than one person is needed to conduct the study, as many wing profiles for each element must be tested in different angles of attack and the distances between the elements, as the way they interact with each other is significantly more complex than a two-element configuration.

Furthermore, there can be many redesigns in the assembly in order to maximize its performance, but every change must be justified through extensive research. Curvatures in the endplate or the main elements can be added, so that the airflow is guided efficiently. Regarding endplates, a small curvature can be made on their design, in order to guide the flow outside of the wheels that are known to produce the grater values of drag. Also, a step in the middle of the airfoil can be added to better guide the flow under the car by cooperating with the nose cone. An example of a design made for future plans that lacks detailed examination is shown in Figure 4.4.

Lastly, several sets of simulations must be conducted in later research that are called aero mapping. Aero mapping is conducted to present how the performance of the aerodynamic package of a vehicle (front wing in our case) alters when several factors change, such as dynamic road clearance and side forces at corners. There are a lot of variables that change when the vehicle accelerates and turns, as its center of pressure (COP) is constantly changing. In this study, the car was assumed to be moving at an average speed of 15 m/s, but its performance is different when the vehicle reaches speeds of 30 m/s or more, as the amount of downforce that is produced is dramatically greater, and so the car is pushed further to the road, which slightly alters the road clearance and thus, the values that were calculated in this study. Cornering of the vehicle results in change of direction of the forces that are applied to the configuration, and for this reason, several simulations at different angles of incoming air must be conducted (15°,30°,45° etc.), to evaluate how the performance of the front wing and the car in general changes.

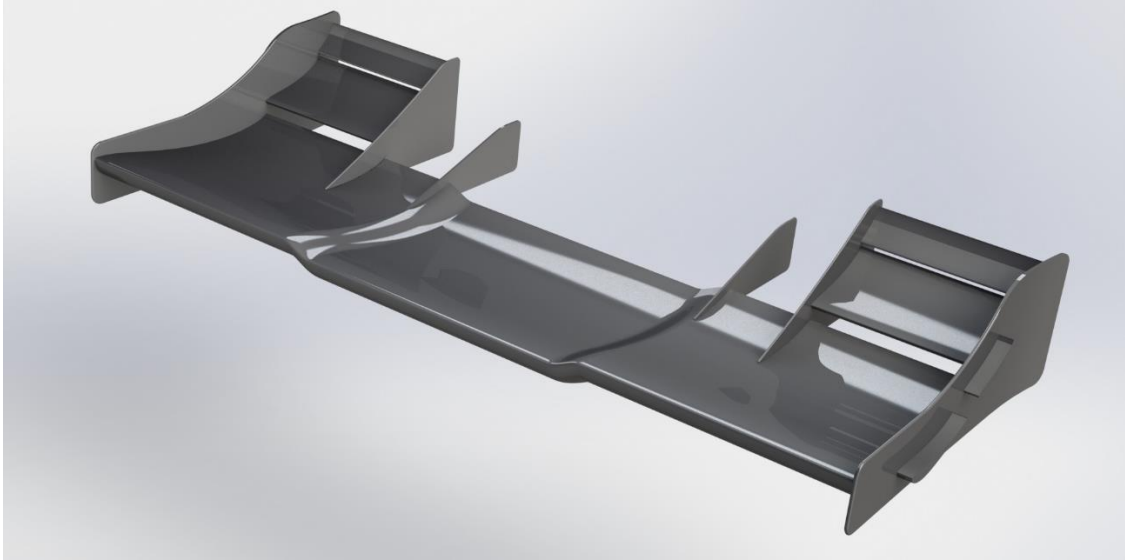


**Figure 4.4** Front wing assembly example for future reference

## References

- Abbott, I.H., Doenhoff, A.E. von, 1959. Theory of wing sections: including a summary of airfoil data, Correc. rep. of : McGraw-Hill Book, 1949. ed. Dover, New York.
- Abd Halim, M.A., Nik Mohd, N.A.R., Mohd Nasir, M.N., Dahalan, M.N., 2018. The Evaluation of  $k$ - $\epsilon$  and  $k$ - $\omega$  Turbulence Models in Modelling Flows and Performance of S-shaped Diffuser. *Int. J. Automot. Mech. Eng.* 15, 5161–5177. <https://doi.org/10.15282/ijame.15.2.2018.2.0399>
- Ahmed, M.R., Narayan, S., Zullah, M.A., Lee, Y.-H., 2011. Experimental and Numerical Studies on a Low Reynolds Number Airfoil for Wind Turbine Blades. *JFST* 6, 357–371. <https://doi.org/10.1299/jfst.6.357>
- Anderson, J.D., 2017. Fundamentals of aerodynamics, Sixth edition. ed, McGraw-Hill series in aeronautical and aerospace engineering. McGraw Hill Education, New York, NY.
- Ansys, 2006. Boundary Conditions.
- Apostolidis, A., Mattas, A., Gaitanis, A., 2019. AERODYNAMIC OPTIMIZATION OF A FORMULA STUDENT CAR.
- Baals, Donald D, 1981. Wind tunnels of NASA / Donald D. Baals and William R. Corliss.
- Barnard, R.H., 2001. Road vehicle aerodynamic design: an introduction, 2nd ed. ed. MechAero Publ, St. Albans.
- Blazek, K.-J. (Ed.), 2001. Computational fluid and solid mechanics: proceedings, First MIT Conference on Computational Fluid and Solid Mechanics, June 12-15, 2001, 1st ed. ed. Presented at the MIT Conference on Computational Fluid and Solid Mechanics, Elsevier, New York.
- Boccuzzi, N., Boland, C., Cain, A., Palmaccio, M., 2022. PSCC Formula SAE Aerodynamic Sub-Team.
- Burr, K.P., Akylas, T.R., Mei, C.C., n.d. CHAPTER TWO TWO-DIMENSIONAL LAMINAR BOUNDARY LAYERS.
- Castro, X., Rana, Z.A., 2020. Aerodynamic and Structural Design of a 2022 Formula One Front Wing Assembly. *Fluids* 5, 237. <https://doi.org/10.3390/fluids5040237>
- Cebeci, T. (Ed.), 2005. Computational fluid dynamics for engineers: from panel to Navier-Stokes methods with computer programs. Horizons Pub. Inc., ; Springer, Long Beach, Calif. : Berlin.
- Dahlberg, H., 2014. Aerodynamic development of Formula Student race car.
- Dhaneswar, P., Narayana, K.S., Brahmateja, P., Kumar, K.S., Dheeraj, B., 2021. CFD Analysis on Rear and Front Wings of FSAE Vehicle 8.
- Duran, I.N., 2022. STUDY OF THE AERODYNAMIC BEHAVIOUR OF A FORMULA 1 FRONT WING FOLLOWING THE 2022 TECHNICAL REGULATIONS. Univeristat Politecnica De Catalunya BarcelonaTech.
- Eckert, M., 2017. Ludwig Prandtl and the growth of fluid mechanics in Germany. *Comptes Rendus Mécanique* 345, 467–476. <https://doi.org/10.1016/j.crme.2017.05.005>
- FSG, F., 2023. FS-Rules\_2023.



- Ganesh Ram, R.K., Cooper, Y.N., Bhatia, V., Karthikeyan, R., Periasamy, C., 2014. Design Optimization and Analysis of NACA 0012 Airfoil Using Computational Fluid Dynamics and Genetic Algorithm. *AMM* 664, 111–116. <https://doi.org/10.4028/www.scientific.net/AMM.664.111>
- Grabis, M., Agarwal, R.K., 2019. Computational Fluid Dynamics Analysis of Inverted Multi-Element Airfoils in Ground Effect, in: *AIAA Scitech 2019 Forum*. Presented at the AIAA Scitech 2019 Forum, American Institute of Aeronautics and Astronautics, San Diego, California. <https://doi.org/10.2514/6.2019-1336>
- Hucho, W.-H., Ahmed, Syed R., Ahmed, Syed Rafeeq (Eds.), 1987. *Aerodynamics of road vehicles: from fluid mechanics to vehicle engineering*, 1. engl. Aufl. ed. Butterworths, London.
- IMechE, 2023. FORMULA STUDENT [WWW Document]. URL <https://www.imeche.org/events/formula-student>
- Kalinowski, M., Szczepanik, M., 2021. Aerodynamic shape optimization of racing car front wing. *IOP Conf. Ser.: Mater. Sci. Eng.* 1037, 012058. <https://doi.org/10.1088/1757-899X/1037/1/012058>
- Katz, J., 2003. Race Car Aerodynamics\_Designing for Speed. *Proceedings of the Institution of Mechanical Engineers, Part P: Journal of Sports Engineering and Technology* 235, 324–338. <https://doi.org/10.1177/1754337119893226>
- Katz, J., Plotkin, A., 1991. *Low-speed aerodynamics: from wing theory to panel methods*, McGraw-Hill series in aeronautical and aerospace engineering. McGraw-Hill, New York.
- Khalil, E.E., 2012. *CFD History and Applications* 4.
- Kuron, M., 2015. 3 Criteria for Assessing CFD Convergence. URL <https://www.engineering.com/story/3-criteria-for-assessing-cfd-convergence>
- Leishman, J.G., 2023. *Introduction to Aerospace Flight Vehicles*, 1st ed. Embry-Riddle Aeronautical University.
- Lu, S., Liu, J., Hekkenberg, R., 2021. Mesh Properties for RANS Simulations of Airfoil-Shaped Profiles: A Case Study of Rudder Hydrodynamics. *JMSE* 9, 1062. <https://doi.org/10.3390/jmse9101062>
- Macknight, N., 1998. *Technology of the F1 Car*. Hazleton Pub.
- Matweb, 2023. Overview of materials for Epoxy/Carbon Fiber Composite.
- McBeath, S., 2006. *Competition car aerodynamics*. Haynes Pub. ; Haynes North America, Sparkford, Yeovil, Somerset, UK : Newbury Park, Calif., USA.
- Nakayama, Y., 2018. Drag and Lift, in: *Introduction to Fluid Mechanics*. Elsevier, pp. 177–201. <https://doi.org/10.1016/B978-0-08-102437-9.00009-7>
- National Air and Space Museum, n.d. The Wright brothers.
- Oxyzoglou, I., 2017. Design & Development of an Aerodynamic Package for an FSAE Race Car. <https://doi.org/10.13140/RG.2.2.24595.37920/1>



- Park, K., Lee, J., 2008. Influence of endplate on aerodynamic characteristics of low-aspect-ratio wing in ground effect. *J Mech Sci Technol* 22, 2578–2589. <https://doi.org/10.1007/s12206-008-0805-y>
- Phersson, L., Carberry, J., Wordley, S., 2009. FORMULA SAE AERODYNAMIC PACKAGE; DESIGN, DEVELOPMENT AND VALIDATION.
- Pope, A., 2009. Basic Wing and Airfoil Theory. Dover Publications.
- Prasanth, A., Biswal, S., Gupta, A., Barodawala, A., 2016. Complete Design and Optimization of the Aerodynamics of a FSAE Car using Solid works.
- Raymer, D.P., 2018. Aircraft design: a conceptual approach, AIAA education series. American Institute of Aeronautics and Astronautics, Inc, Reston, VA.
- Rossis, K., Ageridis, G., Bergeles, G., 1993. Αεροδυναμική Αυτοκινήτου. NTUA, Athens.
- Sathyabama, 2022. Automotive Aerodynamics.
- Savliya, H., 2019. Nose Design for Formula Student Vehicle with Aerodynamic Components 9.
- Selig, M.S., Donovan, J.F., Fraser, D.B., 1989. Airfoils at Low Speeds.
- Seward, D., 2014. Race car design. Palgrave/Macmillan Education, London.
- Shehadi, M., 2021. Testing Ground-effect Aerodynamics on a Scaled F1 Car, in: 2021 ASEE Virtual Annual Conference Content Access Proceedings. Presented at the 2021 ASEE Virtual Annual Conference Content Access, ASEE Conferences, Virtual Conference, p. 36524. <https://doi.org/10.18260/1-2--36524>
- Shreyas Vaidya, Chinmay Kulkarni, Sinhgad Academy of Engineering, Pune, 2017. Aerodynamic Development of a Formula Sae Car: Initial Design Stage. *IJERT V6*, *IJERTV6IS120020*. <https://doi.org/10.17577/IJERTV6IS120020>
- Simscale, 2023. Incompressible Turbulent Airflow Around a Spoiler.
- UIUC Airfoil Data Site [WWW Document], n.d. URL [https://m-selig.ae.illinois.edu/ads/coord\\_database.html](https://m-selig.ae.illinois.edu/ads/coord_database.html) (accessed 9.16.23).
- Versteeg, H.K., Malalasekera, W., 2007. An introduction to computational fluid dynamics: the finite volume method, 2nd ed. ed. Pearson Education Ltd, Harlow, England ; New York.
- Wendt, J.F., Anderson, J.D., Von Karman Institute for Fluid Dynamics (Eds.), 2008. Computational fluid dynamics: an introduction, 3rd ed. ed. Springer, Berlin ; [London].
- White, F.M., 1999. Fluid mechanics, 4th ed. ed. McGraw-Hill, Boston.
- White, F.M., Xue, H., 2021. Fluid mechanics, Ninth edition. ed. McGraw-Hill, New York, NY.
- Williams, E., 2021. Engineering Fluid Mechanics.
- Witheridge, G., 2020. An Introduction to Race Car Aerodynamics, 1st ed. Catchments and Creeks Pty Ltd, Bargara, Queensland.



Wordley, S., Saunders, J., 2006. Aerodynamics for Formula SAE: Initial Design and Performance Prediction. Presented at the SAE 2006 World Congress & Exhibition, p. 10. <https://doi.org/10.4271/2006-01-0806>

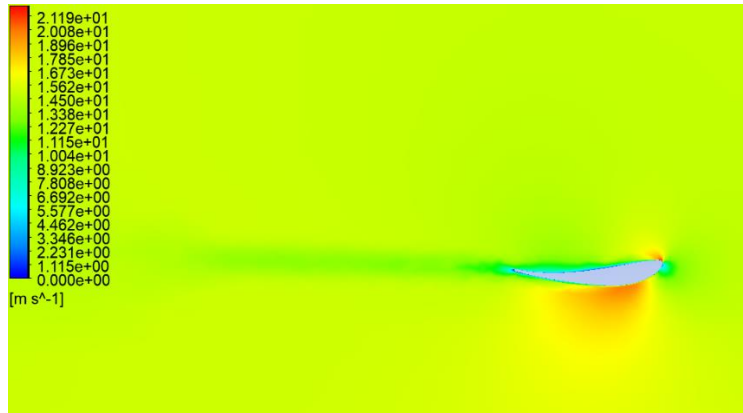
Wu, J.-D., Liu, J.-C., 2011. Development of a predictive system for car fuel consumption using an artificial neural network. *Expert Systems with Applications* 38, 4967–4971. <https://doi.org/10.1016/j.eswa.2010.09.155>



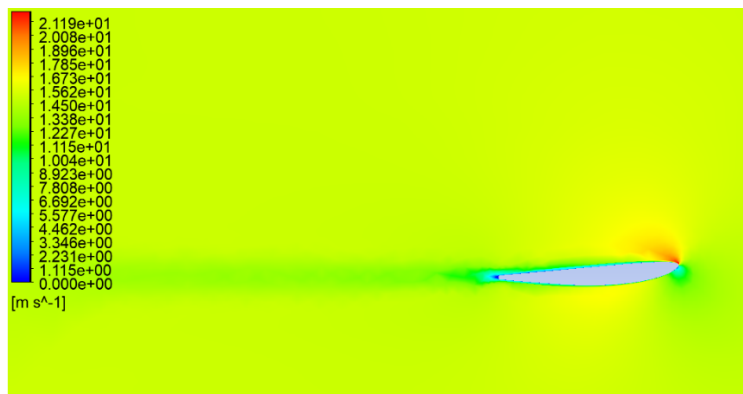
## Appendix A

### A.1 Velocity and pressure contours of Selig 1223, Selig 3021, Selig 1210 and Eppler 423 at $-3^\circ$ , $0^\circ$ and $9^\circ$ AOA

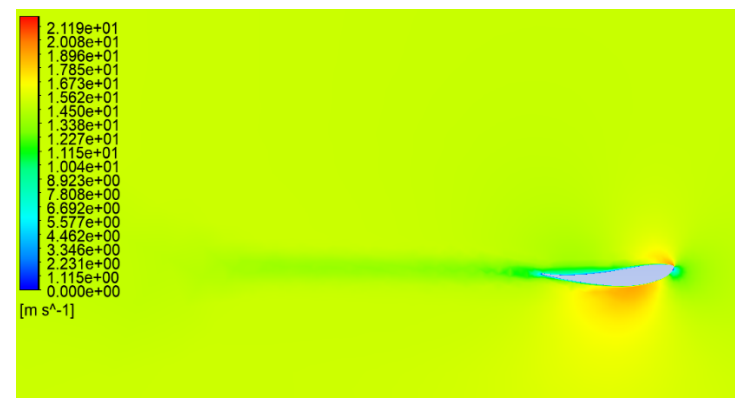
- S1213 at  $-3^\circ$  AOA – Velocity contour



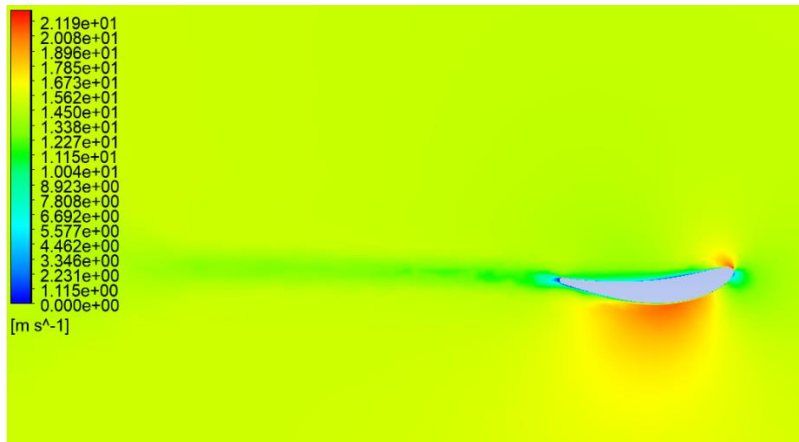
- S3021 at  $-3^\circ$  AOA – Velocity contour



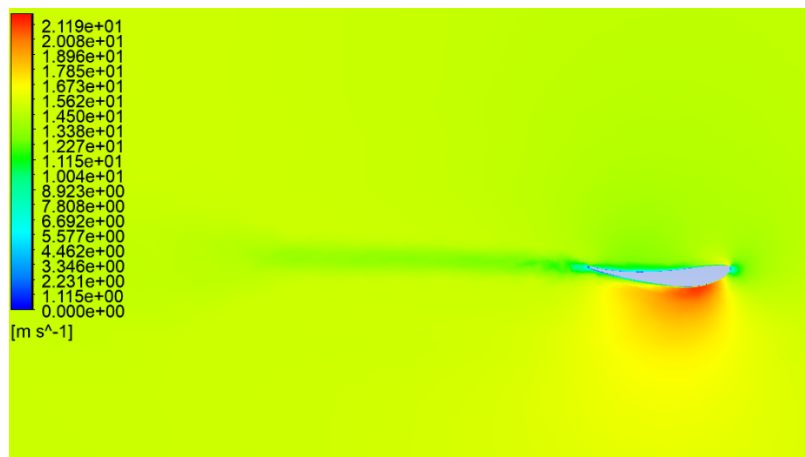
- S1210 at  $-3^\circ$  AOA – Velocity contour



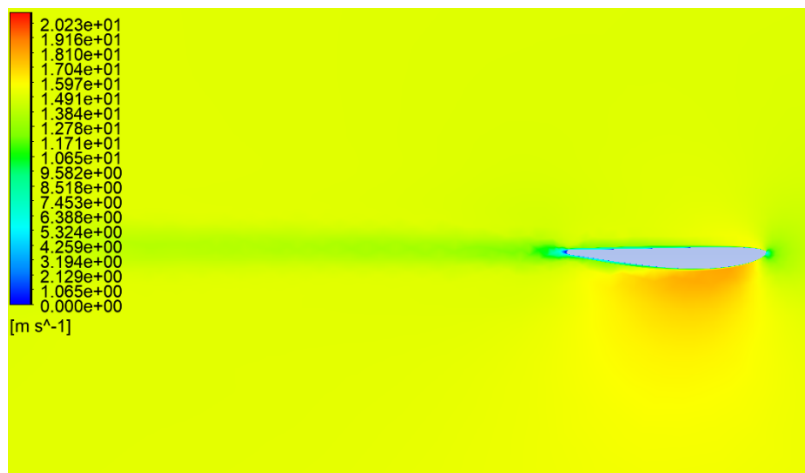
- E423 at  $-3^\circ$  AOA – Velocity contour



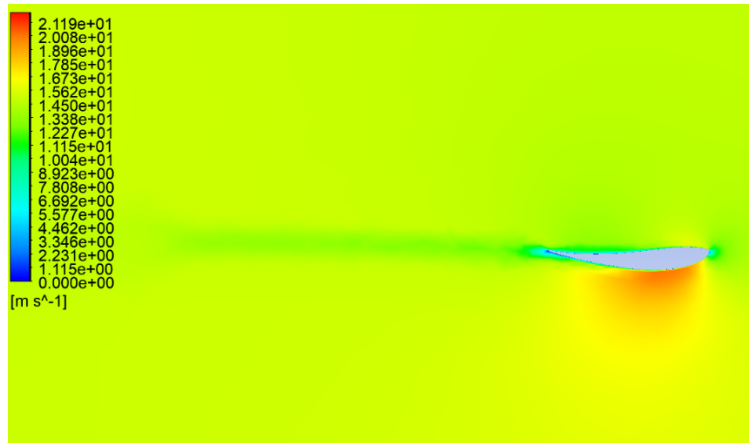
- S1213 at  $0^\circ$  AOA – Velocity contour



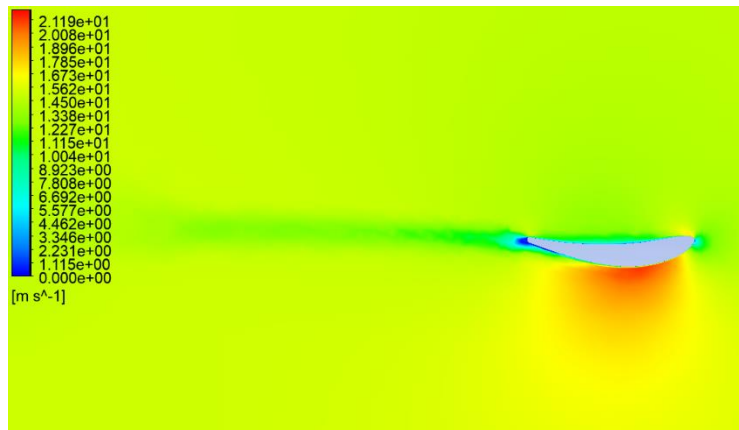
- S3021 at  $0^\circ$  AOA – Velocity contour



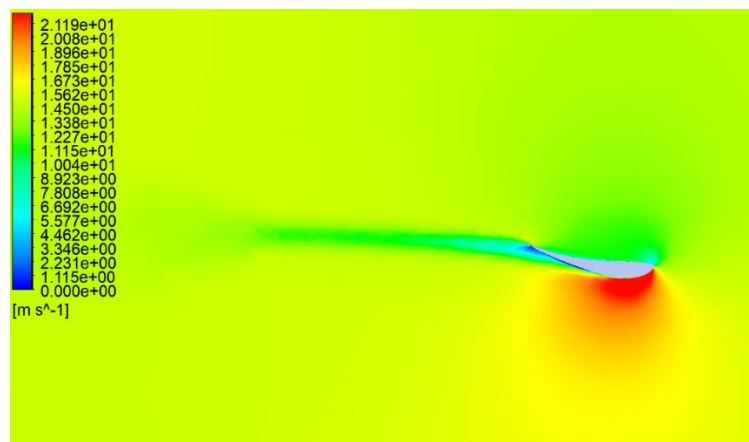
- S1210 at 0° AOA – Velocity contour



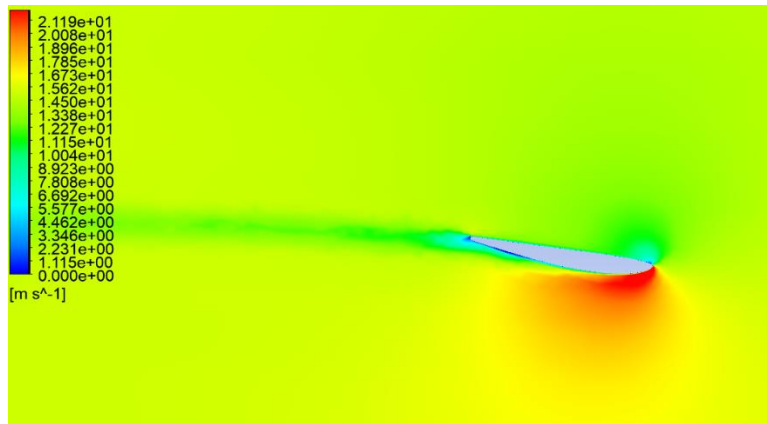
- E423 at 0° AOA – Velocity contour



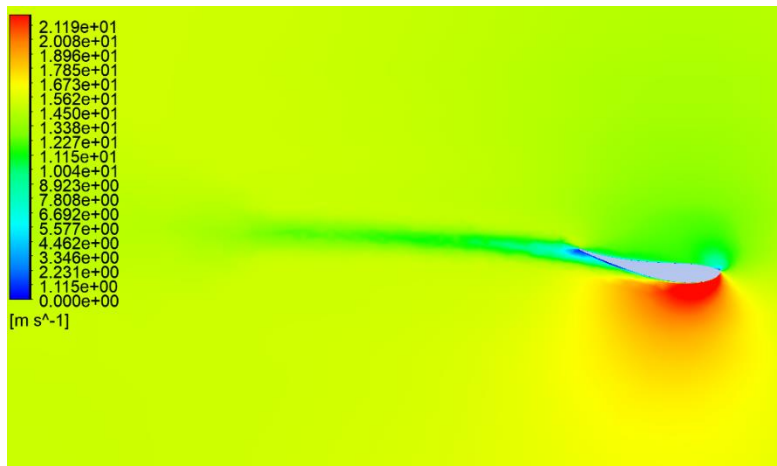
- S1223 at 9° AOA – Velocity contour



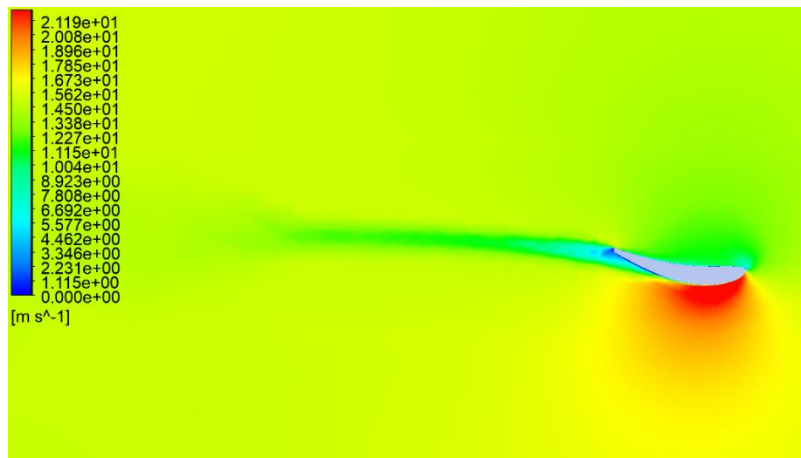
- S3021 at 9° AOA – Velocity contour



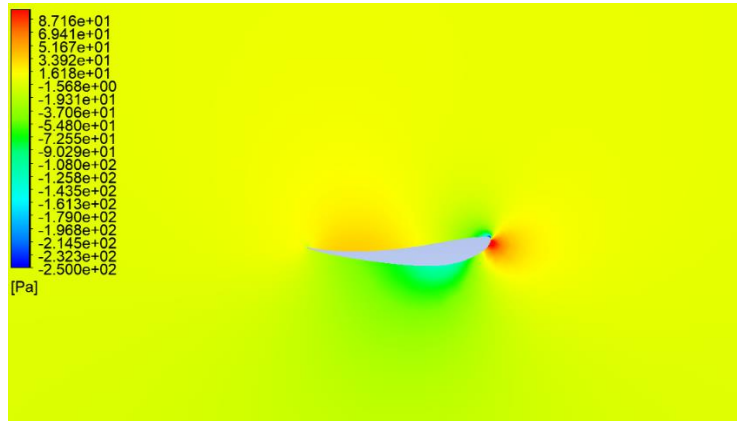
- S1210 at 9° AOA – Velocity contour



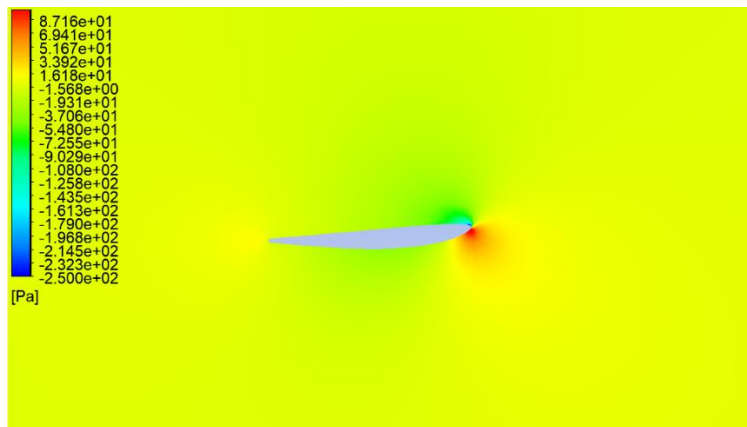
- E423 at 9° AOA – Velocity contour



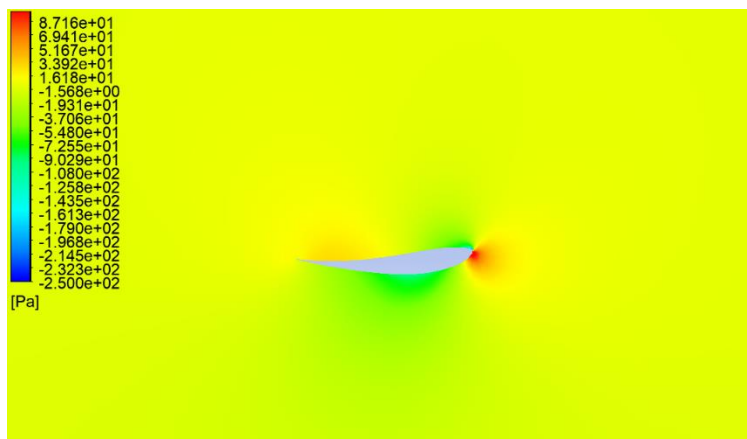
- S1213 at  $-3^\circ$  AOA – Pressure contour



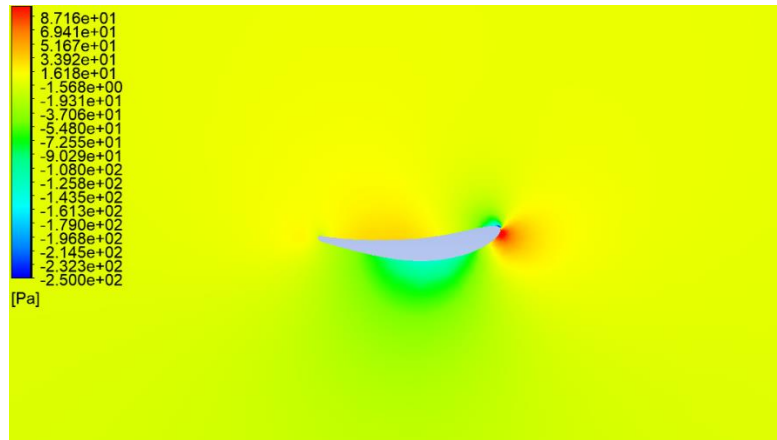
- S3021 at  $-3^\circ$  AOA – Pressure contour



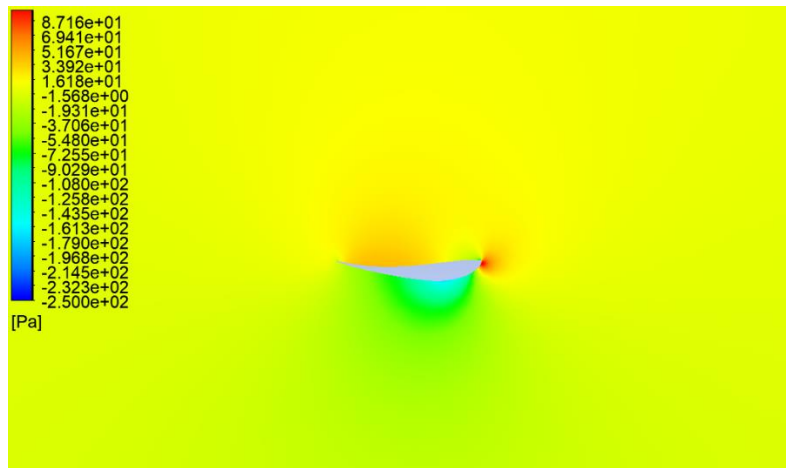
- S1210 at  $-3^\circ$  AOA – Pressure contour



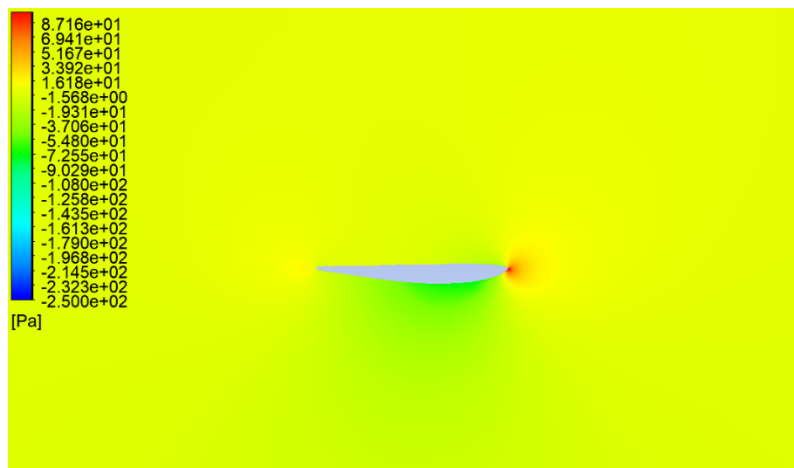
- E423 at  $-3^\circ$  AOA – Pressure contour



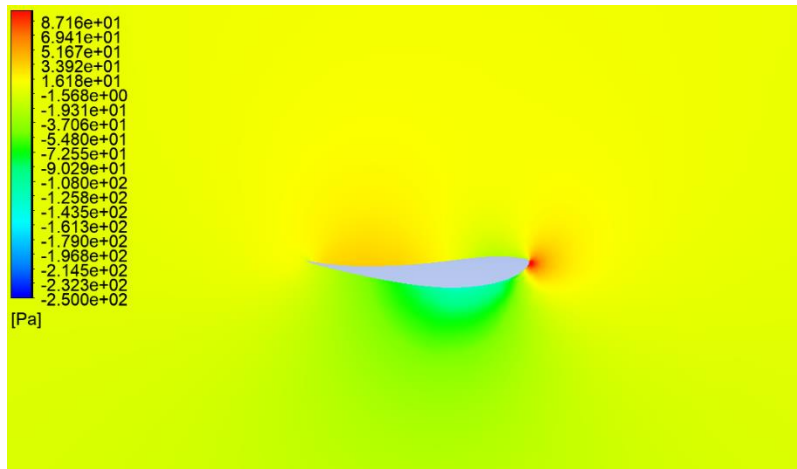
- S1213 at  $0^\circ$  AOA – Pressure contour



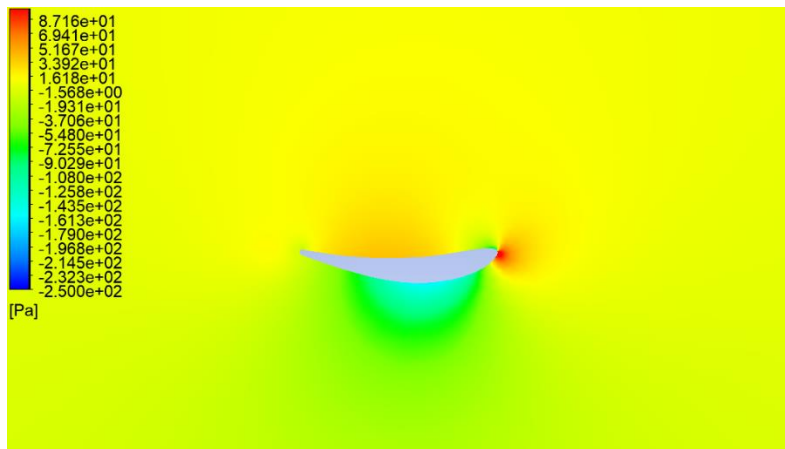
- S3021 at  $0^\circ$  AOA – Pressure contour



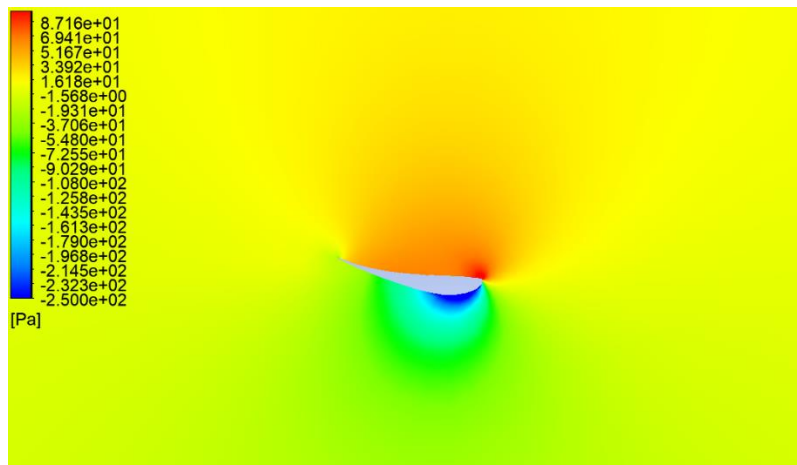
- S1210 at 0° AOA – Pressure contour



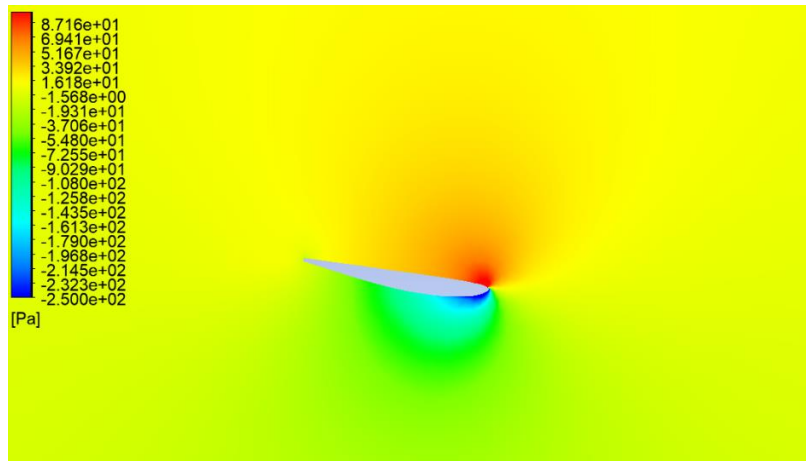
- E423 at 0° AOA – Pressure contour



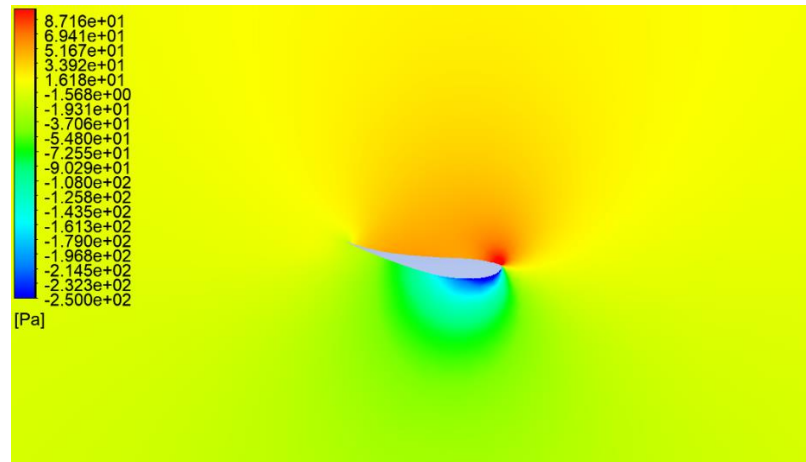
- S1223at 9° AOA – Pressure contour



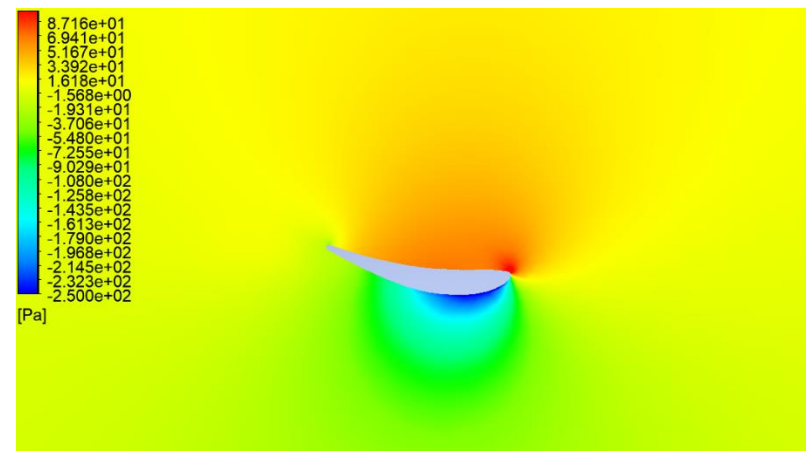
- S3021at 9° AOA – Pressure contour



- S1210at 9° AOA – Pressure contour



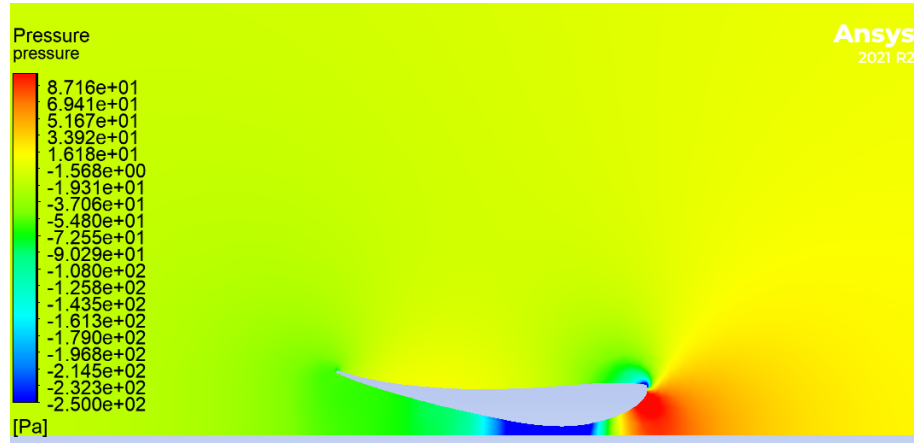
- E423at 9° AOA – Pressure contour



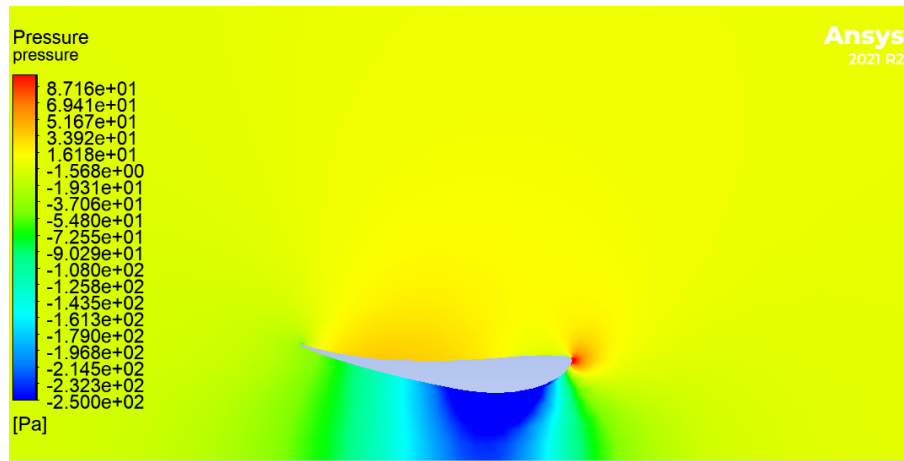


## A.2 Pressure contours of Selig 1223 at 3° AOA for $h_1=10$ mm and $h_1=90$ mm

- Selig 1223 at 3° AOA for  $h_1=10$  mm

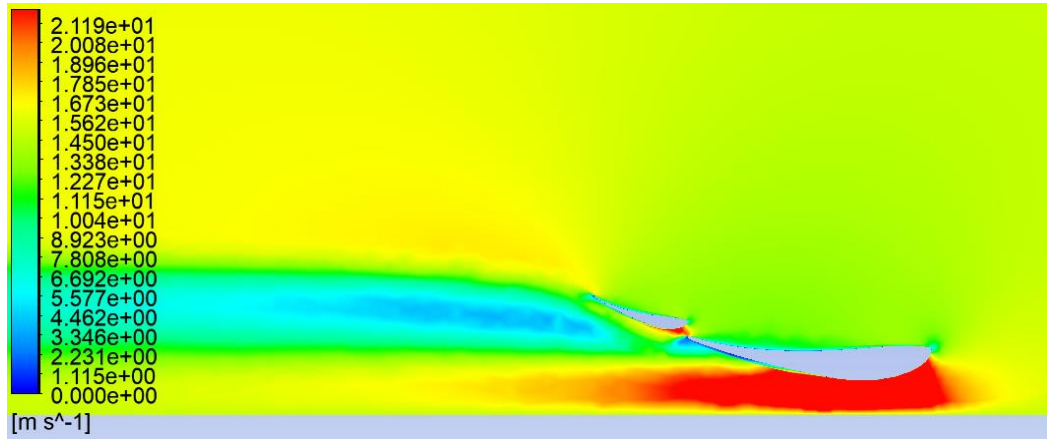


- Selig 1223 at 3° AOA for  $h_1=90$  mm

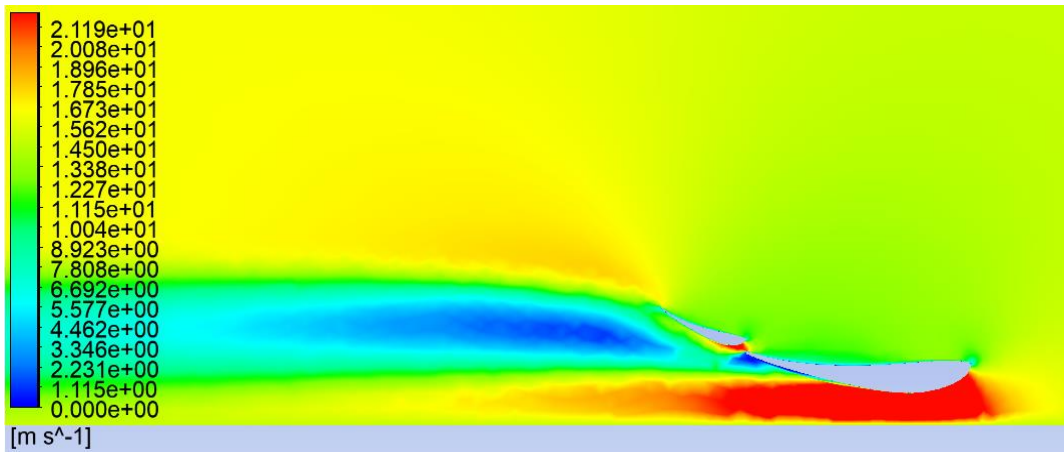


### A.3 Velocity and pressure contours of Selig 1223 (flap) at 15°, 20° and 45° AOA

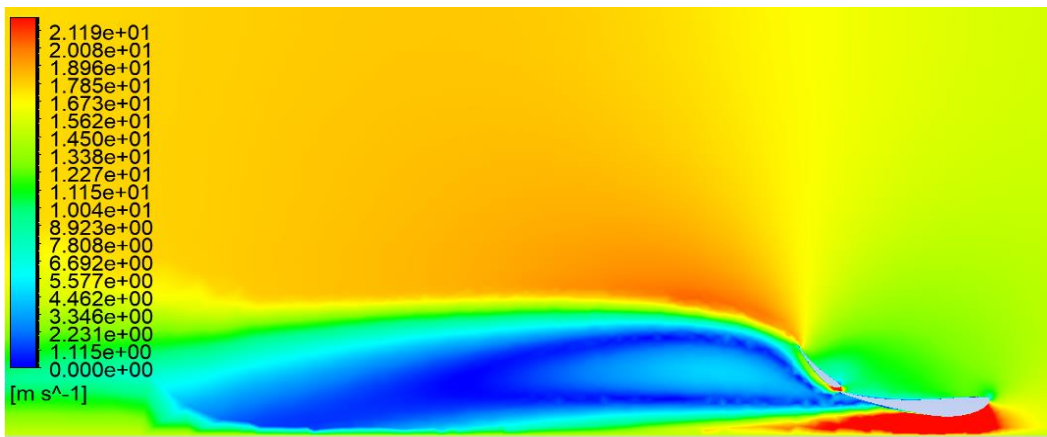
- S1223 (flap) at 15° AOA – Velocity contour



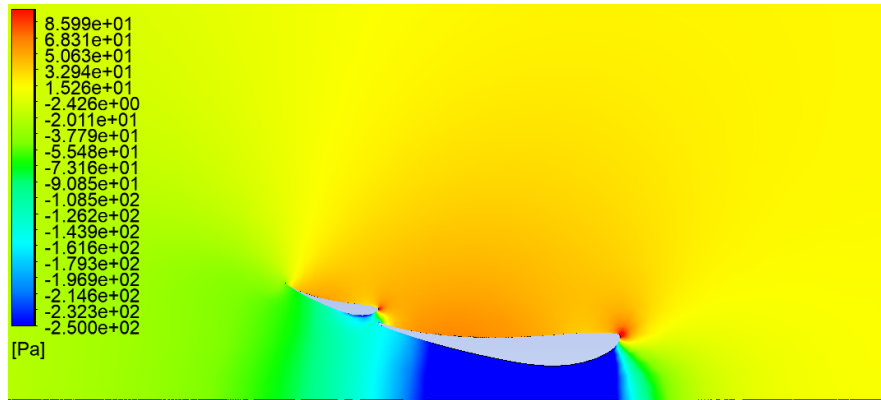
- S1223 (flap) at 20° AOA – Velocity contour



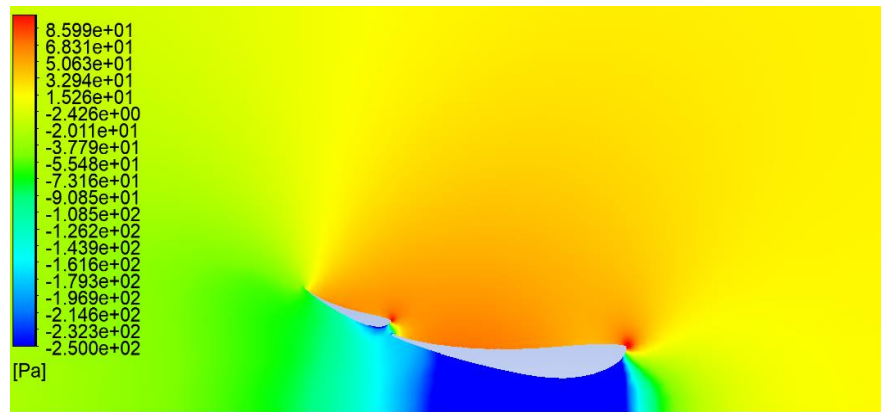
- S1223 (flap) at 45° AOA – Velocity contour



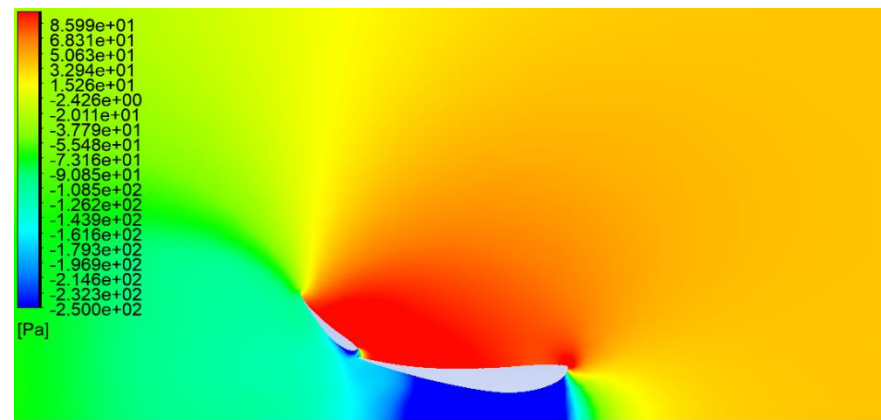
- S1223 (flap) at 15° AOA – Pressure contour



- S1223 (flap) at 20° AOA – Pressure contour

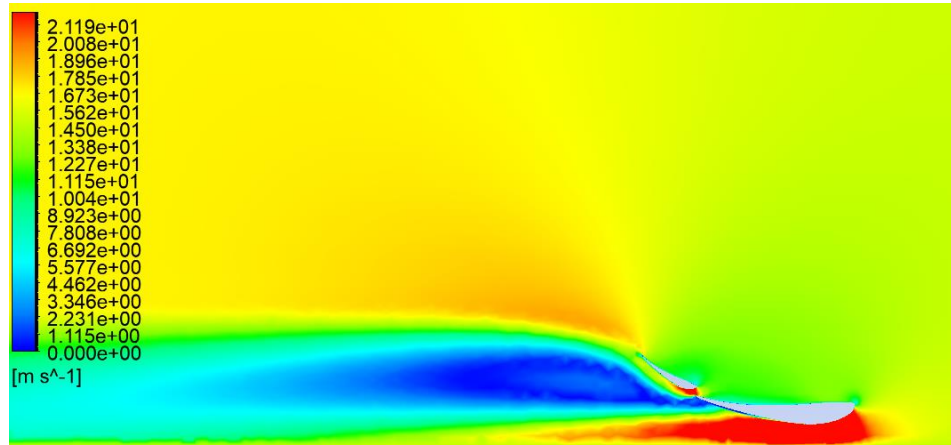


- S1223 (flap) at 45° AOA – Pressure contour

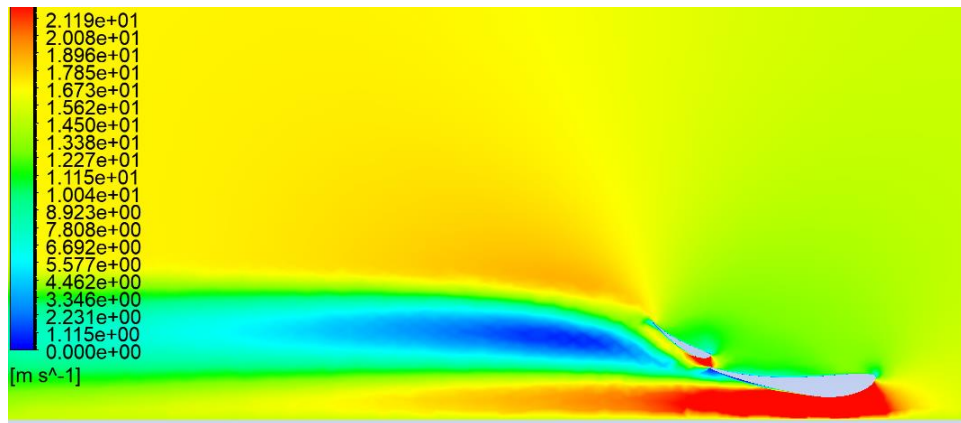


### A.4 Velocity and pressure contours of vertical distance $h_2=15$ mm and $h_2= 20$ mm

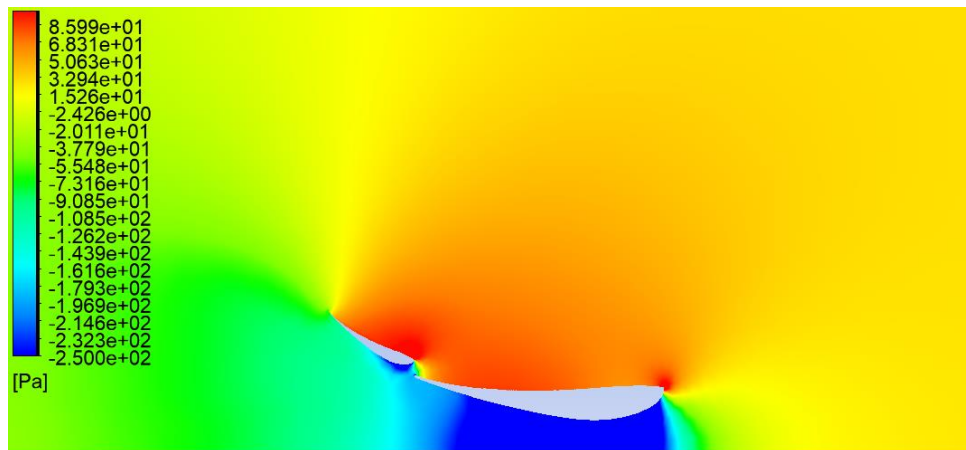
- Vertical distance  $h_2= 15$  mm – Velocity contour



- Vertical distance  $h_2= 20$  mm – Velocity contour

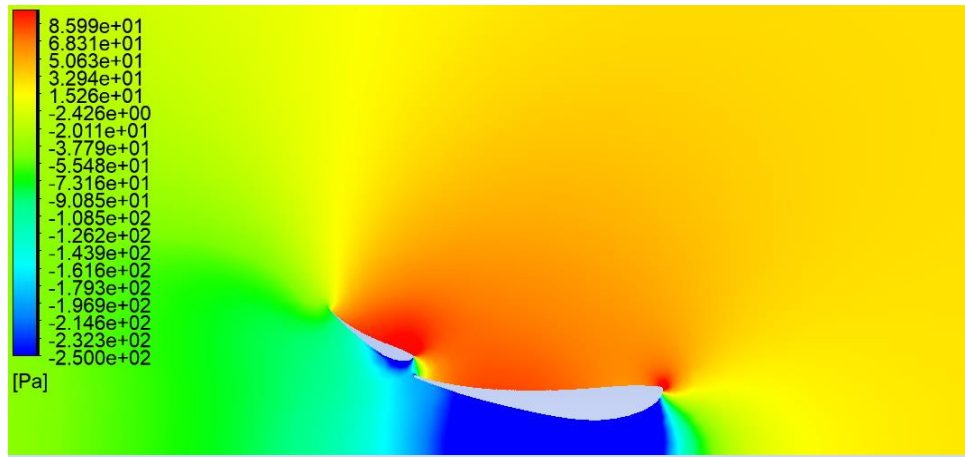


- Vertical distance  $h_2= 15$  mm – Pressure contour



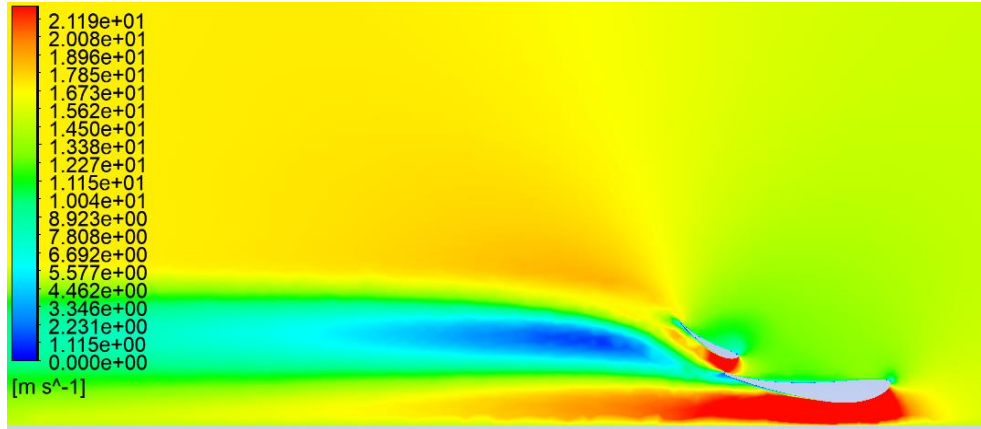


- Vertical distance  $h_2 = 20$  mm – Pressure contour

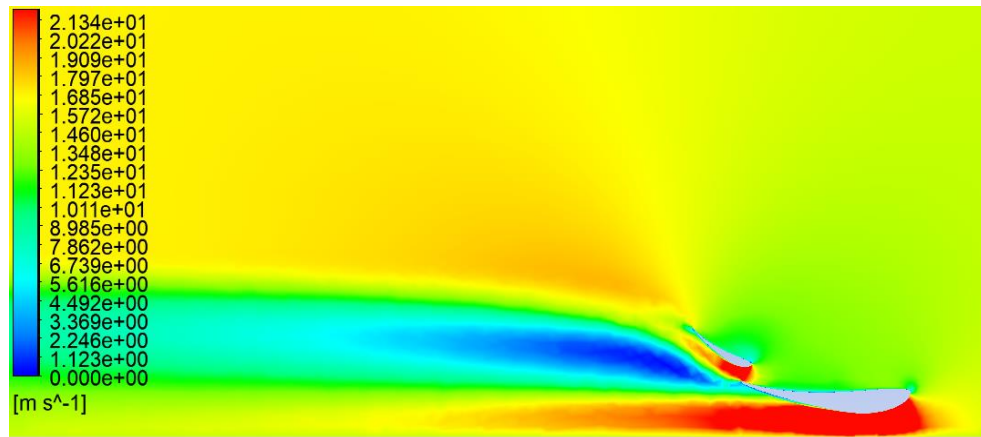


**A.5 Velocity and pressure contours of horizontal distance  $h_3=-30$  mm,  $h_3=-20$  mm,  $h_3=-10$  mm,  $h_3=10$  mm,  $h_3=20$  mm and  $h_3=30$  mm**

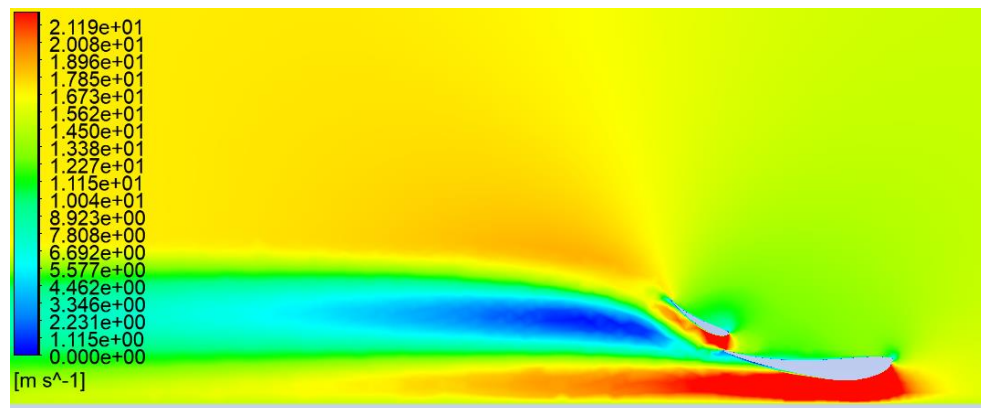
- Vertical distance  $h_3 = -30$  mm – Velocity contour



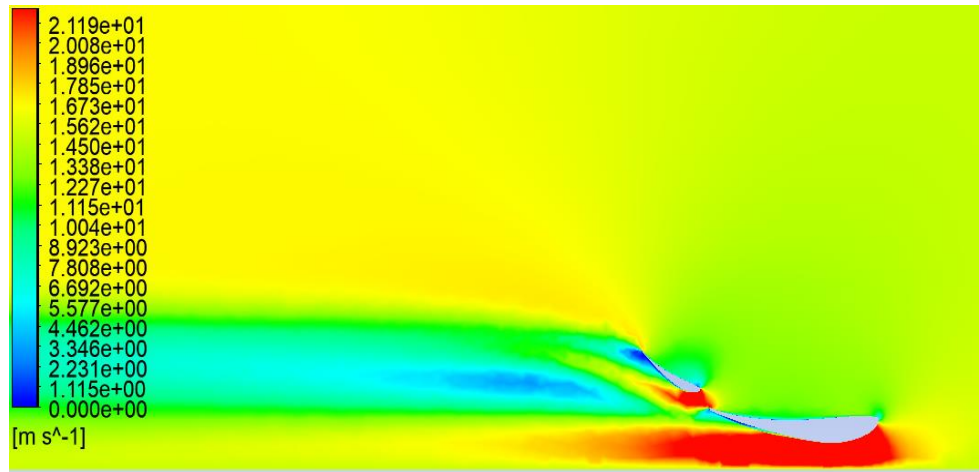
- Vertical distance  $h_3 = -20$  mm – Velocity contour



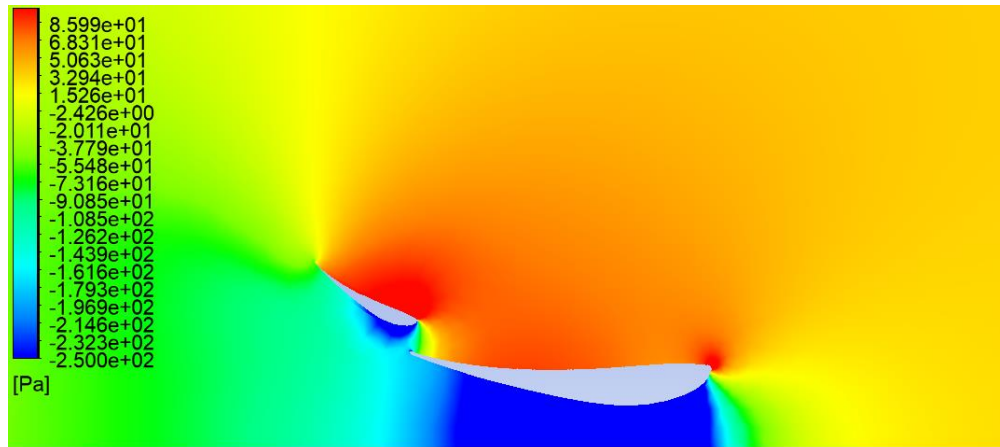
- Vertical distance  $h_3 = -10$  mm – Velocity contour



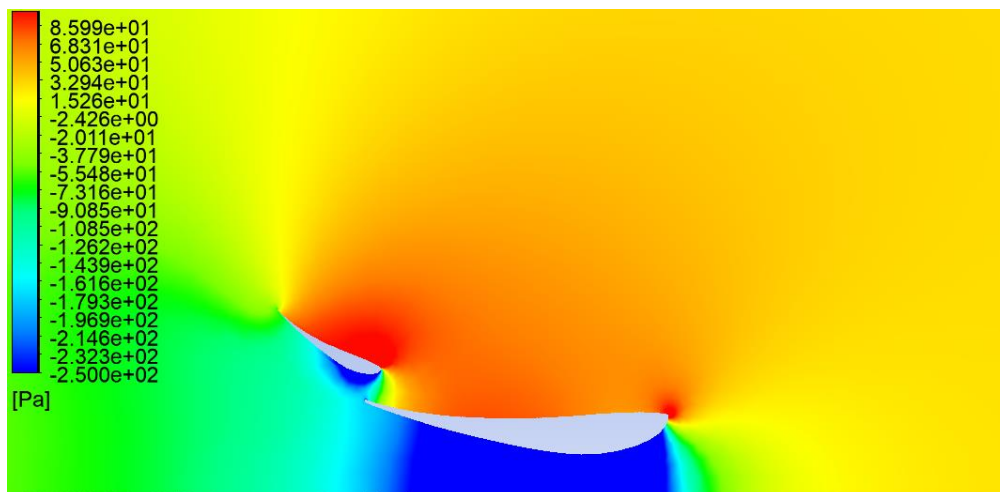
- Vertical distance  $h_3 = 30$  mm – Velocity contour



- Vertical distance  $h_3 = -30$  mm – Pressure contour

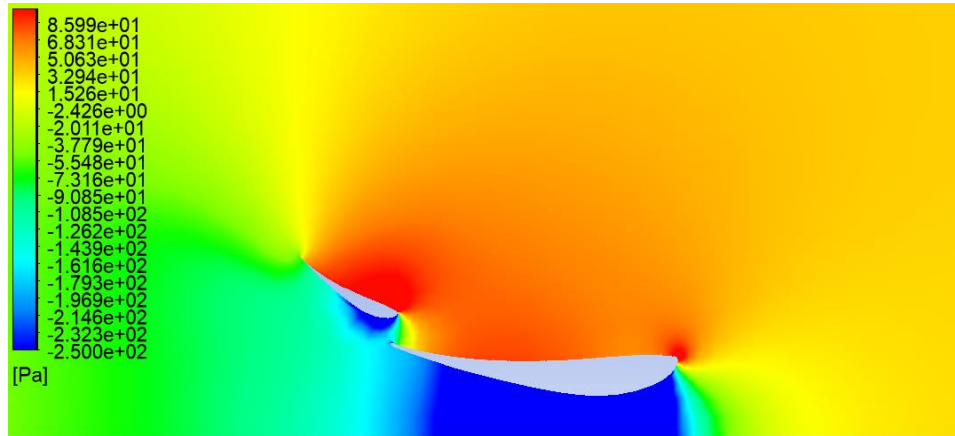


- Vertical distance  $h_3 = -20$  mm – Pressure contour

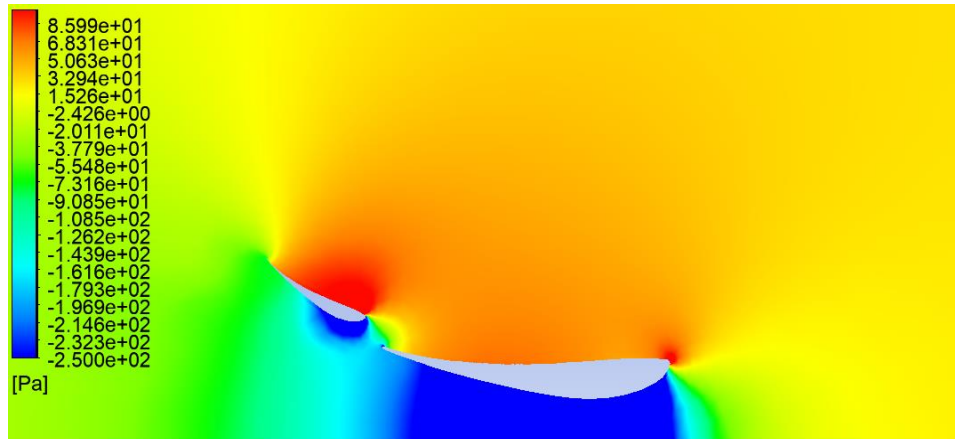




- Vertical distance  $h_3 = -10$  mm – Pressure contour



- Vertical distance  $h_3 = 30$  mm – Pressure contour







## Appendix B

In this appendix presents the coordinates ("UIUC Airfoil Data Site," n.d.) of the four airfoil profiles that were studied.

### B.1 Selig 1223 coordinates

X	Y
1.00000	0.00000
0.99838	0.00126
0.99417	0.00494
0.98825	0.01037
0.98075	0.01646
0.97111	0.02250
0.95884	0.02853
0.94389	0.03476
0.92639	0.04116
0.90641	0.04768
0.88406	0.05427
0.85947	0.06089
0.83277	0.06749
0.80412	0.07402
0.77369	0.08044
0.74166	0.08671
0.70823	0.09277
0.67360	0.09859
0.63798	0.10412
0.60158	0.10935
0.56465	0.11425
0.52744	0.11881
0.49025	0.12303
0.45340	0.12683
0.41721	0.13011
0.38193	0.13271
0.34777	0.13447
0.31488	0.13526
0.28347	0.13505
0.25370	0.13346
0.22541	0.13037
0.19846	0.12594
0.17286	0.12026
0.14863	0.11355
0.12591	0.10598
0.10482	0.09770
0.08545	0.08879
0.06789	0.07940
0.05223	0.06965



0.03855	0.05968
0.02694	0.04966
0.01755	0.03961
0.01028	0.02954
0.00495	0.01969
0.00155	0.01033
0.00005	0.00178
0.00044	-0.00561
0.00264	-0.01120
0.00789	-0.01427
0.01718	-0.01550
0.03006	-0.01584
0.04627	-0.01532
0.06561	-0.01404
0.08787	-0.01202
0.11282	-0.00925
0.14020	-0.00563
0.17006	-0.00075
0.20278	0.00535
0.23840	0.01213
0.27673	0.01928
0.31750	0.02652
0.36044	0.03358
0.40519	0.04021
0.45139	0.04618
0.49860	0.05129
0.54639	0.05534
0.59428	0.05820
0.64176	0.05976
0.68832	0.05994
0.73344	0.05872
0.77660	0.05612
0.81729	0.05219
0.85500	0.04706
0.88928	0.04088
0.91966	0.03387
0.94573	0.02624
0.96693	0.01822
0.98255	0.01060
0.99268	0.00468
0.99825	0.00115
1.00000	0.00000



## B.2 Selig 1210 coordinates

X	Y
1.00000	0.00000
0.99837	0.00101
0.99398	0.00397
0.98753	0.00832
0.97908	0.01317
0.96811	0.01811
0.95437	0.02328
0.93796	0.02874
0.91898	0.03443
0.89754	0.04032
0.87376	0.04637
0.84779	0.05254
0.81980	0.05879
0.78997	0.06506
0.75851	0.07130
0.72561	0.07747
0.69151	0.08349
0.65642	0.08932
0.62058	0.09490
0.58423	0.10016
0.54763	0.10505
0.51105	0.10948
0.47473	0.11335
0.43891	0.11653
0.40378	0.11892
0.36955	0.12046
0.33652	0.12091
0.30456	0.12000
0.27347	0.11784
0.24341	0.11462
0.21445	0.11047
0.18681	0.10556
0.16069	0.09994
0.13622	0.09362
0.11351	0.08672
0.09269	0.07932
0.07388	0.07149
0.05719	0.06332
0.04282	0.05484
0.03068	0.04593
0.02054	0.03672
0.01239	0.02755
0.00626	0.01866
0.00217	0.01030



0.00016	0.00277
0.00023	-0.00345
0.00337	-0.00773
0.01034	-0.01070
0.02071	-0.01324
0.03417	-0.01529
0.05052	-0.01685
0.06959	-0.01786
0.09118	-0.01830
0.11512	-0.01810
0.14119	-0.01715
0.16911	-0.01524
0.19906	-0.01183
0.23157	-0.00697
0.26670	-0.00124
0.30427	0.00504
0.34404	0.01158
0.38575	0.01814
0.42909	0.02446
0.47370	0.03032
0.51919	0.03551
0.56515	0.03986
0.61113	0.04320
0.65666	0.04543
0.70127	0.04646
0.74446	0.04625
0.78575	0.04479
0.82465	0.04214
0.86071	0.03837
0.89349	0.03364
0.92255	0.02809
0.94754	0.02192
0.96791	0.01530
0.98299	0.00890
0.99284	0.00390
0.99828	0.00095
1.00000	0.00000

### B.3 Selig 3021 coordinates

X	Y
1.00000	0.00000
0.99663	0.00039
0.98679	0.00172
0.97104	0.00419
0.94996	0.00769
0.92398	0.01193
0.89336	0.01670
0.85840	0.02198
0.81959	0.02776
0.77748	0.03393
0.73266	0.04038
0.68572	0.04694
0.63730	0.05341
0.58801	0.05954
0.53839	0.06504
0.48891	0.06964
0.43996	0.07312
0.39190	0.07536
0.34513	0.07632
0.29999	0.07596
0.25685	0.07433
0.21611	0.07151
0.17816	0.06753
0.14331	0.06243
0.11182	0.05631
0.08392	0.04930
0.05983	0.04156
0.03968	0.03329
0.02358	0.02472
0.01160	0.01615
0.00374	0.00799
0.00008	0.00099
0.00191	-0.00427
0.00984	-0.00852
0.02320	-0.01232
0.04178	-0.01547
0.06542	-0.01789
0.09395	-0.01957
0.12712	-0.02053
0.16464	-0.02085
0.20614	-0.02059
0.25118	-0.01986
0.29928	-0.01876
0.34988	-0.01742



0.40237	-0.01592
0.45612	-0.01433
0.51047	-0.01273
0.56476	-0.01115
0.61834	-0.00963
0.67056	-0.00821
0.72079	-0.00690
0.76840	-0.00570
0.81283	-0.00462
0.85355	-0.00365
0.89005	-0.00278
0.92187	-0.00193
0.94876	-0.00107
0.97048	-0.00035
0.98660	0.00003
0.99661	0.00006
1.00001	0.00000



#### B.4 Eppler 423 coordinates

X	Y
1.00000	0.00000
0.99655	0.00159
0.98706	0.00650
0.97304	0.01434
0.95530	0.02381
0.93358	0.03376
0.90734	0.04400
0.87671	0.05481
0.84221	0.06620
0.80436	0.07803
0.76373	0.09010
0.72090	0.10215
0.67644	0.11391
0.63092	0.12506
0.58491	0.13524
0.53893	0.14410
0.49347	0.15116
0.44870	0.15593
0.40464	0.15828
0.36149	0.15824
0.31947	0.15590
0.27885	0.15138
0.23987	0.14485
0.20286	0.13657
0.16816	0.12676
0.13611	0.11562
0.10700	0.10337
0.08106	0.09023
0.05852	0.07646
0.03953	0.06232
0.02421	0.04812
0.01262	0.03419
0.00481	0.02093
0.00071	0.00879
0.00002	0.00088
0.00033	-0.00192
0.00071	-0.00362
0.00125	-0.00518
0.00157	-0.00590
0.00194	-0.00656
0.00237	-0.00717
0.00288	-0.00771
0.00348	-0.00823
0.00415	-0.00874



0.00571	-0.00969
0.00751	-0.01057
0.01065	-0.01177
0.01365	-0.01266
0.02892	-0.01485
0.04947	-0.01482
0.07533	-0.01236
0.10670	-0.00740
0.14385	-0.00002
0.18727	0.00922
0.23688	0.01913
0.29196	0.02865
0.35163	0.03687
0.41449	0.04283
0.47867	0.04626
0.54275	0.04760
0.60579	0.04715
0.66690	0.04501
0.72503	0.04126
0.77912	0.03625
0.82836	0.03050
0.87219	0.02444
0.91012	0.01844
0.94179	0.01286
0.96692	0.00794
0.98519	0.00390
0.99629	0.00106
1.00000	0.00000



SOFTWARE

